Semi-Classical and Quantum Monte Carlo Simulations in Optical Lattices

Stephan Peter Winklbauer

Laser Cooling Group
Department of Physics and Astronomy
University College London

A thesis submitted to the University of London in the
Faculty of Science for the degree of Doctor of Philosophy

July 2003

Abstract

This thesis gives an account of work done on semi-classical and quantum Monte Carlo simulations in far-detuned optical lattices.

Firstly, the basic principles of laser cooling of atoms are presented including a short introduction to optical lattices in the near and far-detuned regime. A detailed analysis is made of the band-structure of optical lattices, using the Bloch formalism, and of the bound-state population distribution appropriate for a thermal sample of trapped atoms. Secondly, a general overview is given of the quantum Monte Carlo method for simulating the dynamics of atom-light interactions. This is followed by a detailed study of the concept of Raman cooling, which is a useful tool to prepare atoms in the ground motional state of the lattice and an important first step to achieving quantum state control with ultra-cold atoms. A simplified model of Raman cooling is introduced and simulated using the quantum Monte Carlo wave-function approach. Then the implementation of simulations of resolved-sideband Raman cooling based on this model is discussed as is how the results were used to optimize the experimental work done by our group. The results of these simulations show for the first time that the quantum Zeno effect has a crucial impact on the efficiency of Raman cooling experiments. Also the experimental measurements of the temperature of Raman sideband cooled atoms for a range of parameters are compared with theoretical results and show a good qualitative agreement.

Thirdly, the results of semi-classical numerical simulations of parametric excitation in optical lattices are presented. It is shown that the modulation of the potential can result in selective parametric excitation of trapped atoms. The theoretical results show good qualitative agreement with experiment.

The thesis is concluded with a description of possible avenues for future studies on quantum state control in optical lattices.

Contents

List of Figures

List of Tables

Acknowledgements

I would like to thank all the people who provided me with inspiration and help during my PhD studies at UCL. Especially, I want to thank my supervisor David Meacher. Firstly, for giving me the opportunity to undertake these studies in his group, and, secondly, for his patience and support over the years. The group dinners he cooked for us were always a welcome distraction from work and a good place to get to know the rest of the group better outside the work environment.

I also want to thank Philip Jones for his invaluable help and support. His expert knowledge of the experiment and dedication was always a big help when I needed it. Many thanks also to Silvia Bergamini, with whom I had the pleasure to work for some years on several projects, for the many fruitful discussions we had over lunch and in coffee breaks. Also thanks to Harry Saunder-Singer and Malika Goonasakera for their good work on the experimental side of our group. Lastly, I want to thank everybody not mentioned here who supported and helped me over the years, from the technicians in the department to the academic staff.

Lastly, I also want to thank Danny Dagan and John Keogh for their moral and personal support they offered me during my PhD.

Chapter 1

Principles of laser cooling

This section gives a short introduction to the atom-light interactions important in laser cooling. The chapter starts out with a short historical overview of laser cooling followed by a discussion of radiation pressure on a model two-level atom. Then the basic principles of Doppler-cooling are introduced and the mechanism underlying Sisyphus cooling discussed. The last part of the chapter consists of a discussion of the aims of this thesis and an outline of the rest of this work.

1.1 Introduction

This section gives a short introduction to the history of laser cooling. Several review papers have been written over the years and the more interested reader is invited to have a look at them [1–8].

The basic idea of laser cooling was first proposed by Hänsch and Schawlow [9] and independently by Wineland and Dehmelt [10] in 1975. Hänsch and

Schawlow showed that in a low-density gas of neutral atoms illuminated by intense, quasi-monochromatic light confined to the lower-frequency half of a resonance line's Doppler width, the translational kinetic energy can be transferred from the gas to the scattered light, this process ending when the atomic velocity is reduced to the ratio of the Doppler width to the natural line width. This type of cooling is nowadays know as Doppler cooling. The first experimental realisation of this idea was achieved by Chu *et al.* [11] in 1985. In their work, an atomic gas was cooled in three spatial dimensions by a viscous force arising from the radiation pressure exerted by a set of laser beams. The force is viscous in the sense that it, like a frictional force, is proportional to the speed of the atom, but does not achieve trapping of the atomic gas. The same group was also the first to observed optical trapping in an optical dipole force trap in 1986 [12]. At the same time Midgall *et al.* [13] succeeded in trapping neutral atoms magnetically and Pritchard *et al.* [14] proposed a stable cold atom trap based only on light forces. The latter proposal avoided problems arising from the optical Earnshaw theorem described in [15]. Shortly afterwards another major milestone was achieved with the first experimental realisation of a magneto-optical trap (MOT) [16]. This trap not only allowed cooling of an atomic gas, but provided for its spatial confinement.

In the following year, experiments carried out by Lett *et al.* [17] resulted in measured temperatures of ($43 \pm 20\,\mu$K), well below the theoretical limit predicted for Doppler cooling ($240\,\mu$K for sodium). This observation puzzled many researchers and led to the proposal of the Sisyphus cooling mechanism, based on the interplay of optical pumping and polarization gradients [18–21].

These processes were not included in the simple theoretical model of Doppler cooling. The beauty of Sisyphus cooling is that it has the potential of localizing the atoms to arrays of sub-wavelength sized potential wells known as *optical lattices.* The interested reader can find a more detailed discussion of optical lattices and the ideas behind them in the review articles [22–26]. This ability to confine atoms in periodic sub-wavelength potential wells made them an ideal testing ground for the investigation of properties of particles in periodic potentials. The advantage over conventional solid state physics materials is that the time-scales involved are much slower, facilitating the observation of processes not accessible in condensed matter experiments. Furthermore, optical lattices display almost perfect long-range correlations in particle positions, without defects, unlike solid-state crystalline materials. Studies of atoms in periodic structures bound by light showed the existence of Bloch oscillations [27], Wannier-Stark ladders [28, 29] and Landau-Zener tunnelling [30]. Optical lattices also have been used in proposals for quantum computation schemes [31, 32], as testing ground for quantum chaos [33] and lithography [34].

1.1.1 Atom-light interactions and light-induced forces

The fundamental principle of momentum conservation during the emission and absorption of a photon by an atom plays a crucial role in the mechanism of laser cooling. Most fundamentally, laser cooling describes the process of loss of translational energy associated with the centre-of-mass motion of atoms induced by repeated optically-induced transitions between their internal states. The important fact about laser cooling is that the velocity spread about the mean velocity of the cooled atomic sample needs to be reduced. Reduction of the mean velocity only, such in atomic beam slowing, is not laser cooling. To gain an understanding of the physics involved, we introduce a quantum mechanical description of the atom. The total wave-function is split into internal and external parts, i.e. $|\Psi\rangle = |p\rangle \otimes |\zeta, F, m\rangle$. Here $|p\rangle$ represents the external part determined by the atomic momentum wave-function $|p\rangle$ and $|\zeta, F, m\rangle$ the internal part, determined by the angular momentum F, the magnetic quantum number m and ζ describing the remaining internal variables.

We start by looking at the atom-light interaction first in the internal atomic states. Consider a two level atom with an excited state $|e\rangle$ and a ground state $|g\rangle$ interacting with a monochromatic quasi-resonant beam with frequency ω_L. The system is described completely by the angular frequency, ω_0, of the atomic transition, the natural line width of the excited state, Γ, the detuning of the laser beam with respect to the atomic transition, $\Delta = \omega_L - \omega_0$, and the Rabi frequency, Ω, for a transition with unit Clebsch-Gordan coefficient. From these parameters, one can define a saturation parameter by

$$s = \frac{\Omega^2/2}{\Delta^2 + \Gamma^2/4}. \tag{1.1}$$

For low saturation ($s \ll 1$) the population is mostly in the ground state, whereas for high saturation ($s \gg 1$) the population is equally distributed between ground and excited states. We can deduce the stationary excited-state population to be (cf. [4]):

$$\Pi_e = \frac{s}{2(1+s)}. \tag{1.2}$$

Hence the atoms emits $\Pi_e \Gamma$ spontaneous photons per time unit, each emission being preceded by the absorption of a photon. It is also worth noting that the square of the Rabi frequency is proportional to the laser intensity. This allows us to define the on-resonance saturation parameter (as in [22]):

$$s_0 \equiv \frac{2\Omega^2}{\Gamma^2} = \frac{I}{I_s}, \tag{1.3}$$

where

$$I_s \equiv \frac{\pi\, h\, \Gamma\, c}{2\, \lambda_L}. \tag{1.4}$$

Here h is the Planck constant, λ_L the wavelength of the laser light and c the speed of light.

Next we consider the external degrees of freedom of the atom-field interaction. As mentioned above, momentum conservation plays a central role in the atom-light interaction via the external wave-function. Consider an atom having a momentum of $\mathbf{p} = \hbar\, \mathbf{k}_a$ and incident photons having a momentum of $\hbar\, \mathbf{k}_{p_i}$. When the atom absorbs an incident photon, the total momentum of the atom-photon system after the absorption process changes to $\hbar\, \mathbf{k}_a' = \hbar\, \mathbf{k}_a + \hbar\, \mathbf{k}_{p_i}$. After a time interval proportional to the corresponding excited state life-time, Γ^{-1}, the atom spontaneously decays back to the ground state. The photons carries away a quantity of momentum $\hbar\, \mathbf{k}_{p_s}$, leaving the atom with a momentum of $\hbar\, \mathbf{k}_{\text{rec}} = \hbar\, \mathbf{k}_a' - \hbar\, \mathbf{k}_{p_s}$. Over many such scattering events the momentum kicks due to the spontaneously emitted photons cancel out on average (cf. 1.6) and the atom experiences a net momentum kick parallel to the direction of the momentum of the incident photons $\hbar \mathbf{k}_{p_i}$:

$$\hbar \mathbf{k}_{\text{rec}}^N = \hbar \mathbf{k}_a + N\hbar \mathbf{k}_{p_i} + \sum_{r=1}^{N} \hbar \mathbf{k}_{p_s}^r, \tag{1.5}$$

$$\lim_{\text{N large}} \sum_{r=1}^{N} \hbar \mathbf{k}_{p_s}^r = 0, \tag{1.6}$$

where N is the number of scattered photons from the incident beam and $\hbar \mathbf{k}_{p_i}$ the momentum transfer from the absorption of an incident photon; $\hbar \mathbf{k}_{p_s}^r$ is the momentum transfer from the r-th single spontaneous emission event and $\hbar \mathbf{k}_{\text{rec}}^N$ the recoil the atom experiences scattering N incident photons. It is seen that an atom in a travelling wave always absorbs photons along a determined direction and emits spontaneous photons isotropically. The net momentum transfer associated with this process is often referred to as radiation pressure. From 1.5 three more quantities can be defined. These are the recoil velocity $\mathbf{v}_{\text{r}}$, the recoil energy E_{r} which can be associated with a recoil temperature T_{r}:

$$\mathbf{v}_{\text{r}} = \frac{\hbar|\mathbf{k}_{\text{rec}}|}{M} = \frac{\hbar k_0}{M}, \tag{1.7}$$

$$E_{\text{r}} = \frac{\hbar^2 k_0^2}{2M}, \tag{1.8}$$

$$T_{\text{r}} = \frac{M v_{\text{r}}^2}{k_B}, \tag{1.9}$$

where M is the mass of the atom and k_B the Boltzmann factor. The force on the atom from one of the laser beams is proportional to the rate of spontaneous emission, $\Gamma\Pi_e$, times the momentum of a single incident photon from this beam, $\mathbf{p}_{\mathrm{ph}} = \hbar\mathbf{k}$ [4]

$$\mathbf{F}_{\mathrm{dissip}} = \Gamma\Pi_e\hbar\mathbf{k}_{p_i} = \frac{\Gamma}{2}\hbar\mathbf{k}_{p_i}\frac{s}{1+s}. \tag{1.10}$$

The total dissipative force the atoms experiences from all incident laser beams is then the sum of all $\mathbf{F}_{\mathrm{dissip}}$ of each individual incident beam and given by

$$\mathbf{F}_{\mathrm{dissip}} = \sum_{\mathbf{k}_{p_i}}\Gamma\Pi_e\hbar\mathbf{k}_{p_i} = \sum_{\mathbf{k}_{p_i}}\frac{\Gamma}{2}\hbar\mathbf{k}_{p_i}\frac{s}{1+s}. \tag{1.11}$$

In the low-saturation limit ($s \ll 1$) equation 1.10 takes the form

$$F_{\mathrm{dissip}} \approx \frac{\Gamma}{2}\hbar\mathbf{k}_{p_i}s = \frac{\Gamma}{4}\hbar\mathbf{k}_{p_i}\frac{\Omega^2/\Gamma^2}{\Delta^2/\Gamma^2 + 1/4}. \tag{1.12}$$

Taking caesium as an example with $\Delta = -\frac{\Gamma}{2}$ and $\Omega = \Gamma$ the dissipative force experienced by the atom is about $3000\,M_{\mathrm{Cs}},\mathbf{g}$. A study of the heating and cooling processes involved [24] [35] showed that in 1D for $\Delta = -\frac{\Gamma}{2}$ the minimum temperature is achieved and is given by

$$T_{\mathrm{D}} = \frac{\hbar\Gamma}{2k_B}. \tag{1.13}$$

For caesium the minimum temperature, the Doppler temperature, defined as $T_D = 125\,\mu\mathrm{K}$, corresponding to an atomic root-mean-square velocity of about $9\,\mathrm{cm\,s^{-1}}$. Hence the minimum achievable temperature is limited by the width of the cooling transition used. The first experimental evidence of radiation pressure was obtained in 1933 in an experiment [36] using atomic beams. This ability to change the atomic momentum allows the acceleration and deceleration of atomic beams, but as mentioned above, it doesn't necessarily give rise to the cooling of an atomic vapor. For cooling the velocity distribution must be narrowed and not only the mean value of the velocity reduced. Further research into possible schemes led to the idea of Doppler-cooling.

1.1.2 Doppler cooling

Doppler cooling has the ability to narrow the atomic velocity distribution of atomic vapors and was first proposed in 1975 by Hänsch and Schawlow [9]. It relies on the Doppler effect to make the scattering force velocity dependent. An atom moving with a velocity $\mathbf{v}_a$ will see the frequency of incident photons of a laser beam shifted by $\nu' = \nu\left(1 \mp \frac{\mathbf{k}_p \cdot \mathbf{v}_a}{c}\right)$, where $\mathbf{k}_p$ is the wave vector of the incident photon. The direction of $\mathbf{k}_p$ is defined to be the z-direction in the following discussion.

It is worth noticing in 1.10 that, if the incident laser beam is red-detuned ($\Delta < 0$) then the atoms experience a net force against their direction of motion along the z-direction [4]. Cooling is achieved during the absorption-emission cycle. Here the atoms always absorb red-detuned photons, but on average emit photons with a frequency of the respective atomic transition. Hence the emitted photons carry away more energy than the atoms gain through the absorption process. The result is an optical molasses, where a viscous type of force slows the atoms down. The name optical molasses is derived from the fact that the atoms experience a viscous force, i.e. $\mathbf{F} \propto \mathbf{v}$. A detailed theoretical study of Doppler cooling can be found in [26]. The first

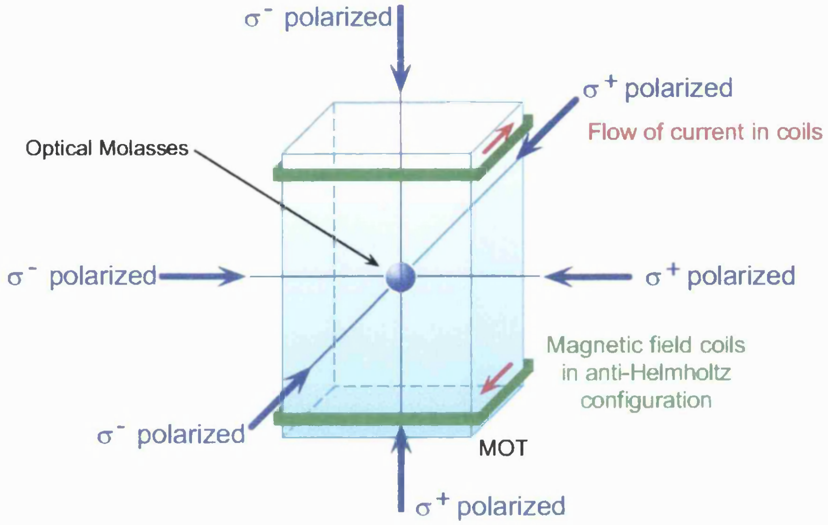

Figure 1.1: Schematic diagram of a MOT. The two coils carry currents flowing in opposite direction with respect to each other to provide a magnetic field gradient. Three pairs of counter-propagating laser beams along the principal axis provide a 3D radiation pressure force. See text for detailed discussion.

experimental realization was achieved in 1985, sodium atoms being cooled with a dye laser [11]. Theoretical work carried out to find a stable configuration of cooling and trapping, obtained only by radiation forces, demonstrated that it is impossible to trap a two-level atom in a stable configuration by radiation pressure alone induced by a set of laser beams. This is known as the *optical Earnshaw theorem* [15]. Research on how to bypass this limitation led to the suggestion by Dalibard of a magneto-optical trap.

1.1.3 The magneto-optical-trap (MOT)

The two-level-approximation correctly describes the Doppler cooling mechanism. In real experiments often atoms with more complex energy level structures are used. The atom used in our experiment is caesium, which possesses

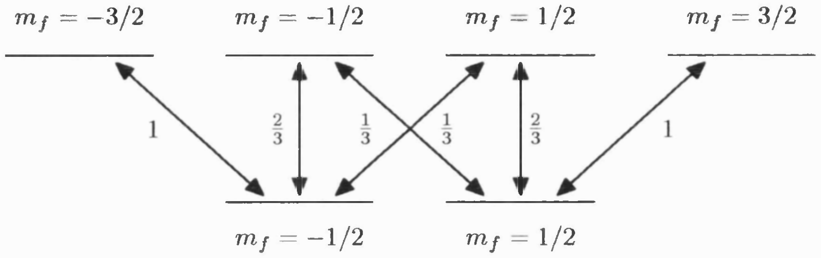

Figure 1.2: Energy-level diagram and corresponding Clebsch-Gordan coefficients squared for a $J_g = \frac{1}{2} \rightarrow J_e = \frac{3}{2}$ transition.

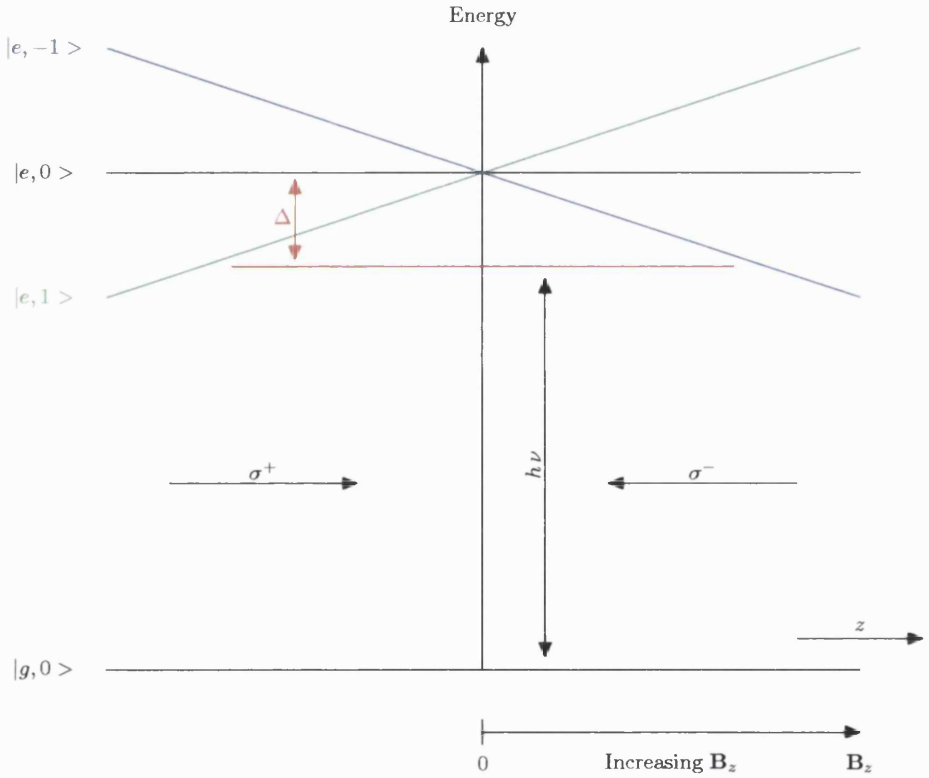

Figure 1.3: Schematic energy level diagram for a magneto-optical trap, also know as a MOT. An atom with a $F_g = 0 \rightarrow F_e = 1$ transition transverses a region with an inhomogeneous magnetic field. The B-field is zero at the centre of the trap introducing a position dependent energy level shift (Zeeman shift) depending on the magnetic quantum number m_f of the level. Two counter-propagating beams with opposite circular polarization detuned from resonance by Δ are chosen in a way as to bring closer to resonance the photons which propagate towards the centre of the trap relative to the position of the atom. See text for a detailed description.

multiply degenerate Zeeman sub-levels in the ground and excited states. This multiplicity in the energy level structure coupled with the angular momentum conservation principle introduces two new phenomena into the model system. There exist selection rules for the various possible transitions arising from the scattering of photons of differing polarizations. The absorption of a σ^p (σ^m) polarized photon increases (reduces) the z-component of the atomic angular momentum, whereas a π-polarized photon does not change it. In addition the different transition amplitudes are weighted by vector-coupling coefficients, better known as Clebsch-Gordan coefficients. The Clebsch-Gordan coefficients govern the coupling strengths of the different possible transitions and have equal value for absorption on the transition $|F, m_F\rangle \rightarrow |F', m'\rangle$ and emission of a photon on the same transition. Figure 1.2 on the page before shows the energy-level diagram of an atom on a $J_g = \frac{1}{2} \rightarrow J_e = \frac{3}{2}$ transition and the corresponding Clebsch-Gordan coefficients squared. The two factors described above govern optical pumping and its effect on the Zeeman level populations as described in [37].

The principle of a MOT is to exert a force on the atoms directed to the centre proportional to their excursion from the trap centre. This can be achieved either by changing the stationary populations of the Zeeman sub-levels with the aid of optical pumping [14] or by inducing a position dependent shift of the energy levels of the trapping transition with the aid of an inhomogenous magnetic field. Figure 1.1 on page 25 shows the experimental implementation of a MOT confining atoms in 3D. The operation of a MOT can be understood in terms of radiation pressure effects similar to those at work in Doppler cooling in optical molasses. However, it has been demonstrated that polarization gradient cooling is also occurring at the trap centre. Let us assume an atom with zero spin on a $J = 0 \rightarrow J' = 1$ transition as shown in figure 1.3 on page 26. A static magnetic field $\mathbf{B}(z) = b\, z\, \hat{\mathbf{z}}$ is applied (with b the field gradient), which induces a position dependent energy shift to the atomic energy levels. The centre of the trap is located at $z = 0$. Two counter-propagating laser beams having σ^+ and σ^- polarization respectively provide a friction force as described above. The frequency of the laser beams are detuned to the red side of the resonance transition. At the centre of the trap the radiation pressure experienced by the atom from each of the laser beams cancel. If the atom is positioned away from the centre of the trap, the atomic levels experience a Zeeman energy shift proportional to their magnetic quantum number. The energy level interacting with the laser beam travelling towards the trap centre is shifted more into resonance than the energy level interacting with the laser beam travelling away from the trap centre. The atom experiences a restoring force which pushes it to the centre of the trap. Notice also that the linear magnetic field gradient induces a linear spatial variation of the Zeeman shifts. Thus the net force has a restoring character and varies linearly in space with the distance the atoms are away from the trap centre.

This method can be easily generalised to 3D by using a quadrupolar magnetic field configuration and three pairs of counter-propagating laser beams. The first experimental implementation of a MOT loaded from an atomic beam was reported in [16] and the first MOT loaded from a low-pressure vapor cell in [38]. A key experiment in 1988 demonstrated that temperatures below the theoretical limit deduced from the Doppler-cooling model could be achieved [17]. An explanation of this experimental observation was proposed by two research groups independently in 1989 [19, 20] and is discussed in the next section.

1.1.4 Sisyphus polarization-gradient cooling

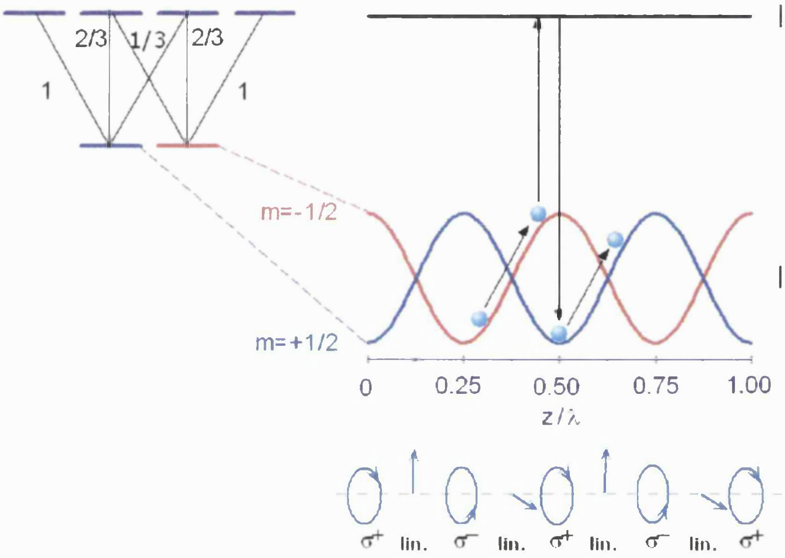

Figure 1.4: The figure shows the level scheme used in the simplest angular momentum configuration giving rise to Sisyphus cooling. The polarization gradients are created by a lin⊥lin laser beam configuration. Zero light shift is between the excited level $|e\rangle$ and the ground state level $|g\rangle$. The ground state levels are red detuned.

Most atoms used in real experiments, like caesium, possess a Zeeman structure in the ground state. In a general beam configuration the laser polarization varies in space, thus inducing position dependent light-shifts and optical pumping rates for the different magnetic sub-levels of the ground state. These two effects combined are the essential ingredients for what is known as polarization-gradient cooling. The type of polarization-gradient cooling that

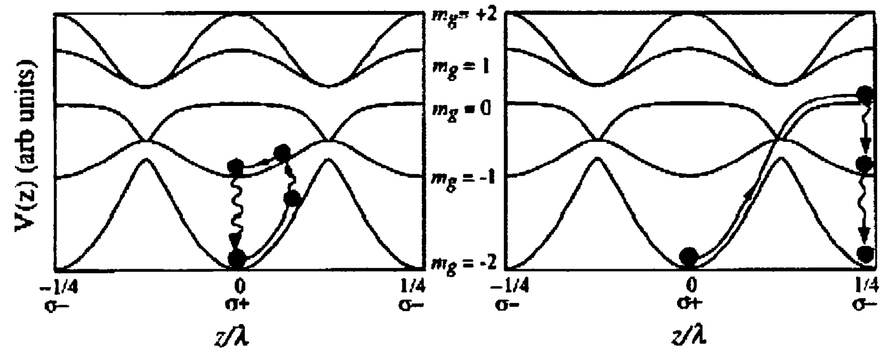

(a) (b)

Figure 1.5: The figure shows the semiclassical pictures of Sisyphus cooling on a $J_g = 2 \rightarrow J_e = 3$ transition. (a) "local cooling" due to optical pumping within a given lattice site. (b) "hopping cooling": The motional coupling between causes transitions between the adiabatic potentials and atoms are optically pumped between lattice sites. Taken from [39].

is relevant to the formation of optical lattices is Sisyphus cooling. For simplicity we consider here the 1D laser configuration shown in figure 1.4, which shows the level scheme of the simplest angular momentum configuration giving rise to Sisyphus cooling. Two counter-propagating laser beams having orthogonal linear polarizations and equal frequency and intensity travelling along the z-direction create a polarization-gradient with a periodicity of $\frac{\lambda}{4}$ between sites of opposite circular polarization, where λ is the optical wavelength. The change in polarization is a result of the phase shift between the two waves varying linearly with z [40].

To elucidate the mechanism behind Sisyphus cooling, consider an atom at a site of σ^- polarization of the optical field, in the internal state $|m = -1/2\rangle$ and moving to the right of figure 1.4. Sites of maximum light-shifts are located at sites of pure circular polarization and form a string of potential wells. The atom moves up the potential hill out of the σ^- well into a regions of increasing σ^+ light. When the atom climbs the potential hill it converts kinetic energy into potential energy. Also the probability of scattering a photon increases more and more and the atom is eventually pumped into the state $|m = +1/2\rangle$. In this anti-Stokes Raman process, the energy of the spontaneously emitted photon is larger than the energy of the absorbed laser photon. The atom looses an amount of energy of order of the depth of the optical potential wells[1]. When the kinetic energy of the atoms is reduced below the well depth of the optical potential, the atoms become trapped in the wells. In general the atoms climb more potential hills than they decend, a situation reminiscent of the predicament of Sisyphus in Greek mythology, who was doomed to roll a stone up a hill only to have to start again at the bottom of the hill after reaching the top.

It is worth noting that the situation described above does not account for the cooling mechanism operating in atoms with angular momentum $F \geq 1$. In the situation described above the cooling mechanism relied on atoms propagating over many lattice wells to take part in the cooling cycle. In atoms with angular momenta $F \geq 1$, there exists the possibility of local cooling, as an atom can undergo a cooling cycle without changing potential wells. Consider for example a caesium atom with an angular momentum of $F = 4$. The ground state manifold is composed of nine degenerate Zeeman sub-levels. When the atoms interacts with the polarization gradients created by the beam configuration described above, each magnetic sub-level experiences dif-

---

[1] The potential depth is defined as the energy difference between the absolute maximum and minimum of the light shifted potentials.

ferent gradients depending on its magnetic quantum number. This situation is shown in figure 1.5 on page 30.

In the local cooling scheme, the atoms rise steep potential hills. The atom is eventually optically pumped onto another potential surface with a minimum at the same spatial location and starts to descend to the bottom of the shallower potential surface. There it is optically pumped back to the lowest potential surface. This comprises one cooling cycle in the local cooling scheme. More kinetic energy is lost in the steep climb than is gained in the descent due to the different curvature of the potential surfaces. Hence energy is dissipated on average in the optical pumping process.

1.2 Aims of this thesis and outline

In general far-detuned optical lattices present an ideal system with which to investigate and develop techniques for coherent control of motional and internal states of trapped atoms. The main advantage of non-dissipative optical potentials is their conservative nature. In them the spontaneous scattering rate is highly suppressed compared to the near-detuned case. Thus decoherence from spontaneous emission is strongly suppressed. Additionally the atoms are isolated from their environment and from the other atoms, allowing for an enhanced coherent life-time of the atomic state. The first step to quantum state control of atoms in far-detuned optical potentials is their preparation in a chosen motional state.

In this thesis I present work I have done on quantum state preparation and manipulation in far-detuned optical lattices. The main goal is to find a suitable set of parameters to optimize 2D resolved-sideband Raman cooling in the experiments of our group. First in chapter 2 an understanding of the properties of the optical lattice used in our experiments are gained through deducing the light-shifted potential surfaces arising from a given lattice beam configuration. This allowed us to calculate the corresponding band-structure and is followed by a study of the population distribution in a harmonic and anharmonic optical potential and the connection between the concepts of vibrational and kinetic temperature.

Chapter 3 provides an introduction to resolved-sideband Raman cooling and deduces a model used in subsequent QMCWF simulations. The results of these simulations offer the possibility to estimate *a priori* an optimal set of parameters and guidance for our experiment. This is followed by the suggestion and discussion of a new beam configuration for 3D resolved-sideband Raman cooling.

Chapter 4 introduces the *Quantum Monte Carlo Wavefunction Method* (aka. QMCWF Method) and outlines the steps needed to implement a simulation using this formalism. The dependence of the results on the parameters are discussed and for the first time the influence of the quantum Zeno effect on the resolved-sideband Raman cooling efficiency is shown. This is followed up by a short historical overview and discussion of the *Quantum Zeno Effect.* Additionally a way to minimize that effect is provided.

Chapter 5 discusses theoretical work I have done for experiments undertaken by Silvia Bergamini [41]. They include simulations of band population measurements using magnetic fields (Zeeman state analysis), which are modelled using semi-classical Monte-Carlo simulations. These allow us to better understand the time-of-flight measurements obtained in those experiments and assess the efficiency of the measurement method used. Also these simulations allow us to determine a convenient set of parameters to implement the Zeeman state analysis set-up. The remainder of chapter 5 is dedicated to an investigation of the effects of parametric heating in a far-detuned optical lattice induced by intensity fluctuations of the laser beams. These parametric excitation experiments allow us also to estimate the anharmonicity of a lattice potential and provide us with a tool either to selectively cool or to heat a sample of trapped atoms.

The last chapter provides an outlook into the future and gives a conclusion encompassing the whole thesis.

Chapter 2

Optical lattices

In this chapter I discuss the cooling and trapping of atoms in periodic structures bound by light, also know as optical lattices. In brief a spatially dependant optical field composed of the lattice beams creates position dependent AC Stark shifts in the atomic energy levels with periodicity on the scale of the optical wavelength. The potentials created in this way can trap atoms with velocities below the critical escape velocity of the lattice which is similar to the well depth, typically of order of magnitude of some tens to hundreds of E_R. The lattices created are ideal lattices and have perfect periodicity. To compare the situation with condensed matter physics, the optical lattice plays the role of the atomic potential and the atoms interact with it as the electrons do in a solid. Contrary to solid state physics where an increasing number of lattice defects (empty atomic positions) result in an increasing perturbation of the potential, in optical lattice the situation is opposite. At low occupancy the optical lattice potential is hardly perturbed by the interaction with the atoms. The higher the occupancy is, the more the optical lattice potential gets perturbed. In typical optical lattice encountered in experiments, the occupancy is about 1 in 10, i.e. one atom occupies every tenth potential well on average.

Many effects observable in solid state physics like tunnelling, paramagnetism and diamagnetism, and transport phenomena can also be observed in optical lattices. The advantage is that the periodicity in the latter is three orders of magnitude longer than in solids. This results in observables have time scales of the same order of magnitude slower. Hence these effects can be measured more readily than in condensed matter physics.

This chapter is structured in the following way. First I will derive an expression for the light-shift operator $\mathbf{\Lambda}_L$ for the case of a near-resonant optical field. Then the scheme is extended to far-detuned optical lattices, often called non-dissipative optical lattices[1]. This is achieved by detuning to the red from the resonance frequency of the lattice trapping resonance frequency as shown in figure 2.1 on the next page. This is followed by a discussion of different experimental configurations in 1D, 2D and 3D and their corresponding optical potential. These examples are used to illustrate how to calculate the optical potential the atoms see from an arbitrary beam configuration. From there I move on to deduce the band-structure in these optical potentials using the Bloch formalism and introduce a general algorithm implemented in Matlab to calculate the corresponding band-structure of an optical lattice created by an arbitrary beam configuration. The final part of the chapter is dedicated to an estimation of the vibrational level populations in an optical lattices using

---

[1] due to their nature of reducing the impact of heating by scattering of lattice photons and the related spontaneous emission process.

a given band-structure.

2.1 Light shifts in optical lattices

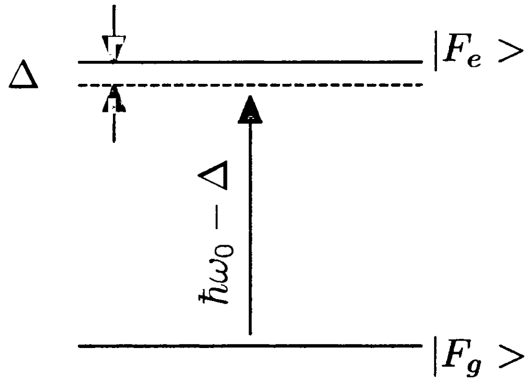

Figure 2.1: This figure shows the ground and excited state levels, $|F_g\rangle$ and $|F_e\rangle$ respectively, of a multi-level atom with hyperfine structure. Here F is the total angular momentum of the atom. The level $|F_g\rangle$ is $(2F_g + 1)$-fold degenerate and the level $|F_e\rangle$ is $(2F_e + 1)$-fold degenerate. A red-detuned laser beam with detuning Δ interacts with the system.

In this section I derive an expression for the light-shift operator Λ_L in a near-resonant optical lattice. This expression is then used to calculate the light-shifts experienced in the ground state hyperfine manifold. Figure 2.1 shows the two level scheme we adopt in this section. The system has a ground state and an excited state, $|F_g\rangle$ and $|F_e\rangle$ respectively. Each manifold is composed of $(2F + 1)$ degenerate energy levels. In the case of caesium on the $|F = 4\rangle \leftrightarrow |F = 5'\rangle$ transition the ground and excited states are composed of nine and eleven degenerate hyperfine levels respectively. A red-detuned[2] laser beam interacts with the system.

---

[2] The frequency of the laser beam is lower than the resonance frequency.

The derivation is split into five parts. First the form of the atom-light interaction in the electric-dipole approximation is outlined. Then the equation of motion for the ground state density matrix is derived initially neglecting the degeneracy of the ground and excited state manifolds. The third step is the adiabatic elimination of the excited state and all its coherences from the density matrix. The next step is to put back the degeneracy of the ground state manifold. Finally, the level shifts are deduced by neglecting the ground state relaxation terms, i.e. optical pumping.

2.1.1 The electric-dipole interaction

In this section we consider the interaction Hamiltonian of an atom interaction with an optical field. First an expression for the optical field operator is deduced followed by the derivation of an expression for the atomic dipole operator. We start out with an optical field $\mathbf{E}$ created by the interaction of two counter-propagating laser beams. The optical field can then be written as

$$\mathbf{E}_L = \frac{1}{2} E_L \hat{\varepsilon}_L e^{-i\omega t} + c.c.,$$

where $\hat{\varepsilon}_L$ is a unit vector pointing in the same direction as the polarization of the corresponding laser beams. By changing from the cartesian to the circular basis

$$\mathbf{E}_L = \frac{1}{2} E_L \sum_{k=-1,0,+1} \varepsilon_k \hat{\mathbf{e}}_k \hat{\mathbf{a}}_k e^{-i\omega t} + c.c.. \tag{2.1}$$

In this equation the $\{\mathbf{e}_k\}$ represent the unit vectors of the circular basis. This basis consists of the vectors $\mathbf{e}_-$,$\mathbf{e}_+$ and $\mathbf{e}_0$ defined as

$$\mathbf{e}_\pm = \mp\frac{1}{\sqrt{2}}\left(\hat{\mathbf{x}} \pm i\hat{\mathbf{y}}\right),$$

$$\mathbf{e}_0 = \hat{\mathbf{z}}.$$

The unit vectors are defined in a way so that $\mathbf{e}_\pm$ represents $\sigma^\pm$-light and $\mathbf{e}_0$ for π-light. It is useful in calculations to remember that

$$\hat{\mathbf{e}}_+^* = -\hat{\mathbf{e}}_-, \quad \hat{\mathbf{e}}_-^* = -\hat{\mathbf{e}}_+, \quad \hat{\mathbf{e}}_z^* = \hat{\mathbf{e}}_z.$$

In the following it is assumed that the single beam amplitude E_L is real and that the amplitudes of the polarization components comprising the beam polarization are normalized to one, i.e.

$$\sum_k |\varepsilon_k|^2 = 1.$$

To make the notation more manageable the raising and lowering operators[3] are normalized so that

$$\mathbf{a}_k\,|n\rangle = |n-1\rangle\,, \tag{2.2}$$

and the normalization factor is subsequently absorbed into E_L. Using the above results, the optical field can be written as

---

[3] which are also called photon creation and destruction operators.

$$\begin{aligned}
\mathbf{E} \; &= \mathbf{E}^{+} e^{-i\omega t} + \mathbf{E}^{-} e^{+i\omega t}, \qquad (2.3)\\
\mathbf{E}^{+} &= \sum_{k} \varepsilon_k \hat{\mathbf{e}}_k \mathbf{a}_k,\\
\mathbf{E}^{-} &= \sum_{k} \varepsilon_k^{*} \hat{\mathbf{e}}_k^{*} \mathbf{a}_k^{+}.
\end{aligned}$$

The atomic dipole-moment is defined as

$$\mathbf{d} = -e\,\mathbf{r}. \qquad (2.4)$$

Here e is the elementary charge of an electron and $\mathbf{r}$ the position operator of the valence electron. The operator $\mathbf{d}$ causes transitions between different states. Remembering that $\sum_i |J_i, m_i\rangle \langle J_i, m_i| = 1$ the atomic dipole moment can be written as

$$\begin{aligned}
\mathbf{d} = -e\,\mathbf{r} = &\sum_{i,j=g,e} |J_i\, m_i\rangle \langle J_i\, m_i\,|\mathbf{d}|J_j\, m_j\rangle \langle J_j\, m_j|\\
&= \sum_{k} d_k \hat{\mathbf{e}}_k\\
&= \sum_{\substack{i,j=g,e\\ k}} |J_i\, m_i\rangle \langle J_i\, m_i\,| d_k |J_j\, m_j\rangle \langle J_j\, m_j|\, \hat{\mathbf{e}}_k\\
&= \sum_{\substack{i,j=g,e\\ k}} C_{J_i\, m_i}^{J_j\, m_j\, 1\, k} D\, |J_i\, m_i\rangle \langle J_j\, m_j|\, \hat{\mathbf{e}}_k, \qquad (2.5)
\end{aligned}$$

where we have assumed the Wigner-Eckart theorem and D is the reduced dipole operator matrix element $D \equiv \langle J_g \,\|d\|\, J_e \rangle$ with $D^\dagger = D$.[4] In equation 2.5 the diagonal terms are zero, since the corresponding Clebsch-Gordan coefficients are, and the equation for the atomic dipole operator can be split into two distinctive parts. This leads to

$$\begin{aligned}\mathbf{d} &= \sum_k C^{J_e\, m_e\, 1\, k}_{J_g\, m_g}\, D\, |J_g\, m_g\rangle \langle J_e\, m_e|\, \hat{\mathbf{e}}_k \\ &+ \sum_k C^{J_g\, m_g\, -1\, k}_{J_e\, m_e}\, D\, |J_e\, m_e\rangle \langle J_g\, m_g|\, \hat{\mathbf{e}}_k \\ &= \mathbf{d}_- + \mathbf{d}_+ . \end{aligned} \tag{2.6}$$

The calculation of Clebsch-Gordan coefficients can be quite tedious and it is more convenient to refer to published tables. Having both these ingredients, the optical field operator and the atomic dipole operator, an expression for the interaction Hamiltonian can be derived. The operator depends on the scalar product of both and substituting equations 2.3 and 2.6, it is given by

---

[4] It states that for any vector operator $\hat{\mathrm{o}}$ with components $\hat{\mathrm{o}}_k$ the relation

$$\langle J_1\, m_1 \,|\hat{\mathrm{o}}|\, J_2\, m_2 \rangle = C^{J_2\, m_2\, 1\, k}_{J_1\, m_1} \langle J_1 \,\|o\|\, J_2 \rangle$$

holds. In this relation the first term is a Clebsch-Gordan coefficient and the second one the reduced matrix element. The two angular momenta linked together via the operator are $|J_i\, m_i\rangle + |1\, k\rangle \rightarrow |J_j\, m_j\rangle$. The Clebsch-Gordan coefficients are only different from zero if the angular momenta involved satisfy the *triangle rule*, i.e. are a linear combination of each other[5], $\Delta(J_1 J_2 1)$, and if, in addition, $m_1 = m_2 + k$.

$$\begin{aligned}\hat{\mathbf{H}}_i &= -\mathbf{E}\cdot\mathbf{d}\\ &= -\left(\mathbf{E}^{+}e^{-i\omega t}+\mathbf{E}^{-}e^{i\omega t}\right)\left(\mathbf{d}^{+}+\mathbf{d}^{-}\right)\\ &= \Big(\left[\mathbf{E}^{+}\cdot\mathbf{d}^{+}+\mathbf{E}^{+}\cdot\mathbf{d}^{-}\right]e^{-i\omega t}\\ &\quad+\left[\mathbf{E}^{-}\cdot\mathbf{d}^{+}+\mathbf{E}^{-}\cdot\mathbf{d}^{-}\right]e^{i\omega t}\Big).\end{aligned} \tag{2.7}$$

The Hamiltonian has four distinct terms of which two can be eliminated by using the rotating-wave approximation. The Hamiltonian then takes the form

$$\begin{aligned}\hat{\mathbf{H}}_i^R &= -\left(\mathbf{E}^{+}\cdot\mathbf{d}^{+}\right)e^{-i\omega t}-\left(\mathbf{E}^{-}\cdot\mathbf{d}^{-}\right)e^{i\omega t}\\ &= -\mathbf{b}e^{-i\omega t}-\mathbf{b}^{\dagger}e^{i\omega t}\quad ,\end{aligned} \tag{2.8}$$

where the operators $\mathbf{b}$ and $\mathbf{b}^{\dagger}$, are introduced, which are the raising and lowering operators previously, but which drive transitions in which a quantum of angular momentum is either gained or lost via a dipole transition. They are $\mathbf{b}^{\dagger}=(\mathbf{E}^{-}\cdot\mathbf{d}^{-})$ and $\mathbf{b}=(\mathbf{E}^{+}\cdot\mathbf{d}^{+})$ respectively. This leads us to the next step, the equation of motion of the ground state density matrix, where the interaction Hamiltonian 2.8 is applied to the evolution of the density matrix of the system.

2.1.2 Equation of motion of the ground state density matrix

The density matrix can be written in matrix form as

$$\hat{\varrho} = \begin{pmatrix} \hat{\varrho}_{gg} & \hat{\varrho}_{ge} \\ \hat{\varrho}_{eg} & \hat{\varrho}_{ee} \end{pmatrix}, \tag{2.9}$$

where $\hat{\varrho}_{gg}$ is the 9×9 ground state density sub-matrix block and $\hat{\varrho}_{ee}$ the 11×11 exited state one. To make the derivation more tractable, the structure in the ground and excited states is at first neglected and then reintroduced later. The density matrix formalism is completely equivalent and replaces the Schrödinger equation formalism with a master equation description. The differential equation which describes the dynamics of the system is now

$$\frac{d\hat{\varrho}}{dt} = -\frac{i}{\hbar}\left[\hat{\mathbf{H}}, \hat{\varrho}\right] + \left(\frac{d\hat{\varrho}}{dt}\right)_{\text{relax}}, \tag{2.10}$$

where the Hamiltonian of the system is given by

$$\hat{\mathbf{H}} = \hat{\mathbf{H}}^0 + \hat{\mathbf{H}}_{AF}, \tag{2.11}$$

where $\hat{\mathbf{H}}^0$ is the atomic Hamiltonian of the isolated system and $\hat{\mathbf{H}}_{AF}$ the Hamiltonian of the atom-field interaction. By writing out the above matrix equation it can be seen that it separates into four expressions, one for each $\hat{\varrho}_{ij}$. To deduce these four equations, firstly we consider the left-hand side of equation 2.10 and secondly the right-hand side. The last step is to split the full matrix equation into four separate equations for each component of the density matrix 2.9. The left hand side becomes

$$\frac{d\hat{\varrho}}{dt} = \begin{pmatrix} \frac{d\hat{\varrho}_{gg}}{dt} & \frac{d\hat{\varrho}_{ge}}{dt} \\ \frac{d\hat{\varrho}_{eg}}{dt} & \frac{d\hat{\varrho}_{ee}}{dt} \end{pmatrix}, \tag{2.12}$$

$$\hat{\mathbf{H}} = \begin{pmatrix} \hat{\mathbf{H}}_{gg} & \hat{\mathbf{H}}_{ge} \\ \hat{\mathbf{H}}_{eg} & \hat{\mathbf{H}}_{ee} \end{pmatrix}. \tag{2.13}$$

On the right hand side first the commutator is considered and then the relaxation term. The density matrix 2.9 and Hamiltonian matrix 2.13 are substituted into the commutator definition, as shown in appendix B.1, and substituted into 2.10 giving

$$\begin{pmatrix} \frac{d\hat{\varrho}_{gg}}{dt} & \frac{d\hat{\varrho}_{ge}}{dt} \\ \frac{d\hat{\varrho}_{eg}}{dt} & \frac{d\hat{\varrho}_{ee}}{dt} \end{pmatrix} = \begin{pmatrix} a_1 & a_2 \\ a_3 & a_4 \end{pmatrix} - \left(\frac{d\hat{\varrho}}{dt}\right)_{\text{relax}}, \tag{2.14}$$

$$a_1 = \hat{\mathbf{H}}_{ge}\hat{\varrho}_{eg} - \hat{\varrho}_{ge}\hat{\mathbf{H}}_{eg}, \tag{2.15}$$

$$a_2 = \hat{\mathbf{H}}_{gg}\hat{\varrho}_{ge} + \hat{\mathbf{H}}_{ge}\hat{\varrho}_{ee} - \hat{\varrho}_{gg}\hat{\mathbf{H}}_{eg} - \hat{\varrho}_{ge}\hat{\mathbf{H}}_{ee}, \tag{2.16}$$

$$a_3 = \hat{\mathbf{H}}_{eg}\hat{\varrho}_{gg} + \hat{\mathbf{H}}_{ee}\hat{\varrho}_{eg} - \hat{\varrho}_{eg}\hat{\mathbf{H}}_{gg} - \hat{\varrho}_{ee}\hat{\mathbf{H}}_{eg}, \tag{2.17}$$

$$a_4 = \hat{\mathbf{H}}_{eg}\hat{\varrho}_{ge} - \hat{\varrho}_{eg}\hat{\mathbf{H}}_{ge}. \tag{2.18}$$

Separating all the terms for the different parts of the matrix equation we get the following differential equations for the evolution of the excited state density matrix:

$$\frac{d\hat{\boldsymbol{\varrho}}_{ee}}{dt} = -\frac{i}{\hbar}\left\{\hat{\mathbf{H}}_{eg}\,\hat{\boldsymbol{\varrho}}_{ge} - \hat{\boldsymbol{\varrho}}_{eg}\,\hat{\mathbf{H}}_{ge}\right\} - \Gamma'\,\hat{\boldsymbol{\varrho}}_{ee} \tag{2.19}$$

$$= -\frac{i}{\hbar}\left\{-\left(\mathbf{E}^{+}\cdot\mathbf{d}^{+}\right)\tilde{\boldsymbol{\varrho}}_{ge} + \tilde{\boldsymbol{\varrho}}_{eg}\left(\mathbf{E}^{-}\cdot\mathbf{d}^{-}\right)\right\} - \Gamma'\,\hat{\boldsymbol{\varrho}}_{ee}, \tag{2.20}$$

$$\hat{\boldsymbol{\varrho}}_{ge} = \tilde{\boldsymbol{\varrho}}_{ge}\,e^{i\omega t}, \tag{2.21}$$

$$\hat{\boldsymbol{\varrho}}_{eg} = \tilde{\boldsymbol{\varrho}}_{eg}\,e^{-i\omega t}. \tag{2.22}$$

In the differential equation for the excited state density matrix the relaxation term describes spontaneous emission. This means it can be written as $\left(\frac{d\hat{\boldsymbol{\varrho}}}{dt}\right)_{\text{relax}} = \Gamma\hat{\boldsymbol{\varrho}}_{ee}$. Also to make the notation simpler the $\hat{\boldsymbol{\varrho}}_{ij}$ in 2.20 are replaced by 2.21 and 2.22. Next we consider the matrix equations for the ground and excited state coherences $\hat{\boldsymbol{\varrho}}_{ge}$ and $\hat{\boldsymbol{\varrho}}_{eg}$,

$$\frac{d\hat{\boldsymbol{\varrho}}_{eg}}{dt} = \frac{d\tilde{\boldsymbol{\varrho}}_{eg}}{dt}e^{-i\omega t} - i\omega_L\tilde{\boldsymbol{\varrho}}_{eg}e^{-i\omega_L t} \tag{2.23}$$

$$\begin{aligned} &= -\frac{i}{\hbar}\left\{\hat{\mathbf{H}}_{eg}\hat{\boldsymbol{\varrho}}_{gg} - \hat{\boldsymbol{\varrho}}_{ee}\hat{\mathbf{H}}_{ee}\right\} - \frac{\Gamma}{2}\tilde{\boldsymbol{\varrho}}_{eg}e^{-i\omega_L t} \\ &\quad - \frac{i}{\hbar}\left(E_e - E_g\right)\tilde{\boldsymbol{\varrho}}_{eg}e^{-i\omega_L t}, \end{aligned} \tag{2.24}$$

$$\begin{aligned} \frac{d\tilde{\boldsymbol{\varrho}}_{eg}}{dt} &= -\frac{i}{\hbar}\left\{-\left(\mathbf{d}^{+}\cdot\mathbf{E}^{+}\right)\hat{\boldsymbol{\varrho}}_{gg} + \hat{\boldsymbol{\varrho}}_{eg}\left(\mathbf{d}^{+}\cdot\mathbf{E}^{+}\right)\right\} \\ &\quad - \left(\frac{\Gamma}{2} - i\Delta\right)\tilde{\boldsymbol{\varrho}}_{eg}, \end{aligned} \tag{2.25}$$

$$\begin{aligned}\frac{d\hat{\boldsymbol{\varrho}}_{ge}}{dt} =& \frac{d\tilde{\boldsymbol{\varrho}}_{ge}}{dt}e^{i\omega t} + i\omega_L\tilde{\boldsymbol{\varrho}}_{ge}e^{i\omega_L t} && (2.26)\\ =& -\frac{i}{\hbar}\left\{\hat{\mathbf{H}}_{ge}\hat{\boldsymbol{\varrho}}_{ee} - \hat{\boldsymbol{\varrho}}_{gg}\hat{\mathbf{H}}_{ge}\right\} - \frac{\Gamma}{2}\tilde{\boldsymbol{\varrho}}_{eg}e^{i\omega_L t}\\ & -\frac{i}{\hbar}\left(E_g - E_e\right)\tilde{\boldsymbol{\varrho}}_{ge}e^{i\omega_L t}, && (2.27)\\ \frac{d\tilde{\boldsymbol{\varrho}}_{ge}}{dt} =& -\frac{i}{\hbar}\left\{-\left(\mathbf{d}^- \cdot \mathbf{E}^-\right)\hat{\boldsymbol{\varrho}}_{ee} + \hat{\boldsymbol{\varrho}}_{gg}\left(\mathbf{d}^- \cdot \mathbf{E}^-\right)\right\}\\ & -\left(\frac{\Gamma}{2} + i\Delta\right)\tilde{\boldsymbol{\varrho}}_{eg}, && (2.28)\end{aligned}$$

where we have set $\Delta \equiv \omega_L - \omega_0$, $\hbar\omega_0 = E_e - E_g$ and the relaxation term to $\frac{d\tilde{\boldsymbol{\varrho}}}{dt}_{\mathrm{relax}} = \frac{\Gamma}{2}\tilde{\boldsymbol{\varrho}}_{eg}e^{-i\omega_L t}$. We are left with the ground state density matrix $\hat{\boldsymbol{\varrho}}_{gg}$. Its differential equation can be written as

$$\begin{aligned}\frac{d\hat{\boldsymbol{\varrho}}_{gg}}{dt} =& -\frac{i}{\hbar}\left\{\hat{\mathbf{H}}_{ge}\,\hat{\boldsymbol{\varrho}}_{eg} - \hat{\boldsymbol{\varrho}}_{ge}\,\hat{\mathbf{H}}_{eg}\right\} + \left(\frac{d\hat{\boldsymbol{\varrho}}}{dt}\right)_{\mathrm{relax}} && (2.29)\\ =& -\frac{i}{\hbar}\left\{-\left(\mathbf{d}^- \cdot \mathbf{E}^-\right)\tilde{\boldsymbol{\varrho}}_{eg} + \tilde{\boldsymbol{\varrho}}_{ge}\left(\mathbf{d}^+ \cdot \mathbf{E}^+\right)\right\} + \left(\frac{d\hat{\boldsymbol{\varrho}}}{dt}\right)_{\mathrm{relax}}. && (2.30)\end{aligned}$$

In this equation the relaxation term describes the optical pumping between the different sub-levels involved. The relaxation term $\left(\frac{d\hat{\boldsymbol{\varrho}}}{dt}\right)_{\mathrm{relax}} \ll \Gamma, \Delta$. This means that the density matrices $\hat{\boldsymbol{\varrho}}_{eg}$, $\hat{\boldsymbol{\varrho}}_{ge}$ and $\hat{\boldsymbol{\varrho}}_{ee}$ evolve much more quickly than the ground state density matrix $\hat{\boldsymbol{\varrho}}_{gg}$ opening the possibility to adiabatically eliminate them. The whole density matrix can be replaced by the steady state values of its components. This is accomplished by setting all time derivatives of the density matrix to zero, i.e.

$$\left(\frac{d\hat{\varrho}_{gg}}{dt}\right) = 0, \qquad \left(\frac{d\hat{\varrho}_{ge}}{dt}\right) = 0,$$
$$\left(\frac{d\hat{\varrho}_{ee}}{dt}\right) = 0, \qquad \left(\frac{d\hat{\varrho}_{eg}}{dt}\right) = 0.$$

We have derived an expression for the evolution of the density matrix and split it into four distinct parts. We are now ready to adiabatically eliminate the excited state and its coherences using the condition above that the time derivatives of the components of the density matrix are zero.

2.1.3 Adiabatic elimination of the excited state coherences

We now adiabatically eliminate the excited state and its coherences from the density matrix. We start by considering the steady state solution of equation 2.20 first by setting the left hand side to zero:

$$0 = -\frac{i}{\hbar}\left\{-\left(\mathbf{E}^{+}\cdot\mathbf{d}^{+}\right)\tilde{\varrho}_{ge} + \tilde{\varrho}_{eg}\left(\mathbf{E}^{-}\cdot\mathbf{d}^{-}\right)\right\} - \Gamma'\,\hat{\varrho}_{ee},$$

hence

$$\tilde{\varrho}_{ee}^{ss} = -\frac{i}{\hbar\Gamma}\left\{-\left(\mathbf{E}^{+}\cdot\mathbf{d}^{+}\right)\tilde{\varrho}_{ge} + \tilde{\varrho}_{eg}\left(\mathbf{E}^{-}\cdot\mathbf{d}^{-}\right)\right\}. \qquad (2.31)$$

Here $\tilde{\varrho}_{ee}^{ss}$ stands for the steady state solution excited state density matrix. The superscripts ss will also be used for the steady state solution density matrices of the ground-excited state coherences. For the differential equations for the ground and excited state coherences, 2.25 and 2.28, we then have

$$\begin{aligned} 0 &= -\frac{i}{\hbar}\left\{-\left(\mathbf{d}^{+}\cdot\mathbf{E}^{+}\right)\hat{\boldsymbol{\varrho}}_{gg}+\hat{\boldsymbol{\varrho}}_{eg}\left(\mathbf{d}^{+}\cdot\mathbf{E}^{+}\right)\right\} \\ &\quad -\left(\frac{\Gamma}{2}-i\Delta\right)\tilde{\boldsymbol{\varrho}}_{eg}, \\ \tilde{\boldsymbol{\varrho}}_{eg}^{ss} &= -\frac{1}{\hbar\left(\Delta+\frac{i\Gamma}{2}\right)}\left\{-\left(\mathbf{d}^{+}\cdot\mathbf{E}^{+}\right)\hat{\boldsymbol{\varrho}}_{gg}+\hat{\boldsymbol{\varrho}}_{eg}\left(\mathbf{d}^{+}\cdot\mathbf{E}^{+}\right)\right\}, \end{aligned} \tag{2.32}$$

$$\begin{aligned} 0 &= -\frac{i}{\hbar}\left\{-\left(\mathbf{d}^{-}\cdot\mathbf{E}^{-}\right)\hat{\boldsymbol{\varrho}}_{ee}+\hat{\boldsymbol{\varrho}}_{gg}\left(\mathbf{d}^{-}\cdot\mathbf{E}^{-}\right)\right\} \\ &\quad -\left(\frac{\Gamma}{2}+i\Delta\right)\tilde{\boldsymbol{\varrho}}_{eg}, \\ \tilde{\boldsymbol{\varrho}}_{ge}^{ss} &= -\frac{1}{\hbar\left(\Delta-\frac{i\Gamma}{2}\right)}\left\{-\left(\mathbf{d}^{-}\cdot\mathbf{E}^{-}\right)\hat{\boldsymbol{\varrho}}_{ee}+\hat{\boldsymbol{\varrho}}_{gg}\left(\mathbf{d}^{-}\cdot\mathbf{E}^{-}\right)\right\}. \end{aligned} \tag{2.33}$$

We are left with the equation for the ground state density matrix $\hat{\boldsymbol{\varrho}}_{gg}$ given in 2.30. All occurrences of the density matrices are replaced by their steady state values, giving

$$\frac{d\hat{\boldsymbol{\varrho}}_{gg}}{dt} = -\frac{i}{\hbar}\left\{\hat{\mathbf{H}}_{ge}\,\hat{\boldsymbol{\varrho}}_{eg}-\hat{\boldsymbol{\varrho}}_{ge}\,\hat{\mathbf{H}}_{eg}\right\}+\left(\frac{d\hat{\boldsymbol{\varrho}}}{dt}\right)_{\mathbf{relax}} \tag{2.34}$$

$$\approx \frac{i}{\hbar}\left\{\left(\mathbf{d}^{-}\cdot\mathbf{E}^{-}\right)\tilde{\boldsymbol{\varrho}}_{eg}-\tilde{\boldsymbol{\varrho}}_{ge}\left(\mathbf{d}^{+}\cdot\mathbf{E}^{+}\right)\right\}+\left(\frac{d\hat{\boldsymbol{\varrho}}}{dt}\right)_{\mathbf{relax}} \tag{2.35}$$

$$\begin{aligned} &= -\frac{i}{\hbar^2}\left\{\left(\frac{\left(\Delta-\frac{i\Gamma}{2}\right)}{\Delta^2+\frac{\Gamma^2}{4}}\right)\left(\mathbf{d}^{-}\cdot\mathbf{E}^{-}\right)\left(\mathbf{d}^{+}\cdot\mathbf{E}^{+}\right)\hat{\boldsymbol{\varrho}}_{gg}\right. \\ &\quad \left. -\left(\frac{\left(\Delta+\frac{i\Gamma}{2}\right)}{\Delta^2+\frac{\Gamma^2}{4}}\right)\hat{\boldsymbol{\varrho}}_{gg}\left(\mathbf{d}^{-}\cdot\mathbf{E}^{-}\right)\left(\mathbf{d}^{+}\cdot\mathbf{E}^{+}\right)\right\} \\ &\quad +\left(\frac{d\hat{\boldsymbol{\varrho}}}{dt}\right)_{\mathbf{relax}}, \end{aligned} \tag{2.36}$$

where we have rationalized the denominators in the fractions and used the fact that the term

$$\begin{aligned}
&\left(\frac{1}{\hbar\left(\Delta+\frac{i\Gamma}{2}\right)}-\frac{1}{\hbar\left(\Delta-\frac{i\Gamma}{2}\right)}\right)\left(\mathrm{d}^{-}\cdot\mathbf{E}^{-}\right)\hat{\varrho}_{ee}\left(\mathrm{d}^{+}\cdot\mathbf{E}^{+}\right)\\
&=\frac{\left(\mathrm{d}^{-}\cdot\mathbf{E}^{-}\right)\hat{\varrho}_{ee}\left(\mathrm{d}^{+}\cdot\mathbf{E}^{+}\right)}{\hbar}\left(\frac{\left(\Delta-\frac{i\Gamma}{2}\right)-\left(\Delta+\frac{i\Gamma}{2}\right)}{\Delta^{2}+\frac{\Gamma^{2}}{4}}\right)\\
&=0 \qquad (2.37)
\end{aligned}$$

cancels out[6]. To calculate the light-shifts from this equation, the relaxation term $\left(\frac{d\hat{\varrho}}{dt}\right)_{\text{relax}}$, which is much smaller than Γ or Δ, is neglected in addition to the anti-commutator terms[7]. By setting

$$\frac{d\hat{\varrho}_{gg}}{dt}=\frac{i}{\hbar}\left[\hat{\Lambda},\,\hat{\varrho}_{gg}\right] \qquad (2.38)$$

the light-shift operator can be deduced to have the functional form

$$\hat{\Lambda}\equiv\frac{1}{\hbar}\frac{\Delta}{\Delta^{2}+\frac{\Gamma^{2}}{4}}\left(\mathrm{d}^{-}\cdot\mathbf{E}^{-}\right)\left(\mathrm{d}^{+}\cdot\mathbf{E}^{+}\right). \qquad (2.39)$$

This concludes the section on the adiabatic elimination of the excited state and its coherences. We have arrived at a stage, where we can reconsider the hyperfine structure in the ground state and introduce it into equation 2.39. This is done in the next section.

---

[6] A step by step version is shown in appendix B.1

[7] $\propto i\Gamma$

2.1.4 Inclusion of the degeneracy of the ground state manifold

The next step is to consider the terms $(\mathbf{d}^- \cdot \mathbf{E}^-)$ and $(\mathbf{d}^+ \cdot \mathbf{E}^+)$ in equation 2.39 on the preceding page. The components of the different terms are given in equations 2.3 on page 40 and 2.6 on page 41. Substitution gives

$$\begin{aligned}
\left(\mathbf{d}^- \cdot \mathbf{E}^-\right) &= \left(\sum_k C_{J_g\, m_g}^{J_e\, m_e\, 1\, k}\, D\, \left|J_g\, m_g\right\rangle \left\langle J_e\, m_e\right| \hat{\mathbf{e}}_k\right) \cdot \left(\sum_m \frac{1}{2} E_L \varepsilon_m^* \hat{\mathbf{e}}_m^* \hat{\mathbf{a}}_m^+\right) \\
&= \sum_k \frac{1}{2} E_L\, D\, \varepsilon_k^*\, C_{J_g\, m_g}^{J_e\, m_e\, 1\, k}\, \left|J_g\, m_g\right\rangle \left\langle J_e\, m_e\right| \hat{\mathbf{a}}_k^+, \qquad (2.40) \\
\left(\mathbf{d}^+ \cdot \mathbf{E}^+\right) &= \sum_l \frac{1}{2} E_L\, D\, \varepsilon_l\, C_{J_g\, m_g}^{J_e\, m_e^{'}\, 1\, l}\, \left|J_e\, m_e^{'}\right\rangle \left\langle J_g\, m_g^{'}\right| \hat{\mathbf{a}}_l, \qquad (2.41)
\end{aligned}$$

$$\begin{aligned}
\left(\mathbf{d}^- \cdot \mathbf{E}^-\right)\left(\mathbf{d}^+ \cdot \mathbf{E}^+\right) = \sum_k \sum_l \left(\frac{E_L\, D}{2}\right)^2 \varepsilon_k^*\, \varepsilon_l\, C_{J_g\, m_g}^{J_e\, m_e\, 1\, k}\, C_{J_g\, m_g}^{J_e\, m_e\, 1\, l} \\
\left|J_g\, m_g\right\rangle \left\langle J_g\, m_g^{'}\right| \hat{\mathbf{a}}_k^+\, \hat{\mathbf{a}}_l. \qquad (2.42)
\end{aligned}$$

We have used the fact that $\left\langle J_e\, m_e \,\middle|\, J_e\, m_e^{'}\right\rangle = \delta_{m_e, m_e^{'}}$. From this follows that $m_e^{'} = m_g^{'} + l = m_e = m_g + k$ or $m_g = m_g^{'} + k - l$. These operators now include the level structure of the ground state with its manifold of hyperfine magnetic sub-states. Using equation 2.41 and 2.42 into 2.39 allows us to introduce the structure in the ground state into the light-shift operator $\mathbf{\Lambda}$ in the next section.

2.1.5 The functional form of the light-shift operator

Introducing the Rabi frequency $\Omega^2 \equiv \frac{E_L D}{\hbar}$ and substituting equations 2.41 and 2.42, the light shift operator becomes

$$\Lambda = \frac{1}{2}\hbar\Delta\left(\frac{\frac{\Omega^2}{2}}{\Delta^2+\frac{\Gamma^2}{4}}\right)\sum_k\sum_l \varepsilon_k^*\,\varepsilon_l\, C_{J_g\, m_g}^{J_e\, m_e\, 1\, k}\, C_{J_g\, m_g}^{J_e\, m_e\, 1\, l}$$

$$\left|J_g\, m_g\right\rangle \left\langle J_g\, m_g^{'}\right|\, \hat{\mathbf{a}}_k^+\, \hat{\mathbf{a}}_l. \tag{2.43}$$

We are now ready to calculate the matrix elements of the light-shift operator. They are

$$\left\langle J_g,\, m_2\right|\hat{\mathbf{\Lambda}}\left|J_g\, m_1\right\rangle = \frac{1}{2}\hbar\Delta\left(\frac{\frac{\Omega^2}{2}}{\Delta^2+\frac{\Gamma^2}{4}}\right)\sum_k\sum_l \varepsilon_k^*\,\varepsilon_l\, C_{J_g\, m_g}^{J_e\, m_e\, 1\, k}\, C_{J_g\, m_g}^{J_e\, m_e\, 1\, l}$$

$$\left\langle J_g,\, m_2\,|\, J_g,\, m_g\right\rangle \left\langle J_g,\, m_g\,\middle|\, \hat{\mathbf{a}}_k^+\, \hat{\mathbf{a}}_l\middle|J_g,\, m_1\right\rangle$$

$$= \frac{1}{2}\hbar\Delta\left(\frac{\frac{\Omega^2}{2}}{\Delta^2+\frac{\Gamma^2}{4}}\right)\sum_k\sum_l \varepsilon_k^*\,\varepsilon_l\, C_{J_g\, m_2=m_1+l-k}^{J_e\, m_e\, 1\, k}\, C_{J_g\, m_1}^{J_e\, m_e=m_1+l\, 1\, l}. \tag{2.44}$$

The last step follows due the chosen normalization in 2.2 for the operators $\hat{\mathbf{a}}_k^+$ and $\hat{\mathbf{a}}_l$. The possible combinations of $\hat{\mathbf{a}}_k^+\,\hat{\mathbf{a}}_l$ are shown in figure 2.2. The local polarization amplitudes are function of positions, $\varepsilon_k = \varepsilon_k(\mathbf{r})$, and so determine the spatial dependency of the light-shift operator. The final step to find the adiabatic potential surfaces is to diagnonalize the light-shift operator $\hat{\mathbf{\Lambda}}(\mathbf{r})$ where the matrix elements are given by

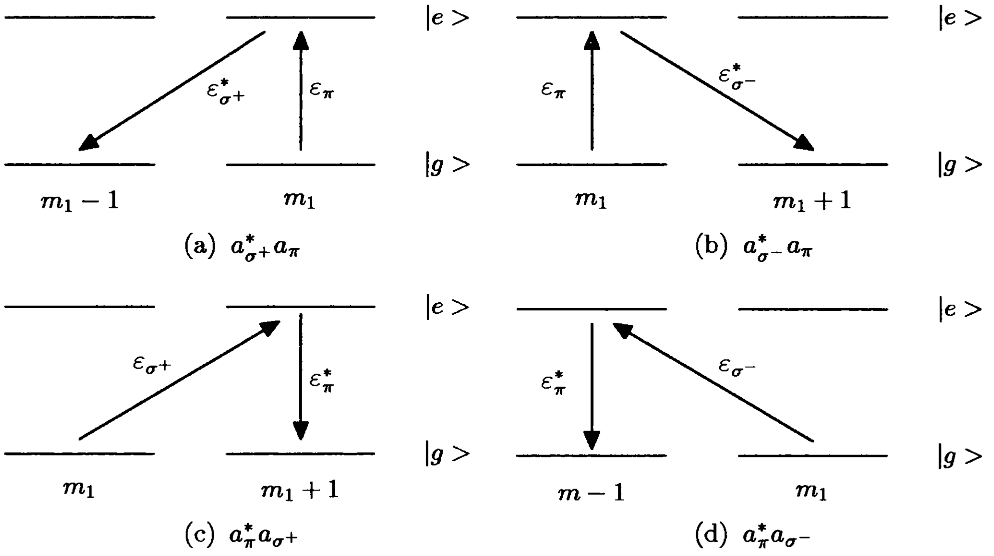

(a) $a^*_{\sigma^+}a_\pi$ (b) $a^*_{\sigma^-}a_\pi$

(c) $a^*_\pi a_{\sigma^+}$ (d) $a^*_\pi a_{\sigma^-}$

Figure 2.2: This figure shows the different contributions to light-shift operator matrix elements. The ε_j are the amplitudes of the different local polarization components when using the circular basis.

$$\Lambda_{m_2,m_1}(\mathbf{r}) = \sum_{k,l} \varepsilon^*_k(\mathbf{r})\varepsilon_l(\mathbf{r})\, C^{J_e\, m_e\, 1\, k}_{J_g\, m_2=m_1+l-k}\, C^{J_e\, m_e=m_1+l\, 1\, l}_{J_g\, m_1} \tag{2.45}$$

This concludes this section where an expression for the matrix elements of the light-shift operator in the near-detuned limit was deduced. To illustrate how the light-shift operator can be used to deduce the optical potential as seen by the atoms, it is used to calculated the adiabatic potential of a 1D lin⊥lin optical lattice on a $J_g = 1/2 \rightarrow J_e = 3/2$ transition.

2.1.6 Adiabatic potential of a 1D lin⊥lin optical lattice on a $J_g = 1/2 \rightarrow J_e = 3/2$ transition

To illustrate how this can be used in calculations the light-shift operator introduced in the previous section is applied to a theoretical two-level atom

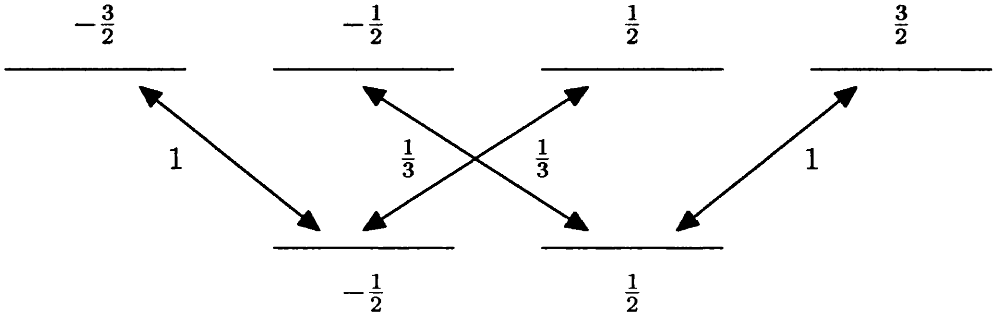

Figure 2.3: This figure shows the level scheme of a 1D lin⊥lin optical lattice on a $J_g = 1/2 \rightarrow J_e = 3/2$ transition. Also shown are the squared Clebsch-Gordan coefficients of the relevant transitions.

on a $J_g = 1/2 \rightarrow J_e = 3/2$ transition. First an optical lattice is created by two counter-propagating laser beams propagating along $\hat{\mathbf{z}}$ having polarizations along $\hat{\mathbf{x}}$ and $\hat{\mathbf{y}}$ as shown in figure 2.6 on page 65. The total electric lattice field is then given by

$$\begin{aligned} \mathbf{E}(\mathbf{z}) =& E_0 \left(\mathbf{x}e^{ikz} + \mathbf{y}e^{-ikz}\right) + c.c. \\ =& \sqrt{2}E_L \left\{\hat{\mathrm{e}}_+ \cos kz + \hat{\mathrm{e}}_- \sin kz\right\}. \end{aligned} \tag{2.46}$$

The total lattice light field contains no π-polarized light. Using the relevant Clebsch-Gordan coefficients shown in figure 2.3, the matrix elements are deduced to be

$$\begin{aligned} \Lambda_{\frac{1}{2}\frac{1}{2}} =& |\varepsilon_{\sigma^+}|^2 \times 1 + |\varepsilon_{\sigma^-}|^2 \times \frac{1}{3} \cdot \frac{1}{2}\hbar\Delta\, s = U_0 \cos^2 kz + \frac{1}{3}\sin^2 kz \\ =& U_0 \left[\frac{1}{3} + \frac{2}{3}\cos^2 kz\right], \end{aligned} \tag{2.47}$$

$$\Lambda_{-\frac{1}{2}-\frac{1}{2}} = U_0 \left[\frac{1}{3} + \frac{2}{3}\sin^2 kz\right], \tag{2.48}$$

$$\Lambda_{\frac{1}{2}-\frac{1}{2}} = 0. \tag{2.49}$$

Thus the eigenstates of Λ are the Zeeman sub-states. This is not generally true in atoms with $J_g \geq 1$, when the eigenstates are spatially dependent linear superpositions of the Zeeman sub-eigenstates $|J_g, m\rangle$. Here Raman transitions with σ^+ and σ^- can link states with $\Delta m = \pm 2$. Figure 2.4 shows the light-shifted potentials represented by equations 2.47 and 2.48. We see that the periodicity of the lattice is $\lambda/2$ for sites with the same m_f and $\lambda/4$ for sites of alternating m_f. The theory is extended to the case of far-detuned optical lattices in the following section.

2.2 Non-dissipative Optical Lattices

In the previous section we discussed near-resonant optical lattices. Now we consider what happens to the interaction between the lattice light and atoms when the laser light is detuned further away from resonance and discuss why this is advantageous for quantum state preparation and control experiments. The disadvantage with Sisyphus cooling in near-detuned optical lattices is that the spontaneous scattering which leads to localization is also responsible for decoherence effects, thus limiting the lifetime of the vibrational coherences. As mentioned in 1.1.1 on page 19, the light shift, U_0, induced by the lattice optical beams is proportional to $\frac{\Gamma}{\Delta}$, whereas the scattering rate Γ' scales as

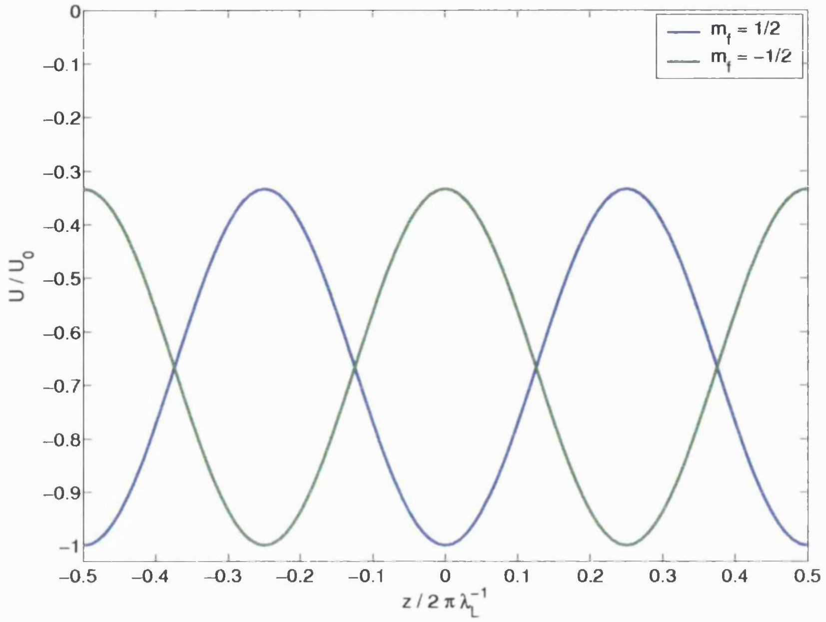

Figure 2.4: This figure shows the light-shifts of a 1D lin⊥lin optical lattice on a $J_g = 1/2 \longrightarrow J_e = 3/2$ transition. We see that the periodicity of the lattice is $\lambda/2$ for sites with the same m_f and $\lambda/4$ for sites of alternating m_f.

$\frac{\Gamma}{\Delta^2}$. Hence the latter decreases much faster than the first when the lattice light is detuned further and further away from resonance. If we increase the lattice laser power in proportion to the detuning, the well depth of the optical potential can be keep constant. It is therefore possible to create a far-detuned optical trapping potential with similar well depth and spatial periodicity as a near-detuned optical potential, but with a highly reduced scattering rate. A typical near-detuned lattice has a scattering rate of about $\Gamma_s' \sim 500\,\text{kHz}$ which can be reduced to about $\Gamma_s' \sim 100\,\text{Hz}$ in a far-detuned one for detunings of several thousands of line-widths.

Additionally, the reduction in the photon scattering rate also decreases the rate of decoherence associated with spontaneous emission and makes far-detuned optical potentials an interesting environment for quantum state preparation and control experiments, which depend on the coherent evolution of the atomic wavepackets.

As the potential is non-dissipative, it is necessary to pre-cool the atoms before making use of this useful feature of far-detuned optical potential. This is normally done by cooling the atoms in a near-resonant lattice first and transferring them to a superimposed far-detuned lattice with similar potential well depth and periodicity. The best transfer efficiencies were observed when the near-detuned light was slowly ramped down and the far-detuned light ramped up, with the aim to maintain a constant potential well depth. Efficiencies of up to 90% were observed in our experiment.

Two useful limits of the spatial dependency of the light-shifts in a far-detuned optical lattice are provided by the adiabatic and diabatic cases. The adiabatic potentials are found by first diagonalizing the optical potential operator 2.62 and then calculating its eigenvalues. The new eigenstates are then superpositions of the Zeeman basis states $|F, m_F\rangle$. Diabatic potentials are calculated by neglecting all off-diagonal contributions to the optical potential operator 2.62. The adiabatic potentials cannot be associated with a pure Zeeman state $|F, m = \pm 4\rangle$, but at positions with pure circular polarization, where Raman coupling between states with $\Delta m = \pm 1$ is almost non-existent, they nearly coincide with the diabatic potentials associated with the stretched states $|F, m = \pm 4\rangle$. When the atoms move away from regions of pure circular polarization, the contribution of the eigenstates from other magnetic sub-levels increases gradually giving rise to avoided crossings midway between the regions of alternate pure circular polarization.

If the Raman coupling between states $\Delta m = \pm 1$ is significant, then adiabatic potentials describe the lattice better as long as the atoms move slow enough through the avoided crossing and undergo Raman transitions to other magnetic sub-states. For fast moving atoms diabatic potentials are a more appropriate description. Since we are considering mostly tightly bound atoms at regions of pure circular polarization, we can use either adiabatic or diabatic potentials. Both nearly coincide at these locations. This also makes calculations easier and faster, since the off-diagonal elements of the optical potential operator are neglected and no diagonalization is necessary to calculate the light-shifts.

2.3 Derivation of the Optical Potential in the Far-detuned Regime and the Fictitious Magnetic Field

We have seen in the foregoing chapters how potentials for cold atoms can be designed through their interactions with electro-magnetic fields. These interactions can be grouped into three categories, namely light-shifts, Zeeman shift and Stark shift.

In the following we are interested in the interaction of atoms with a low-intensity monochromatic light source and static external magnetic fields, a common situation in laser cooling. The aim is to derive a convenient form for the optical potential of alkali-metal atoms in a far-detuned optical trap. Considering a low-intensity monochromatic light source and an static external magnetic field, the potential the atom sees, can be written as [42]

$$\hat{U}(\mathbf{x}) = -\mathbf{E}_L(\mathbf{x}) \cdot \hat{\boldsymbol{\alpha}} \cdot \mathbf{E}_L(\mathbf{x}) - \hat{\boldsymbol{\mu}} \cdot \mathbf{B}, \tag{2.50}$$

$$\mathbf{E}_L(\mathbf{x}, t) = \mathrm{Re}\left\{\mathbf{E}_L(\mathbf{x})\, e^{-i\omega_L t}\right\},$$

$$\hat{\boldsymbol{\alpha}} = -\sum_e \frac{\hat{\mathbf{d}}_{ge}\, \hat{\mathbf{d}}_{eg}}{\hbar \Delta_{ge}}.$$

Here $\mathbf{E}_L(\mathbf{x}, t)$ represents the total electric field of the lattice beams and $\hat{\boldsymbol{\alpha}}$ the atomic polarizability tensor operator in the far-off resonant limit; Δ_{ge} is the detuning from the $|g\rangle \rightarrow |e\rangle$ resonance and $\hat{\mathbf{d}}_{ge}$ the electric dipole operator coupling the states involved. Governing the interaction with a magnetic field is the magnetic dipole operator $\hat{\boldsymbol{\mu}} = \hbar\gamma\hat{\mathbf{F}}$, where γ is the gyromagnetic ratio and $\hat{\mathbf{F}}$ the total angular momentum operator.

The adiabatic potentials can now be found by diagonalising $\hat{U}(\mathbf{x})$. The atom used in our experiment is caesium, an alkali-metal atom with a hyperfine level structure. This means that the atomic polarizability tensor becomes [42]

$$\hat{\boldsymbol{\alpha}} = -\sum_{F'} \frac{P_F\, \hat{\mathbf{d}}\, P_{F'}\, \hat{\mathbf{d}}\, P_F}{\hbar \Delta_{F,F'}}, \tag{2.51}$$

where

$$P_F = \sum_m |F, m\rangle \langle F, m|$$

and

$$P_{F'} = \sum_{m'} |F', m'\rangle \langle F', m'|$$

are the projection operators for the ground and excited hyperfine manifolds. Making a change of basis to the spherical one and using the notation

$$\hat{\alpha}_{q',q} = \mathbf{e}^*_{q'} \cdot \hat{\boldsymbol{\alpha}} \cdot \mathbf{e}_q, \tag{2.52}$$

we can write the atomic polarizability tensor as

$$\hat{\alpha}_{q',q} = \tilde{\alpha} \sum_{F'} \frac{\Delta_{F_{\max},F'_{\max}}}{\Delta_{F,F'}} f_{F,F'} \sum_{m_f} C^{F',m+q}_{F,m+q-q'} \, C^{F',m+q}_{F,m} \times |F, m+q-q'\rangle \langle F, m|. \tag{2.53}$$

In this expression $f_{F'F}$ represent the relative oscillator strengths for the decay $|F'\rangle \rightarrow |F\rangle$, $\Delta_{F,F'}$ the detuning of the laser beams from the resonance involved, $|F_{\max} = J + I\rangle$ and $|F'_{\max} = J' + I\rangle$ the"stretched" states and the $C^{F',m'}_{F,m}$ are the Clebsch-Gordan coefficients for the $|F, m\rangle \rightarrow |F', m'\rangle$ dipole transition. See [42] for a derivation of this equation.

Last but not least the characteristic polarizability scalar for the $|J\rangle \rightarrow |J'\rangle$ transition is defined as

$$\tilde{\alpha} \equiv \frac{|\langle J' \,||d||J\rangle|^2}{\hbar \Delta_{F_{\max},F'_{\max}}} \tag{2.54}$$

where $\langle J' \,||d||J\rangle$ is the reduced matrix element of the dipole operator and $\Delta_{F_{\max},F'_{\max}}$ the detuning from the resonance of the "stretched" states involved. This more complex system will in general create coherences between the ground-state magnetic sub-levels via stimulated Raman transitions. These coherences can then be exploited to control and manipulate the state of the atomic wavepacket.

As mentioned earlier we are interested in the coherent evolution of the atomic state and its manipulation. We should therefore be as far-detuned as possible from the atomic resonance to minimize decoherence effects as much as possible. Now in the limit where the detuning is much larger than the hyperfine level splitting, equation 2.54 on the page before reduces to [42]

$$\tilde{\alpha} \approx P_F \hat{\alpha} \left(J \longrightarrow J'\right) P_F, \tag{2.55}$$

where $\hat{\alpha} \left(J \longrightarrow J'\right)$ is the polarizability tensor of the $|J\rangle \longrightarrow |J'\rangle$ transition. Thus for a very far-detuned optical lattice the alkali-metal atoms behave in a similar way as atoms on the well studied $\left|J = \frac{1}{2}\right\rangle \longrightarrow \left|J' = \frac{3}{2}\right\rangle$ transition. The operator $\hat{\alpha} \left(J \longrightarrow J'\right)$ is a rank-2 tensor and as shown in [42] it can be written as

$$\hat{\alpha}_{ij} \left(J \longrightarrow J'\right) = \tilde{\alpha} \left(\frac{2}{3}\delta_{ij}\hat{I} - \frac{i}{3}\varepsilon_{ijk}\hat{\sigma}_k\right). \tag{2.56}$$

where ε_{ijk} is the total anti-symmetric tensor and the matrices $\hat{\boldsymbol{\sigma}}_k$ are the Pauli spin matrices as given in appendix C. The Pauli spin matrices and the identity matrix form a complete set and form a basis for the vector space of all 2 × 2 matrices. If we express the lattice light as

$$\mathbf{E}_L \left(\mathbf{x}, t\right) = \mathrm{Re}\left\{E_1 \boldsymbol{\varepsilon}_L \left(\mathbf{x}\right) e^{-i\omega_L t}\right\}, \tag{2.57}$$

where $\boldsymbol{\varepsilon}_L(\mathbf{x})$ is the local polarization of the lattice light and E_1 the single beam amplitude[8], we can rewrite the optical potential in the form

$$\hat{U}_F(\mathbf{x}) = -\frac{2}{3}U_1 \left|\boldsymbol{\varepsilon}_L(\mathbf{x},\mathbf{y})\right|^2 \hat{I} + \frac{i}{3}U_1 \left|\boldsymbol{\varepsilon}_L^*(\mathbf{x},\mathbf{y}) \times \boldsymbol{\varepsilon}_L(\mathbf{x},\mathbf{y})\right|. \tag{2.58}$$

The first term is proportional to the modulus squared of the local laser light polarization and independent of the hyperfine state the atom is in. Additionally it scales like the local intensity of the lattice light. Its functional form is given by

$$U_J = -\frac{2}{3}U_1 \left|\boldsymbol{\varepsilon}_L(\mathbf{x},\mathbf{y})\right|^2. \tag{2.59}$$

Here U_1 represents the single beam light shift for a transition with unit Clebsch-Gordan coefficient and $\boldsymbol{\varepsilon}_L(\mathbf{x},\mathbf{y})$ the local lattice light polarization. It can easily be calculated as shown in section 2.5.1 on page 65 for a 1D far-detuned optical lattice.

The second term has the form of the Zeeman interaction with a fictitious transverse magnetic field, whose direction depends on the local polarization of the lattice light field. The usefulness of the fictitious magnetic field is that its varies with the same periodicity as the optical potential, i.e. on a sub-wavelength scale. This cannot be achieved with an applied external transverse magnetic field and so opens up new experimental applications to be explored. A useful one is resolved-sideband Raman cooling, which is described in detail

---

[8] It was assumed for convenience that the beams all have equal amplitudes E_1, so it can be conveniently factored out.

in chapter 3. The shift to the energy levels due to the fictitious magnetic field is dependent on the hyperfine state of the atom and is given by

$$\mathbf{B}_{\mathrm{fic}}(\mathbf{x},\mathbf{y}) = \frac{i}{3}U_1 \left|\varepsilon_L^*(\mathbf{x},\mathbf{y}) \times \varepsilon_L(\mathbf{x},\mathbf{y})\right|. \tag{2.60}$$

Using Landé's projection theorem for the *stretched* ground hyperfine level with $F = I + J$, equation 2.58 on the page before can be recast as

$$\hat{U}_F(\mathbf{x}) = U_J(\mathbf{x})\,\hat{I} + \mathbf{B}_{\mathrm{fic}}(\mathbf{x}) \cdot \frac{\hat{\mathbf{F}}}{F}. \tag{2.61}$$

The advantage of this representation is that it is basis independent and very convenient for calculations. From equations 2.58 on the preceding page and 2.61 it can be seen that in the limit of infinite detuning coherences between the states $|F, m\rangle$ and $|F, m \pm 2\rangle$ go to zero. Also the fictitious magnetic field described with equation 2.60 goes to zero if the light field is everywhere linearly polarized. In this case only the term 2.59 on the page before survives, which gives rise to a light shift independent of the magnetic substate of the atom.

This concludes the section on light-shifts in non-dissipative optical lattices. The next two sections show examples of calculated optical potentials and describes ways how to manipulate them by means of changing the beam configuration.

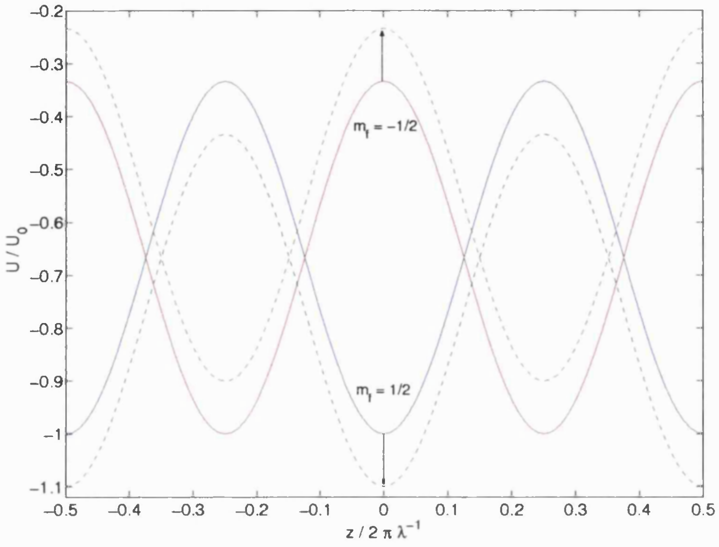

Figure 2.5: This figure shows the effect of an applied external parallel magnetic field in a 1D optical lattice. Note that the sign of the shift is dependent on the sign of the m_f level.

2.4 Effects of Static Magnetic Fields in Optical Lattices

This section describes what happens when an additional static magnetic field is added to an optical lattice. Applying a static magnetic field to an optical lattice modifies equation 2.61 to

$$\hat{U}_F(\mathbf{x}) = U_J(\mathbf{x})\,\hat{I} + \left(\mathbf{B}_{\text{fic}}(\mathbf{x}) + \mathbf{B}_{\text{ext}}\right) \cdot \frac{\hat{\mathbf{F}}}{F}. \tag{2.62}$$

The applied external magnetic field $\mathbf{B}_{\text{ext}}$ splits into two parts, a transverse component $\mathbf{B}_{\text{t}}$ and a parallel component $\mathbf{B}_{\text{p}}$ to the chosen quantization axis of the lattice. For simplicity we assume here that the quantization axis is oriented along the positive z-direction, i.e. $\mathbf{B}_{\text{p}} = \mathbf{B}_{\text{z}}$ and $\mathbf{B}_{\text{t}} = \mathbf{B}_{\text{x}} + \mathbf{B}_{\text{y}}$.

A magnetic field parallel to the quantization axis along the z-direction simply adds a Zeeman shift to the m_f-level. This energy shift is given by

$$\Delta E = g_F \, \mu_B \, m_f \, B_z, \tag{2.63}$$

where g_F is the gyromagnetic ratio and μ_B the Bohr magneton. This term adds only to the diagonal elements of the optical potential operator **U** and is different for each m_f-level. Figure 2.5 shows this. The difference between the fictitious magnetic field $\mathbf{B}_{\mathrm{fic}}$ and an applied parallel external static magnetic field $\mathbf{B}_{\mathrm{z}}$ is that the first changes over a length scale of order of magnitude of the optical wavelength whereas the latter gives rise to a uniform m_f-level dependent shift of the $|F, m_F\rangle$ states. This effect can be exploited to modify the optical potential to give rise to paramagnetism as reported in [43] and enhance the populations of the stretched states [44] [43].

A transverse magnetic field $\mathbf{B}_{\mathrm{t}} = \mathbf{B}_{\mathrm{x}} + \mathbf{B}_{\mathrm{y}}$ on the other hand, mixes the atomic states and establishes coherences between different magnetic sublevels with $\Delta m = \pm 1$. It contributes off-diagonal matrix elements to the optical potential operator **U** and arises from the transverse components of the angular momentum operator **F**. Expressed in the $\{|F, m\rangle\}$ basis set, the angular momentum operator is a combination of raising and lowering operators coupling states with $\Delta m = \pm 1$, i.e

$$\mathbf{F}_{\pm} \, |F, m_F\rangle = \hbar \sqrt{F(F+1) - m(m \pm 1)} \, |F, m_F \pm 1\rangle \tag{2.64}$$

Using these coherences one can enhance the population of the stretched states by optical pumping. The effects of a static parallel and transverse magnetic field are used in resolved-sideband Raman cooling, where two vibrational level pairs $|F, m_F = -4\rangle$ and $|F, m_F = -4\rangle$ are shifted into resonance by the parallel magnetic field and optical coherences are established by the transverse fictitious magnetic field $\mathbf{B}_{\mathrm{fic}}$ by adding a π-polarization component to the lattice light field.

2.5 Examples of Optical Lattices

This section shows examples of 1D, 2D and 3D far-detuned optical lattices. I describe here how the optical potential can be deduced from the beam configuration used to produce the lattice and how the lattice geometry can be manipulated by the choice of laser beam polarization and incidence angles. A comprehensive theoretical review of beam configurations and the corresponding optical lattice can be found in [45].

2.5.1 Optical lattices in 1D

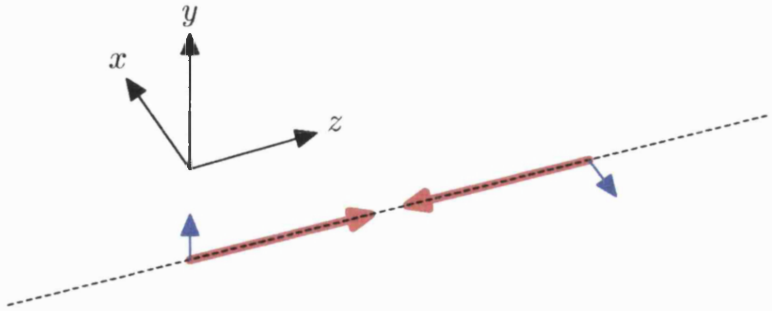

Figure 2.6: This figure shows the lin⊥lin configuration to create an optical lattice in 1D. It uses two counter-propagating laser beams with crossed polarizations.

In this section I present examples of 1D far-detuned optical lattices using the Hamiltonian 2.61 derived by Jessen and Deutsch in [42]. Consider the beam configuration depicted in figure 2.6. It is composed of two counter propagating laser beams along the z-axis with crossed polarizations along the x and y directions. The polarization of the beam travelling along the negative z-direction is chosen to subtend an angle of θ with the polarization of the counter propagating one. The latter is chosen to have a polarization along the the positive y-direction. This configuration is often referred to as the lin-θ-lin configuration. The electric fields for the two beams are given by

$$\begin{aligned}
\mathbf{E}_{z^+} &= E_L\,\hat{\mathbf{y}}\,e^{ikz} && (2.65)\\
\mathbf{E}_{z^-} &= E_L\,e^{-ikz}\,\left(\hat{\mathbf{y}}\cos\theta + \hat{\mathbf{x}}\sin\theta\right), && (2.66)\\
\mathbf{E}_{z} &= E_L\,\left\{\mathbf{E}_{z^+} + \mathbf{E}_{z^-}\right\},\\
&= E_L\left\{\left(e^{ikz} + e^{-ikz}\cos\theta\right) + \sin\theta\hat{\mathbf{e}}^{-ikz}\right\}, && (2.67)
\end{aligned}$$

where E_L is the single beam amplitude assumed to be the same for both counter propagating beams and relates to the intensity by $I_{beam} = |E_L|^2$. The lattice has a quantization direction along z. The Hamiltonian (cf. 2.61) is given by

$$\begin{aligned}
\mathbf{H} &= -\frac{2}{3}|\mathbf{e}_L(z)|^2\,\hat{I} + \frac{i}{3}(\mathbf{e}_L^*(z)\times\mathbf{e}_L(z))\cdot\frac{\mathbf{F}}{F} && (2.68)\\
&= -\frac{2}{3}U_{\text{const}} + \frac{i}{3}(B_{\text{fic}})\cdot\frac{\mathbf{F}}{F}, && (2.69)\\
\frac{\mathbf{F}}{F} &= \sum_{m_i}\frac{m_i}{F_g}\,|F_g, m_i\rangle\,\langle F_g, m_i|.
\end{aligned}$$

To deduce the functional form of the light shift operator, the quantities $|\mathbf{e}_L(z)|^2$ and $\mathbf{e}_L^*(z) \times \mathbf{e}_L(z)$ are needed. Substitution gives

$$\mathbf{e}_L = \begin{pmatrix} e^{-ikz}\sin\theta \\ e^{-ikz}\cos\theta + e^{ikz} \\ 0 \end{pmatrix}, \tag{2.70}$$

$$\begin{aligned} |\mathbf{e}_L|^2 &= \left| \begin{pmatrix} e^{-ikz}\sin\theta \\ e^{-ikz}\cos\theta + e^{ikz} \\ 0 \end{pmatrix} \right|^2 \\ &= \begin{pmatrix} e^{ikz}\sin\theta \\ e^{ikz}\cos\theta + e^{-ikz} \\ 0 \end{pmatrix} \begin{pmatrix} e^{-ikz}\sin\theta \\ e^{-ikz}\cos\theta + e^{ikz} \\ 0 \end{pmatrix} \\ &= \sin^2\theta + \cos^2\theta + e^{2ikz}\cos\theta + e^{-2ikz}\cos\theta \\ &= 2\left(1 + \cos\theta\,\cos 2kz\right), \end{aligned} \tag{2.71}$$

$$\begin{aligned} \mathbf{e}_L^* \times \mathbf{e}_L &= \begin{pmatrix} e^{ikz}\sin\theta \\ e^{ikz}\cos\theta + e^{-ikz} \\ 0 \end{pmatrix} \times \begin{pmatrix} e^{-ikz}\sin\theta \\ e^{-ikz}\cos\theta + e^{ikz} \\ 0 \end{pmatrix} \\ &= \begin{pmatrix} 0 \\ 0 \\ 2\sin\theta\sin 2kz \end{pmatrix}. \end{aligned} \tag{2.72}$$

Substituting this into the Hamiltonian gives

$$\begin{aligned}\mathbf{H}(z) = &-\frac{4}{3}E_L\,(1+\cos\theta\,\cos 2kz)\,\hat{\mathrm{I}}\\ &+\frac{2i}{3}E_L\sin\theta\sin 2kz\sum_{m_i}\frac{m_i}{F_g}\,|F_g,m_g\rangle\,\langle F_g,m_g|.\end{aligned} \tag{2.73}$$

This Hamiltonian can now be used to calculated the light-shifts for the different m_f levels. In the band-structure near the bottom of the wells the atoms are in the Lamb-Dicke regime and the centre-of-mass motion can be approximated by a thermally excited harmonic oscillator. Thus expanding the potential around a minimum and only considering the quadratic term in the displacement, the oscillation frequency can be deduced to be

$$\hbar\,\omega_{\mathrm{osc}} = g\,\sqrt{U_0\,E_r}, \tag{2.74}$$

where g is a constant depending on the lattice geometry. By applying a transverse magnetic field the different light-shifted m_f levels can be mixed together and optical double well potential created. Here one has full control over the barrier width and height by adjusting the angle θ. Adding random perturbations to the optical potential one then could study the tunnelling dynamics in noisy environments. Another possibility is to rotate the polarization of one laser beam using an opto-electric modulator. The effect would be two potentials associated with $m_f = -1/2$ and $m_f = 1/2$ respectively moving in opposite directions acting like a conveyor belt. If the rotation speed is slow enough so that tightly bound atoms remain localized they would be accelerated in opposite directions. Another use for the opto-electric modulator is the possibility to simulate a fluctuating barrier. By choosing $\theta(t) = \theta_0 \pm \theta_{\mathrm{mod}}$ one could simulated a periodic or random variation for θ_{mod} and for the corresponding barrier height and width.

2.5.2 Going to Higher Dimensions

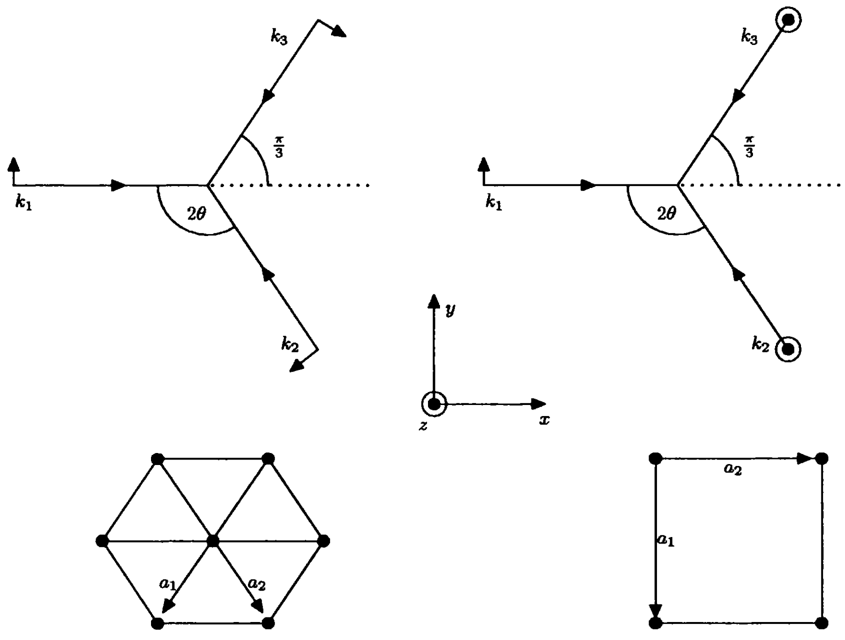

Figure 2.7: This figure shows the two possible beam configurations to achieve a 2D optical lattice. We use this type of set-up in our experiments. Shown also is the corresponding lattice symmetry below the respective beam configuration.

In 1993 Grynberg et al [3] suggested that the topography of an optical lattice can be kept constant without having to phase-lock the trapping lasers. They showed that one only needs N laser beams to create $(N-1)$-dimensional optical lattices. Then the relative phase fluctuations of the individual beams are simply producing a spatial translation of the optical lattice. In general

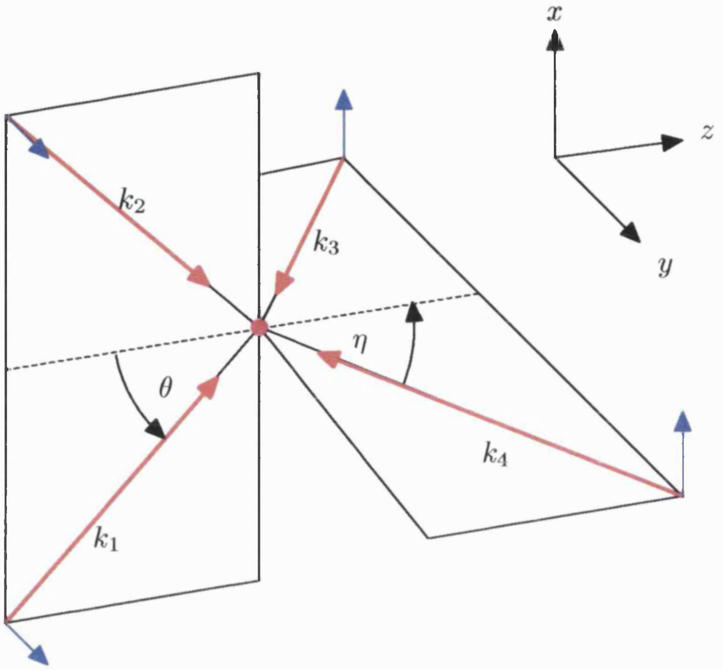

Figure 2.8: This figure shows a possible beam configurations to achieve a 3D optical lattice. This is the beam configuration with the smallest number of beams to achieve a 3D lattice.

these fluctuations are slow enough for the atoms to be able to follow them adiabatically. This insight reduced the complexity in creating higher dimensional optical lattices and this geometry is used in our experiment.

The interested reader is referred to an excellent paper by Petsas et al [45] in which many theoretical possible beam configurations are discussed and investigated. Figure 2.7 shows two possible beam configurations to create a 2D optical lattice taken from this paper. First we consider the configuration on the left of this figure. This configuration is also the one used in our 2D resolved-sideband Raman cooling experiment, where an angle of $\theta = \pi/3$ is used. The different possible choices of the relative polarizations of the beams change the relative positions of σ^+ and σ^- sites, i.e. change the basis of the

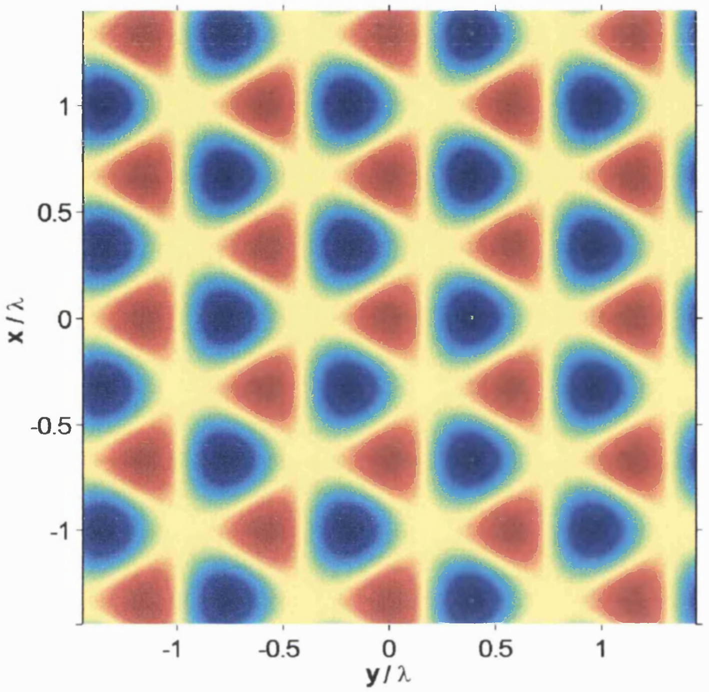

Figure 2.9: This figure shows a 2D lattice calculated using the beam configuration on the left of figure 2.7 on page 69. θ was chosen to be 60°.

unit cell. From [42] the lattice electric field is given by

$$\begin{aligned}\mathbf{E_L}(\mathbf{x}) = \frac{E_1 e^{-iky}}{\sqrt{2}} \Big[&- \mathbf{e}_+ \left\{ 1 + 2e^{iK_y y} \cos(K_x x) \right\} \\ &+ \mathbf{e}_- \left\{ 1 + 2e^{iK_y y} \cos(K_x x - 2\theta) \right\} \Big],\end{aligned} \tag{2.75}$$

where $K_x = k \sin\theta$, $K_y = k(1 + \cos\theta)$, E_1 is the single beam amplitude and $\mathbf{e_q}$ the unit vectors of the rotating basis, $\mathbf{e_q} \in \{\mathbf{e}_+, \mathbf{e}_-, \mathbf{e}_\pi\}$. The quantization axis of the lattice is chosen to be the $\hat{\mathbf{z}}$-direction. The direct and reciprocal unit vectors for this configuration are given by

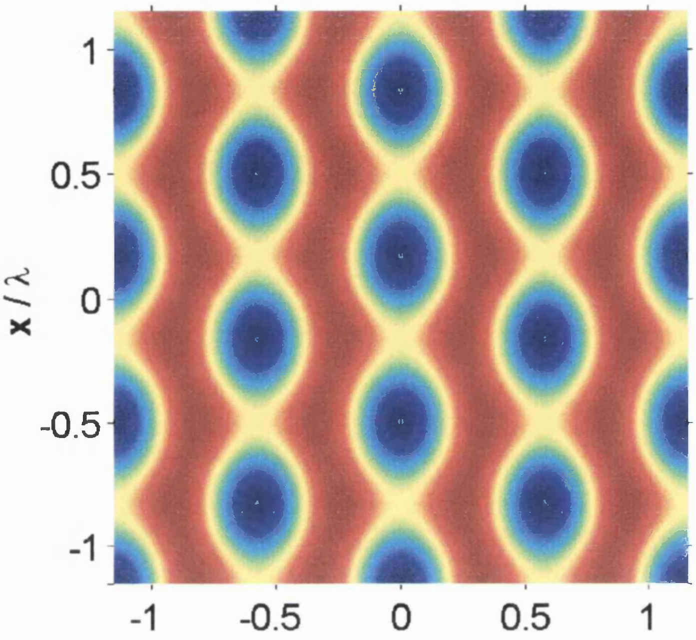

Figure 2.10: This figure shows a 2D lattice calculated using the beam configuration on the right of figure 2.7 on page 69. θ was chosen to be 60°.

$$\mathbf{b}_1 = -\frac{2}{3}\lambda_L \mathbf{e}_x, \qquad \mathbf{b}_1^* = -\frac{3\pi}{\lambda_L}\mathbf{e}_x + \frac{\sqrt{3}\pi}{\lambda_L}\mathbf{e}_y, \tag{2.76}$$

$$\mathbf{b}_2 = -\frac{1}{3}\lambda_L \mathbf{e}_x + \frac{\sqrt{3}}{4}\lambda_L \mathbf{e}_y, \qquad \mathbf{b}_2^* = \frac{\sqrt{3}\pi}{\lambda_L}\mathbf{e}_y. \tag{2.77}$$

These form a basis associated with a primitive cell consisting of a σ^+ and σ^- site. An interesting conclusion from this calculation is, that for a choice of $\theta = \pi/3$ the two direct lattice vectors are equal in length.

The second configuration described in figure 2.7 has the polarizations of two of the lattice beams perpendicular to the lattice plane. As stated in [45] this necessitates a choice for the different amplitudes to be $E_2 = E_3 = E_1/2$, where E_1 is the amplitude of the beam travelling along the $\hat{\mathbf{x}}$-direction. The lattice electric field is then given by

$$\begin{aligned}\mathbf{E_L}(\mathbf{x}) =&\frac{E_1 e^{-iky}}{\sqrt{2}}\left[-\mathbf{e}_+\left\{1+2e^{iK_y y}\cos\left(K_x x\right)\right\}\right.\\&\left.+\,\mathbf{e}_-\left\{1+2e^{iK_y y}\cos\left(K_x x\right)\right\}\right]\end{aligned} \tag{2.78}$$

and the quantization axis is chosen to be in the $x-y$-plane along $\mathbf{k}_1$. This configuration represents an anti-ferromagnetic optical lattice owing to the fact that there are as many potential wells of one circular polarization as from the other with equal potential depth. The main difference between the two configurations is that for the configuration of figure 2.10, the lattice possesses potential wells of pure circular polarization at all positions of maximum light shift for any angle θ. On the contrary the configuration of figure 2.10 only possesses potential wells with pure circular polarization for a choice of $\theta = \pi/3$.

This concludes the discussion of 2D optical lattices and we end this section with a look at 3D optical lattices. We start with the configuration described in figure 2.6 in 1D. First one beam is split into two in the $x-z$-plane with an including angle of θ as shown in figure 2.8. Then the other laser beam is split into two in the $z-y$-plane with including angle η. The polarizations of the beams are kept as in the 1D configuration. This configuration produces a 3D optical lattices with pure σ^+ and σ^- lattice sites. This configuration was first discussed in [46].

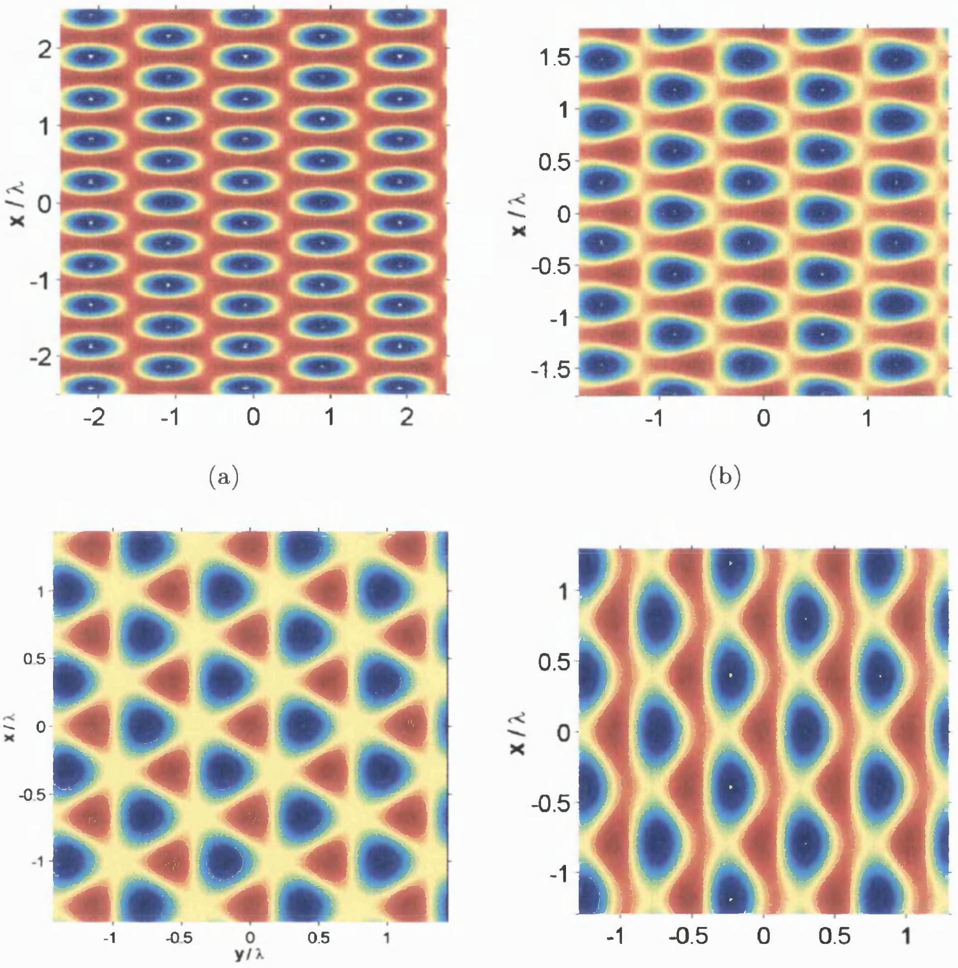

(a)

(b)

(c)

(d)

Figure 2.11: This figure shows calculated potential surfaces for a 2D optical lattice with varying θ. The beam configuration on the left of figure 2.7 on page 69 was used. The angles θ are: (a) $\theta = 30°$, (b) $\theta = 45°$, (c) $\theta = 60°$, (d) $\theta = 75°$.

2.6 Band-Structure Calculations

Optical lattices can also be described as periodic structures bound by light. As in solid state physics this periodicity gives rise to a band-structure of the energy levels in the optical potential wells. We base our treatment of the band-structure in periodic structures bound by light on the Bloch formalism presented in [47, pp 138-139]. We apply this formalism to 1D and implement it in MatLab. Thus we can deduce the band energy eigenvalues and eigenfunctions for arbitrary optical lattice geometries. The eigenfunctions allow us to deduce a localized Wannier basis for the individual potential wells. These localized Wannier function have the advantage that they are localized in contrast to the delocalized Bloch basis. Using this Wannier basis is useful to discuss atoms localized in potential wells.

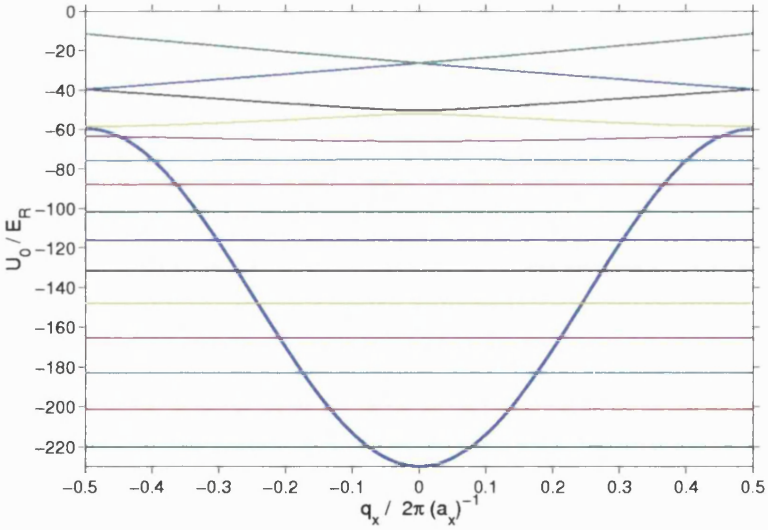

Figure 2.12: Band structure for a potential depth of $170\,\mathrm{E_R}$, cut in the x-direction. a_x and q_x are respectively the period of the potential and the component of the quasi-momentum in the x-direction.

Consider an atom in a 1D optical lattice. The Schrödinger equation gov-

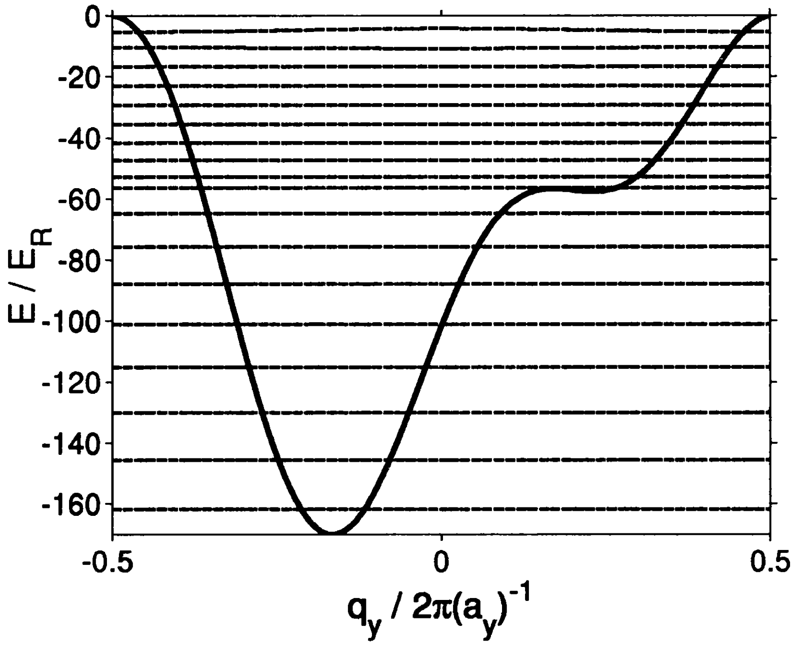

Figure 2.13: Band structure for a potential depth of 170 E_R, cut in the y-direction. a_y and q_y are respectively the period of the potential and the component of the quasi-momentum in the y-direction.

erning the dynamics of the atom has a general form of

$$\mathbf{H}\psi = \left(-\frac{\hbar^2}{2M}\nabla^2 + \mathbf{U}(\mathbf{r})\right)\psi = \mathcal{E}\psi. \tag{2.79}$$

In this equation M is the mass of the atom and the potential $\mathbf{U}$ has the periodicity of the optical lattice. Bloch's theorem now states that the eigenstates ψ of the Hamiltonian 2.79 for a potential with periodicity $\mathbf{U}(\mathbf{r}+\mathbf{R}) = \mathbf{U}(\mathbf{r})$, where $\mathbf{R}$ is a vector of the Bravais lattice, can be chosen to be plane-waves times a function with the periodicity of the Bravais lattice, i.e.

$$\psi_{n\mathbf{k}}(\mathbf{r}) = e^{i\mathbf{k}\cdot\mathbf{r}}\, u_{n\mathbf{k}}(\mathbf{r}). \tag{2.80}$$

The index n is know as the band index. It arises due to the fact that for a given wavevector $\mathbf{k}$ there exist many independent eigenstates labelled by this index. It is important to note that the periodicity in the functions $u_{n\mathbf{k}}(\mathbf{r})$ also imply the same periodicity in the wave-functions $\psi_{n\mathbf{k}}(\mathbf{r})$, i.e.

$$\psi_{n\mathbf{k}}(\mathbf{r}+\mathbf{R}) = e^{i\mathbf{k}\cdot\mathbf{R}}\psi_{n\mathbf{k}}(\mathbf{r}) \tag{2.81}$$

for every $\mathbf{R}$ in the Bravais lattice. We impose the Born-von Karman boundary conditions on the wave-function. Using the primitive cell of the underlying Bravais lattice this condition is given by [47]

$$\psi\left(\mathbf{r}+\sum_{i=1}^{3} N_i\,\mathbf{a}_i\right) = \psi(\mathbf{r}). \tag{2.82}$$

The parameters $\mathbf{a}_i$ are the three primitive vectors defining the primitive unit cell and the $N_i \in \{1, 2, ..., N^{1/3}\}$ are integers. N is the total number of primitive cells in the optical lattice and $N = N_1\,N_2\,N_3$. Hence the general form of the allowed Bloch vectors can be deduced to be

$$\mathbf{k} = \sum_{i=1}^{3} \frac{m_i}{N_i}\mathbf{b}_i, \quad m_i \in \mathbb{Z}_0. \tag{2.83}$$

Another point worth noting is, that the number of allowed wave vectors in a primitive cell of the reciprocal lattice is equal to the number of potential wells in the optical lattice.

We will now deduce a set of algebraic equations which will allow us to calculate the band-structure of an arbitrary optical lattice. First the wave-function is expanded in the set of all plane waves that satisfy the Born-von Karman boundary conditions:

$$\psi(\mathbf{r}) = \sum_{\mathbf{q}} c_{\mathbf{q}} e^{i\mathbf{q}\cdot\mathbf{r}}. \tag{2.84}$$

In this equation $\mathbf{q}$ is a reciprocal lattice vector allowed by the boundary conditions imposed. Next the potential $U(\mathbf{r})$ is also expanded using plane waves. Since the potential is periodic in the lattice, this expansion will only contain plane waves with wave vectors that are vectors of the reciprocal lattice. Hence the potential becomes

$$U(\mathbf{r}) = \sum_{\mathbf{K}} U_{\mathbf{K}}\, e^{i\mathbf{K}\cdot\mathbf{r}}. \tag{2.85}$$

The expansion coefficients are given by the Fourier integral

$$U_{\mathbf{K}} = \frac{1}{v} \int_{\text{cell}} d\mathbf{r}\, e^{-i\mathbf{K}\cdot\mathbf{r}}\, U(\mathbf{r}), \tag{2.86}$$

where v is the volume of the unit cell. Note also that since the potential $U(\mathbf{r})$ is real, the Fourier coefficients satisfy $U_{-\mathbf{K}} = U_{\mathbf{K}}$. It is convenient to set the spatial average U_0 of the potential over a primitive cell to zero, i.e.

$$U_0 = \frac{1}{v} \int_{\text{cell}} d\mathbf{r}\, U(\mathbf{r}) = 0. \tag{2.87}$$

Substituting both the wave-function $\psi(\mathbf{r})$ and the potential $U(\mathbf{r})$ into the Schrödinger equation 2.79 Ashcroft and Mermin showed that the Schrödinger equation can be replaced by a set of algebraic equations and be restated in momentum space as [47]

$$\left(\frac{\hbar^2}{2M}(\mathbf{k}-\mathbf{K})^2-\mathcal{E}\right)c_{\mathbf{k}-\mathbf{K}}+\sum_{\mathbf{K}'}U_{\mathbf{K}'-\mathbf{K}}c_{\mathbf{k}-\mathbf{K}'} \tag{2.88}$$

and using the relation $\mathbf{q}=\mathbf{k}-\mathbf{K}$. The vectors $\mathbf{k}$, $\mathbf{K}$ and $\mathbf{K}'$ are reciprocal lattice vectors. This allows us to rewrite the wave-function expansion as

$$\psi_{\mathbf{k}}(\mathbf{r})=\sum_{\mathbf{K}}c_{\mathbf{k}-\mathbf{K}}e^{i(\mathbf{k}-\mathbf{K})\cdot\mathbf{r}} \tag{2.89}$$

$$=e^{i\mathbf{k}\cdot\mathbf{r}}\left(\sum_{\mathbf{K}}c_{\mathbf{k}-\mathbf{K}}e^{-i\mathbf{K}\cdot\mathbf{r}}\right) \tag{2.90}$$

$$=e^{i\mathbf{k}\cdot\mathbf{r}}u(\mathbf{r}) \tag{2.91}$$

showing the Bloch form 2.80. Since we are interested in tightly bound atoms in an optical lattice, it is advantages to use a localized Wannier basis than an unlocalized plane wave basis like the Bloch basis. They can be defined as [47]

$$\phi_n(\mathbf{r}-\mathbf{R})=\frac{1}{v_0}\int d\mathbf{k}\, e^{-\mathbf{R}\cdot\mathbf{k}}\psi_{n\,\mathbf{k}}(\mathbf{r}), \tag{2.92}$$

where v_0 is the volume in k-space of the first Brillouin zone. Figures 2.12 and 2.13 on page 76 show the calculated band-structure of two 1D cuts through an optical lattice potential well using this formalism. The code to do these calculations was implemented using MatLab.

	$U_0 = 230\,\mathrm{E_R}$		$U_0 = 170\,\mathrm{E_R}$	
n	E_n	σ_n	E_n	σ_n
0	$-220\,\mathrm{E_R}$	$< 10^{-4}$	$-162\,\mathrm{E_R}$	$< 10^{-4}$
1	$-201\,\mathrm{E_R}$	$< 10^{-4}$	$-145\,\mathrm{E_R}$	$< 10^{-4}$
2	$-183\,\mathrm{E_R}$	$< 10^{-4}$	$-130\,\mathrm{E_R}$	$< 10^{-4}$
3	$-165\,\mathrm{E_R}$	$< 10^{-4}$	$-115\,\mathrm{E_R}$	$< 10^{-4}$
4	$-148\,\mathrm{E_R}$	$< 10^{-4}$	$-101\,\mathrm{E_R}$	10^{-4}
5	$-132\,\mathrm{E_R}$	$< 10^{-4}$	$-87\,\mathrm{E_R}$	1.6×10^{-3}
6	$-116\,\mathrm{E_R}$	6×10^{-4}	$-74\,\mathrm{E_R}$	2.0×10^{-2}
7	$-102\,\mathrm{E_R}$	7.5×10^{-3}	$-63\,\mathrm{E_R}$	1.8×10^{-1}
8	$-88\,\mathrm{E_R}$	7.2×10^{-2}	$-53\,\mathrm{E_R}$	1.1
9	$-76\,\mathrm{E_R}$	5.1×10^{-1}	$-44\,\mathrm{E_R}$	3.9
10	$-65\,\mathrm{E_R}$	2.4	$-36\,\mathrm{E_R}$	7.9
11	$-56\,\mathrm{E_R}$	6.4	$-25\,\mathrm{E_R}$	11
12	$-46\,\mathrm{E_R}$	11	$-14\,\mathrm{E_R}$	13

Table 2.1: This table shows the results of a 1D band-structure calculations for two different well depths. Also shown is the level width σ_n. The effects of anharmonicity broadens higher lying energy levels. A calculated potential of $\approx$ 700 data points was used and 70 wells were included in the calculation.

2.7 Population Distribution over Vibrational Levels

This section deals with the characteristics of the population distribution over the vibrational levels in a harmonic and anharmonic oscillator. Firstly we introduce the concept of the kinetic temperature of an ensemble of atoms and link it to the corresponding vibrational temperature. Then we examine the level populations for a 1D and 2D harmonic oscillator and finally extend them to the anharmonic case.

n_y	$\sigma_n/\mathrm{E_R}$	$\Delta_n/\mathrm{E_R}$	n_x	$\sigma_n/\mathrm{E_R}$	$\Delta_n/\mathrm{E_R}$
0	$< 10^{-4}$	16	0	$< 10^{-4}$	16
1	$< 10^{-4}$	16	1	$< 10^{-4}$	16
2	$< 10^{-4}$	15	2	$< 10^{-4}$	15
3	$< 10^{-4}$	14	3	$< 10^{-4}$	14
4	$< 10^{-4}$	13	4	1.0×10^{-4}	14
5	$< 10^{-4}$	12	5	1.7×10^{-3}	13
6	$< 10^{-4}$	11	6	2.1×10^{-2}	12
7	$< 10^{-4}$	8.2	7	0.19	10
8	$< 10^{-4}$	3.5	8	1.1	8.6
9	$< 10^{-4}$	5.5	9	4.0	8.4

Table 2.2: Calculated band energy separations Δ_n and level widths σ_n for 1D cuts through the light-shift potential along the x and y directions respectively, for the case of $U_{max} = 170\,\mathrm{E_R}$ (giving $\omega_0 \approx 2\pi \times 33\mathrm{kHz}$ and nine bound bands in the x-direction). For increasing n the anharmonicity becomes more significant, which results in the broadening of the bands and, because of the lack of rotational symmetry of the potential wells, the difference between x and y characteristic vibrational frequencies becoming increasingly large.

2.7.1 Kinetic Temperature

There are two temperature concepts frequently used to characterize atoms bound in optical lattices, the vibrational temperature, T_{vib}, and the kinetic temperature, T_{kin}. The kinetic temperature of a sample of atoms is related to its spread in its momentum distribution. This spread can be characterized statistically by its variance $(\Delta p)^2$ as

$$(\Delta p)^2 = \int_{-\infty}^{+\infty} p^2 \,\Pi(p)\, dp - \left(\int_{-\infty}^{+\infty} p\, \Pi(p)\, dp \right)^2 , \qquad (2.93)$$

where p is the momentum and $\Pi(p)$ the normalized momentum probability distribution of the atomic sample. In the harmonic approximation $\Pi(p)$ is generally assumed to be a Gaussian with a variance $(\Delta p)^2 = \sigma_p^2$:

$$\Pi(p) = \frac{1}{\sqrt{2\pi}\sigma_p} e^{-\frac{p^2}{2\sigma_p^2}} \tag{2.94}$$

This allows us to define the kinetic temperature of the atomic sample in terms of its variance by

$$T_{\text{kin}} = \frac{\sigma_p^2}{M\,k_B} \tag{2.95}$$

where M is the mass of an atom in the sample and k_B the Boltzmann constant.

2.7.2 Vibrational Temperature

Consider an atomic sample bound in an optical lattice. The diabatic potential wells can be approximated by harmonic oscillator potentials. The eigenstates then become $|F, m_F\rangle \otimes |n\rangle$. In this representation $|F, m_F\rangle$ describes the atomic state characterized by the angular momentum F and the magnetic quantum number m and $|n\rangle$ describes a state in the vibrational level manifold seen by the atoms. The vibrational temperature is related to the distribution of the atoms over the available vibrational states in a potential well. For a thermally excited sample the population Π_n of level $|n\rangle$ is a function of the vibrational energy. Hence the normalized population distribution over the vibrational levels is given by

$$\Pi_n = \frac{e^{-\frac{E_n}{k_B T_{\text{vib}}}}}{\sum_m e^{\frac{E_m}{k_B T_{\text{vib}}}}} \tag{2.96}$$

where E_n is the energy of the n-th vibrational level. This allows us to define the mean vibrational excitation of the atomic sample as an ensemble average of the occupation number n as

$$\overline{n} \equiv \sum_n n \, \Pi_n \tag{2.97}$$

Thus if $\overline{n}$ is known, the vibrational temperature T_{vib} of the ensemble can be deduced and vice versa. So how can we relate the kinetic temperature to the corresponding vibrational temperature of the sample? They are related to each other by looking at the relationship of the momentum distributions of the individual vibrational levels and the measured momentum distribution of the same sample. In general an optical lattice is a large ensemble of independent harmonic oscillators. Hence the measured momentum distribution will be a population weighted sum of the individual momentum probability distributions of the individual vibrational levels. In other words the variance of momentum $(\Delta p)^2$ for all atoms in the optical lattice is a population weighted sum of the variances of the momentum probability distributions $(\Delta p_n)^2$ of the individual vibrational levels:

$$(\Delta p)^2 = \sum_n (\Delta p_n)^2 \, \Pi_n \tag{2.98}$$

From this equation the kinetic temperature of the sample can be deduced. Hence the kinetic temperature T_{kin} scales with respect to the recoil temperature T_{r} as the momentum variance $(\Delta p)^2$ to the recoil momentum variance $\hbar^2 k_L^2$, i.e.

$$\frac{(\Delta p)^2}{\hbar^2 k_L^2} = \frac{T_{\mathrm{kin}}}{T_{\mathrm{r}}} \tag{2.99}$$

where the recoil temperature is given by $T_\mathrm{r} = \frac{\hbar^2 k_L^2}{M k_B}$. To calculate the variances of momentum $(\Delta p)^2$ of the vibrational levels we consider a harmonic oscillator model in the following. The variance $(\Delta p_n)^2$ is then given by

$$(\Delta p_n)^2 = \langle n \,|\, \hat{\mathrm{p}}^2 | n \rangle - (\langle n \,|\, \hat{\mathrm{p}} | n \rangle)^2 \tag{2.100}$$

$$= \langle n \,|\, \hat{\mathrm{p}}^2 | n \rangle \equiv p_n^2 \tag{2.101}$$

The last step follows, since for a harmonic oscillator the matrix element $\langle n \,|\, \hat{\mathrm{p}} | n \rangle = 0$. Thus using the ground state variance $p_0^2 = \frac{M \hbar\omega_\mathrm{osc}}{2}$ these matrix elements are given by

$$p_n^2 = p_0^2 \, (2n + 1) \tag{2.102}$$

Hence the variance in momentum becomes

$$(\Delta p)^2 = p_0^2 \, (2\overline{n} + 1) \tag{2.103}$$

Since for a thermally excited harmonic oscillator the ensemble average momentum distribution is exactly described by a Gaussian, the kinetic temperature can be expressed in terms of the mean vibrational excitation as

$$\frac{(\Delta p)^2}{p_0^2} = \frac{T_\mathrm{kin}}{T_0} = (2\overline{n} + 1) \tag{2.104}$$

where we have introduced the ground state kinetic temperature as $T_0 = \frac{p_0^2}{M k_B}$. Another useful quantity which can be defined here is a Boltzmann factor:

$$q_B \equiv e^{-\frac{\hbar\,\omega_{\mathrm{osc}}}{k_B T_{\mathrm{vib}}}} \tag{2.105}$$

This Boltzmann factor simplifies the calculations of the population distributions in multi-dimensional harmonic traps. In 1D the population distribution and mean occupation number become

$$\Pi_n = \frac{q_B^n}{\sum_m q_B^m} = (1 - q_B) q_B^n \tag{2.106}$$

$$\overline{n} = (1 - q_B) \sum_n n\, q_B^2 = \frac{q_B}{1 - q_B} \tag{2.107}$$

The last steps were achieved by recognizing the geometrical sum involved. In D dimensions the population becomes

$$\Pi_n = (1 - q_B)^D q_B^n \tag{2.108}$$

Real optical lattices are anharmonic and the quantities introduced in this section are appropriate only for deeply bound atoms. The next section discusses how the anharmonicity of the lattice can be taken into account.

2.7.3 Population Distribution of an Anharmonic Oscillator in 1D and 2D

In this section we discuss the characteristics of the population distribution over the vibrational levels in an anharmonic oscillator. Firstly, we examine the distribution in an one dimensional anharmonic oscillator and then extend the

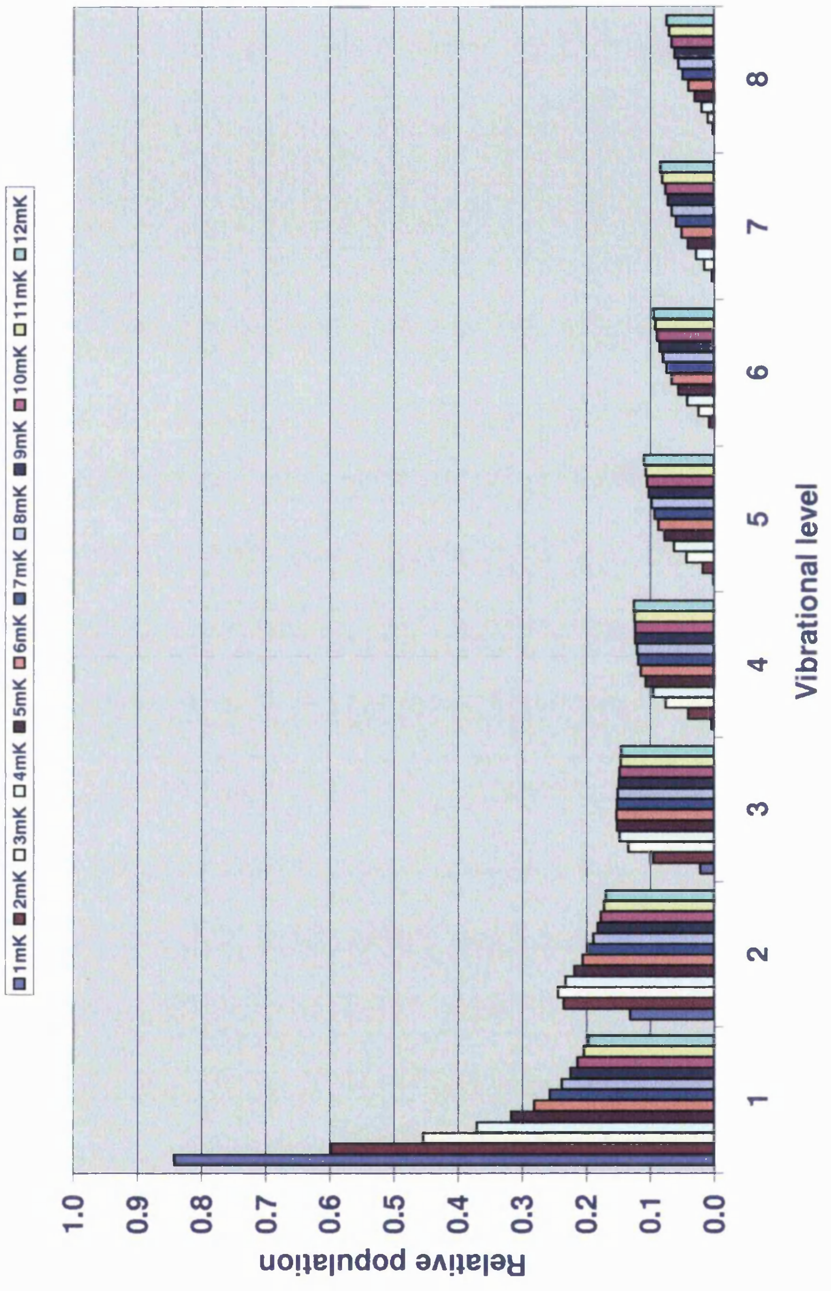

Figure 2.14: The figure shows the population distribution of a 1D anharmonic oscillator for 12 different vibrational temperatures. The maximum light shift is $U_0 = 230\,\mathrm{E_R}$. Each colour represents one of a set of vibrational temperatures ranging from $1\,\mu$K to $12\,\mu$K.

discussion to two spatial dimensions. We need this information to compare our experimental results with the calculated ones.

In the previous section we have been looking at the population distribution in a harmonic oscillator type of potential. The population distribution function Π_n of an oscillator level n and the ensemble average of the occupation number n are given by

$$\Pi_n = \frac{e^{-\frac{E_n}{k_B T_{\text{vib}}}}}{\sum_m e^{\frac{E_m}{k_B T_{\text{vib}}}}} \tag{2.109}$$

$$\overline{n} \equiv \sum_n n \, \Pi_n \tag{2.110}$$

with the definitions as in equation 2.96 and 2.97. Those definitions are quite general. Section 2.6 introduced the formalism to deduce the band-structure in an optical lattice potential will. This calculations allow us to deduce the energies of the levels in the anharmonic oscillator potential well. Thus instead of using the harmonic oscillator energies $E_n = \hbar\omega(n+1/2)$, we can use the real anharmonic energies in equation 2.109 and 2.110. This allows us to deduce the normalized population distribution function and ensemble average of the occupation number for a one dimensional anharmonic oscillator. Figure 2.14 shows calculated normalized population distributions for different vibrational temperatures and different well depths in an 1D anharmonic oscillator.

This scheme can easily be extended to higher dimensions. Here the energy levels are $n + 1$-fold degenerate and the total populations are given by

$$\Pi_n^{x,y} = \Pi_s^x \times \Pi_t^y \tag{2.111}$$

$$\Pi_n^{x,y} = \left[\frac{e^{-\frac{E_s}{k_B T_{\text{vib}}}}}{\sum_m e^{\frac{E_m}{k_B T_{\text{vib}}}}} \right] \tag{2.112}$$

$$\left[\frac{e^{-\frac{E_s}{k_B T_{\text{vib}}}}}{\sum_\ell e^{\frac{E_\ell}{k_B T_{\text{vib}}}}} \right] \tag{2.113}$$

where $n = n_x + n_y = s + t$. Since the energy levels are $n+1$-fold degenerate, the populations of the degenerate sub-levels are all equal. Hence we only need to calculate the relative populations of the $|n_x\rangle\,|n_y = 0\rangle$ vibrational levels. The remaining relative populations can be derived from those values.

A similar procedure can be adopted for the mean vibrational excitation $\overline{n}$:

$$\overline{n} \equiv \sum_n n\,\Pi_n^{x,y} \tag{2.114}$$

Equipped with these two equations the appropriate quantities for an anharmonic oscillator can be deduced as have been for an harmonic one in the previous section. This 2D anharmonic oscillator population model is used subsequently to derive the mean excitation of atoms in the simulation after a Raman cooling sequence of given length. The calculated populations show also that for low enough vibrational temperatures the populations of higher lying levels is negligible compared to lower lying levels. Table 2.3 on the next page shows some calculated population distribution for a maximum light shift of $U_0 = 230\,\mathrm{E_R}$ of the stretched states with $m_f = \pm 4$ and are subsequently

	$\lvert n_x, n_y\rangle$						
β	$\lvert 0,0\rangle$	$\lvert 1,0\rangle$	$\lvert 2,0\rangle$	$\lvert 3,0\rangle$	$\lvert 4,0\rangle$	$\lvert 5,0\rangle$	$\lvert 6,0\rangle$
1.87	0.701	0.112	0.019	0.003	$5.9 \cdot 10^{-4}$	$1.1 \cdot 10^{-4}$	$2.5 \cdot 10^{-5}$
0.62	0.198	0.108	0.059	0.033	0.019	0.011	0.007
0.31	0.076	0.056	0.042	0.031	0.023	0.018	0.015
0.21	0.050	0.040	0.033	0.027	0.023	0.019	0.018
0.16	0.039	0.034	0.029	0.025	0.019	0.019	0.019

Table 2.3: This table shows 2D level populations for different vibrational temperatures using a Maxwell-Boltzmann distribution. Shown are the populations Π_n for $n = n_x + n_y, n_y = 0, n_x \in \{0,1,2,3,4,5,6\}$. Section 2.7.1 on page 81 describes in detail how the values in the table are calculated.

used in the data analysis of the results of the resolved-sideband Raman cooling quantum Monte Carlo wave-function simulations. This is complemented by figure 2.15, which shows the population distribution for a set of values of β, where

$$\beta = \frac{\hbar\omega_0}{k_b T}. \tag{2.115}$$

2.8 Conclusion

In this chapter I have given an introduction to optical lattices and their properties. The chapter started with an introduction to light-shifts in near-detuned optical lattices and a formalism on how to calculate them was introduced. This was followed by an treatment of light-shifts on non-dissipative optical lattices. In this section the idea of a fictitious magnetic field was introduced and a compact form of the light shift Hamiltonian deduced. Then the effects of static magnetic fields in optical lattices were reviewed, followed by some examples of optical lattices. To deduce the allowed energy states of bound atoms in optical lattices a Bloch formalism was used to deduce the energy bands in the lattice and to construct a basis of localized Wannier functions. Lastly, the population distribution over vibrational levels in an optical lattice was discussed in detail and the harmonic model extended to take account of the anharmonicity present in a real optical lattice. Equipped with those tools, we can now move on to discuss the powerful formalism of QMCWF simulations in the next chapter.

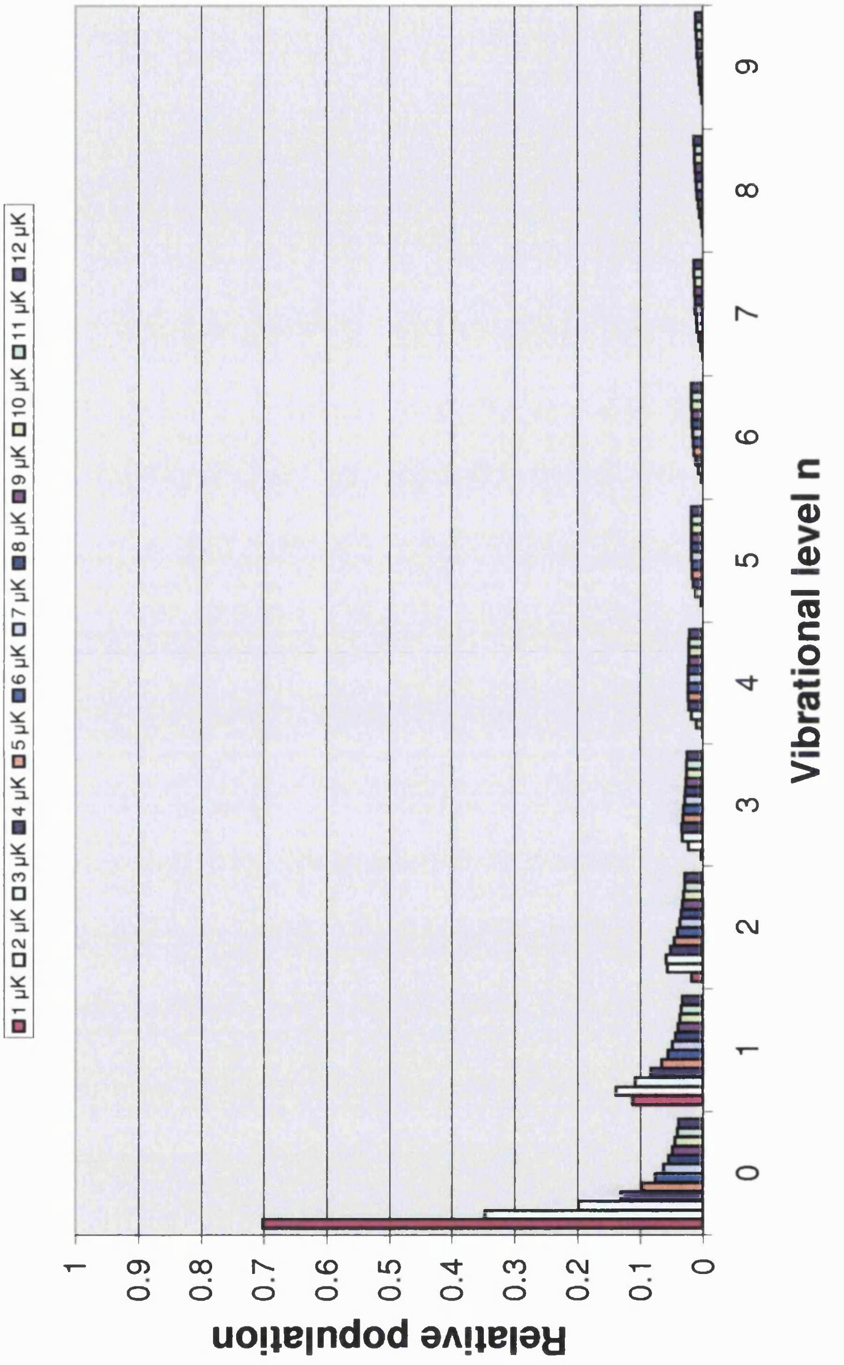

Figure 2.15: The figure shows the population distribution of a 2D anharmonic oscillator for 12 different vibrational temperatures for $\nu_x = n$ and $\nu_y = 0$. The maximum light shift is $U_0 = 230\,\mathrm{E_R}$. Each colour represents one of a set of vibrational temperatures ranging from $1\,\mu\mathrm{K}$ to $12\,\mu\mathrm{K}$.

Chapter 3

Resolved Sideband-Raman Cooling

3.1 Introduction

One of the great challenges of modern science is to prepare, manipulate and measure the quantum state of a physical system. Indeed the ability to carry out these types of operations reliably is one of the main requirements to implement quantum computational schemes. Mastering the control of a system of quantum states may also allow us to study the detailed interaction of atoms with their environment and investigate how they respond to perturbations introduced in a controllable fashion.

An interesting system to study in this context are non-dissipative optical lattices discussed in section 2.2. The main advantage they provide is the isolation of the atoms from their environment. Subsequently, incoherent interactions can be deliberately introduced to study in detail the decoherent responses of the system related to them. In these structures bound by light the scattering of lattice photons is highly suppressed compared to a similar near-detuned system. Another advantage is the ability to easily manipulate a wide range of physical parameters which characterize the trapping potential. These can be achieved through changes to the laser beam geometry, beam polarization, laser frequency and the addition of static electric or magnetic fields. Also the multi-level nature of the atom-lattice interactions let us explore Hamiltonian evolutions beyond the Jaynes-Cummings model[1] and open up a window to a wide variety of theoretical and experimental studies [42]. Another encouraging fact is that the incoherent processes present in photon-atom interactions can largely be suppressed in the far-detuned regime, allowing atomic wavepackets to evolve coherently over longer times [48].

The aim of this chapter is to present theoretical work done on the 2D Raman cooling scheme presented in [49] and of a discussion of our own implementation of a 3D Raman cooling scheme. To implement an efficient Raman cooling scheme two basic ingredients are needed. First optical potentials have to be designed to provide an efficient trapping potential with well defined local polarization variations. Secondly the lattice needs to provide a suitable Raman coupling which can transfer enough atoms to the ground state before recoil heating becomes important. The design of optical potentials was already described in 2.2 on page 54. In this chapter we deduce an expression for Raman coupling in 2D and 3D optical lattices. The 2D scheme is then used in the next chapter to implement a theoretical description of resolved-sideband Raman cooling in 2D with the aid of a quantum Monte Carlo formalism.

---

[1] Interaction of a spin-$\frac{1}{2}$ system with an harmonic oscillator.

3.2 Resolved Sideband-Raman Cooling

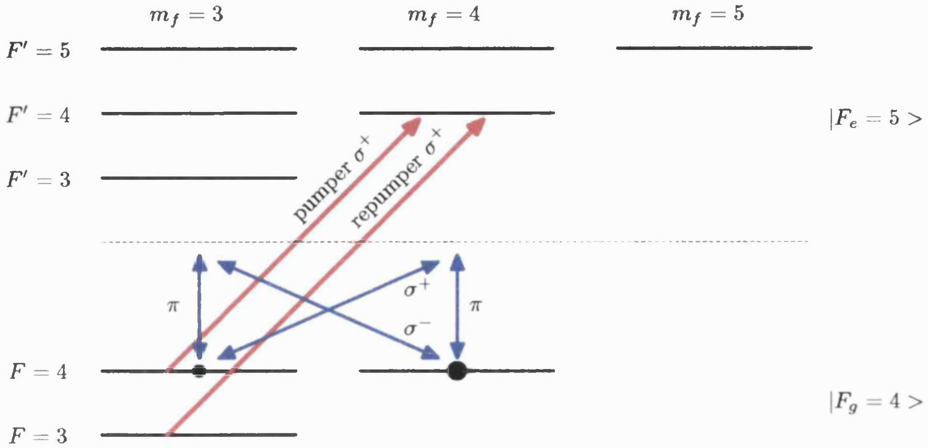

Figure 3.1: Raman cooling level scheme. Two vibrational levels are brought into resonance by a transverse magnetic field. Raman transitions transfers populations from $|m_f = 4, n>$ to $|m_f = 3, n-1>$ represented by the dark blue arrows (coherent coupling). By optical pumping (red arrow) with the Raman pumper beam (σ^+ polarized), tuned to $F = 4 \to F' = 4$, the atom loses one quantum of vibration in the overall process. After several cycles most of the atoms end up in the vibrational ground state. The atoms can also decay to $F' = 3$ and are recycled by a Raman repumper beam (σ^+ polarized), tuned to the $F = 3 \to F' = 4$ transition.

Resolved-sideband Raman cooling was discussed in detail by Jessen and Deutsch in [42] and the first experiment was successfully undertaken in 1998 [49]. As described earlier the atoms are in the tight binding regime and are found mostly at the bottom of the potential wells. Thus tunnelling between different potential wells is negligible and we can consider each potential well independently from each other. At the potential minimum, i.e. at locations of maximum light shift, the optical potential has pure circular polarization. Hence the most deeply bound states have negligible admixture of Zeeman sub-states other than $m = \pm F$.

If now vibrational levels associated with different light-shifted surfaces become degenerate by applying an external magnetic field (c.f. figure 3.1), a coupling between these two surfaces is established. The coupling strength is described by a transverse component of the fictitious magnetic field (c.f. equation 2.62 on page 63 in section 2.3). Thus the near-degenerate vibrational levels get coherently mixed and population transfer between them is initiated. Resolved-sideband Raman cooling relies on this coupling between magnetic sub-levels in an atom. Figure 3.3 on page 97 shows the two lowest energy light-shifted potential surfaces of a σ^+ potential well, belonging to the magnetic sub-levels $m_f = 4$ and $m_f = 3$ respectively. Superimposed on them is their corresponding band-structure. In the following the consider atoms bound in the optical lattice with an angular momentum of $F = 4$ in sub-states with magnetic quantum numbers $m_f = 4$ and $m_f = 3$. These are described by kets of the form $|F, m_f\rangle$. Each potential well possesses a vibrational manifold associated with it. This is described by the state kets $|n = n_x + n_y\rangle$ where n is the vibrational quantum number. Hence the atoms are being described to be in states $|F, m_f\rangle \otimes |n\rangle = |F, m_f\rangle\, |n\rangle$. By applying a weak magnetic field with the appropriate sign and magnitude the level pairs $|F = 4, m_f = 4\rangle\, |n\rangle$ and $|F = 4, m_f = 3\rangle\, |n - 1\rangle$ can be brought successively into degeneracy. The necessary magnetic field strengths are shown in Figure 3.4 on page 99. An optical coherence between this level pair is introduced by an added π-component to the lattice optical field. This coupling initiates a coherent evolution between the two states and is often referred to as Rabi oscillations. By adding a Raman pumper beam with σ^+ polarization to the system the population in $|4, m_f = 3\rangle\, |n - 1\rangle$ can be optically pumped into the

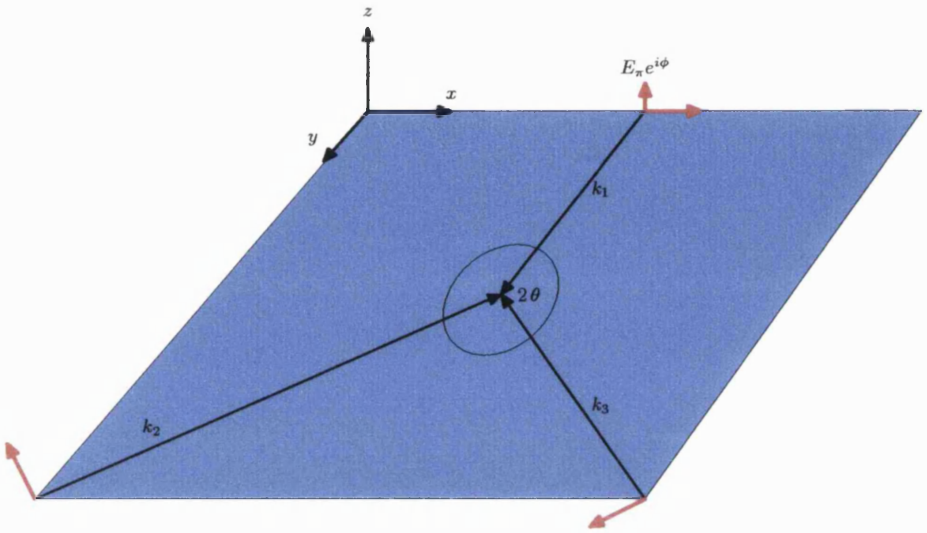

Figure 3.2: This figure shows a three-beam 2D optical lattice. The polarizations of the lattice beams is in the x-y-plane. The beam along the y-direction has an additional π-component with a phase shift of φ with respect to the in-plane component.

excited state manifold $F' = 4$. Since we are in the Lamb-Dicke regime this level predominantly decays into $|F = 4, m_f = 4\rangle\,|n - 1\rangle$, i.e. the wavepacket predominately preserves its symmetry.

There is also the possibility for the atom to decay into the $F = 3$ manifold. The disadvantage in this case being that atoms decaying from $F' = 4$ end up on a potential hill. Leaving the atoms too long in this level causes unwanted heating and spreading of the atomic wavepacket. To avoid this a Raman repumper beam with the same polarization as the Raman pumper beam is used to recycle these atoms quickly back to the $F' = 4$ manifold providing quick enough recycling before the atomic wavepacket can evolve significantly. Looking at the transition strengths given in [22] we see that the repumper beam can efficiently pump the atoms back into the $F' = 4$ manifold. On average the atoms scatter one pumper and one repumper photon in one cooling

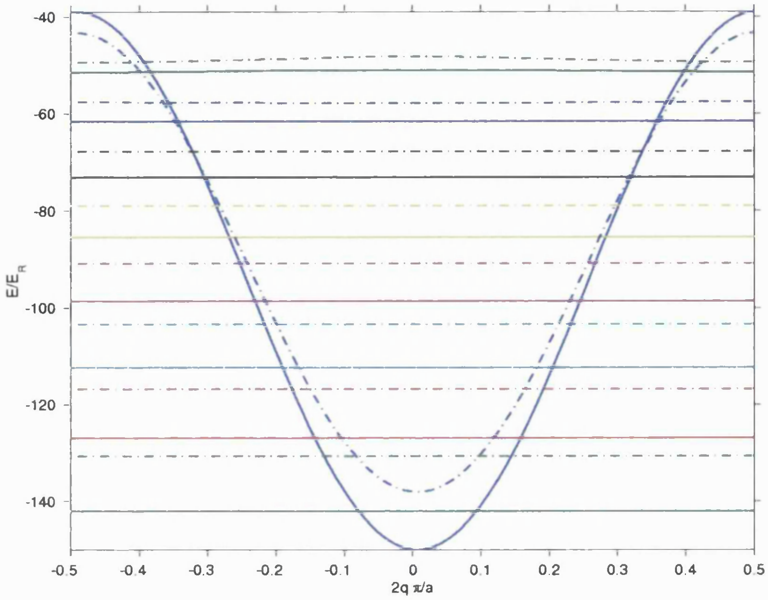

Figure 3.3: The figure shows the band-structure for a potential well with $m_f = 3$ (dashed) and $m_f = 4$ (solid). The maximum light shift is $U_0 = 150\,\mathrm{E_R}$

cycle [49], an assertion that is also supported by our quantum Monte Carlo simulations.

Figure 3.2 on the preceding page shows the beam configuration for a three-beam 2D lattice. The beam along the y-direction has an additional π-component with a phase shift of φ with respect to the in-plane component. This additional component provides the Raman coupling.

The first step in the modelling of resolved-sideband Raman cooling was to use the already implemented band structure code to deduce the vibrational levels structure as shown in figure 3.3. The potential wells for F=4 with $m_f = 3$ (dashed) and $m_f = 4$ (solid) are shown and the corresponding band structure is superimposed. This allows us to calculate the necessary magnetic fields to bring the two levels $|F = 4, m_f = 4\rangle\,|n\rangle$ and $|F = 4, m_f = 3\rangle\,|n-1\rangle$

Transition	B_r in mG
$\|4,4\rangle\,\|1\rangle \leftrightarrow \|4,3\rangle\,\|0\rangle$	21
$\|4,4\rangle\,\|2\rangle \leftrightarrow \|4,3\rangle\,\|1\rangle$	25
$\|4,4\rangle\,\|3\rangle \leftrightarrow \|4,3\rangle\,\|2\rangle$	28
$\|4,4\rangle\,\|4\rangle \leftrightarrow \|4,3\rangle\,\|3\rangle$	31
$\|4,4\rangle\,\|5\rangle \leftrightarrow \|4,3\rangle\,\|4\rangle$	34

Table 3.1: This table shows calculated values for the required magnetic field B_r to bring the levels involved in the corresponding transition into resonance.

into resonance. As an example, the B-fields necessary for a lattice with maximum light shift of $U_0 = 150\,\mathrm{E_R}$ to bring the levels $|4,4\rangle\,|n\rangle$ and $|4,3\rangle\,|n-1\rangle$ into resonance are shown in table 3.1. These results are readily used in the simulations implemented in the next chapter.

Extending the existing Matlab code base, these calculations have been automated to produce graphs like figure 3.4. These show the calculated B_{Raman} versus well depths. This information is subsequently used to aid the choice of our experimental parameters. The graph also shows that the lowest transition crosses the zero B-field line at around 247 $\mathrm{E_R}$. This is an upper limit for the maximum light shift we can chose in our experiments[2].

Another useful number can be determined by looking at the first and second Raman sidebands. Taking the difference between the magnetic fields required to bring a pair of vibrational states into resonance, one with $\Delta n = 1$ and $\Delta n = 2$, we see that this is nothing more than the energy difference between the second and first exited state of the $m_f = 4$ potential. Hence this method provides an independent measurement of the vibrational frequency of an optical lattice by invoking the relation[3] $\Delta E[\mathrm{E_R}] = 0.17 \times \mathrm{B}[\mathrm{mG}]$.

---

[2] We usually work in the regime of small light-shifts, $U_0 < 247\,\mathrm{E_R}$.

[3] This can easily be derived by considering the Zeeman energy shift formula, substituting for the constants and changing units to $\mathrm{E_R}$ and mG.

This finishes our short introduction to resolved-sideband Raman cooling. The next section describes the scheme used in our experiments.

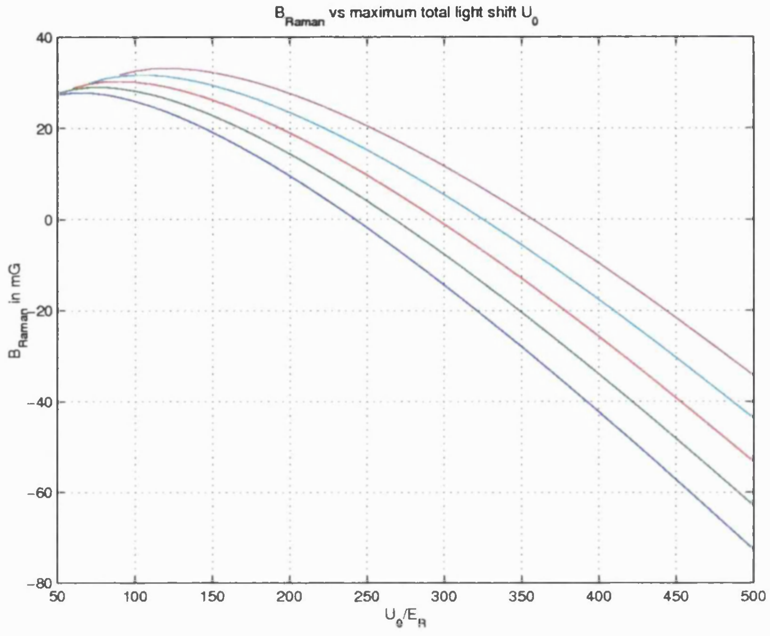

Figure 3.4: The figure shows the required Raman magnetic field for different maximum light-shifts. From this graph we can can read the required B_{Raman} range for a given maximum light shift. $(blue) : |4,1 > \rightarrow |3,0 >, (green) : |4,2 > \rightarrow |3,1 >, (red) : |4,3 > \rightarrow |3,2 >, (light\,blue) : |4,4 > \rightarrow |3,3 >, (lilac) : |4,5 > \rightarrow |3,4 >$.

3.3 Scheme used in our experiment

There are different experimentally feasible implementations of resolved-sideband Raman cooling in a 2D optical lattice possible. We have chosen to follow the experimental realization of [49] and a more in-depth description can be found in it. The only difference to the configuration discussed in the paper is how the beam configuration is orientated. In our experiment the beam configuration is rotated by 90° as shown in 3.5 on the next page with respect to

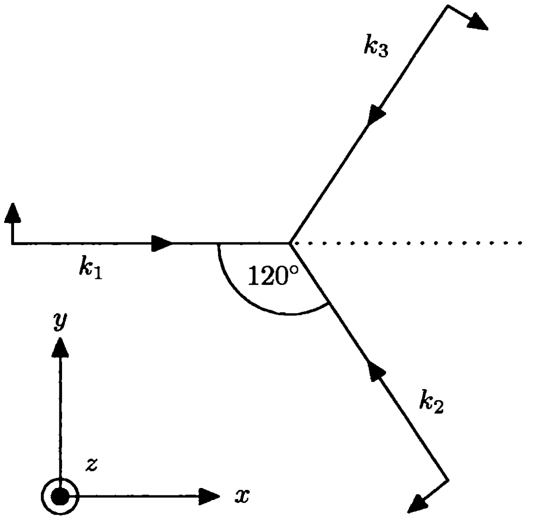

Figure 3.5: This figure shows the beam configuration we use in our experiment. Note that it is the same configuration used in [49] but rotated by 90°.

the one in the paper. We have chosen this beam configuration due to space constraints on our optical bench.

First the atoms are trapped with a MOT. After that they are loaded into a near-detuned lattice and subsequently adiabatically transferred to a superimposed far-detuned lattice. The use of non-dissipative potentials is necessary to minimize the interaction of the atoms and the lattice beams so to avoid unwanted heating. Then the atoms in the optical lattice are spin-polarized to maximize the population of the proper magnetic sub-states used in the following Raman cooling cycle. Next a static magnetic field introduces an additional energy shift to the magnetic sub-levels and brings the lowest pair, $|F = 4, m_f = 4\rangle\,|1\rangle \leftrightarrow |F = 4, m_f = 3\rangle\,|0\rangle$, into resonance. The subsequent Raman cooling cycle splits into two processes, a coherent evolution and an incoherent scattering event. The Raman coupling is strong enough to also provide coupling to higher lying state pairs. The atoms descend the vibrational level ladder and end up in the lowest state of the $m_f = 4$ vibrational manifold. We have achieved resolved Raman sideband cooling in our experiment and experimental results will be discussed in the next chapter in context with our simulations. With this method we can prepare the atoms in the lowest vibration state of motion. Up to 80% end up in this ground state, far above the maximum value of $\sim$ 30% achieved by polarization-gradient cooling alone corresponding to a temperature of $\approx 1\,\mu$K. Elsewhere temperatures down to 290 nK have been observed [50] with similar resolved-sideband Raman cooling schemes. This leads us to deduce expressions for the Raman coupling strength in 2D and 3D in the remainder of this chapter.

3.4 Calculation of the Raman Coupling in 2D

In this section I will derive an expression for the Raman coupling matrix elements given the spatial dependence of the optical field in the optical lattice. Section 2.3 on page 57 describes in detail how the lattice electric field can be derived for an arbitrary beam configuration. We follow the treatment of Jessen and Deutsch [42] using the electric field of a 2D lattice, which is given by

$$\begin{aligned}\mathbf{E_L}(\mathbf{x}) =& \frac{E_1 e^{-iky}}{\sqrt{2}}\big[-\mathbf{e}_+ \left\{1 + 2e^{iK_y y}\cos\left(K_x x\right)\right\} \\ &+ \mathbf{e}_- \left\{1 + 2e^{iK_y y}\cos\left(K_x x - 2\theta\right)\right\}\big] \\ &+ \mathbf{e}_\pi E_\pi e^{-iky} e^{i\varphi},\end{aligned} \tag{3.1}$$

where $K_x = k\sin\theta$, $K_y = k(1+\cos\theta)$, E_1 is the single beam amplitude and $\mathbf{e_q}$ the unit vectors of the rotating basis, $\mathbf{e_q} \in \{\mathrm{e}_+, \mathrm{e}_-, \mathrm{e}_\pi\}$. The lattice electric field contains a π-polarized component with a real amplitude E_π and a relative phase $e^{i\varphi}$. The beam configuration for this symmetry is shown in figure 3.2 on page 96 and for simplicity in the following, the relative phases of the beams were chosen so as to put a maximum of the intensity of the σ^+-polarized light at the origin.

From equation 3.1 on the preceding page we can derive the effective field governing the coupling between the $|m = F\rangle$ and $|m = F-1\rangle$ levels using the optical potential 2.50 on page 58 and substituting for the local polarizations from equation 3.1 on the preceding page. The effective magnetic field B_{eff} is then given by

$$\begin{aligned} B_x^{\text{fic}} + B_y^{\text{fic}} = -\frac{2U_1}{3}\frac{E_\pi}{E_1}\{&2\sin\theta\sin(K_x x-\theta)\cos(K_y y-\varphi) \\ &2i\cos\theta\cos(K_x x-\theta)\sin(K_y y-\varphi) - i\sin\varphi\}. \end{aligned} \tag{3.2}$$

Here U_1 represents the single beam light shift. The coupling matrix elements are given by (cf. equation 16 in [42])

$$U_{m,m\pm1} = \frac{\left\langle \{n'\}, m\pm1 \middle| \left[B_x^{\text{tot}}(\mathrm{x}) \mp \imath B_y^{\text{tot}}(\mathrm{x})\right] \hat{F}_\pm \middle| \{n\}, m \right\rangle}{2F} \tag{3.3}$$

where $\mathbf{B}_{\text{tot}}$ is given by the sum of the effective and all external magnetic fields applied, $\mathbf{B}_{\text{tot}} = \mathbf{B}_{\text{fic}} + \mathbf{B}_{\text{ext}}$, n the vibrational level under consideration in the respective manifolds $|m \pm 1, n \pm 1\rangle$ and $|m, n\rangle$. $\hat{F}_{\pm}$ is the Franck-Condon overlap given by

$$\mathbf{F}_{\pm} \left|F, m_F\right\rangle = \hbar\sqrt{F(F+1) - m(m \pm 1)} \left|F, m \pm 1\right\rangle \tag{3.4}$$

Substituting 3.2 on the page before into 3.3 on the preceding page and expanding around the minimum of the potential well at the origin to first order in the small parameters kx and ky results in [42]

$$\begin{aligned} U_{F,F-1} \approx \; & -\frac{U_1}{\sqrt{2F}}\frac{E_\pi}{E_1}\left\langle\left\{n_x^{'}, n_y^{'}\right\}, F-1\right| \Big[-e^{i\varphi} + \frac{1}{2}e^{-i\varphi}kx \\ & \qquad + i\left(e^{i\varphi} - \frac{1}{2}e^{-i\varphi}\right)ky\Big]\left|\left\{n_x^{'}, n_y^{'}\right\}, F\right\rangle \end{aligned} \tag{3.5}$$

$$\begin{aligned} = & -\frac{U_1}{\sqrt{2F}}\frac{E_\pi}{E_1}\Big\{\left\langle\left\{n_x^{'}\right\}, F-1\right|\left[\frac{1}{2}e^{-i\varphi}kx\right]|\left\{n_x^{'}\right\}, F\Big\rangle \\ & + \left\langle\left\{n_y^{'}\right\}, F-1\right| i\left(e^{i\varphi} - \frac{1}{2}e^{-i\varphi}\right)ky|\left\{n_y^{'}\right\}, F\Big\rangle \\ & + \left\langle\left\{n_x^{'}, n_y^{'}\right\}, F-1\right| -e^{i\varphi}|\left\{n_x^{'}n_y^{'}\right\}, F\Big\rangle\Big\} \end{aligned} \tag{3.6}$$

where a harmonic approximation for the vibrational levels was used. Choosing $\varphi = \pi/2$ gives maximum coupling for the odd parity states in which case the coupling matrix elements for vibrational change of one quantum along x and y can be rewritten as

$$U_{F,F-1}\left(n_x, n_y\right) = U^{(x)}_{F,F-1} + U^{(y)}_{F,F-1} \quad , \tag{3.7}$$

where

$$U^{(x)}_{F,F-1} \approx iU_R\sqrt{n_x} \quad , \tag{3.8}$$

$$U^{(y)}_{F,F-1} \approx 3U_R\sqrt{n_y} \quad , \tag{3.9}$$

$$U_R = \frac{U_1}{2\sqrt{2F}} \frac{E_\pi}{E_1} \eta \quad . \tag{3.10}$$

Here η is the Lamb-Dicke parameter and is given by

$$\eta = \left(\frac{\mathrm{E_R}}{\hbar\omega_{osc}} \right)^{1/2} = \left(\frac{2}{15} \frac{\mathrm{E_R}}{U_1} \right)^{1/4} \quad . \tag{3.11}$$

For the worst possible phase of $\phi = n\pi, n \in \mathbb{N}_0$, both couplings have equal magnitude.

Figure of merit for coherent manipulation

Jessen and Deutsch define a figure of merit κ for coherent manipulation in [42],

$$\kappa \equiv \frac{U_R}{\hbar\gamma_s} \gg 1. \tag{3.12}$$

In this definition $\hbar/U_R$ is the time scale for coherent manipulation and γ_s the photon scattering rate. For good coherent manipulation of the atomic state one requires that the time scale $\hbar/U_R$ for coherent evolution is shorter than the lifetime of the Raman coherence between the states $|F, n\rangle$ and $|F-1, n+1\rangle$. The latter one is dominated by the decay of the $|F-1, n+1\rangle$ due to optical pumping which is of order of magnitude of the inverse photon scattering rate γ_s^{-1}. Jessen and Deutsch derived for the $2D$ configuration

$$\kappa \equiv \frac{U_R}{\hbar\gamma_s} \approx \frac{0.047}{\sqrt{F}}\frac{E_\pi}{E_1}\frac{|\Delta|}{\Gamma}\left(\frac{\mathrm{E_R}}{U_1}\right)^{1/4} \tag{3.13}$$

The larger this figure of merit is the better. Consider for example Cs ($F = 4$) in a lattice with $U_1 = 54\,\mathrm{E_R}$, $\Delta = -5 \cdot 10^3\Gamma$ and $E_\pi = 0.3E_1$, which are similar in order of magnitude to values used in our experiment. Substituting this into equation 3.13 gives $\kappa \approx 13$. It can easily be seen that increasing the detuning, provided that sufficient laser power is available, or increasing the π-component E_π can improve the feasibility of coherent manipulation. We recently bought a Ti-Sapphire laser which can provide sufficient power for much higher detunings Δ than the MOPAs used before.

Figure of merit for sideband cooling

As we are interested in preparing most atoms in the vibrational ground state, i.e. preparing well localized Wannier states, a figure of merit for sideband cooling can be defined. Since the atoms are in the Lamb-Dicke regime, resolved-sideband Raman cooling allows in principle the removal of one quantum of vibration every few oscillation periods. This means that the vibrational excitation must be much smaller than the oscillation period of the atomic wavepacket, i.e.

$$\frac{d\bar{n}}{dt} \ll \omega_{\mathrm{osc}}. \tag{3.14}$$

In the harmonic approximation this condition can be rewritten as

$$\left(\frac{\hbar\omega_{\text{osc}}}{\text{E}_{\text{R}}}\right)^2 \gg \frac{\hbar\gamma_s}{\text{E}_{\text{R}}} \tag{3.15}$$

This condition is easily met by several orders of magnitude in lattices with detunings of more than several thousands line widths. Considering now the time scale of population transfer in resolved-sideband Raman cooling, $\frac{\hbar}{|U_R|}$, a figure of merit for sideband cooling can be defined as

$$\frac{|U_R|}{\hbar\frac{d\bar{n}}{dt}} \equiv \kappa' \gg 1. \tag{3.16}$$

The rate of vibrational excitation is to leading order in the Lamb-Dicke parameter η given by

$$\frac{d\bar{n}}{dt} = \gamma_s\left(\Delta k z_0\right)^2. \tag{3.17}$$

In this relation, γ_s is the photon scattering rate of the lattice beams and $(\hbar\Delta k)$ the mean-squared momentum transfer of a photon scattering event, calculated by averaging the momentum components along the lattice directions over the dipole emission pattern. Last and not least, z_0 is the ground-state variance and is related to the Lamb-Dicke parameter to lowest order by

$$\eta = k_L z_0 = \sqrt{E_r/\hbar\omega_{\text{osc}}} \tag{3.18}$$

where we have ignored the difference in curvature of the wells involved. Jessen and Deutsch deduced in [42] for the figure of merit for sideband cooling in a configuration as in figure 3.5 on page 100

$$\kappa_x^{'} \approx 0.17 \frac{E_\pi}{E_1} \frac{|\Delta|}{\Gamma} \left(\frac{U_1}{\mathrm{E_R}} \right)^{1/4} , \quad \kappa_y^{'} = 3\kappa_x^{'} . \tag{3.19}$$

For parameters used in our experiment($U_1 \approx 54\,\mathrm{E_R}, \Delta \approx -4000\Gamma, E_\pi/E_1 = 0.3$) the figure of merits are $\kappa_x^{'} \approx 553$ and $\kappa_y^{'} \approx 1659$.

3.5 Calculation of the Raman Coupling in 3D

This section discusses resolved-sideband Raman cooling in a 3D far-detuned optical lattice. The configuration chosen is the one depicted in figure 2.8 on page 70. One advantageous property of this configuration is that phase fluctuations in the laser beams translate only into spatial shifts of the locations of maximum light shifts and do not change the structure of the lattice as such [3]. Raman cooling in higher dimensions is an important tool which can improve the accuracy of atomic clocks and deliver a more advantageous starting point for atomic fountains. This section is structured in the following way. We place a σ^+ well at the origin. Then a Raman coupling is introduced by adding a π-component to the electric lattice field. This is achieved by tipping the polarization of two lattice beams out of their usual position. It is found that the magnitude of the Raman coupling connecting states with $\Delta m = 1$ is a function of the relative spatial phase of the σ and π field components. Therefore, the Raman coupling for this configuration is calculated and the optimal relative spatial phase of the π-component, which maximizes the odd coupling, is deduced. Last the coupling matrix elements are derived. A closer look at the various π-components resulting from the tipping of different pairs of laser beams shows that we have to tip the polarization of two beams having opposite sign of k_z out of their usual positions. Tipping the polarization of two beams with the same sign of k_z doesn't work and no Raman coupling is induced along the z-direction. Figure 3.6 shows the configuration we are suggesting for resolved-sideband Raman cooling in 3D and our choice of lattice beam which are going to be tipped. The named quantities shown are also used in the subsequent equations in this section.

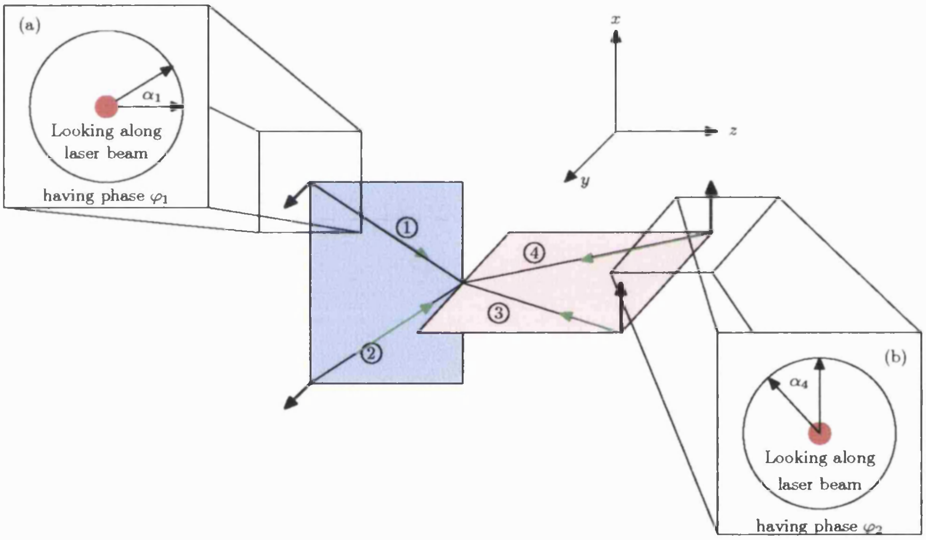

Figure 3.6: This figure shows a possible beam configurations to achieve resolved-sideband Raman cooling in a 3D optical lattice. The beams are numbered 1-4. The polarizations of beam 1 and 4 are tipped out of their usual position by an angle α_1 or α_4 respectively. Additionally a phase shift $\varphi_{1,4}$ respectively is applied to the π-components of beams 1 and 4 to maximize the odd parity coupling. The green arrows represent the wave vectors of the corresponding lattice beam.

In this configuration we can introduce a phase shift to the two tipped beams by changing their linear polarization to an elliptical one. This elliptical polarization can be decomposed into two orthogonal linear polarizations with arbitrary phase shift between them (cf figure 3.7). We will exploit this later to maximize the odd Raman coupling which couples states of different parity. There are two possible configurations. We can vary the phases between the orthogonal components of each tipped lattice beam individually. This gives rise to the cases where

1. $\varphi_1 \neq 0$ and $\varphi_4 = 0$
2. $\varphi_1 \neq 0$ and $\varphi_4 \neq 0$.

To deduce the lattice light-field, a script using the symbolic toolbox in Matlab was written. The necessary quantities needed in the implementation of the script are the wave vectors for the different lattice beams and the polarization vectors of each beam. The wave vectors are shown here and are the same for both cases:

$$\mathbf{k}_1 = k\begin{pmatrix} -\sin\theta \\ 0 \\ \cos\theta \end{pmatrix} \quad \mathbf{k}_2 = k\begin{pmatrix} \sin\theta \\ 0 \\ \cos\theta \end{pmatrix} \quad \mathbf{k}_3 = k\begin{pmatrix} 0 \\ -\sin\theta \\ -\cos\theta \end{pmatrix} \quad \mathbf{k}_4 = k\begin{pmatrix} 0 \\ \sin\theta \\ -\cos\theta \end{pmatrix}$$

The numbering of the wave vectors follows the scheme described in figure 3.6. The polarization vectors are listed in the appropriate section below including the phase shifts.

3.5.1 Tipped configuration with one beam having a phase shift φ_1

In this configuration we tip the polarization of the beam numbered 1 in figure 3.6 by an angle α_1 counterclockwise. We then can decompose the resulting polarization vector into two orthogonal components, one along the original direction[4] and one perpendicular to it. By varying the relative phase between the two components we can maximize the odd coupling and the resulting polarization is elliptical. This situation is shown in figure 3.7.

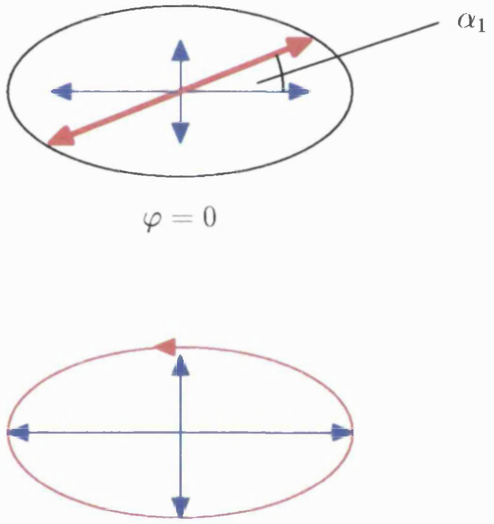

$\varphi = 0$

$\varphi = \frac{\pi}{2}$

Figure 3.7: This figure shows what happens when we tip one of the polarizations out of the its normal position by an angle α_1. When the phase shift φ is zero, the resolved components (blue) are in phase and the sum polarization vector of both components is linear (red). Adding a phase shift $\varphi \neq 0$ to one of the components produces elliptical polarization as is shown for a phase shift of $\varphi = \frac{\pi}{2}$.

Hence the polarization vectors used to deduce the total light-field including

---

[4] along $\alpha_1 = 0$.

a phase-shift are given by

$$\mathbf{p}_1 = \begin{pmatrix} 0 \\ \cos\alpha_1 \\ 0 \end{pmatrix} + \begin{pmatrix} \cos\theta\sin\alpha_1\exp(i\varphi) \\ 0 \\ \sin\alpha_1\sin\theta\exp(i\varphi) \end{pmatrix} = \begin{pmatrix} \cos\theta\sin\alpha_1\exp(i\varphi) \\ \cos\alpha_1 \\ \sin\alpha_1\sin\theta\exp(i\varphi) \end{pmatrix}$$

$$\mathbf{p}_2 = \begin{pmatrix} 0 \\ 1 \\ 0 \end{pmatrix} \quad \mathbf{p}_3 = \begin{pmatrix} 1 \\ 0 \\ 0 \end{pmatrix} \quad \mathbf{p}_4 = \begin{pmatrix} \cos\alpha_4 \\ -\cos\theta\sin\alpha_4 \\ \sin\alpha_4\sin\theta \end{pmatrix}$$

We can then write the electric field vectors of the lattice beams as

$$\begin{aligned} \mathbf{E}_1 &= A_1\,\mathbf{p}_1\exp(i\textstyle\sum(\mathbf{k}_1\cdot\mathbf{r})) \quad & \mathbf{E}_2 &= A_1\,\mathbf{p}_2\exp(i\textstyle\sum(\mathbf{k}_2\cdot\mathbf{r})) \\ \mathbf{E}_3 &= A_1\,\mathbf{p}_3\exp(i\textstyle\sum(\mathbf{k}_3\cdot\mathbf{r})) \quad & \mathbf{E}_4 &= A_1\,\mathbf{p}_4\exp(i\textstyle\sum(\mathbf{k}_4\cdot\mathbf{r})) \end{aligned} \tag{3.20}$$

Thus the total light-field decomposed into its circular components reads as

$$\begin{aligned} E_+ =& \frac{A_1}{2}(1-i)\Big\{-\cos\theta\sin\alpha_1\exp(i\varphi_1)\exp(-ikx\sin\theta + ikz\cos\theta) \\ & -\exp(-iky\sin\theta - ikz\cos\theta) - i\exp(ikx\sin\theta + ikz\cos\theta) \\ & -\cos\alpha_4\exp(iky\sin\theta - ikz\cos\theta) - i\cos\alpha_1\exp(-ikx\sin\theta + ikz\cos\theta) \\ & -i\cos\theta\sin\alpha_4\exp(iky\sin\theta - ikz\cos\theta)\Big\} \end{aligned} \tag{3.21}$$

$$
\begin{aligned}
E_{-} =& \frac{A_1}{2}(1-i)\Big\{ \cos\theta \sin\alpha_1 \exp(i\varphi_1) \exp(-ikx\sin\theta + ikz\cos\theta) \\
&+ \exp(-iky\sin\theta - ikz\cos\theta) - i\exp(ikx\sin\theta + ikz\cos\theta) \\
&+ \cos\alpha_4 \exp(iky\sin\theta - ikz\cos\theta) - i\cos\alpha_1 \exp(-ikx\sin\theta + ikz\cos\theta) \\
&- i\cos\theta\sin\alpha_4 \exp(iky\sin\theta - ikz\cos\theta)\Big\} \qquad (3.22)
\end{aligned}
$$

$$
\begin{aligned}
E_{\pi} =& \frac{A_1\sin\theta}{\sqrt{2}}\Big\{ -(1-i)\sin\alpha_1\exp(i\varphi_1) + (1+i)\sin\alpha_4 \\
&+ ikx(1-i)\sin\theta\sin\alpha_1\exp(i\varphi_1) + iky(1+i)\sin\theta\sin\alpha_4 \\
&- ikz\cos\theta\left[(1+i)\sin\alpha_4 + (1-i)\sin\alpha_1\exp(i\varphi_1)\right]\Big\} \qquad (3.23)
\end{aligned}
$$

Using the formalism described in section 2.3 on page 57, the Raman coupling can be deduced using [42]

$$
U_{m,m\pm1} = \frac{\langle\{n'\}, m\pm1\,|\,[\mathbf{B}^{x}_{\mathrm{tot}} \mp i\mathbf{B}^{y}_{\mathrm{tot}}]\,\mathbf{F}_{\pm}|\{n\}, m\rangle}{2F} \qquad (3.24)
$$

where $\mathbf{B}_{\mathrm{tot}}$ is the sum of the external and the effective magnetic field. Substituting equations 3.21, 3.22 and 3.23 into 2.60 we deduce for the effective field governing the coupling

$$
\begin{aligned}
B^{+}_{\text{eff}} =& \frac{B^x_{\text{eff}} + iB^y_{\text{eff}}}{\sqrt{2}} \\
=& -\frac{iU_1\sqrt{6}}{48}\frac{A_\pi}{A_1}\Big\{ \\
& 8i\sin\alpha_4 + 8\cos\varphi_1\sin\alpha_1 + 8\cos\varphi_1\sin\alpha_1\cos\alpha_4 \\
& -8i\sin\alpha_1\sin\varphi_1 + 8i\cos\alpha_1\sin\alpha_4 - 8i\cos\alpha_1\sin\alpha_1\sin\varphi_1 \\
& +4\cos\varphi_1\sin\alpha_4\sin\alpha_1 + 4i\cos\varphi_1\sin\alpha_4\sin\alpha_1 \\
& +kx(4\sqrt{3}\sin\varphi_1\sin\alpha_1 + 2\sqrt{3}\sin\varphi_1\sin\alpha_4\sin\alpha_1 \\
& +4\sqrt{3}\sin\varphi_1\sin\alpha_1\cos\alpha_4 + 2i\sqrt{3}\sin\varphi_1\sin\alpha_4\sin\alpha_1 \\
& +8i\sqrt{3}\sin\alpha_1\cos\varphi_1) \\
& +ky(8\sqrt{3}\sin\alpha_4 + 4\sqrt{3}\sin\varphi_1\sin\alpha_1\cos\alpha_4 \\
& -4\sqrt{3}\sin\varphi_1\sin\alpha_1 + 2\sqrt{3}\sin\varphi_1\sin\alpha_4\sin\alpha_1 \\
& +2i\sqrt{3}\sin\varphi_1\sin\alpha_4\sin\alpha_1) \\
& +kz(-8\sin\varphi_1\sin\alpha_1 - 8\sin\varphi_1\sin\alpha_1\cos\alpha_4 \\
& -4\sin\varphi_1\sin\alpha_4\sin\alpha_1 - 4i\sin\varphi_1\sin\alpha_4\sin\alpha_1) \\
& \Big\}
\end{aligned} \tag{3.25}
$$

We are interested in the matrix elements $U_{F,F-1}$, hence substituting 3.25 into 3.24 allows us to find the functional dependence of the Raman coupling around the minimum of the potential well. Furthermore we use the harmonic approximation for the band structure. Thus we find for to first order for the Raman coupling for the small parameters kx, ky and kz,

$$
\begin{aligned}
U_{F,F-1} &\approx \frac{\langle\{n_x^{'}, n_y^{'}, n_z^{'}\}, F-1 \,|\, [B^x_{\mathrm{tot}} \mp iB^y_{\mathrm{tot}}] \,|\{n_x, n_y, n_z\}, F\rangle}{\sqrt{2F}} \\
&= -\frac{iU_1\sqrt{3}}{48\sqrt{F}}\frac{A_\pi}{A_1}\Big\langle\{n_x^{'}, n_y^{'}, n_z^{'}\}, F-1\Big|\Big\{ \\
&\quad 8i\sin\alpha_4 + 8\cos\varphi_1\sin\alpha_1 + 8\cos\varphi_1\sin\alpha_1\cos\alpha_4 \\
&\quad - 8i\sin\alpha_1\sin\varphi_1 + 8i\cos\alpha_1\sin\alpha_4 - 8i\cos\alpha_1\sin\alpha_1\sin\varphi_1 \\
&\quad + 4\cos\varphi_1\sin\alpha_4\sin\alpha_1 + 4i\cos\varphi_1\sin\alpha_4\sin\alpha_1 \\
&\quad + kx(4\sqrt{3}\sin\varphi_1\sin\alpha_1 + 2\sqrt{3}\sin\varphi_1\sin\alpha_4\sin\alpha_1 \\
&\quad + 4\sqrt{3}\sin\varphi_1\sin\alpha_1\cos\alpha_4 + 2i\sqrt{3}\sin\varphi_1\sin\alpha_4\sin\alpha_1 \\
&\quad + 8i\sqrt{3}\sin\alpha_1\cos\varphi_1) \\
&\quad + ky(8\sqrt{3}\sin\alpha_4 + 4\sqrt{3}\sin\varphi_1\sin\alpha_1\cos\alpha_4 \\
&\quad - 4\sqrt{3}\sin\varphi_1\sin\alpha_1 + 2\sqrt{3}\sin\varphi_1\sin\alpha_4\sin\alpha_1 \\
&\quad + 2i\sqrt{3}\sin\varphi_1\sin\alpha_4\sin\alpha_1) \\
&\quad + kz(-8\sin\varphi_1\sin\alpha_1 - 8\sin\varphi_1\sin\alpha_1\cos\alpha_4 \\
&\quad - 4\sin\varphi_1\sin\alpha_4\sin\alpha_1 - 4i\sin\varphi_1\sin\alpha_4\sin\alpha_1) \\
&\quad \Big\}\,|\{n_x, n_y, n_z\}, F\rangle \qquad (3.26)
\end{aligned}
$$

Maximum coupling is achieved for a phase of $\varphi = \pm\frac{\pi}{2}$ as can be seen from figures 3.8 and 3.9. For a choice of phase of $\varphi = \frac{\pi}{2}$ the odd Raman coupling has equal magnitude for the x and y-coupling and the z-coupling is maximized. Another interesting choice of phase is at $\varphi = 0$, where the z-coupling vanishes. Here the x and y coupling have equal magnitude again. Thus we have the situation of 2D Raman cooling in a 3D lattice. Choosing $\varphi = \frac{\pi}{2}$ to maximize

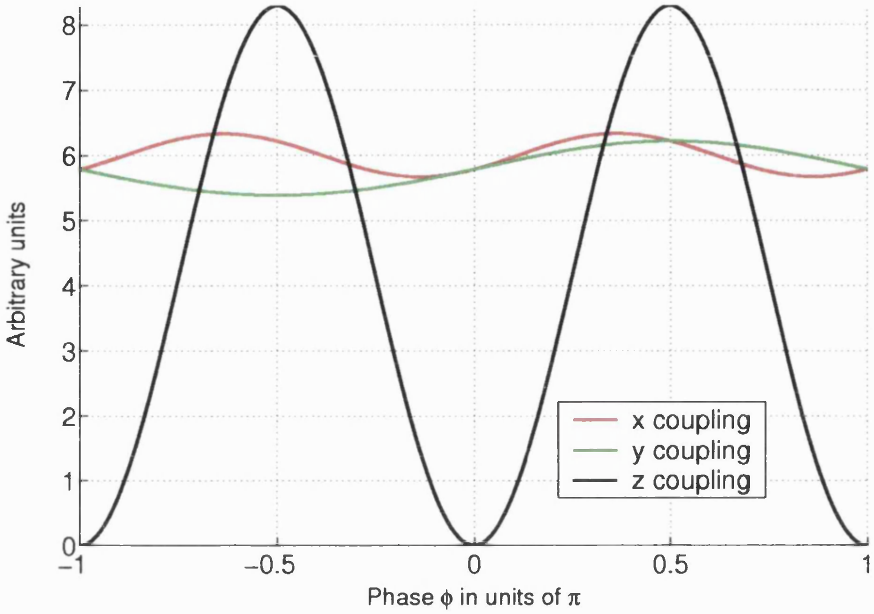

Figure 3.8: This figure shows the phase dependence of the odd Raman coupling for $\alpha_1 = \alpha_4$.

the odd coupling term, the matrix elements for a vibrational change of one quantum along x, y and z are hence

$$U^{(x)}_{F,F-1} \approx -\frac{\sqrt{3}}{2} U_R \, \eta_x \left(2i \sin\alpha + 2i \sin\alpha \cos\alpha + \sin^2\alpha(i-1)\right) \tag{3.27}$$

$$U^{(y)}_{F,F-1} \approx -\frac{\sqrt{3}}{2} U_R \, \eta_y \left(2i \sin\alpha + 2i \sin\alpha \cos\alpha + \sin^2\alpha(i-1)\right) \tag{3.28}$$

$$U^{(z)}_{F,F-1} \approx U_R \, \eta_z \Big(2i \sin\alpha + 2i \sin\alpha \cos\alpha + \sin^2\alpha(i-1)\Big) \tag{3.29}$$

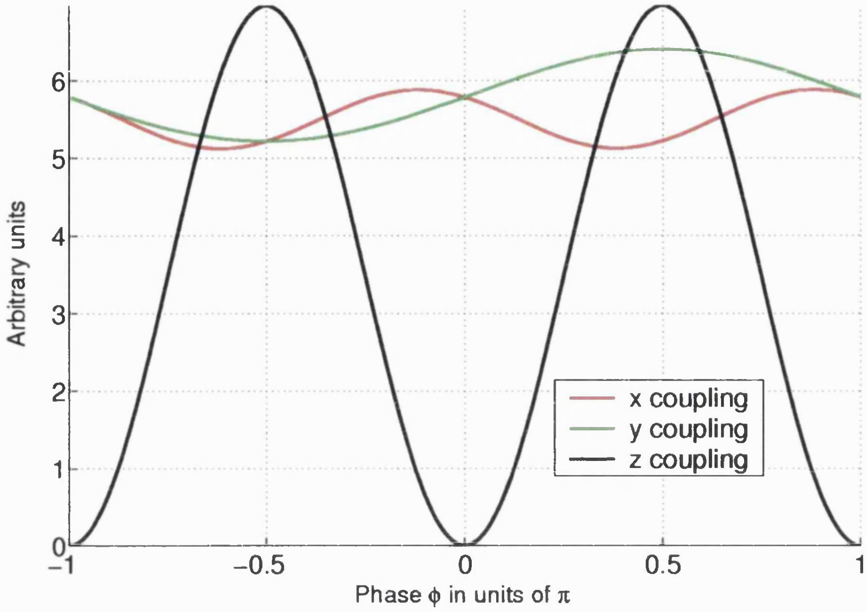

Figure 3.9: This figure shows the phase dependence of the odd Raman coupling for $\alpha_1 = -\alpha_4$.

$$U_R = \frac{\sqrt{3}}{\sqrt{F}} \frac{U_1}{12} \frac{A_\pi}{A_1} \tag{3.30}$$

where the Lamb-Dicke parameters are

$$\eta_{x,y,z} = \sqrt{\frac{n_{x,y,z}\,\mathrm{E_R}}{\hbar\omega_{x,y,z}}} \tag{3.31}$$

Thus it is possible with this configuration to implement 3D resolved-sideband Raman cooling. The next step is to investigate the situation where both tipped beams possesses a phase shift.

3.5.2 Tipped configuration with two beams having phase shifts φ_1 or φ_4 respectively

This part covers the deduction of the Raman coupling strength when we vary the phase relation between the orthogonal components of each tipped beam independently by φ_1 or φ_4 respectively. Again a σ^+ well is shifted to the origin. Changing the relative phase between the polarization components of each tipped beam, the polarization vectors used to deduce the total light-field including the phase-shifts are thus given by

$$\mathbf{p}_1 = \begin{pmatrix} 0 \\ \cos\alpha_1 \\ 0 \end{pmatrix} + \begin{pmatrix} \cos\theta\sin\alpha_1\exp(i\varphi_1) \\ 0 \\ \sin\alpha_1\sin\theta\exp(i\varphi_1) \end{pmatrix} = \begin{pmatrix} \cos\theta\sin\alpha_1\exp(i\varphi_1) \\ \cos\alpha_1 \\ \sin\alpha_1\sin\theta\exp(i\varphi_1) \end{pmatrix}$$

$$\mathbf{p}_2 = \begin{pmatrix} 0 \\ 1 \\ 0 \end{pmatrix} \qquad \mathbf{p}_3 = \begin{pmatrix} 1 \\ 0 \\ 0 \end{pmatrix}$$

$$\mathbf{p}_4 = \begin{pmatrix} \cos\alpha_4 \\ 0 \\ 0 \end{pmatrix} + \begin{pmatrix} 0 \\ -\cos\theta\sin\alpha_4\exp(i\varphi_4) \\ \sin\alpha_4\sin\theta\exp(i\varphi_4) \end{pmatrix} = \begin{pmatrix} \cos\alpha_4 \\ -\cos\theta\sin\alpha_4\exp(i\varphi_4) \\ \sin\alpha_4\sin\theta\exp(i\varphi_4) \end{pmatrix}$$

We can then write the electric field vectors of the lattice beams again as

$$\begin{aligned}
\mathbf{E}_1 &= A_1\,\mathbf{p}_1 \exp(i\sum(\mathbf{k}_1\cdot\mathbf{r})) \quad \mathbf{E}_2 = A_1\,\mathbf{p}_2\,\exp(i\sum(\mathbf{k}_2\cdot\mathbf{r}))\\
\mathbf{E}_3 &= A_1\,\mathbf{p}_3\,\exp(i\sum(\mathbf{k}_3\cdot\mathbf{r})) \quad \mathbf{E}_4 = A_1\,\mathbf{p}_4\,\exp(i\sum(\mathbf{k}_4\cdot\mathbf{r}))
\end{aligned} \tag{3.32}$$

and deduce the different components of the total light field as

$$\begin{aligned}
E_+ =& \frac{A_1}{\sqrt{2}}\Big\{-\cos\theta\sin\alpha_1\exp(i\varphi_1)\exp(-ikx\sin\theta+ikz\cos\theta-\frac{i\pi}{4})\\
&-\exp(-iky\sin\theta-ikz\cos\theta-\frac{i\pi}{4})\\
&-\cos\alpha_4\exp(i\varphi_4)\exp(iky\sin\theta-ikz\cos\theta-\frac{i\pi}{4})\\
&-i\cos\alpha_1\exp(-ikx\sin\theta+ikz\cos\theta-\frac{i\pi}{4})\\
&-i\exp(ikx\sin\theta+ikz\cos\theta-\frac{i\pi}{4})\\
&-i\cos\theta\sin\alpha_4\exp(i\varphi_4)\exp(iky\sin\theta-ikz\cos\theta-\frac{i\pi}{4})\Big\}
\end{aligned} \tag{3.33}$$

$$\begin{aligned}
E_- =& \frac{A_1}{\sqrt{2}}\Big\{\cos\theta\sin\alpha_1\exp(i\varphi_1)\exp(-ikx\sin\theta+ikz\cos\theta-\frac{i\pi}{4})\\
&+\exp(-iky\sin\theta-ikz\cos\theta-\frac{i\pi}{4})\\
&+\cos\alpha_4\exp(i\varphi_4)\exp(iky\sin\theta-ikz\cos\theta-\frac{i\pi}{4})\\
&-i\cos\alpha_1\exp(-ikx\sin\theta+ikz\cos\theta-\frac{i\pi}{4})\\
&-i\exp(ikx\sin\theta+ikz\cos\theta-\frac{i\pi}{4})\\
&-i\cos\theta\sin\alpha_4\exp(i\varphi_4)\exp(iky\sin\theta-ikz\cos\theta-\frac{i\pi}{4})\Big\}
\end{aligned} \tag{3.34}$$

$$\begin{aligned}E_\pi =&A_1 \sin\theta\Big\{ - \sin\alpha_1 \exp(i\varphi_1)\exp(-ikx\sin\theta + ikz\cos\theta - \frac{i\pi}{4})\\&+ \sin\alpha_4 \exp(i\varphi_4)\exp(iky\sin\theta - ikz\cos\theta - \frac{i\pi}{4})\Big\}\end{aligned} \tag{3.35}$$

Again we have chosen $\theta = \frac{\pi}{3}$. Using these local polarization vector components, we can easily deduce the effective magnetic field,

$$
\begin{aligned}
B_{\text{eff}}^{+} =& \frac{B_{\text{eff}}^{x} + iB_{\text{eff}}^{y}}{\sqrt{2}} \\
=& -\frac{iU_1\sqrt{6}}{24}\frac{A_\pi}{A_1}\Big\{ \\
& - 4i\cos\alpha_1\sin\alpha_1\sin\varphi_1 + 4\sin\alpha_4\sin\varphi_4 + 4i\cos\alpha_1\sin\alpha_4\cos\varphi_4 \\
& + 4\sin\alpha_1\cos\varphi_1 + 4i\sin\alpha_4\cos\varphi_4 + 2\sin\alpha_4\sin\alpha_1\cos(\varphi_1 - \varphi_4) \\
& + 2i\sin\alpha_4\sin\alpha_1\cos(\varphi_1 - \varphi_4) + 4\cos(\varphi_1 - \varphi_4)\sin\alpha_1\cos\alpha_4 \\
& - 4i\sin\alpha_1\sin\varphi_1 \\
& + kx(2\sqrt{3}\sin\alpha_1\sin\varphi_1 + \sqrt{3}\sin\alpha_4\sin\alpha_1\sin(\varphi_1 - \varphi_4) \\
& + 2\sqrt{3}\sin(\varphi_1 - \varphi_4)\sin\alpha_1\cos\alpha_4 + 2i\sqrt{3}\sin\alpha_4\sin\varphi_4 \\
& + i\sqrt{3}\sin\alpha_4\sin\alpha_1\sin(\varphi_1 - \varphi_4) - 2i\sqrt{3}\cos\alpha_1\sin\alpha_4\sin\varphi_4 \\
& + 4i\sqrt{3}\sin\alpha_1\cos\varphi_1) \\
& + ky(\sqrt{3}\sin\alpha_4\sin\alpha_1\sin(\varphi_1 - \varphi_4) + 2\sqrt{3}\sin(\varphi_1 - \varphi_4)\sin\alpha_1\cos\alpha_4 \\
& + 4\sqrt{3}\sin\alpha_4\cos\varphi_4 + i\sqrt{3}\sin\alpha_4\sin\alpha_1\sin(\varphi_1 - \varphi_4) \\
& - 2i\sqrt{3}\sin\alpha_4\sin\varphi_4 - 2i\sqrt{3}\cos\alpha_1\sin\alpha_4\sin\varphi_4 - 2\sqrt{3}\sin\alpha_1\sin\varphi_1) \\
& + kz(-4\sin(\varphi_1 - \varphi_4)\sin\alpha_1\cos\alpha_4 - 2\sin\alpha_4\sin\alpha_1\sin(\varphi_1 - \varphi_4) \\
& - 4\sin\alpha_1\sin\varphi_1 + 4i\cos\alpha_1\sin\alpha_4\sin\varphi_4 + 4i\sin\alpha_4\sin\varphi_4 \\
& - 2i\sin\alpha_4\sin\alpha_1\sin(\varphi_1 - \varphi_4))\Big\} \qquad (3.36)
\end{aligned}
$$

We are interested in the matrix elements $U_{F,F-1}$, hence substituting 3.25 into 3.24 allows us to find the functional dependence of the Raman coupling around the minimum of the potential well. Furthermore we use the harmonic approximation for the band structure. Thus we find for to first order for the

Raman coupling for the small parameters kx, ky and kz,

$$
\begin{aligned}
U_{F,F-1} &\approx \frac{\langle\{n_x^{'}, n_y^{'}, n_z^{'}\}, F-1 \,|\, [B^x_{\text{tot}} \mp i B^y_{\text{tot}}] \,|\{n_x, n_y, n_z\}, F\rangle}{\sqrt{2F}} \\
&= -\frac{iU_1\sqrt{3}}{72\sqrt{F}}\frac{A_\pi}{A_1}\Big\langle\{n_x^{'}, n_y^{'}, n_z^{'}\}, F-1\Big|\Big\{ \\
&- 4i\cos\alpha_1\sin\alpha_1\sin\varphi_1 + 4\sin\alpha_4\sin\varphi_4 + 4i\cos\alpha_1\sin\alpha_4\cos\varphi_4 \\
&+ 4\sin\alpha_1\cos\varphi_1 + 4i\sin\alpha_4\cos\varphi_4 + 2\sin\alpha_4\sin\alpha_1\cos(\varphi_1-\varphi_4) \\
&+ 2i\sin\alpha_4\sin\alpha_1\cos(\varphi_1-\varphi_4) + 4\cos(\varphi_1-\varphi_4)\sin\alpha_1\cos\alpha_4 \\
&- 4i\sin\alpha_1\sin\varphi_1 \\
&+ kx(2\sqrt{3}\sin\alpha_1\sin\varphi_1 + \sqrt{3}\sin\alpha_4\sin\alpha_1\sin(\varphi_1-\varphi_4) \\
&+ 2\sqrt{3}\sin(\varphi_1-\varphi_4)\sin\alpha_1\cos\alpha_4 + 2i\sqrt{3}\sin\alpha_4\sin\varphi_4 \\
&+ i\sqrt{3}\sin\alpha_4\sin\alpha_1\sin(\varphi_1-\varphi_4) - 2i\sqrt{3}\cos\alpha_1\sin\alpha_4\sin\varphi_4 \\
&+ 4i\sqrt{3}\sin\alpha_1\cos\varphi_1) \\
&+ ky(\sqrt{3}\sin\alpha_4\sin\alpha_1\sin(\varphi_1-\varphi_4) + 2\sqrt{3}\sin(\varphi_1-\varphi_4)\sin\alpha_1\cos\alpha_4 \\
&+ 4\sqrt{3}\sin\alpha_4\cos\varphi_4 + i\sqrt{3}\sin\alpha_4\sin\alpha_1\sin(\varphi_1-\varphi_4) \\
&- 2i\sqrt{3}\sin\alpha_4\sin\varphi_4 - 2i\sqrt{3}\cos\alpha_1\sin\alpha_4\sin\varphi_4 - 2\sqrt{3}\sin\alpha_1\sin\varphi_1) \\
&+ kz(-4\sin(\varphi_1-\varphi_4)\sin\alpha_1\cos\alpha_4 - 2\sin\alpha_4\sin\alpha_1\sin(\varphi_1-\varphi_4) \\
&- 4\sin\alpha_1\sin\varphi_1 + 4i\cos\alpha_1\sin\alpha_4\sin\varphi_4 + 4i\sin\alpha_4\sin\varphi_4 \\
&- 2i\sin\alpha_4\sin\alpha_1\sin(\varphi_1-\varphi_4)) \\
&\Big\}\,|\{n_x, n_y, n_z\}, F\rangle
\end{aligned}
\tag{3.37}
$$

Maximum coupling is achieved for a phase of $\varphi = \varphi_1 = \varphi_4 = \frac{\pi}{2}$ when $\alpha_1 =$

α_4 as can be seen from figures 3.10 on page 124. If we choose $\alpha_1 = -\alpha_4$ and $\varphi_1 = -\varphi_4$ the optimal phase is $\approx 68°$ (cf 3.11). In the following, we calculate the coupling matrix elements for the case depicted in figure 3.10 for which $\alpha_1 = \alpha_4$ and $\varphi = \varphi_1 = \varphi_4 = \frac{\pi}{2}$. For this choice of phase the odd Raman coupling has equal magnitude for the x and y-component and the z-component is maximized. Thus the matrix elements for a vibrational change of one quantum along x, y and z are hence

$$U^{(x)}_{F,F-1} \approx -\frac{\sqrt{3}}{2} U_R\, \eta_x \left(\sin\alpha(i-1) + \cos\alpha \sin\alpha\right) \tag{3.38}$$

$$U^{(y)}_{F,F-1} \approx -\frac{\sqrt{3}}{2} U_R\, \eta_y \left(\sin\alpha(1-i) + \cos\alpha \sin\alpha\right) \tag{3.39}$$

$$U^{(z)}_{F,F-1} \approx U_R\, \eta_z \left(-\sin\alpha(i+1) - \cos\alpha \sin\alpha\right) \tag{3.40}$$

$$U_R = \frac{\sqrt{3}}{\sqrt{F}} \frac{U_1}{12} \frac{A_\pi}{A_1} \tag{3.41}$$

where the Lamb-Dicke parameters are

$$\eta_{x,y,z} = \sqrt{\frac{n_{x,y,z}\, \mathrm{E_R}}{\hbar\omega_{x,y,z}}} \tag{3.42}$$

3.6 Conclusion

In this chapter I have discussed resolved-sideband Raman cooling in two and three dimensions. The 2D case is based on the paper by Jessen and Deutsch [42], whilst I have investigated an original scheme for Raman cooling in 3D. Quantum Monte-Carlo wavefunction simulations have been implemented for the 2D case and the results are presented and discussed in the next chapter. It is of interest to implement and run also simulations for the 3D resolved-sideband Raman cooling scheme discussed here. This hasn't been done to date and such work is beyond the scope of this thesis.

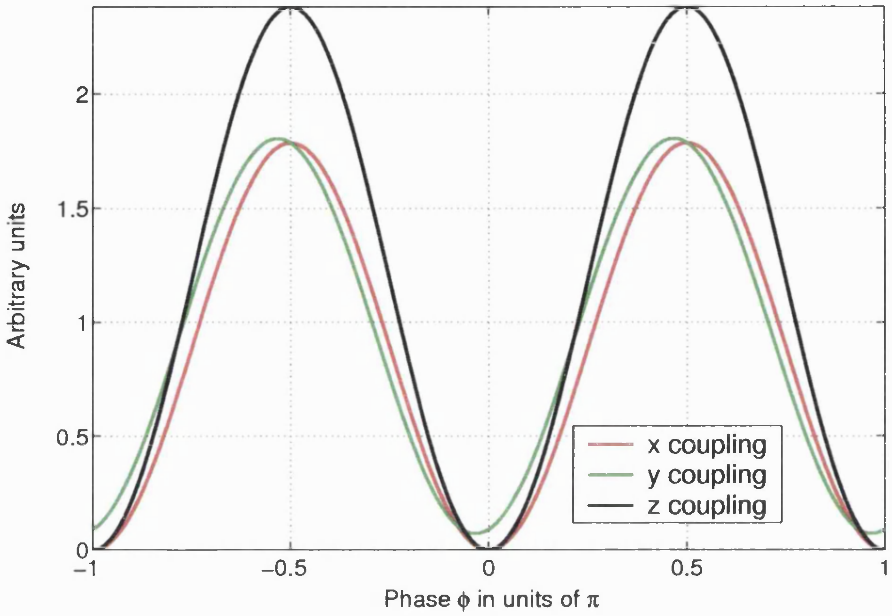

Figure 3.10: This figure shows the phase dependence of the odd Raman coupling for $\alpha_1 = \alpha_4$ and $\varphi_1 = \varphi_4$. The figure for $\alpha_1 = -\alpha_4$ gives a is similar result. The optimal phase to maximize the odd coupling is $\frac{\pi}{2}$.

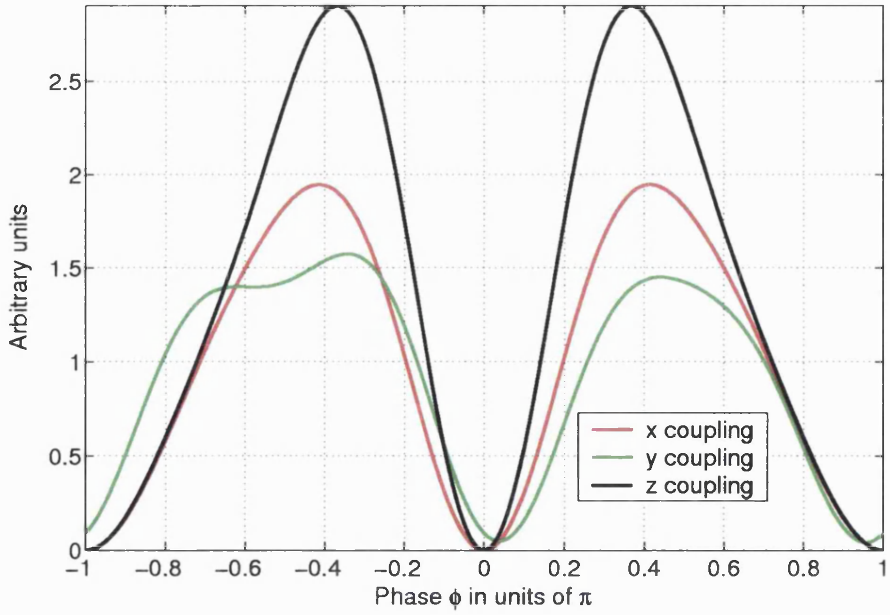

Figure 3.11: This figure shows the phase dependence of the odd Raman coupling for $\alpha_1 = -\alpha_4$ and $\varphi_1 = \varphi_4$. The figure for $\alpha_1 = -\alpha_4$ gives a is similar result. The optimal phase to maximize the odd coupling is $\approx 68°$.

Chapter 4

QMCWF Simulations

This section presents the theoretical basis used to implement a quantum Monte Carlo simulation of resolved sideband-Raman cooling in a far-detuned optical lattice. First a general introduction to the quantum Monte Carlo formalism is given followed the description of the general method which is the basis for all quantum Monte Carlo models. Then the previous treatment of light-shifts (cf. section 2.1 on page 37) is revisited and recast in the view of this quantum Monte Carlo formalism. Subsequently a detailed derivation of the optical Raman coupling in 2D is presented and a model system constructed with which resolved-sideband Raman cooling is simulated. Finally the transition amplitudes are calculated for the different event channels in the model.

4.1 The Quantum Monte Carlo Wavefunction Method

Dissipation plays a central role in quantum optics. In 1993 a new calculational approach was published in [51] and coined the quantum Monte Carlo wavefunction method. Often a master equation approach is used for small system coupled to a large reservoir. Here a linear equation for the time evolution of the reduced system density matrix is written down and traced over the reservoir variables of the total density matrix, i.e. $\rho_S = \mathrm{Tr}_{\mathrm{res}}(\rho)$. This leads to a master equation of the form

$$\dot{\boldsymbol{\rho}}_S = \frac{i}{\hbar}[\boldsymbol{\rho}, \mathbf{H}_S] + \mathcal{L}_{\mathrm{relax}}(\boldsymbol{\rho}_S) \tag{4.1}$$

where $\mathbf{H}_S$ is the Hamiltonian of the isolated system and $\mathcal{L}_{\mathrm{relax}}$ is the relaxation superoperator acting on the density matrix ρ_S. It is assumed here the density matrix is local in time and that $\dot{\boldsymbol{\rho}}$ therefore only depends on $\boldsymbol{\rho}_S$. This is called the Markov approximation.

The quantum Monte Carlo wave-function approach is equivalent to a master equation treatment. This approach is of interest because if a Hilbert space of a quantum system of dimensions $N \gg 1$ is considered, the number of variables involved in a wave-function treatment is of order N, whereas for a density matrix treatment is of order N^2. Hence the computational effort is reduced significantly. Additionally, also new insights into the study of single-quantum systems can be gained through this method.

The article by Mølmer, Castin and Dalibard [51] provides a detailed introduction and several short examples of how this method works and how the formalism can be applied to real world physical problems. The interested reader is referred to this article for a detailed discussion of the QMCWF method.

4.2 QMCWF formalism and far-detuned optical lattices

The aim of this section is to relate the treatment of light-shifts using a density-matrix formalism to the quantum Monte Carlo wave-function technique described earlier. This is done in order to identify the appropriate Hermitian and non-Hermitian parts of the Hamiltonian. In the density matrix formalism, the evolution of the density matrix can be written as:

$$\frac{d\hat{\boldsymbol{\sigma}}}{dt} = \frac{-i}{\hbar^2}\left\{\frac{\Delta - i\frac{\Gamma}{2}}{\Delta^2 + \frac{\Gamma^2}{4}}\left(\mathrm{d}^- \cdot \boldsymbol{\varepsilon}^-\right)\left(\mathrm{d}^+ \cdot \boldsymbol{\varepsilon}^+\right)\sigma - \sigma\frac{\Delta + i\frac{\Gamma}{2}}{\Delta^2 + \frac{\Gamma^2}{4}}\left(\mathrm{d}^- \cdot \boldsymbol{\varepsilon}^-\right)\left(\mathrm{d}^+ \cdot \boldsymbol{\varepsilon}^+\right)\right\} \tag{4.2}$$

after the excited states have been eliminated from the system, as shown in section 2.1. In this equation $\boldsymbol{\sigma} \equiv |\varphi\rangle\langle\varphi|$, Δ is the detuning from resonance of the lattice beams, Γ the natural linewidth, $\hat{\mathrm{d}}$ the dipole operator and $\boldsymbol{\varepsilon}$ the field amplitude associated with the trapping laser. This equation can be rewritten in a more compact form as

$$\frac{d\hat{\boldsymbol{\sigma}}}{dt} = \frac{-i}{\hbar^2}\left[\Lambda_L, \hat{\boldsymbol{\sigma}}\right] - \frac{i}{\hbar^2}\left\{-\frac{i\Gamma}{2\Delta}\Lambda_L, \hat{\boldsymbol{\sigma}}\right\} \tag{4.3}$$

where the light-shift operator $\mathbf{\Lambda}$ was introduced as

$$\mathbf{\Lambda} \equiv \frac{1}{2}\hbar\Delta\, s(\mathbf{r})\left(\mathbf{d}^{-}\cdot\varepsilon_L^{*}\right) \tag{4.4}$$

$$s(\mathbf{r}) \equiv \frac{\Omega_R^2/2}{\Delta^2+\frac{\Gamma^2}{4}} \tag{4.5}$$

$$\Omega_R \equiv \frac{D\,E_l}{\hbar} \tag{4.6}$$

Here $s(\mathbf{r})$ is the saturation parameter at low saturation[1] and Ω_R is the Rabi frequency. To connect the two approaches we use the following reasoning:

$$\hat{\sigma} = |\varphi\rangle\langle\varphi| \tag{4.7}$$

$$\therefore \dot{\hat{\sigma}} = |\dot{\varphi}\rangle\langle\varphi| + |\varphi\rangle\langle\dot{\varphi}| \tag{4.8}$$

$$= \frac{-i}{\hbar}\left\{\hat{\mathbf{H}}\,|\varphi\rangle\langle\varphi| + |\varphi\rangle\langle\varphi|\,\hat{\mathbf{H}}^{+}\right\} \tag{4.9}$$

Substituting a non-Hermitian Hamiltonian $\hat{\mathbf{H}} = \hat{\mathbf{H}}_{\mathrm{H}} - \frac{i\hat{\gamma}}{2}$ composed of an Hermitian part $\hat{\mathbf{H}}_{\mathrm{H}}$ and a non-Hermitian one $\frac{i\hat{\gamma}}{2}$, equation 4.9 becomes

$$\dot{\hat{\sigma}} = \frac{-i}{\hbar}\left[\hat{\mathbf{H}}_H, \hat{\sigma}\right] - \frac{i}{\hbar}\left\{\frac{-i\hat{\gamma}}{2}, \hat{\sigma}\right\} \tag{4.10}$$

Comparing equation 4.10 with 4.3 relates the light-shift operator $\mathbf{\Lambda}_L$ and the non-Hermitian operator $\hat{\gamma}$ of the quantum Monte Carlo wave-function formalism to give

---

[1] In the regime of high saturation, $\Gamma_s \rightarrow \frac{\Gamma}{2}$

N	1000
Δ_R	2Γ
E_π/E_1	0.5
δt	$1\mu s$

Table 4.1: This table shows the parameters chosen for figures 4.2 to 4.3 on pages 147–148. N represents the number of atoms, Δ_R the detuning of the Raman repumper, E_π/E_1 the ratio of the π-component of the lattice field to the single beam electric amplitude and δt the time step used in our finite difference implementation of the dynamical evolution of the QMCWF Hamiltonian.

$$\hat{\mathbf{H}} = \hat{\mathbf{H}}_H - \frac{i\Gamma}{2\Delta}\mathbf{\Lambda}_L = \hat{\mathbf{H}}_H - \frac{i\hat{\gamma}}{2} \tag{4.11}$$

This result is used next to derive the transition amplitudes for our model of resolved-sideband Raman cooling.

4.3 Implementation

This section describes the implementation of a quantum mechanical description of Raman cooling using the quantum Monte Carlo wavefunction method. First we introduce a model system and then derive the appropriate channel amplitudes for the transitions involved. Finally we characterise the random number generator chosen and give a brief overview of the model implementation in C++.

4.3.1 The model

In this section we introduce a model for resolved-sideband Raman cooling which we use in our numerical simulations. The model is shown in fig-

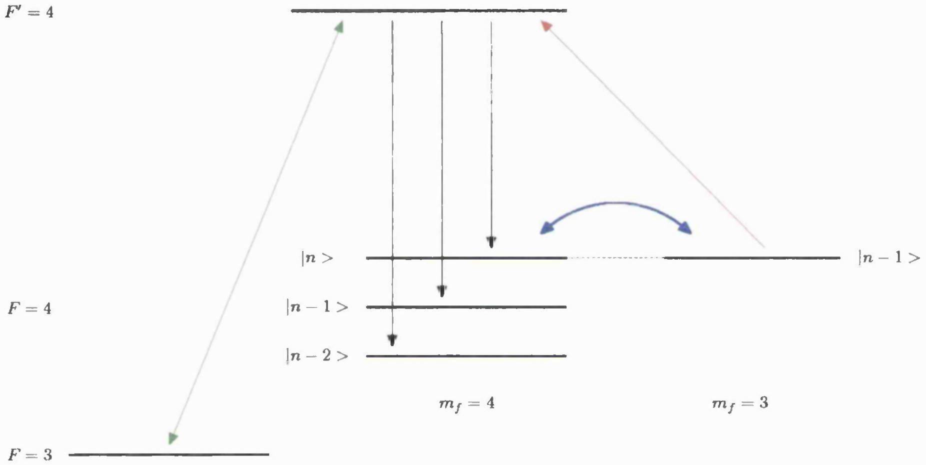

Figure 4.1: Raman cooling scheme. Two vibrational levels are brought into resonance by a transverse magnetic field. Raman transitions transfers populations from $|m_f = 4, n >$ to $|m_f = 3, n-1 >$ represented by the dark blue arrow (coherent coupling). By optical pumping (red arrow) and subsequent decay (black arrows) the atom looses one quantum of vibration in the overall process. After several cycles most of the atoms end up in the vibrational ground state. The atoms can also decay to $F' = 3$ and are recycled by a Raman repumper beam tuned to this resonance (green arrow).

ure 4.1 on the preceding page. It is the basic building block of the Raman cooling ladder. The full system consists of a string of these basic building blocks coupled together by optical pumping. The lowest vibrational state $|4, 0\rangle$ is dark with respect to the Raman coupling. In this state the atoms accumulate after they have descended the Raman cooling ladder.

The system is modelled on a two level atom with a coherent coupling between the two levels $|m_f = 4, n\rangle$ and $|m_f = 3, n-1\rangle$, known as the Raman coupling, and optical pumping provided by the Raman pumper beam as shown in figure 4.1. To maximize the population transfer between the two levels $|m_f = 4, n\rangle$ and $|m_f = 3, n-1\rangle$, they are shifted into resonance using a static magnetic field. Typical values of the applied magnetic field B_R are of the order of $0 \rightarrow 200\,\text{mG}$. Figure 3.4 on page 99 shows the magnitudes of B_R for a set of maximum light-shifts for different vibrational levels. The coherent coupling is provided by the lattice light itself. This coherent evolution is interrupted by scattering a photon from the Raman pumper beam. This transfers the atom into the $F' = 4$ excited state manifold from which the atom can decay into one of several states as described in 3.2 on page 94.

This model is used to drive a quantum mechanical description of our system which will provide the necessary equations to implement a quantum Monte Carlo simulation of resolved-sideband Raman cooling. The first step is to derive the Hamiltonian of our system. It is given by

$$\mathbf{H} = \mathbf{H}_0 + \frac{\mathbf{p}^2}{2m} + \mathbf{\Lambda}_L + \mathbf{\Lambda}_R + \mathbf{\Lambda}_p \tag{4.12}$$

Here $\mathbf{H}_0$ is the Hamiltonian of the isolated system being $\mathbf{H}_0 |\varphi\rangle = \hbar\omega |\varphi\rangle$

and the term $\frac{\mathbf{p}^2}{2m}$ describes the motional couplings of the wave-function. $\mathbf{\Lambda}_L$ describes the effect of the lattice light field, $\mathbf{\Lambda}_R$ the effect of the Raman coupling and $\mathbf{\Lambda}_p$ takes the effect of the Raman pumper beam into account. The wave-function of our two level system can be written as

$$|\varphi\rangle = a(t)\,|u_\alpha\,\varphi\rangle + b(t)\,|u_\beta\,\varphi\rangle \tag{4.13}$$

where φ represents the external part of the wave-function and $u_{\alpha/\beta}$ the internal ones.The coefficients a and b are complex time-dependent quantities, which are normalized so that $\langle\varphi\,|\,\varphi\rangle = 1$. The external part of the wave-function describes the atomic wavepacket evolving on the light shifted potential. The internal part describes the evolution in context of the vibrational level structure and the ac-stark shifted m_f levels. We generally choose $u_\alpha = |F = 4, m_f = 4\rangle$ and $u_\beta = |4, 3\rangle$ for a given vibrational level n in our two level model[2]. We can now substitute this expression into the Schrödinger equation

$$\dot{\varphi} = -\frac{i}{\hbar}\mathbf{H}\varphi \tag{4.14}$$

yielding

$$|\dot{\varphi}\rangle = \dot{a}(t)u_\alpha\varphi + a(t)u_\alpha\dot{\varphi} + \dot{a}(t)u_\beta\,\varphi + a(t)u_\beta\,\dot{\varphi} \tag{4.15}$$

Multiplying the Schrödinger equation 4.14 by $\langle\varphi\,u_\alpha a(t)|$ from the left, results in

---

[2] Remember that it splits into sub-systems connected by optical pumping

$$\begin{aligned}\dot{a}(t) + a(t)\,\langle\varphi\,|\,\dot{\varphi}\rangle = -\frac{i}{\hbar}\Big\{&\hbar\omega_\alpha + \langle\varphi\,u_\alpha|\Lambda_L|\varphi\,u_\alpha\rangle \\ &+ \langle\varphi\,u_\alpha|\Lambda_R|\varphi\,u_\alpha\rangle + \langle\varphi\,u_\alpha|\frac{\mathbf{p}^2}{2m}|\varphi\,u_\alpha\rangle\Big\}\end{aligned} \tag{4.16}$$

Neglecting the motional coupling $\langle\varphi u_\beta|\frac{\mathbf{p}^2}{2m}|\varphi\,u_\alpha\rangle$, which are the off-diagonal matrix elements of the kinetic energy operator, and using the fact that

$$\langle\varphi|\dot{\varphi}\rangle = -\frac{i}{\hbar}\,\langle\varphi|\frac{\mathbf{p}^2}{2m} + U_k(\mathbf{x})|\varphi\rangle \tag{4.17}$$

we see that some terms in 4.16 cancel out and we are left with

$$\dot{a}(t) = -i\omega_\alpha\,a(t) + \langle\varphi\,u_\alpha|\Lambda_R|\varphi\,u_\alpha\rangle\;b(t) \tag{4.18}$$

We can follow the same steps by multiplying 4.14 on the page before with $\langle\varphi u_\beta b(t)|$ from the left and get

$$\dot{b}(t) = -i\omega_\alpha\,b(t) + a(t)\;\langle\varphi u_\beta\,|\,\Lambda_R|\varphi u_\beta\rangle - \frac{\Gamma'_p}{2\hbar\Delta}\,b(t) \tag{4.19}$$

where the last term arises from $\langle\varphi\,u_\alpha\,|\,\Lambda_p|\varphi\,u_\alpha\rangle$. This last term doesn't show up in equation 4.18 since only levels $|F = 4, m_f = 3, n-1\rangle$ are coupled to the excited state manifold through the Raman pumper. Γ'_p is the scattering rate and Δ the detuning from resonance of the Raman pumper. Γ'_p can easily be calculated from the relation

$$\Gamma'_p = \frac{\Gamma}{2}\left(\frac{\frac{I}{I_{sat}}}{4\left(\frac{\Delta}{\Gamma}\right)^2 + 1}\right) \tag{4.20}$$

in the limit of small saturation parameter s. Here Γ is the natural linewidth, 5.22 MHz, for caesium and Δ the detuning of the Raman pumper beam from atomic resonance. This detuning is of order of 2Γ in our experiment. Last but not least we can rewrite the Raman coupling part as

$$\langle \varphi u_\beta | \Lambda_R | \varphi \, u_\alpha \rangle = U_R \left(i\sqrt{n_x} + 3\sqrt{n_y} \right) \tag{4.21}$$

$$\langle \varphi \, u_\alpha | \Lambda_R^* | \varphi u_\beta \rangle = U_R^* \left(-i\sqrt{n_x} + 3\sqrt{n_y} \right) \tag{4.22}$$

where $n = n_x + n_y$ is the total vibrational excitation of the atoms at the start of one Raman cycle. $U_R = U_R(x, y)$ is the 2D Raman coupling as defined in 3.4 on page 101. Looking at equation 3.5 on page 103, the Raman coupling separates into terms proportional to kx and ky to first order. Hence equations 4.18 and 4.19 separate for our 2D Raman coupling scheme to first order. The set of differential equations to consider is therefore

$$\dot{a}_x = -i\omega_\alpha^x \, a(t) + \langle \varphi u_\beta \, | \, \Lambda_R^x | u_\alpha \varphi \rangle \; b_x(t) \tag{4.23}$$

$$\dot{b}_x = -i\omega_\beta^x \, b(t) + \langle \varphi \, u_\alpha \, | \, (\Lambda_R^x)^* | u_\beta \varphi \rangle \; a_x(t) - \frac{\Gamma_p'}{2\Delta_p \hbar} \, b_x(t) \tag{4.24}$$

$$\dot{a}_y = -i\omega_\alpha^y \, a(t) + \langle \varphi u_\beta \, | \, \Lambda_R^y | u_\alpha \varphi \rangle \; b_y(t) \tag{4.25}$$

$$\dot{b}_y = -i\omega_\beta^y \, b(t) + \langle \varphi \, u_\alpha \, | \, (\Lambda_R^y)^* | u_\beta \varphi \rangle \; a_y(t) - \frac{\Gamma_p'}{2\Delta_p \hbar} \, b_y(t), \tag{4.26}$$

where Γ_p' is defined in 4.20 on the page before and Δ_p is the detuning of the Raman pumper beam. Numerical solutions of this set of linear differential equations are used in the simulation. The next step is to look at what happens if a photon is scattered from the Raman pumper beam.

If the atoms has scattered a photon from the Raman pumper beam it is transferred into the excited state manifold $|F' = 4, m_f = 4\rangle$. From this excited state $|F' = 4, m_f = 4, n-1\rangle$ the atom can decay into one of the 5 different states $|F = 3, m_f = 3, n-1\rangle$, $|F = 4, m_f = 4, n\rangle$, $|F = 4, m_f = 4, n-1\rangle$, $|F = 4, m_f = 4, n-2\rangle$ and $|F = 4, m_f = 3, n-1\rangle$. This is illustrated in the level scheme diagram 4.1 on page 130. By considering the oscillator strengths for Caesium (cf. section 4.3.2 on page 137), we can deduce that 51% of the atoms decay into the $|F = 3, m_f = 3, n-1\rangle$, 3% into $|F = 4, m_f = 3\rangle$ and 46% decay into the $|F = 4, m_f = 4\rangle$ vibrational states. The z-dependence separates out in our 2D problem. This means that the matrix element $\langle n\,|\,z|n\rangle = 1$ and does not need be considered in the following treatment. The transition matrix elements for going from surface $|i\rangle \rightarrow |j\rangle$ by absorbing a photon and emitting one in directions $\mathbf{k}_{q'}$ and $\mathbf{k}_q$ is proportional to the matrix element

$$\mathbf{r} = x\,\hat{\mathbf{x}} + y\,\hat{\mathbf{y}}$$

$$\langle n_j^y|\,\langle n_j^x\,|\exp\left[-i\left(\mathbf{k}_q - \mathbf{k}_{q'}\right)\cdot\mathbf{r}\right]|n_i^x\rangle\,|n_i^y\rangle = (*) \tag{4.27}$$

where $|n_i^x\rangle\,|n_i^y\rangle$ represents the vibrational state of the atom. Equation 4.27 can be expanded to first order assuming harmonic oscillator eigenfunctions $|n_i^x\rangle\,|n_i^y\rangle$ resulting in

$$
\begin{aligned}
(*) =& \langle n_j^y| \left\langle n_j^x \middle| \sum_{\ell} \frac{\left[-i\left(\mathbf{k}_q - \mathbf{k}_{q'}\right)\cdot \mathbf{r}\right]^{\ell}}{\ell!} |n_i^x\rangle \right\rangle |n_i^y\rangle \\
\approx&\ \langle n_j^y| \langle n_j^x \,|\, \left[-i\left(\mathbf{k}_q - \mathbf{k}_{q'}\right)\cdot \mathbf{r}\right] |n_i^x\rangle\, |n_i^y\rangle \\
=& \langle n_j^y| \langle n_j^x| \left[1 - i\left(\mathbf{k}_q^x - \mathbf{k}_{q'}^x\right) x\right] \\
&\qquad + \left[-i\left(\mathbf{k}_q^y - \mathbf{k}_{q'}^y\right) y\right] \\
&\qquad + \left[-i\left(\mathbf{k}_q^z - \mathbf{k}_{q'}^z\right) z\right] |n_i^x\rangle\, |n_i^y\rangle \\
=&\delta_{n_j^x n_i^x}\delta_{n_j^y n_i^y} - i\Big\{ \left(\mathbf{k}_q^x - \mathbf{k}_{q'}^x\right) \langle n_j^x| \langle n_j^y \,|\, x|n_i^y\rangle\, |n_i^x\rangle \\
&\qquad + \left(\mathbf{k}_q^y - \mathbf{k}_{q'}^y\right) \langle n_j^x| \langle n_j^y \,|\, y|n_i^y\rangle\, |n_i^x\rangle \\
&\qquad + \left(\mathbf{k}_q^z - \mathbf{k}_{q'}^z\right) \langle n_j^x| \langle n_j^y \,|\, z|n_i^y\rangle\, |n_i^x\rangle \Big\} \\
=&\delta_{n_j^x n_i^x}\delta_{n_j^y n_i^y} \\
&- i\Big\{ \left(\mathbf{k}_q^x - \mathbf{k}_{q'}^x\right) \delta_{n_j^y n_i^y} \sqrt{\frac{\hbar}{2m\Omega_0}} \left[\delta_{n_j^x (n_i^x - 1)} \sqrt{n_i^x} + \delta_{n_j^x (n_i^x - 1)} \sqrt{n_i^x + 1}\right] \\
&\quad \left(\mathbf{k}_q^y - \mathbf{k}_{q'}^y\right) \delta_{n_j^x n_i^x} \sqrt{\frac{\hbar}{2m\Omega_0}} \left[\delta_{n_j^y (n_i^y - 1)} \sqrt{n_i^y} + \delta_{n_j^y (n_i^y - 1)} \sqrt{n_i^y + 1}\right] \Big\} \\
=&\delta_{n_j^x n_i^x}\delta_{n_j^y n_i^y} \\
&- i\Big\{ \left(\frac{\mathbf{k}_q^x}{|\mathbf{k}_\mathrm{R}|} - \frac{\mathbf{k}_{q'}^x}{|\mathbf{k}_\mathrm{R}|}\right) \delta_{n_j^y n_i^y} \sqrt{\frac{\mathrm{E_R}}{\hbar\Omega_0}} \left[\delta_{n_j^x (n_i^x - 1)} \sqrt{n_i^x} + \delta_{n_j^x (n_i^x - 1)} \sqrt{n_i^x + 1}\right] \\
&- \left(\frac{\mathbf{k}_q^y}{|\mathbf{k}_\mathrm{R}|} - \frac{\mathbf{k}_{q'}^y}{|\mathbf{k}_\mathrm{R}|}\right) \delta_{n_j^x n_i^x} \sqrt{\frac{\mathrm{E_R}}{\hbar\Omega_0}} \left[\delta_{n_j^y (n_i^y - 1)} \sqrt{n_i^y} + \delta_{n_j^y (n_i^y - 1)} \sqrt{n_i^y + 1}\right] \Big\}
\end{aligned}
$$

where we have introduced the recoil energy $\mathrm{E_R}$ and the recoil momentum $\hbar k_R$ using the relations

$$\mathrm{E_R} = \frac{\hbar^2 k_R^2}{2m} \tag{4.28}$$

$$\sqrt{\frac{\hbar}{2m\Omega_0}} = \frac{1}{|\mathbf{k}_\mathrm{R}|}\sqrt{\frac{\mathrm{E_R}}{\hbar\Omega_0}} \tag{4.29}$$

The last step follows, since the Raman pumper beam is incident perpendicular to the plane of the lattice which is defined by the x-y-plane, i.e.

$$\mathbf{k}_{q'} = k_R \begin{pmatrix} 0 \\ 0 \\ 1 \end{pmatrix}$$

This expansion is justified, since the atoms are in the Lamb-Dicke regime. In the next section we use this result to calculate the channel amplitudes to go from a initial state $|i\rangle$ to a final state $|j\rangle$. This describes the incoherent scattering of a Raman pumper photon.

4.3.2 Calculation of the transition probabilities

In this section we derive an expression for the relative transition probabilities for the various possible channels for the incoherent scattering of a Raman pumper photon. The following notation is used here: $|\varphi\rangle$ is the external atomic state, and $|u_i\rangle = |m_f\rangle \otimes |n = n_x + n_y\rangle$ the internal one. Generally the probability go from a surface i to j by scattering of a photon of polarization $\hat{\mathbf{e}}_{q'}$ and emission of one with polarization $\hat{\mathbf{e}}_q$ in a direction $\mathbf{k}_{q'}$ and $\mathbf{k}_q$ respectively is proportional to

$$P_{i\to j} \propto \left| \sum_{q\,q'} \langle u_j \,|\, \left(\mathbf{d}^- \varepsilon_q^0\right) \left(\mathbf{d}^+ \varepsilon_{q'}\right) |u_i\rangle \right|^2 . \tag{4.30}$$

Here ε_k is the associated field amplitude of the laser field, i.e. $E_L = \varepsilon_0 \sum_q \varepsilon_q \underline{\hat{e}}_q$ and $\left(\mathbf{d}^- \varepsilon_q^0\right)$ is the vacuum field amplitude[3]. If we include the external wave-functions $|\varphi\rangle$ equation 4.30 reads

$$P_{i\,\varphi\to j\,\varphi'} \propto \left| \sum_{q\,q'} \langle u_j\,\varphi \,|\, e^{-ik_{q'}x} \left(\mathbf{d}^- \varepsilon_q^0\right) \left(\mathbf{d}^+ \varepsilon_{q'}(\mathbf{x})\right) e^{-ik_q x} |u_i\,\varphi\rangle \right|^2 , \tag{4.31}$$

where φ' is the kicked external wave-function after the event and φ the initial one. ε_q^0 is the vacuum field amplitude and assumed to be constant[4] and $\varepsilon_{q'}(\mathbf{x})$ the associated field amplitude of the scattering event. The kicked wave-function can also be written as

$$\varphi'(\mathbf{x}) = \exp\left\{i\mathbf{x}\left(\mathbf{k}_{q'} - \mathbf{k}_q\right)\right\} \varphi(\mathbf{x}) \tag{4.32}$$

Substituting this into 4.31 we get

$$P_{i\,\varphi\to j\,\varphi'} \propto \left| \sum_{q\,q'} \int_V dx \,\langle u_j \,|\, \left(\mathbf{d}^- \varepsilon_q^0\right) \left(\mathbf{d}^+ \varepsilon_{q'}(\mathbf{x})\right) e^{-i\mathbf{x}(\mathbf{k}_q - \mathbf{k}_{q'})} |u_i\rangle \, |\varphi(\mathbf{x}, t(\varepsilon))|^2 \right|^2 . \tag{4.33}$$

Equation 4.33 can now be broken up into its different parts to simplify the calculation of the channel amplitudes. Let us consider the matrix element of the internal wave-functions first. It is given by

---

[3] $q\epsilon\{-1, 0, +1\}$ for σ^-, π and σ^- respectively.

[4] as in simple cases like free space

$$
\begin{aligned}
I_1 =& \left\langle u_j \,\middle|\, \left(\mathbf{d}^{-}\boldsymbol{\varepsilon}_q^0\right) \left(\mathbf{d}^{+}\boldsymbol{\varepsilon}_{q'}(\mathbf{x})\right) e^{-i\mathbf{x}(\mathbf{k}_q-\mathbf{k}_{q'})} \middle| u_i \right\rangle && (4.34)\\
=& \left\langle j \,\middle|\, \left(\mathbf{d}^{-}\boldsymbol{\varepsilon}_q^0\right) \left(\mathbf{d}^{+}\boldsymbol{\varepsilon}_{q'}(\mathbf{x})\right) \middle| i \right\rangle \left\langle n_i \,\middle|\, e^{-i\mathbf{x}(\mathbf{k}_q-\mathbf{k}_{q'})} \middle| n_j \right\rangle && (4.35)\\
=& I_a \cdot I_b. && (4.36)
\end{aligned}
$$

Here I_a is the matrix elements for the light shifted surfaces and I_b for the vibrational structure associated with each surface. I_a can readily be calculated to be

$$
I_a = \left(\boldsymbol{\varepsilon}_q^0\right) \boldsymbol{\varepsilon}_{q'}(\mathbf{x})\, C^*_{i+q'\,j}\, C_{i\,i+q'}. \tag{4.37}
$$

The dependence on the vibrational structure is explicitly taken into account in the model described in section 4.3, hence it can be neglected in the calculation of the relative channel amplitudes. Putting everything together the final channel amplitude is given by

$$
P_{i\varphi\rightarrow j\varphi'} \propto \left| \sum_{\substack{q\,q' \\ j\equiv i+q'-q}} C^*_{i+q'\,j}\, C_{i\,i+q'} \int_V dx \left|\varphi\left(\mathbf{x}, t(\varepsilon)\right)\right|^2 \right|^2 . \tag{4.38}
$$

The Raman pumper is σ^+ polarized and hence $q' = +1$. Additionally the Clebsch-Gordan coefficients are independent of the position vector $\mathbf{x}$ and the initial surface is given by $i = 3$. Thus equation 4.38 reduces to

$$
P_{3\varphi\rightarrow j\varphi'} \propto \left(\int_V dx \left|\varphi\left(\mathbf{x}, t(\varepsilon)\right)\right|^2 \right) \times \sum_{\substack{q\,1 \\ j\equiv 4-q}} C^*_{4j}\, C_{3\,4} \tag{4.39}
$$

Looking up the Clebsch-Gordan coefficients in appendix A.4 on page 210 and neglecting the modulus of the external wave-function[5] this reduces to the following relative channel amplitudes

$$P_{3\,\varphi\rightarrow 4\,\varphi'} \propto C^*_{44}\,C_{34} \tag{4.40}$$

$$P_{3\,\varphi\rightarrow 3\,\varphi'} \propto C^*_{43}\,C_{34} \tag{4.41}$$

$$P_{3\,\varphi\rightarrow 2\,\varphi'} \propto 0 \tag{4.42}$$

The last one is zero since only σ^+ Raman pumper photons take part in the optical pumping process under consideration. Hence the ratio between the two non zero rates is

$$\frac{P_{3\,\varphi\rightarrow 4\,\varphi'}}{P_{3\,\varphi\rightarrow 3\,\varphi'}} \approx \frac{2}{1}. \tag{4.43}$$

Using the formalism in [52][6] we can calculate the relative intensities for the different emission directions. These are often referred to as the oscillator strengths. Carrying out this calculation results in a probability of 84% to emit a π photon and 16% to emit a σ^- photon. Hence the total relative channel amplitudes are given by

$$P\,(\pi) \approx 0.914 \tag{4.44}$$

$$P\,(\sigma+) \approx 0.086. \tag{4.45}$$

---

[5] as we are only interested in the relative amplitudes

[6] cf. page 160

We also have to calculate the transition probabilities from the $|F' = 4, 4\rangle$ to the $|F = 3, m_f = 3\rangle$ manifold. To make things easier I have used the transition matrix elements given in [22][7]. A simplified version is shown in A.3 on page 210, which shows only the relevant strengths. The relative channel amplitudes P_{ij} are then proportional to

$$P_{ij} \propto |\mathrm{CG}_{ij}| \cdot f, \tag{4.46}$$

where $|\mathrm{CG}_{ij}|$ is the corresponding Clebsch-Gordan coefficient for the transition under consideration and f the oscillator strength. Table 4.2 shows the calculated relative channel amplitudes which are relevant in our system.

Transition	CG	f	$\lvert CG\rvert \cdot f$
$\lvert 4,4\rangle \leftrightarrow \lvert 4,4\rangle$	0.89447	2352	46%
$\lvert 4,4\rangle \leftrightarrow \lvert 4,3\rangle$	0.44721	588	3%
$\lvert 4,4\rangle \leftrightarrow \lvert 3,3\rangle$	1.0	2100	51%

Table 4.2: The table shows the calculated relative channel amplitudes for the different transitions $|F, m\rangle \leftrightarrow |F', m'\rangle$ important in our Raman cooling model. CG is the Clebsch-Gordan coefficient and f the oscillator strength taken from [22].

4.3.3 Random number generator

After a long search on the internet to find a suitable research grade random number generator I decided to use one from the GNU scientific library GSL[8]. This library provides a uniform interface for all random number generators it

---

[7] The channel amplitudes for the $|4,3\rangle \leftrightarrow |4,4\rangle$ and $|4,4\rangle \leftrightarrow |4,4\rangle$ transitions agree with the previous calculated ones using the formalism from [52].

[8] cf. http://www.gsl.org

supplies and makes it easy to change between different ones without changing the implementation in the code.

The random number generator I have chosen is called *gfsr4* and is like a lagged-Fibonancci generator. It produces each number as an xor'd sum of four previous values. This type of generators is also know as *Four-tap shift-register-sequence random-number generators* [53]. A simple test which produced 10000000 random numbers was implemented to see if the resulting random number distribution is adequate for our problem. The random number generator passes the tests and is subsequently used in all simulations presented in this chapter.

4.3.4 Implementation in detail

This section gives a short overview of how the QMCWF Raman cooling code is implemented. The program is controlled by an input file which contains the details of all simulations the code should execute. This control file has the following entries:

- Number of atoms N in simulation
- Raman pumper detuning Δ_p in units of Γ
- Maximum light-shift U_1 in units of $\mathrm{E_R}$
- Ratio E_π/E_1
- Vibrational frequency of lattices Ω_0
- Initial vibrational excitation n_0^x of atom along x-direction

- Initial vibrational excitation n_0^y of atom along y-direction
- Initial value of wave function expansion coefficient a_0^x for Ket $|4,4\rangle\,|n_x\rangle$
- Initial value of wave function expansion coefficient b_0^x for Ket $|4,3\rangle\,|n_x\rangle$
- Initial value of wave function expansion coefficient a_0^y for Ket $|4,4\rangle\,|n_y\rangle$
- Initial value of wave function expansion coefficient b_0^y for Ket $|4,3\rangle\,|n_y\rangle$
- Start of Raman pumper beam intensity ramp t_p in units of ms
- End of Raman pumper beam intensity ramp t_p in units of ms
- Value of Raman pumper beam intensity before start of ramp
- Value of Raman pumper beam intensity before at the end of ramp
- Start of Raman re-pumper beam intensity ramp t_p in units of ms
- End of Raman re-pumper beam intensity ramp t_p in units of ms
- Value of Raman re-pumper beam intensity before start of ramp
- Value of Raman pumper beam intensity before at the end of ramp

Each line is an individual simulation run. A control file can contain as many simulations and is only limited by the resources the computer system is able to provide to it[9]. To illustrate the usage of the control file, an excerpt of one is shown in table 4.3 on the next page.

The information about the energies of the vibrational levels is hard-coded. The values for the energy levels are provided by using the results of a band

---

[9] Like memory, disk space etc.

1:	1000	2	0.001	230	0.5	39000	1	0	1	0	1	0	15	20	0.002	0.002	15	20	1	1
2:	1000	2	0.001	230	0.5	39000	1	0	1	0	1	0	15	20	0.004	0.004	15	20	1	1
3:	1000	2	0.001	230	0.5	39000	1	0	1	0	1	0	15	20	0.006	0.006	15	20	1	1
4:	1000	2	0.001	230	0.5	39000	1	0	1	0	1	0	15	20	0.008	0.008	15	20	1	1
5:	1000	2	0.001	230	0.5	39000	1	0	1	0	1	0	15	20	0.01	0.01	15	20	1	1
6:	1000	2	0.001	230	0.5	39000	1	0	1	0	1	0	15	20	0.012	0.012	15	20	1	1
7:	1000	2	0.001	230	0.5	39000	1	0	1	0	1	0	15	20	0.014	0.014	15	20	1	1
8:	1000	2	0.001	230	0.5	39000	1	0	1	0	1	0	15	20	0.016	0.016	15	20	1	1
9:	1000	2	0.001	230	0.5	39000	1	0	1	0	1	0	15	20	0.018	0.018	15	20	1	1

Table 4.3: This example shows some lines from a control file for the 2D QMCWF simulations.

structure calculation for a particular maximum light-shift. Given these values, the code then subsequently derives the appropriate level-shifts to bring the lowest three levels given by $|4,4\rangle\,|n_x = 0, n_y = 0\rangle$, $|4,3\rangle\,|n_x = 1, n_y = 0\rangle$ and $|4,3\rangle\,|n_x = 0, n_y = 1\rangle$, into resonance.

The rest of the code loops over the number of simulations specified in the control file. At the beginning of the loop all parameters are initialized with the appropriate values from the control file. The control file specifies the number of atoms for which independent QMCWF simulations should be carried out. For each atom a finite difference method is used to numerically evaluate the time evolution of the expansion coefficients of the atomic wavefunction. After each time step[10] δt, it is checked if a quantum jump has occurred. On the one hand, if none happened, the wavefunction is renormalized and a new iteration is started. On the other hand, if a quantum jump has occurred, the appropriate interaction channel is chosen by considering the channel amplitudes deduced in section 4.3.2. After the quantum jump the resultant atomic wavefunction is reset according to the interaction channel and normalized. Possible interaction channels are: $|4,n\rangle$, $|4,n-1\rangle$, $|4,n-2\rangle$ and $|3,n-1\rangle$. After each simulation the results are written to disk for subsequent data analysis. Additionally a log-file is saved with the simulation parameters used and the filename of the data file.

Since many simulations have been run during the course of this thesis, the data analysis was automated to save time and reduce the amount of human error. The data analysis is based on a set of scripts using AWK, C++ and PERL. The data analysis usually takes about 10 h. The script approach also

---

[10] A maximum evolution time of 20ms was used in all simulations.

has the advantage that it was easy to extract different views of the data. It is possible to produce a set of files which shows the dependence of the kinetic energy versus the Raman pumper intensity on the fly from the analyzed data. Another script using the same analyzed data, produced graphs showing the dependency of the kinetic energy versus the Raman cooling duration. The visualization is automated using MatLab. A script was written to automatically read in the results files and plot the data using a template. All simulations results in this section have been produced in this way. Taking the time to develop a sophisticated data analysis paid off in the end by saving a lot of time on data analysis considering the large amount of data produced.

4.4 Calculation results

In this section the results from quantum Monte Carlo simulations of resolved-sideband Raman cooling are presented and discussed. Calculations for different set of parameters were run using the model described in section 4.3. The ultimate aim was to find optimized parameters for Raman cooling to be used in our experimental implementation of resolved sideband Raman cooling to maximize the number of atoms in the vibrational ground state. At the end of this chapter these results are compared to experimental measurements from our experiment.

Table 4.1 on page 129 shows the common parameters used to produce figures 4.2 to 4.8 on pages 147–153.

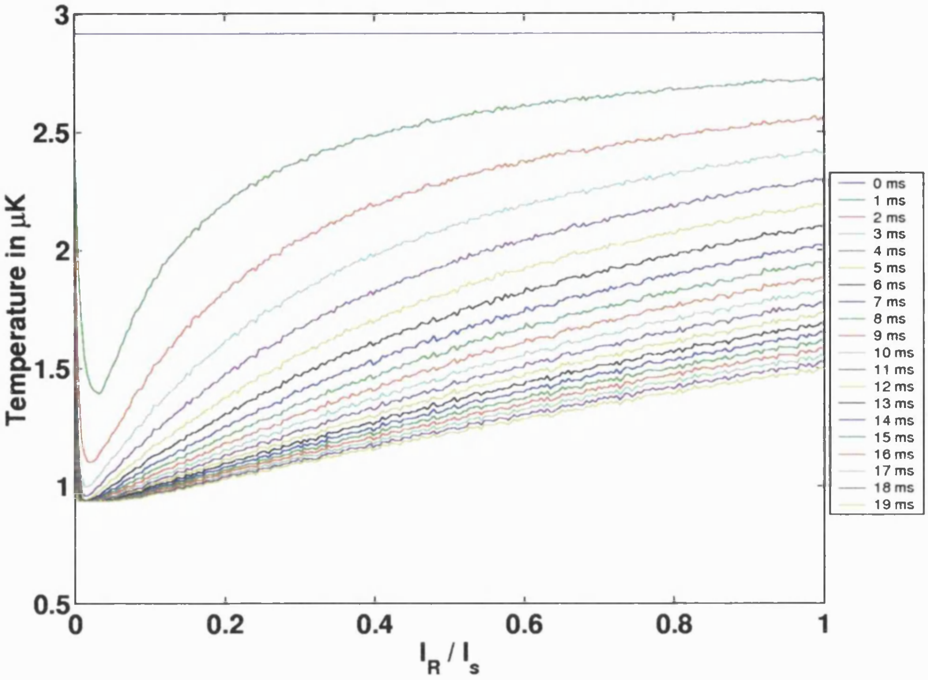

Figure 4.2: This figure shows the kinetic temperature T_{kin} plotted against the Raman pumper intensity I_R in units of the saturation intensity I_s. The atoms were assumed to have had an initial vibrational temperature T_{vib} of $3\,\mu$K at the start of the Raman cooling cycle. The calculated final kinetic temperatures are shown for Raman cooling durations from $0\,$ms to $19\,$ms.

4.4.1 Discussion of simulation results

In this section I will discuss the results of my simulations. Each section highlights a different parameter dependence of Raman cooling and how its efficiency depends on the chosen value.

Dependence on the ratio of E_π/E_1

Inspecting equations 3.7 to 3.9 on pages 103–104 it can be seen that the Raman coupling strength is directly proportional to the ratio of the π-component of the lattice light field to the single beam electric field amplitude E_1, i.e.

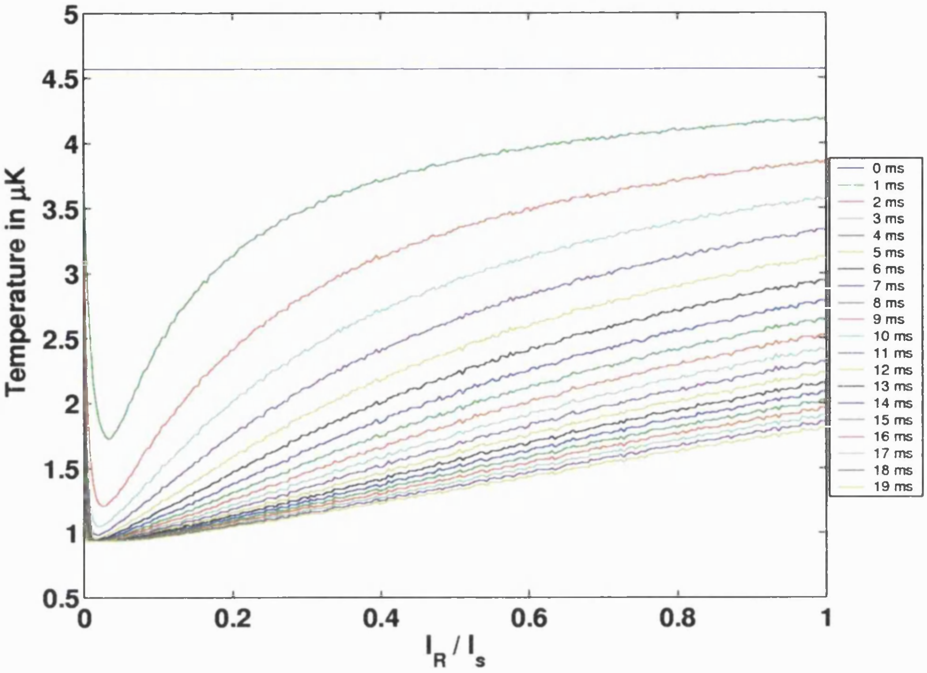

Figure 4.3: This figure shows the kinetic temperature T_{kin} plotted against the Raman pumper intensity I_R in units of the saturation intensity I_s. The atoms were assumed to have had an initial vibrational temperature T_{vib} of $9\,\mu\mathrm{K}$ at the start of the Raman cooling cycle. The calculated final kinetic temperatures are shown for Raman cooling durations from $0\,\mathrm{ms}$ to $19\,\mathrm{ms}$. Note that there is about 13.5% of atoms in vibrational levels with $n = n_x + n_y > 5$. We only include levels with $n <= 5$ into our calculations. Hence the graph shows smaller kinetic temperatures than there are actual in the lattice. See text for a detailed discussion of this.

$$U_R \propto \frac{E_\pi}{E_1} \tag{4.47}$$

Several simulations were run for E_π/E_1 in the range of 0.1 to 0.5 and are show for comparison in figure 4.9 on page 154.

As expected the efficiency of the transfer to the vibrational ground state via resolved-sideband Raman cooling is dependent on this ratio. The higher this ratio the better is the transfer, hence the aim should be to choose an

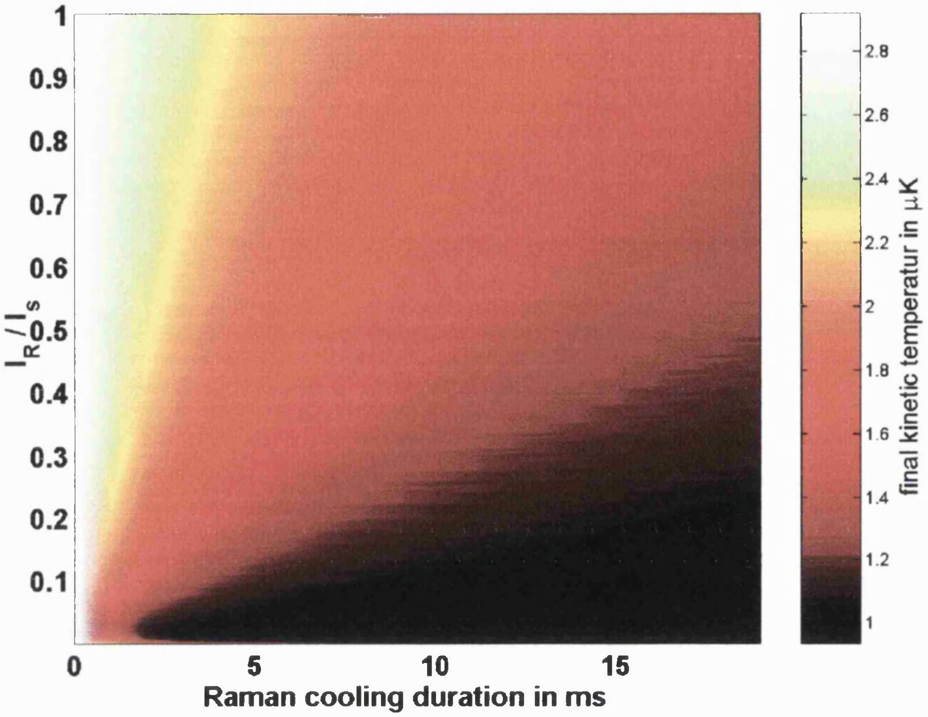

Figure 4.4: This figure shows the final kinetic temperature T_{kin} plotted against the Raman pumper intensity I_R in units of the saturation intensity I_s for Raman cooling durations of $0\,\mathrm{ms}$ to $19ms$. The atoms were assumed to have had an initial vibrational temperature T_{vib} of $3\,\mu\mathrm{K}$ at the start of the Raman cooling cycle. The figure shows that good Raman cooling can be achieved for Raman pumper intensities $I_R < 0.2 I_s$ and Raman cooling durations of $5\,\mathrm{ms}$ to $10\,\mathrm{ms}$. At this set of parameters the Raman pumper intensity I_R is of the order of magnitude of the Raman coupling U_R as discussed in the text.

as high value as possible for this parameter. It is also an easy way to see the effect of the quantum Zeno effect. By changing the ratio in subsequent Raman cooling experiments is should be possible to see a direct dependence on the efficiency of the transfer to the vibrational ground state. If this is done for a Raman pumper strength up to $h\Gamma_p \sim 0.05 I/I_0$ for different E_π/E_1 and then the same set at $h\Gamma_p \sim 0.5 I/I_0$, a dependence on the final kinetic temperatures similar as shown in the figures 4.9(a)-(c) should be observed.

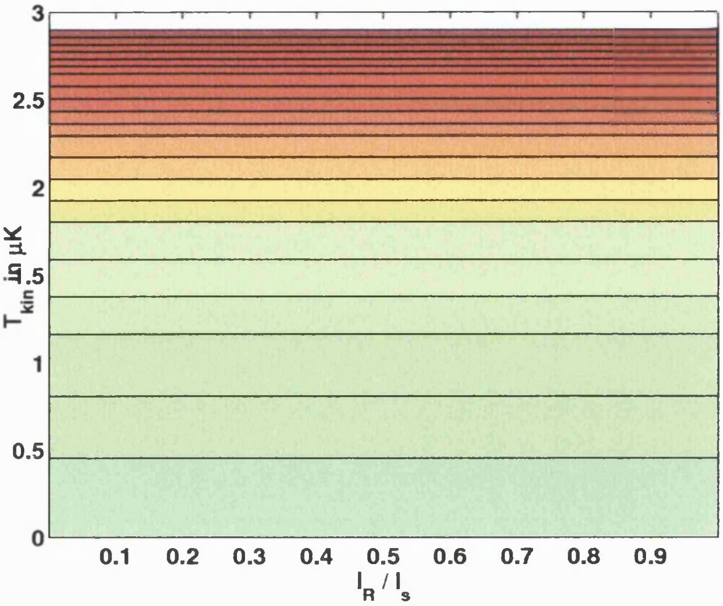

Figure 4.5: This figure shows the contribution to the kinetic temperature of the different vibrational levels at the start of the Raman cooling. See text for a detailed description. The colours represent different vibrational levels. They are ordered in ascending order $(n_x|n_y)$: $(0|0), (0|1), (1|0), (0|2), (1|1), (2|0)$ etc.

Hence the higher the ratio E_π/E_1 is chosen the lower should the measured final kinetic temperature be for a particular Raman pumper strength.

Also shown in the figures 4.10, 4.11 and 4.5-4.8 is the dependence of the final kinetic temperature on the ratio of E_π/E_1 for different Raman cooling durations. For small ratios of $E_\pi/E_1 \sim 0.1$ the Raman coupling strength U_R is small and the quantum Zeno effect[11] kicks in earlier freezing the population transfer. Longer Raman cooling times hardly improve the total transfer efficiency. Going to higher values for E_π/E_1 improves the efficiency and Raman pumper intensities which are comparable to the Raman coupling strength a good transfer efficiency can be achieved.

---

[11] See appendix D and section 4.4.2.

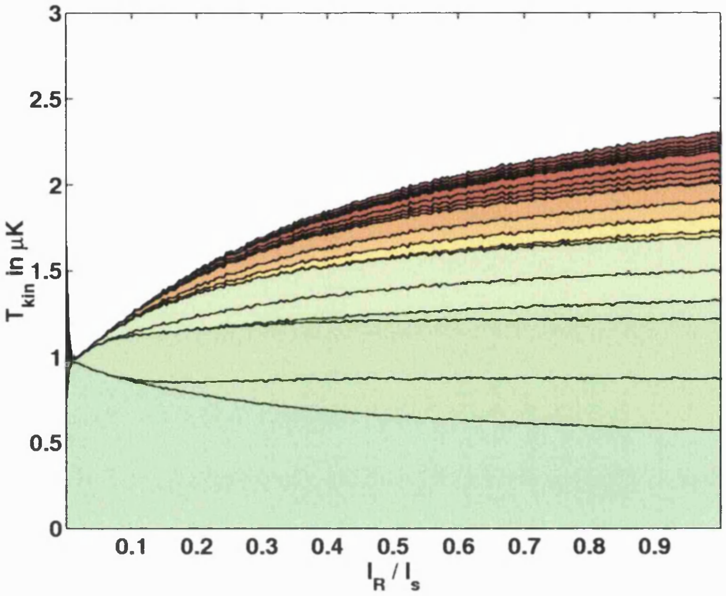

Figure 4.6: This figure shows the contribution to the kinetic temperature of the different vibrational levels after 4 ms of Raman cooling. See text for a detailed description. The colours represent different vibrational levels. They are ordered in ascending order $(n_x|n_y)$: $(0|0), (0|1), (1|0), (0|2), (1|1), (2|0)$ etc.

Dependence on Raman pumper intensity

Another degree of freedom in resolved-sideband Raman cooling is the intensity of the Raman pumper beam. As can be seen in figure 4.2 on page 147 the transfer efficiency to the vibrational ground state is dependent on the magnitude of this intensity. Optimal transfer is achieved when the Raman pumper strength is chosen to be comparable to the smallest Raman coupling involved. In the configuration under investigation this is the coupling $U_R\,(n_x = 1, n_y = 0)$ between the states $|m_f = 4, \{n_x = 1, n_y = 0\}\rangle$ and $|m_f = 3, \{n_x = 0, n_y = 0\}\rangle$, i.e. when

$$\frac{\hbar\Gamma_p'}{U_R\,(n_x, n_y)} \sim 1, \tag{4.48}$$

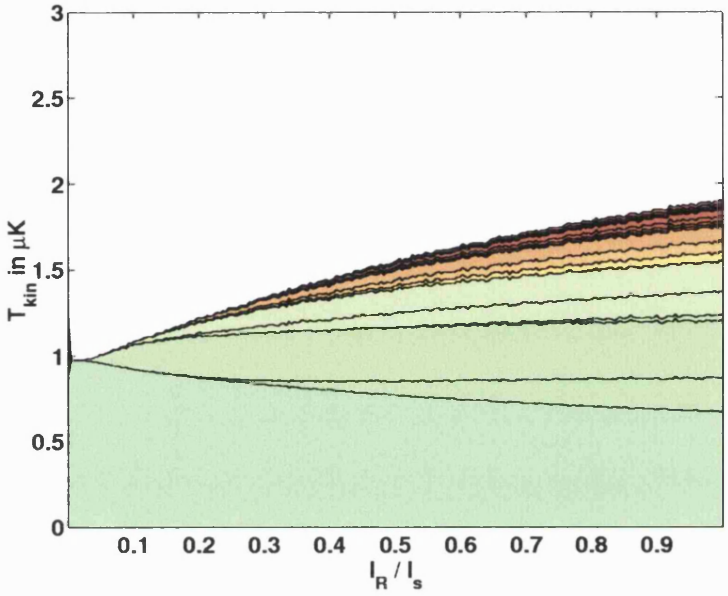

Figure 4.7: This figure shows the contribution to the kinetic temperature of the different vibrational levels after 9 ms of Raman cooling. See text for a detailed description. The colours represent different vibrational levels. They are ordered in ascending order $(n_x|n_y)$: $(0|0), (0|1), (1|0), (0|2), (1|1), (2|0)$ etc.

where Γ_p' is the effective scattering rate of the Raman pumper as described in equation 4.20 on page 133. (cf. equation 3.8 on page 104). This dependence strongly suggests that the part of the Raman cooling cycle responsible for the freezing of the population transfer is related to the last steps in the Raman cooling ladder as can be seen in figures 4.5 to 4.8 on pages 150–153. Population gets trapped in higher lying states and further transfer to the vibrational ground state is inhibited. The detrimental effect sets in when the Raman pumper strength $h\gamma_p'$ becomes comparable to the Raman coupling strength of the respective level and increases beyond it. Passing this threshold suppresses the population transfer between the level pair. Therefore every vibrational level pair has a different Raman pumper strength threshold, where

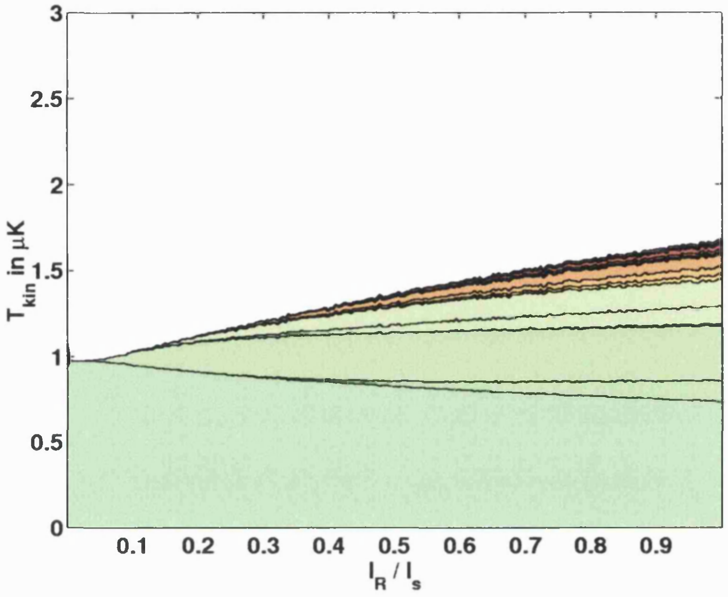

Figure 4.8: This figure shows the contribution to the kinetic temperature of the different vibrational levels after 14 ms of Raman cooling. See text for a detailed description. The colours represent different vibrational levels. They are ordered in ascending order $(n_x|n_y)$: $(0|0), (0|1), (1|0), (0|2), (1|1), (2|0)$ etc.

the effects of the quantum Zeno effect kick in. The consequence of this is that the lower lying levels, for which the Raman coupling is smallest, will be the first to freeze out, when the Ramam repumper strength is increased beyond this threshold. Since the majority of the population is in those lower lying vibrational levels, the impact will be greatest there. The result of this is, as can be seen in figure 4.6 after 4 ms of Raman cooling, that a considerable amount of population cannot be transferred via a Raman cooling cycle to any lower lying vibrational levels.

This dependence on the Raman pumper intensity limits the efficiency of the pumping to the vibrational ground state for too high Raman pumper intensities. The reason for this turns out to be an analogue of the Quantum

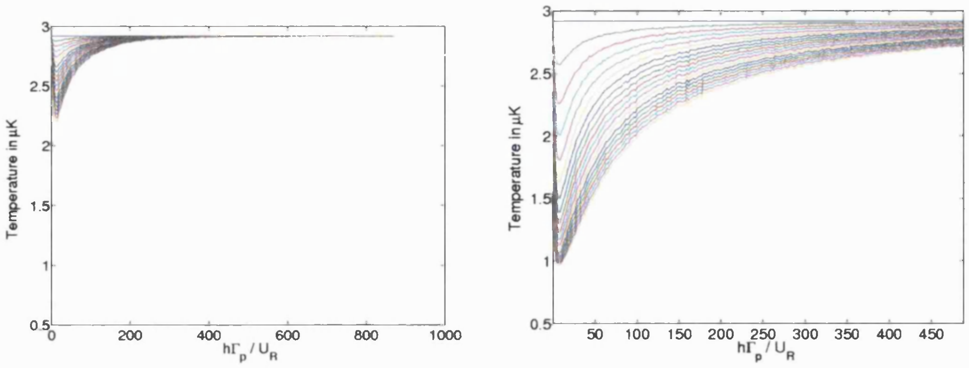

(a) $E_\pi/E_1 = 0.1$ (b) $E_\pi/E_1 = 0.3$

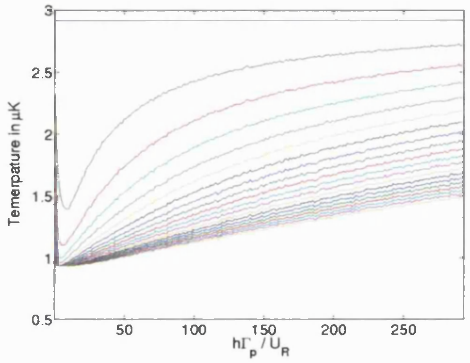

(c) $E_\pi/E_1 = 0.5$

Figure 4.9: This figure shows a plot of the final kinetic temperature versus the Raman pumper strength in units of the lowest Raman coupling $U_R\,(n_x = 1, n_y = 0)$ for different ratios E_π/E_1. The ratios are: (a) $E_\pi/E_1 = 0.1$, (b) $E_\pi/E_1 = 0.3$ and (c) $E_\pi/E_1 = 0.5$. The same colour scheme as in figure 4.2 on page 147 was used.

Zeno effect. The Zeno effect is introduced in appendix D on page 220 and the connection between Raman cooling and this quantum Zeno effect is discussed in summary in section 4.4.2.

Dependence on maximum well depth

The next dependence we want to have a closer look at is the one on the maximum well depth of the optical lattice. The Raman coupling is directly

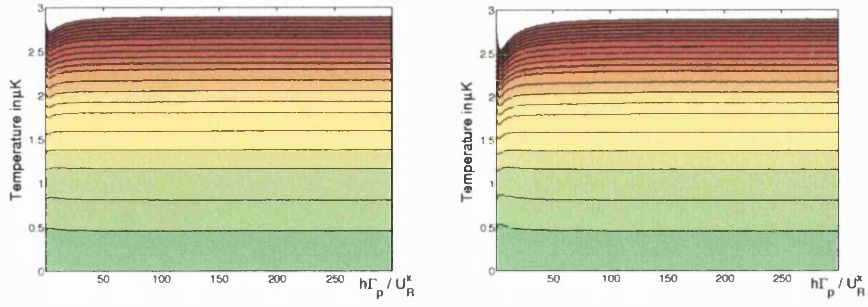

(a) 4 ms (b) 9 ms

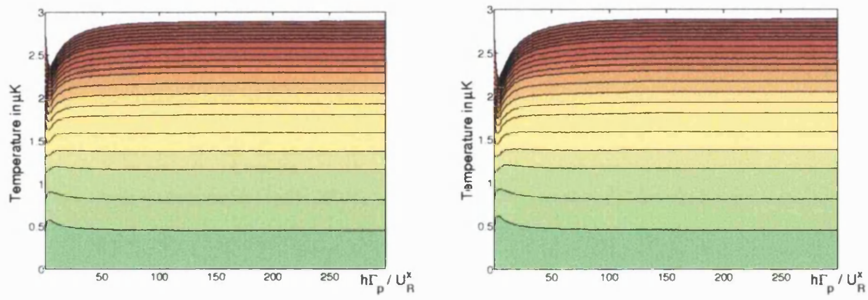

(c) 14 ms (d) 19 ms

Figure 4.10: This figure shows a plot of the final kinetic temperature versus the Raman pumper strength in units of the lowest Raman coupling $U_R\,(n_x = 1, n_y = 0)$ at different times during the Raman cooling cycle. The magnitude of E_π was chosen to be $0.1E_1$. The Raman cooling times are: (a) 4 ms, (b) 9 ms, (c) 14 ms and (d) 19 ms. The colours represent different vibrational levels. They are ordered in ascending order $(n_x|n_y)$: $(0|0), (0|1), (1|0), (0|2), (1|1), (2|0)$ etc.

proportional to this quantity. Hence we expect an improved transfer to the vibrational ground state for larger well depths. A problem arises when the maximum well depth crosses the $243\,\mathrm{E_R}$ level. Then the lowest Raman level pair $|m_f = 4, \{n = 0\}\rangle$ and $|m_f = 3, \{n = 1\}\rangle$ become degenerate. For bigger light-shifts, the Raman B-field must change sign to bring them into resonance again in contrast to higher lying level pairs. Since we want generally to return to zero applied magnetic field at the end of the Raman cooling cycle to undertake quantum state control experiments, higher lying resonance are

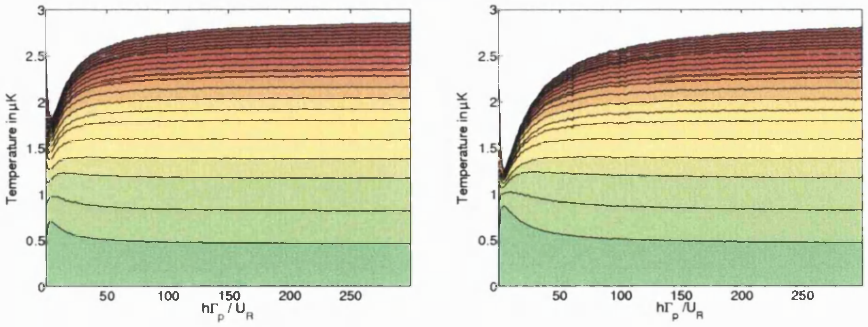

(a) 4 ms (b) 9 ms

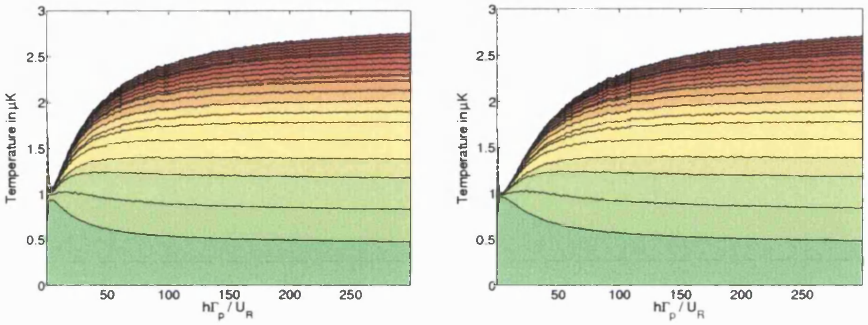

(c) 14 ms (d) 19 ms

Figure 4.11: This figure shows a plot of the final kinetic temperature versus the Raman pumper strength in units of the lowest Raman coupling $U_R\,(n_x = 1, n_y = 0)$ at different times during the Raman cooling cycle. The magnitude of E_π was chosen to be $0.3E_1$. The Raman cooling times are: (a) 4 ms, (b) 9 ms, (c) 14 ms and (d) 19 ms. The colours represent different vibrational levels. They are ordered in ascending order $(n_x|n_y)$: $(0|0), (0|1), (1|0), (0|2), (1|1), (2|0)$ etc.

re-coupled again. Those unwanted level crossings can give rise to unwanted heating.

Another important fact to note is that in real experiments the beam profile is not absolutely flat. Depending on the beam source, the maximum well depth can vary by several percent. Special care has to be taken for efficient Raman cooling experiments as a basis for subsequent quantum state control. If we are near the cut-off at $U_0 = 243\,\mathrm{E_R}$ mark, some wells might have a light-

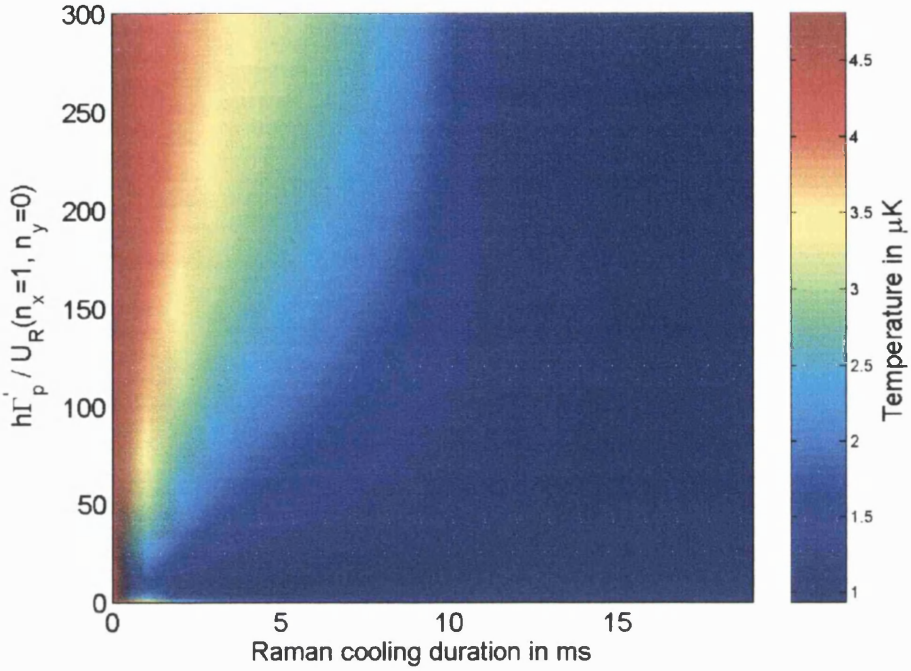

Figure 4.12: This figure shows the Raman pumper strength $h\Gamma_p^{'}$ in units of the lowest Raman coupling $U_r\,(n_x = 1, n_y = 1)$ plotted against the kinetic temperature T_{kin}. The atoms were assumed to have had an initial vibrational temperature T_{vib} of $12\,\mu$K at the start of the Raman cooling cycle. The calculated final kinetic temperatures are shown for Raman cooling durations from $0\,$ms to $19\,$ms.

shift already larger than this and some might be below it. These levels are not properly coupled together and only inefficient coherent coupling exists. Thus it is important to get an as clean beam profile as possible, so that the number of degenerate level pairs is maximized.

4.4.2 The Quantum Zeno Effect and Raman Cooling

The simulations results strongly suggest that for particular choices of Raman pumper intensities the population transfer to the vibrational ground state is inhibited. Further investigations into this observation allowed us to link

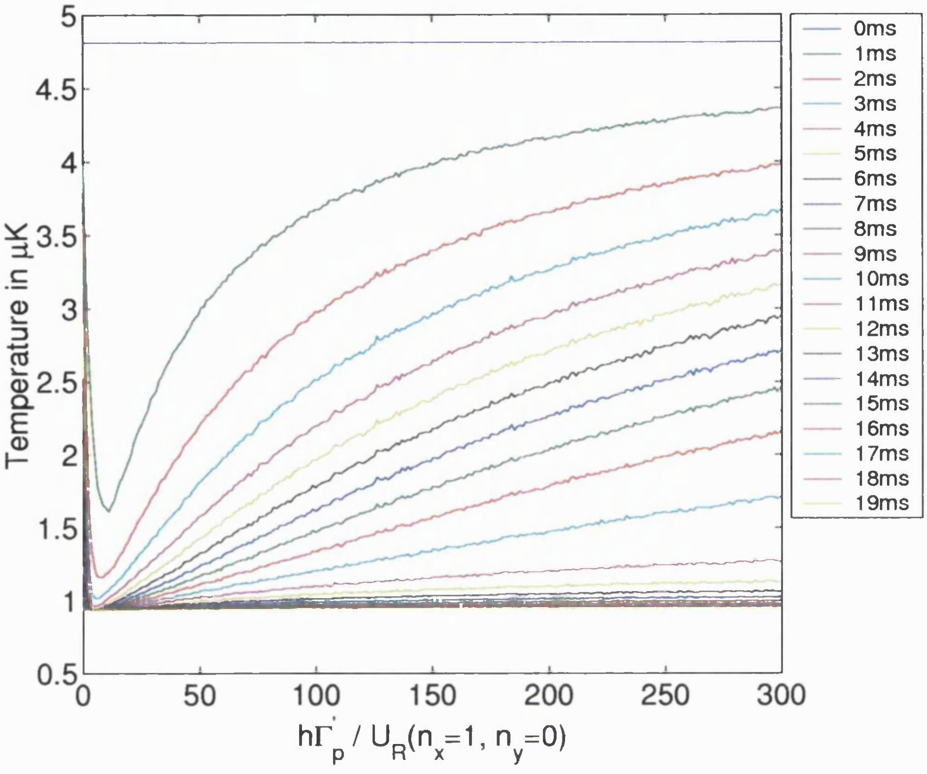

Figure 4.13: This figure shows the kinetic temperature T_{kin} plotted against the Raman pumper intensity I_R in units of the saturation intensity I_s. The atoms were assumed to have had an initial vibrational temperature T_{vib} of $12\,\mu$K at the start of the Raman cooling cycle. The calculated final kinetic temperatures are shown for Raman cooling durations from $0\,$ms to $19\,$ms.

this suppression of the population transfer induced by the coherent coupling to the quantum Zeno effect. Some background information on this effect is agglomerated in appendix D. To our knowledge we have been the first to make this connection. A schematic of what happens is shown in figure 4.15. A coherence is established between two degenerate level pairs $|g_4, n\rangle$ and $|g_3, n-1\rangle$. The coherent coupling is induced by the lattice light-field. In the situation (a) the intensity of the Raman pumper is low enough not to destroy the population transfer induced by the coherent coupling. Increasing

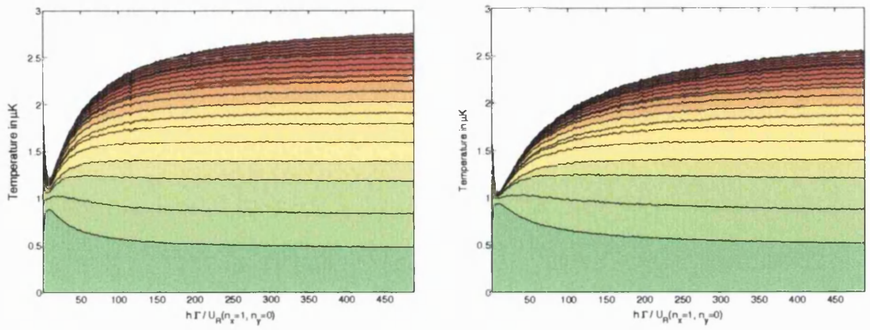

(a) 4 ms (b) 9 ms

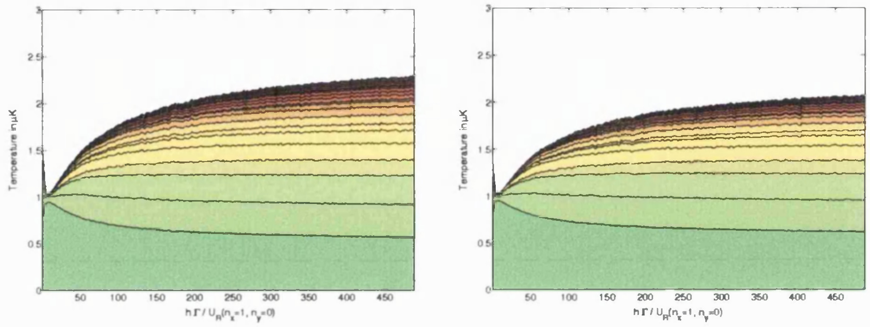

(c) 14 ms (d) 19 ms

Figure 4.14: This figure shows a plot of the final kinetic temperature versus the Raman pumper strength in units of the lowest Raman coupling $U_R\,(n_x = 1, n_y = 0)$ at different times during the Raman cooling cycle. The intensity of the Raman pumper was ramped to $0.5\, I/I_{\text{sat}}$ between 5 ms and 10 ms from its initial value. The Raman cooling times are: (a) 4 ms, (b) 9 ms, (c) 14 ms and (d) 19 ms. The colours represent different vibrational levels. They are ordered in ascending order $(n_x|n_y)$: $(0|0), (0|1), (1|0), (0|2), (1|1), (2|0)$ etc.

the intensity of the Raman pumper as shown in (b) has a detrimental effect on the coherent coupling and the population transfer freezes out.

Many QMCWF simulations have been run for a variety of parameter ranges. The observation was that when the Raman pumper intensity becomes comparable to the strength of the coherent coupling, the population transfer is inhibited. This can be linked directly to the resolved-sideband Raman cooling scheme. Here a set of Raman cooling unit systems (c.f. figure 4.1)

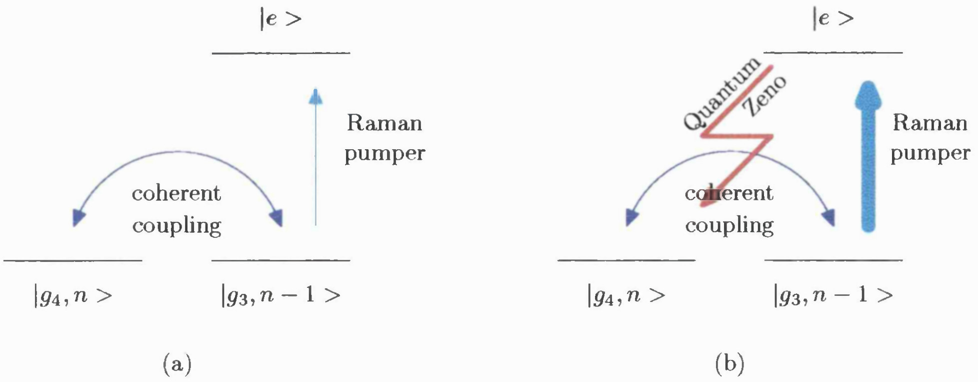

Figure 4.15: This figure shows a schematic of the Quantum Zeno Effect in resolved-sideband Raman cooling. A coherence exists between two degenerate level pairs $|g_4, n\rangle$ and $|g_3, n-1\rangle$ induced by the lattice light-field. A Raman pumper beam optically pumps the atoms. If the intensity of it is chosen to be larger than the coherent or Raman coupling, then the quantum Zeno effect freezes out the population transfer (cf (b)). For low enough intensities the population transfer is not affected (cf (a)).

are linked together by optical pumping. A property of the Raman cooling is that its strength is dependent on the vibrational quantum number of the level $|F = 4, n\rangle$ in the level pair and is proportional to $\sqrt{n}$. If we call the strength of the Raman coupling for this lowest level pair with $n = 0$ U_R, the population transfer freezes out if the Raman pumper strength surpasses U_R. Hence population can be trapped in higher lying level pairs and the increase in ground state population is minimal. This can be seen in figure 4.14. Here the x-axis shows the initial Raman pumper intensity in units of the lowest Raman coupling. For low enough intensities population is transferred to lower lying levels. Between 5 ms and 10 ms we ramp Raman pumper intensity to $0.5 I/I_{\text{sat}}$. The population transfer freezes out and even for longer Raman cooling durations hardly any population is transferred to a lower lying state. Since Raman cooling is an important and efficient tool for quantum state preparation, it is worth looking for ways how to minimize the impact of the quantum Zeno effect. One suggestion to do so is described in the next section.

4.4.3 How to circumvent the quantum Zeno effect

The aim of the investigations in this chapter is to deduce optimized parameter ranges to improve our Raman cooling experiment. Hence the inhibition of population transfer to the vibrational ground state due to the Zeno effect needs to be addressed. Subsequent investigations using the QMCWF formalism showed that the freezing out of the population transfer due to quantum Zeno can be circumvented by ramping the Raman pumper intensity I_R from an initial higher value $(I_R \approx 0.05 I/I_{\mathrm{sat}} \approx U_R\,(n_x = 1, n_y = 0)$ to approximately the size of the lowest Raman coupling in the Raman cooling ladder $(I_R \approx 0.05 I/I_{\mathrm{sat}} \approx U_R\,(n_x = 1, n_y = 0))$. Figures 4.17(a) to 4.17(f) show the simulation results when the Raman pumper intensity is ramped in that way.

The converse happens when the Raman pumper intensity is ramped up from $0.05\, I/I_{sat}$ to $0.5\, I/I_{sat}$. Then the population transfer is almost frozen out at the beginning of the ramp and not much more cooling is achieved afterwards anymore, even for longer Raman cooling times as is shown in figure 4.14.

4.4.4 Experimental Results

This section is dedicated to the experimental results obtained by our group. They are not exhaustive but confirm the general trend outlined in 4.4.1 on page 147. In the experiment shown in figure 4.16 the atoms were Raman

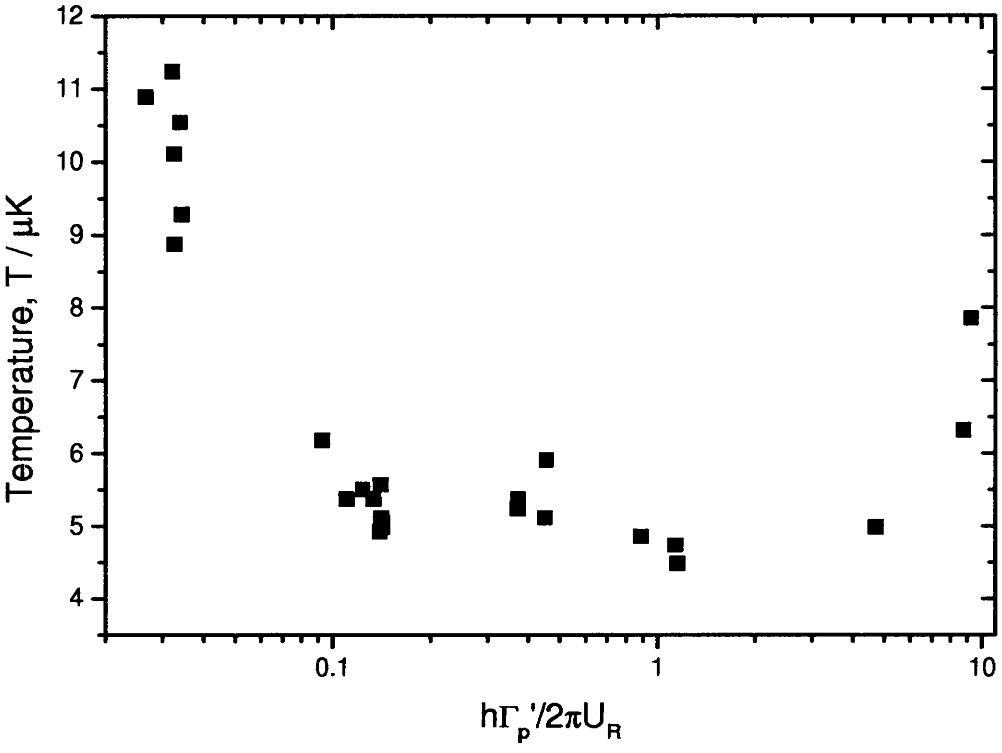

Figure 4.16: This figure shows some experimental results for the final temperature of resolved sideband Raman cooling for different Raman pumper intensities. The atoms were cooled for 10 ms in a far-detuned optical lattice 4000Γ detuned from resonance. The other parameters were $U_1 = 54\,\mathrm{E_R}$, $B_{\mathrm{Raman}} = 200\,\mathrm{mG}$, error $\Delta T \approx \pm 0.5\,\mu\mathrm{K}$.

cooled for a duration of 10 ms. The lattice beams had a single beam light shift of $U_1 = 54\,\mathrm{E_R}$, giving a total potential well depth of $U_0 = 243\,\mathrm{E_R}$. The far-detuned lattice beams had a diameter of 3 mm and 83 mW per beam, which is 1048 saturation intensities. The detuning was $\Delta = 4000\Gamma$ and a magnetic field B_R of 200 mG was applied to shift the levels $|m_f = 4, n = 1\rangle$ and $|m_f = 3, n = 0\rangle$ into resonance.

Looking at figure 4.16 we can readily see that the final temperature has a minimum when the Raman pumper intensity is comparable to the smallest Raman coupling U_R in the system. For higher Raman pumper intensities the final temperatures rise again, suggesting an inhibition of the population transfer to the vibrational ground state. We attribute this to the quantum Zeno effect and it is the first time indications for this have been observed.

4.5 Conclusion

This section introduced the Quantum Monte Carlo Wavefunction Method, a versatile formalism used to develop a model for resolved-sideband Raman cooling. The formalism is then applied to far-detuned lattices and the necessary equations deduced to implement a model for resolved-sideband Raman cooling.

Many simulations have been carried out for this work and selected results are reviewed in the course of this chapter. A surprising and original observation was the discovery of the role of the quantum Zeno effect in resolved-sideband Raman cooling and its detrimental effect on the efficiency of the coherent population transfer when the Raman pumper intensity becomes greater than the magnitude of the Raman coupling introducing the coherence. Being aware of the quantum Zeno effect allowed us to devise a scheme by which we can circumvent its effect by ramping the Raman pumper intensity from an arbitrary higher lying value to about the size of the smallest Raman coupling present in the system. This allows a lot of freedom for the choice of the initial Raman pumper intensity provided it is ramped down at any time during the duration Raman cooling cycle. Another interesting consequence of the fact that the Raman coupling is three times bigger along the y-direction than along the x-direction is that the quantum Zeno effect can trap a signif-

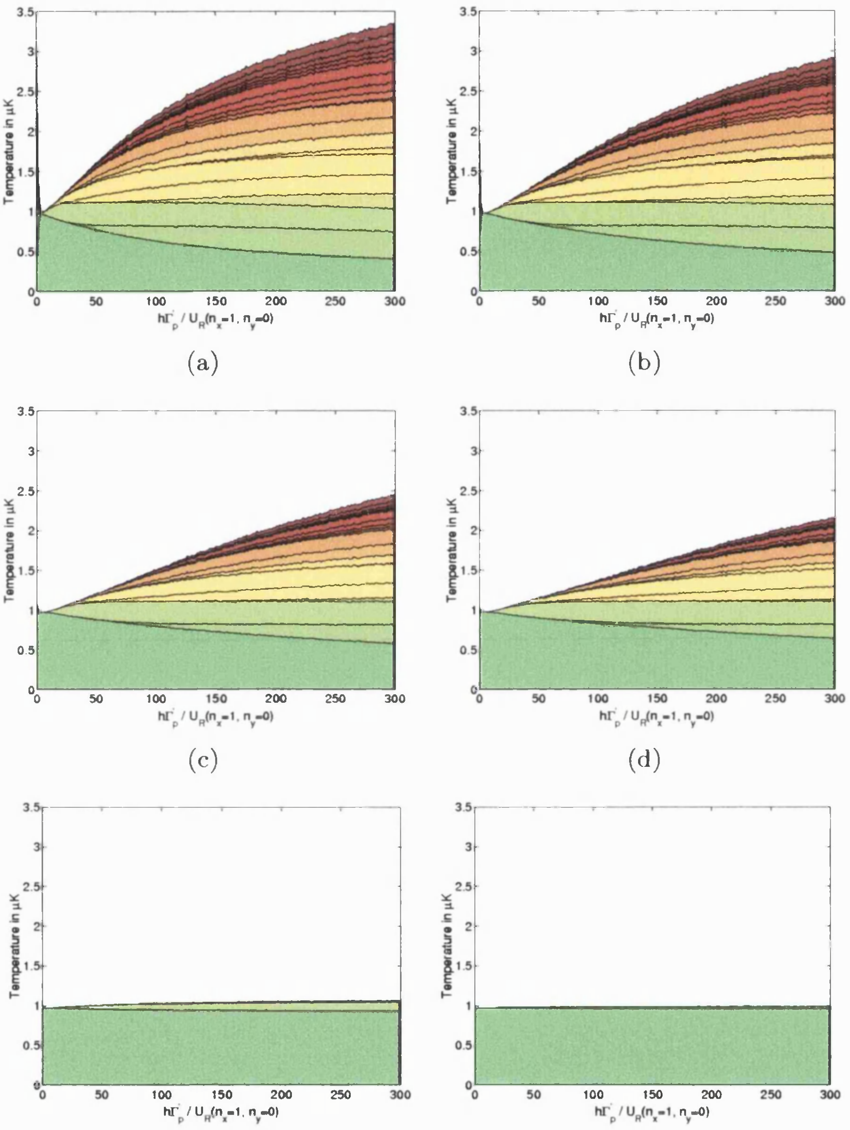

(a) (b) (c) (d) (e) (f)

Figure 4.17: This figure shows a plot of the final kinetic temperature versus the Raman pumper strength in units of the lowest Raman coupling $U_R\,(n_x = 1, n_y = 0)$ at different times during the Raman cooling cycle. The intensity of the Raman pumper was ramped to $0.05\,I/I_{\mathrm{sat}}$ between 5 ms and 10 ms from its initial value. The Raman cooling times are: (a) 4 ms, (b) 6 ms, (c) 8 ms, (d) 9 ms, (e) 14 ms and (f) 19 ms. The colours represent different vibrational levels. They are ordered in ascending order $(n_x|n_y)$: $(0|0), (0|1), (1|0), (0|2), (1|1), (2|0)$ etc.

icant amount of population in the vibrational state $|m_f = 4, n_x = 1, n_y = 0\rangle$ if the Raman repumper intensity is to larger than the corresponding Raman coupling along x.

In the last part of this chapter we present some experimental results from out group. Due to experimental constraints we have not been able to much more experimental work on this, but it will be very interesting to investigate this phenomenon of the quantum Zeno effect in resolved-sideband Raman cooling and its consequences further experimentally.

Chapter 5

Diagnostic Tools for Atoms in Optical Lattices

5.1 Introduction

To prepare, manipulate and measure the quantum state of a physical system is one of the great challenges of modern science. The introduction section in [42] provides a detailed account of the contribution that work on optical lattices could make to achieve this goal. The advantage of optical lattices over other systems is that the experimenter has a wide ranging control over the characteristics of the trapping potential through the manipulation of laser beam geometry, beam polarization, beam intensity, laser beam frequency and through the addition of static electric and magnetic fields.

This variety of control possibilities naturally raises the need for suitable diagnostic tools to accompany them to monitor their impact on the system and optimize their efficiency. Quantum state preparation using resolved-sideband

Raman cooling aims to prepare as many atoms as possible in the vibrational ground state of the lattices in one of the stretched states $|F = 4, m = \pm 4\rangle$. The efficiency of this preparation method can be increased if we start with a maximized population in the appropriate stretched state with regard to the other states of the $|F = 4, m\rangle$-manifold. This requires a diagnostic tool providing us with the means to measure the population distribution over the different $|F = 4, m\rangle$ states. This Zeeman state analysis can be achieved with a Stern-Gerlach type set-up. These measurements also can be used to optimize the far-detuned lattice set-up and correct alignment errors of the lattice beams. Another tool needed in the context of Raman cooling is one to monitor the population distribution over the vibrational states of the lattice. This turned out to be all the more important when we realized laser beam fluctuations could cause parametric heating of our atomic sample, which could limit the vibrational temperature that we could reach by Raman cooling. Parametric excitation is in itself an interesting topic, as we are working in anharmonic trapping potentials and it is therefore considered in some detail in the following.

In general parametric excitation is a useful tool to investigate the properties of far-detuned optical lattices [54–57]. It was used, for example, by Friebel *et al.* [54] and by Anderson *et al.* [58] to measure the vibrational frequency of the lattice and enabled them to characterize important lattice parameters in their experiments. Parametric excitation was also used as a model to evaluate heating induced by excitation through intensity fluctuations of the laser beams both in the time and space domain. Jáuregui [59] provided an exhaustive theoretical study of parametric heating in harmonic potentials, investigating it with a non-perturbative and perturbative approach. The non-perturbative approach establishes a link between the classical and quantum description of the system and gives useful insights into the problem. In the rest of the chapter we will use the perturbative approach, which allows us to take into account the effect of the anharmonicity of the optical lattice, which is prevalent in shallow traps. Such a model can be used to study the vibrational frequency, potential well depth and anharmonicity of the lattice under investigation. It enables us to understand the consequences of anharmonicity of the lattice potential and the influence of the non-uniformity of the laser beam intensity profile in experiments. The main motivation to investigate these effects more closely is to evaluate the different heating sources in our resolved-sideband Raman cooling experiments and after identifying them, trying to minimize their impact. An important conclusion of this investigation was that heating due to stochastic intensity fluctuations shouldn't play a significant role on the typical time scales of our experiments [41].

The other useful diagnostic tool in laser cooling that is described is the measurements of the distribution of Zeeman state populations using a Stern-Gerlach type set-up. These measurements can be used to monitor and improve the efficiency of laser-cooling in far-detuned optical traps. Monitoring the population distribution allows one to make sure that more than 80% of the atoms end up in the stretched states of the lattice before the start of the Raman cooling cycle, providing more advantageous initial conditions for this method. Simulations of a Zeeman state analysis type of measurement have been implemented with Matlab, where atoms are released from an optical lattice, fall through a magnetic field gradient and are subsequently measured by recording their time-of-arrival spectrum. The results of this simulations allowed us to make the right design choices for the magnetic field coils producing the necessary magnetic field gradient and deduce appropriate parameters, like coil current and coil position, to resolve the different Zeeman state peaks. These measurements have also been used by Silvia Bergamini to investigate the phenomenon of spin-temperature in optical lattices in her thesis [41]. First I will discuss our work on Zeeman state analysis. The second part of this chapter is then dedicated to a discussion of our work on parametric excitation.

5.2 Zeeman State Analysis

In the absence of any external magnetic fields, equal numbers of atoms become trapped in the σ^+ and σ^- sites of an optical lattice as a consequence of Sisyphus cooling . This symmetry can be broken by applying an external static magnetic field $\mathbf{B}_z$ parallel to the quantization axis of the lattice [43]. In the case of the 2D symmetry used in our experiments (cf. figure 3.5 on page 100) this is the direction perpendicular to the lattice plane. This magnetic field $\mathbf{B}_z$ introduces a Zeeman state dependent energy shift to the atomic eigenstates $|F, m_F\rangle$. This opens up the possibility, discussed in section 2.4 on page 63 of increasing the population of one of the stretched states $|F, m = \pm F\rangle$ at the expense of the other one. This is used, for example, in resolved-sideband Raman cooling, described in detail in section 3 on page 92. There an external static magnetic field is imposed on the far-detuned lattice phase to spin-polarize the lattice and increase the population of the particular stretched state used in the Raman cooling cycle [43]. This increases the efficiency of resolved-sideband Raman cooling as a simple consequence of the fact that fewer atoms start in wells with the *wrong* polarization and therefore reduces the number of optical pumping photons scattered. Raithel et al [60] have shown that the different energy-shifts of the ground state sub-levels give rise to a local cooling mechanism for large total angular momenta F in addition to cooling on the $F = 1/2 \leftrightarrow F' = 3/2$ transition often used as a model for Sisyphus cooling. There the cooling process is non-local, i.e. the atoms change their initial state and reverse their polarization when they are cooled through the optical pumping process and end up in the neighbouring potential well. For atoms with large angular momenta F the hyperfine state manifold offers the possibility for the atom to undergo an optical pumping cycle without changing the potential well. The reasoning for this can be found in more detail in section 1.1.4 on page 29.

The Zeeman state-dependent force on an atom is exploited in the Zeeman state analysis method discussed in this chapter. Here a magnetic field, which changes linearly with position, induces a spatial variation in the Zeeman energy shift and thus of the magnetic interaction energy of the atoms. The latter gives rise to a spatially dependent force which can be used to distinguish atoms in different Zeeman sub-states and thereby to measure their relative populations in experiments.

The experimental procedure is as follows. The atoms are released from a spin-polarized optical lattice by switching off the trapping beams. If no magnetic field gradient is present the atoms in different magnetic sub-levels feel the same acceleration due to gravity. The time-of-arrival spectrum is then similar to a Gaussian as shown in figure 5.1 on page 178. If a magnetic field gradient is present the atoms feel an additional state-dependent magnetic dipole force besides gravity, proportional to their m_F quantum number. For large enough field gradients the time-of-arrival spectra separates into distinguishable peaks associated with individual m_F quantum numbers as shown in figure 5.2. This allows one to measure the relative populations of the Zeeman sub-states associated with distinct m_F magnetic dipole moments as well as to deduce a phenomenological *spin temperature* associated with these sub-states.

The exploitation of the Zeeman shifts arising from the interaction of the atomic magnetic dipole moment and a magnetic field gradient is also extensively used to tailor atomic beams. For example, experiments on magnetic atom optical components have been carried out, such as magnetic mirrors [61] [62], refractive components [63], and magnetic surface traps [64]. Stern-Gerlach type of experiments have also recently been use to measure the quantum state of an atom with an arbitrarily large angular momentum [65].

This rest of the section is organized as follows. First the interaction of an atom with a magnetic field is discussed and the magnetic field of a square coil is deduced. Next the implementation of a Zeeman state analysis time-of-arrival measurement is described followed by a discussion and comparison with experimental results.

5.2.1 Atoms interacting with a magnetic field

The interaction of an atom with an external magnetic field is governed by the magnetic dipole moment of the atom. It is given by

$$\boldsymbol{\mu} = \gamma \mathbf{F} = -\frac{g_F \mu_B}{\hbar} \mathbf{F} \tag{5.1}$$

$$[\mu] = \mathrm{JT^{-1}}, \quad [F] = \mathrm{J\,s\,rad^{-1}}, \quad [\gamma] = \mathrm{rad\,s^{-1}\,T^{-1}}$$

where γ is the gyromagnetic ratio, g_F the Landé factor associated with the angular momentum state F and μ_B the Bohr magneton. Subjecting an atom to a magnetic field gives rise to an interaction energy W [66], a torque $\mathbf{\Gamma}$ [67] and a net force $\mathbf{F}$ [67]:

$$W = -\boldsymbol{\mu} \cdot \mathbf{B} \tag{5.2}$$

$$\mathbf{\Gamma} = \boldsymbol{\mu} \times \mathbf{B} \tag{5.3}$$

$$\mathbf{F} = -\boldsymbol{\nabla} W \tag{5.4}$$

Combining equations 5.2 and 5.4 gives for the components of the force F

$$\begin{aligned}\mathbf{F} &= -\nabla W \\ &= \nabla\left(\boldsymbol{\mu} \cdot \mathbf{B}\right) \\ &= \left(\boldsymbol{\mu} \cdot \frac{d\mathbf{B}}{dx}\right)\hat{\mathbf{x}} + \left(\boldsymbol{\mu} \cdot \frac{d\mathbf{B}}{dy}\right)\hat{\mathbf{y}} + \left(\boldsymbol{\mu} \cdot \frac{d\mathbf{B}}{dz}\right)\hat{\mathbf{z}}\end{aligned}$$

Since this net force F is proportional to the gradient of the magnetic field $\mathbf{B}$, an atom in a uniform magnetic field experiences no net force. The magnetic dipole precesses with a frequency

$$\nu_L = \frac{\omega_L}{2\pi} = -\frac{\gamma\,|\mathbf{B}|}{2\pi} \tag{5.5}$$

called the Larmor frequency. Hence the projection of the magnetic dipole moment along the direction of the magnetic field **B** remains constant. If the atom is placed in an inhomogenous magnetic field, the magnetic dipole experiences a net force proportional to the magnitude of the magnetic field and proportional to its magnetic dipole moment. Quantum mechanically an atom placed in a uniform magnetic field directed along the quantization axis of the atom possesses simultaneous eigenstates $|\Phi_m\rangle = |F, m_F\rangle$ belonging to both operators $\mathbf{F}^2$ and $\mathbf{F}_z$. For simplicity we define the quantization axis to coincide with the z-direction. The magnetic field $\mathbf{B}_z = B_z\,\hat{\mathbf{z}}$ gives rise to an energy shift of [67]

$$\Delta E_m = \mu_B\, g_F\, m_F\, |\mathbf{B}_z| \tag{5.6}$$

The time dependence can be introduced as usual in quantum mechanics by

$$\begin{aligned} |\Phi_m(t)\rangle &= \sum_m c_m(t)\,|\Phi_m\rangle \\ &= \sum_m A_m\, e^{-i\,E_m\,t/\hbar}\ |\Phi_m\rangle \\ &= \sum_m A_m\, e^{-i m\,\omega_L\,t}\ |\Phi_m\rangle \end{aligned} \tag{5.7}$$

Hence the time evolution of the coefficients c_m can be written as

$$c_m(t) = \exp\{-i\, m\, \omega_L\, t\}\, c_m \tag{5.8}$$

This allows us to deduce the time evolution of the populations associated with the different magnetic sub-levels $\pi_m(t)$, which are $\pi_m(t) = |c_m(t)|^2$. Substituting 5.8 reveals that the populations do not change with time. A change in $\mathbf{B}_z$ only changes the magnitude of the Larmor frequency.

Allowing for the magnetic field to have also transverse components $\mathbf{B_t} = \mathbf{B}_x + \mathbf{B}_y$, in addition to a parallel one $\mathbf{B}_z$, also induces couplings between different Zeeman sub-states [67]. The consequence of this is that the populations of the different magnetic sub-states are no longer constant with time, unless the magnitude of the transverse field component is much smaller than the parallel component or equally $|\mathbf{B}|$, i.e.

$$B \gg \frac{2\pi}{\omega_L} \frac{d|\mathbf{B}_t|}{dt} \tag{5.9}$$

If the Larmor frequency is much bigger than the rate of change of the magnetic field, then the internal and external degrees of freedom decouple and the angular momentum of the atom can adiabatically follow those variations and maintain the component of the magnetic dipole moment along the quantization axis. Time averaging the magnetic dipole moment over the Larmor period results in only a constant component along the quantization axis and it follows from equation 5.4 and 5.9 that

$$\mathbf{F} = \langle \mu \rangle \nabla |\mathbf{B}(r)| \tag{5.10}$$

where $\langle \mu \rangle$ is the time-averaged magnetic dipole moment. The consequence of this is also that the force is only dependent on the magnitude of the magnetic field alone and not on its direction.

5.2.2 Outline of Simulation

To simulate time-of-arrival spectrum measurements a model was implemented based on a classical Monte Carlo method. The atoms were assumed to be released from an optical lattice characterised by a kinetic temperature and atomic cloud size.

The first step of the implementation was to deduce the magnetic field of a square current-carrying coil and its spatial dependence (cf. section F). This magnetic field gradient gives rise to an additional force on the atoms besides gravity and influences the atomic motion dependent on the magnetic dipole moment of the atom. The zero of the magnetic field was chosen to be above the optical lattice region to ensure that the atoms do not experience a region of zero magnetic field. Consider, for example, an atom in a magnetic sub-state m_f. When it moves into a region of zero magnetic field, the orientation of the atomic magnetic dipole can freely evolve as it looses its quantization direction. When the atom moves again into a region of non-zero magnetic field a new quantization axis is introduced. The atomic magnetic dipole realigns itself. The process is random and the magnetic moments before and after transversing the zero magnetic field region are uncorrelated. Thus atoms moving through this zero can be subject to a magnetic dipole realignment rendering the experimental measurement of Zeeman sub-state populations invalid. Initially an atom with a magnetic dipole moment m_F is put at the origin. The atoms in an optical lattice are assumed to have a Maxwell-Boltzmann velocity distribution. At typical temperatures of optical lattices this distribution is similar to a Gaussian. Hence we base the choice of initial velocity on a Gaussian distribution and choose a random direction for the velocity vector. The defining mean velocity is defined by the temperature of the optical lattice. The next step is to calculate the trajectory of the atom until it passes through the time-of-fight measurement plane. When the atom passes through this plane we can deduced if it is detected by the time-of-flight beam or not, hence offering us a method to assess the efficiency of our experimental time-of-flight set-up as a function of the applied magnetic field gradient, the atomic cloud size and the kinetic temperature of the atoms before their release.

To extend the above method to a cloud of atoms trapped in an optical lattice some enhancements have been introduced. To reflect the initial position spread of the atoms in an optical lattice the starting position of the atom was chosen randomly assuming a Gaussian density distribution over the size of the optical lattice. The centre of the optical lattice was chosen to be the origin of our coordinate system. The effect of this position spread is that the time-of-arrival spectrum is broadened. Hence to deduce the temperature in an optical lattice from a time-of-arrival spectrum necessitates an correction for the initial size of the atomic cloud. In addition the atoms in an optical lattice are assumed to have a Gaussian velocity distribution which is assumed to be spatially isotropic. Hence the time-of-arrival spectrum for a cloud of atoms released from an optical lattice without a magnetic field gradient is then similar to a Gaussian as can be seen in figure 5.1. The atoms in the different magnetic states cannot be not resolved. Switching on a magnetic field gradient slowly before the atoms are released and repeating the above time-of-flight measurement adds additional state-dependent force to the gravitational one. If the gradient is high enough, the time-of-arrival spectrum splits into distinctive peaks associate with atoms populating different magnetic dipole moment states. This situation is shown in figure 5.2. In the end of each simulation the results are saved to disk to facilitate further data analysis.

5.2.3 Results and Discussion

The first implementation step of the Zeeman state analysis implementation was to simulate a time-of-arrival spectrum of atoms released from an optical lattice accelerated by gravity in zero magnetic field. The expected time-of-arrival spectrum is a Gaussian with a standard deviation proportional to the kinetic temperature of the atoms in the optical lattice. The result is shown in figure 5.1. The simulation allowed us not only to calculate the expected time-of-arrival spectrum, but also to identify the contribution of different magnetic Zeeman states to the overall signal.

The next step was to introduce the effect of atoms falling through a magnetic field gradient. As described above the atoms experience a m_f-level dependent force and for large enough magnetic field gradients the time-of-arrival spectrum can be resolved into a set of peaks corresponding to an individual Zeeman state. This is shown in figure 5.2 and for comparison an experimental time-of-arrival measurement is shown on figure 5.3. The re-

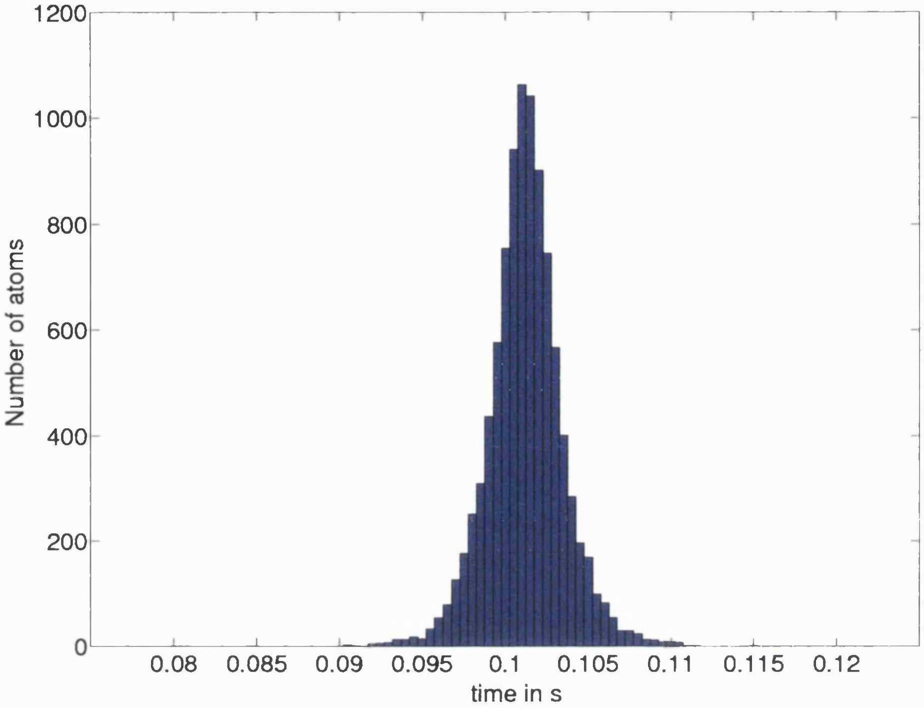

Figure 5.1: The figure shows a calculated time-of-arrival spectrum. The atoms were assumed to have had an initial temperature of 10 μK. No magnetic field gradient was present. A initial cloud size was 1 mm and 10000 atoms were used to calculate the figure. 4.4% of the atom missed the TOF beam.

sults of these calculations allowed us to deduce the distribution of the atoms over the different Zeeman states and optimize the far-detuned lattice cooling efficiency. The overall aim of our Zeeman state analysis and parametric excitation experiments was to prepare as large a fraction of the atoms as possible in the stretched states of the far-detuned lattice, thus providing an improved starting point for efficient Raman cooling and state preparation and to study the effects of laser beam noise and the corresponding heating effects.

This ends the section on our Zeeman state analysis experiments. The code was used in conjunction with experiments presented in the thesis by Silvia

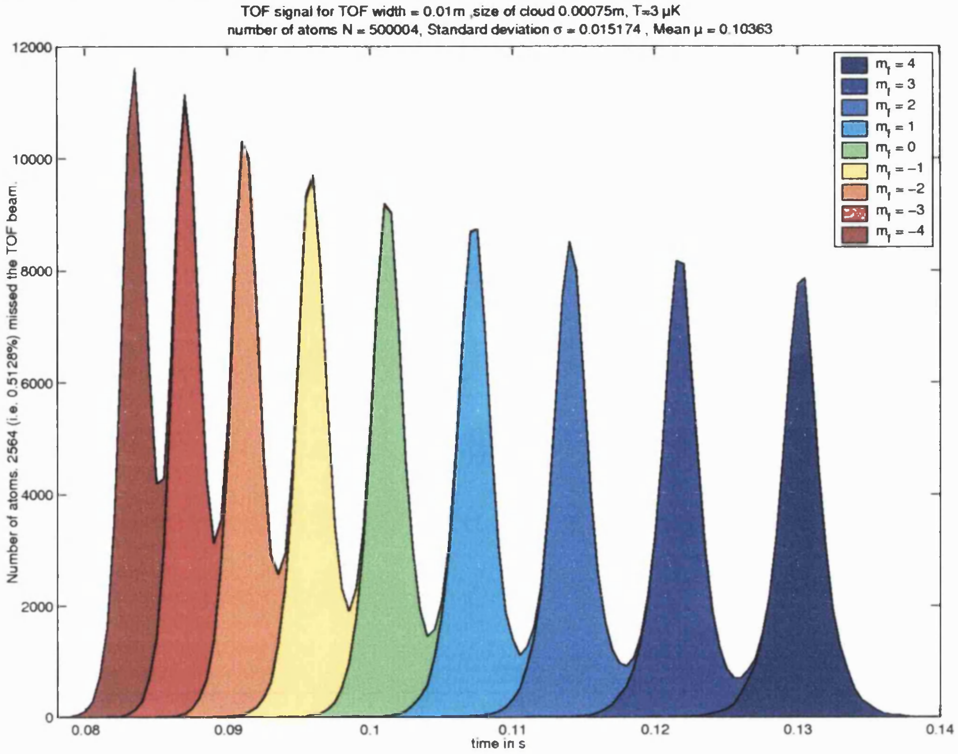

Figure 5.2: The figure shows a calculated time-of-arrival spectrum. The atoms were assumed to have had an initial temperature of $3\,\mu$K.

Bergamini [41].

5.3 Parametric Excitation

5.3.1 Perturbative Treatment

The content of this section extends the work of Jáuregui et. al. [55], Savard *et al.* [56], Jáuregui [59] on parametric excitation. The perturbative approach is the approach of choice here, since it can easily take the effect of anharmonicity into account prevalent in optical lattice potentials, whereas the non-perturbative approach is valid only in quadratic potentials and can only offer qualitative guidance. In the systems of shallow traps, anharmonic-

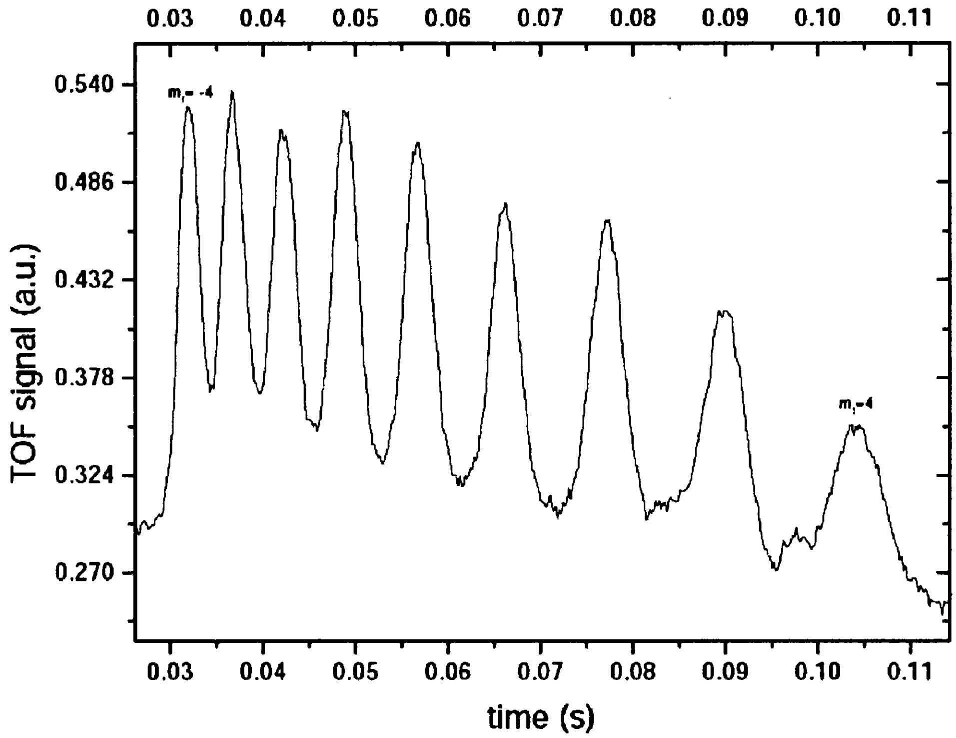

Figure 5.3: The figure shows a measured time-of-arrival spectrum. The TOF beam was 5 cm below the optical lattice. There is a time offset on the temporal axis. The figure is courtesy of Silvia Bergamini.

ity is an important property and necessitates the introduction of appropriate modifications to the standard perturbative treatment based on the harmonic oscillators approximation.

In our experiments parametric heating is obtained by applying small intensity fluctuations to the laser beams in a periodic fashion. This can be described by an effective Hamiltonian

$$
\begin{aligned}
\mathbf{H} = & \frac{p^2}{2M} + \frac{1}{2} M \omega_0^2 \left[1 + \epsilon(t)\right] x^2 && (5.11) \\
= & \mathbf{H}_0 + \mathbf{H}_{\mathrm{mod}} && (5.12)
\end{aligned}
$$

where $\epsilon(t)$ is the fractional modulation in the spring constant and given by

$$\epsilon(t) = \frac{I(t) - I_0}{I_0} \tag{5.13}$$

In this expression $I(t)$ is the intensity at time t and I_0 the unmodulated intensity. Additionally it is assumed that $\epsilon(t) \ll 1$. Considering a far-detuned trap, the effective potential can be written as [56]

$$V(x) = \frac{1}{2}M\omega_0^2 x^2 = -\frac{1}{4}\alpha\,|\mathcal{E}(x)|^2 \tag{5.14}$$

In this equation α is the atomic polarizability and $\mathcal{E}(x)$ the slowly-varying radiation field amplitude. The unperturbed Hamiltonian of the system is defined by

$$\mathbf{H} = \frac{p^2}{2M} + V(x) \tag{5.15}$$

In the following we will work in the interaction picture where the equation of motion of a state is given by the differential equation

$$i\hbar\frac{d\Psi_H(t)}{dt} = \epsilon(t)\,\tilde{V}(x,t)\,|\Psi_H(t)\rangle \tag{5.16}$$

To be able to use this picture we have to convert the state ket $|\Psi_S\rangle$ and the potential operator $V(x,t)$ from the Schrödinger picture to the interaction picture. This is achieved by introducing time-dependent unitary operators resulting in the following transformation equations:

$$|\Psi_H(t)\rangle = e^{i\mathbf{H}_0 t/\hbar}|\Psi_S\rangle \tag{5.17}$$

$$\tilde{V}(x,t) = e^{i\mathbf{H}_0 t/\hbar}\,V(x,t)\,e^{-i\mathbf{H}_0 t/\hbar} \tag{5.18}$$

Thus the unitary evolution operator $\tilde{U}(t)$ satisfies the integral equation

$$\tilde{U}(t) = 1 - \frac{i}{\hbar}\int_0^t \epsilon(t)\,\tilde{V}(x,t)\,\tilde{U}(t')\,dt' \tag{5.19}$$

These are all the ingredients we need to deduce the transition matrix elements as [59]

$$\begin{aligned}\left\langle f \,\middle|\, \tilde{U}(t)|i\right\rangle =&\delta_{fi} - \frac{i}{\hbar}\,V_{fi}\int_0^t dt'\,\epsilon(t')e^{i\omega_{fi}t'} \\ &\frac{1}{\hbar}\sum_n V_{fn}V_{ni}\int_0^t dt'\,\epsilon(t')e^{i\omega_{fn}t'}\int_0^t dt''\,\epsilon(t'')e^{i\omega_{ni}t''} + \ldots\end{aligned} \tag{5.20}$$

with

$$V_{fi} \equiv \langle f\,|\,V|i\rangle = E_f\delta_{fi} - \left\langle f \,\middle|\, \frac{p^2}{2M}|i\right\rangle \tag{5.21}$$

Hence an average transition rate for a transition from state $|i\rangle$ to $|f\rangle$ in a time period t can be evaluated, providing the changes in the wave function induced by the unitary operator $\tilde{U}(t)$ are small enough in the interval $(0,t)$. Thus

$$R_{f\leftarrow i} = \frac{1}{T}\left|\left\langle f \,\middle|\, \tilde{U}^{(n)}(t)|i\right\rangle\right|^2 \tag{5.22}$$

using n-th order perturbation theory. Additionally, if the heating is induced by a controlled modulation of the confining potential, i.e. $\epsilon(t) = \epsilon_0 \cos(\omega t)$, the transition rate can be approximated up to second order in ϵ_0 by

$$\begin{aligned}\left\langle f \middle| \tilde{U}^{(2)}(t)|i \right\rangle =& \delta_{fi} + \frac{i}{2\hbar}\epsilon_0\, t\, V_{fi}\left[\xi\left((\omega_{fi}+\omega)t\right) + \xi\left((\omega_{fi}-\omega)t\right)\right] \\ &- \left(\frac{\epsilon_0}{2\hbar}\right)^2 t \sum_k V_{fk}V_{ki}\Big\{\frac{1}{i(\omega_{ki}+\omega)}\Big[\xi\left((\omega_{fi}+2\omega)t\right) + \xi\left(\omega_{fi}t\right) \\ &\qquad - \xi\left((\omega_{fk}+\omega)t\right) - \xi\left((\omega_{fk}-\omega)t\right)\Big] \\ &\qquad + \frac{1}{i(\omega_{ki}-\omega)}\Big[\xi\left((\omega_{fi}-2\omega)t\right) + \xi\left(\omega_{fi}t\right) \\ &\qquad - \xi\left((\omega_{fk}+\omega)t\right) - \xi\left((\omega_{fk}-\omega)t\right)\Big]\Big\}\end{aligned} \tag{5.23}$$

where we have introduced the function $\xi(x) = e^{ix/2}\frac{\sin(x/2)}{x/2}$ to simplify the notation. As pointed out in [59] this is only valid if the unitary evolution induced by $\tilde{U}(t)$ changes the wave function in the interval $[0, t]$ only by a small amount. Thus the matrix elements for a harmonic oscillator with frequency ω_0 become

$$V_{fk} = \frac{\hbar\,\omega_0}{4}\left[(2f+1)\delta_{fk} + \sqrt{f(f-1)}\delta_{f,k+2} + \sqrt{(f+1)(f+2)}\delta_{f,k-2}\right] \tag{5.24}$$

Substituting this into equation 5.23 results in the following three combinations of $V_{fk}V_{ki}$ being different from zero:

(i) $V_{f,f\pm2}V_{f\pm2,f\pm4}$. Here the resonant terms appear in the combination

$\xi\left((4\omega_0 \pm 2\omega)t\right) - \xi\left((2\omega_0 \pm \omega)t\right)$ and the transitions associated with this are highly suppressed.

(ii) $V_{fk}V_{kf}$. Here resonances occur at $\omega \in \{0, 2\omega_0\}$. For $w \sim 2\omega_0$ the contribution of the transition amplitude is given by

$$\begin{aligned}\frac{\varepsilon^2 t}{2\hbar\omega_0}\Big[&|V_{f,f+2}|^2\left(\frac{\xi(0)-\xi(-[2\omega_0-\omega]t)}{i(\omega-\omega_0)}\right)\\ &+|V_{f,f-2}|^2\left(\frac{\xi(0)-\xi(+[2\omega_0-\omega]t)}{i(\omega-\omega_0)}\right)\Big]\end{aligned} \tag{5.25}$$

(iii) $V_{f,f\pm2}V_{f\pm2,f\pm2}$ and $V_{f,f}V_{f,f\pm2}$. Here the transitions can be viewed as a combination of two virtual transitions $k \longrightarrow i \longrightarrow i$ or $k \longrightarrow k \longrightarrow i$. The corresponding resonance frequency is the fractional frequency $\omega = |\omega_{fi}|/2 = \omega_0$. Hence the transition probability for a modulation frequency of $\omega \sim \omega_0$ is given by

$$\begin{aligned}|\langle f\,|\,U^{(2)}(t)|i\rangle\,|^2 &\sim \left(\frac{\varepsilon}{2\hbar}\right)^2\frac{t^2}{\omega_0^2}|V_{if}|^2(V_{ff}-V_{ii})\frac{\sin^2[(\omega-\omega_0)t/2]}{(\omega-\omega_0)^2t^2/4}\\ &\simeq \frac{\varepsilon^4\,\omega_0^2\,t^2}{1024}(f-i)^2\big[f(f-1)\delta_{f,i+2}\\ &\quad+(f+1)(f+2)\delta_{f,i-2}\big]\frac{\sin^2[(\omega-\omega_0)t/2]}{(\omega-\omega_0)^2t^2/4}\end{aligned} \tag{5.26}$$

In all the above cases, the non-resonant terms $\xi(\omega' t)$, $\omega' \neq 0$, give rise to an oscillatory behaviour in the transition probabilities. This is consistent with the results found in [59] for the exact evaluation of the transition probability amplitudes for the problem. Considering sufficiently long evolution times $\omega' t \gg 1$ and the delta-function representation

$$\delta(\zeta) = \frac{2}{\pi} \lim_{t \to \infty} \frac{\sin^2(\zeta\, t/2)}{\zeta^2\, t} \tag{5.27}$$

only the resonant terms give rise to significant contributions. Thus the dominant transition probability amplitudes of a fractional frequency resonance at $\omega = 2\,\omega_0/n$ arises, when n-th order perturbation theory is applied to the problem. These transitions can be viewed as n-steps procedures consisting of n virtual transitions, in which $n-1$ of them do not change the state and only one of them does. Hence equation 5.26 describes approximately the transition probability amplitudes for a transition $i \longrightarrow i \pm 2$, where the source has a frequency of $\omega = \omega_0$.

5.3.2 First Order Perturbation Theory

In this section we apply first order perturbation theory to the problem of parametric excitation and subsequently – in the next section – extend the formalism to a second order perturbation theory treatment. Considering the matrix elements of the perturbation perturbing the system

$$\mathbf{H}_{fi} = \frac{1}{2} M \omega_0^2 \epsilon(t) < f\,|x^2|\,i >, \tag{5.28}$$

we can calculate the average transition rates $\mathcal{R}_{f \leftarrow i}$ between two different levels $|f>$ and $|i>$ as [55]

$$\mathcal{R}_{f\leftarrow i} = \frac{1}{T}\left|\frac{-i}{\hbar}\int_0^T dt'\,\mathbf{H}_{fi}(t')\exp\{i\omega_{fi}t'\}\right|^2 \tag{5.29}$$

$$= \frac{\pi}{2\hbar^2}\left|T(f,i)\right|^2 S(\omega_{fi}) \tag{5.30}$$

$$\omega_{fi} = \frac{E_f - E_i}{\hbar} \tag{5.31}$$

where $T(f,i) = \langle f\,|\,V_{\text{eff}}|i\rangle$ is the matrix element of the space part of the perturbation and $S(\omega)$ is the one-sided power spectrum of the two-time correlation function associated with the excitation field amplitude. It is defined as

$$S(\omega) = \frac{2}{\pi}\int_0^T \cos(\omega\,\tau)\,\langle\varepsilon(t)\,\varepsilon(t+\tau)\rangle\,d\tau \tag{5.32}$$

and $\langle\varepsilon(t)\,\varepsilon(t+\tau)\rangle$ is the correlation function for the fractional intensity fluctuations. The one-sided power spectrum is defined in a way, so that if it integrated over all frequencies it equals the square of the root-mean-squared fractional modulation of the spring constant ε_0, i.e.

$$\int_0^\infty d\omega\,S(\omega) = \int_0^\infty d\nu\,S(\nu) = \langle\varepsilon^2(t)\rangle \equiv \varepsilon_0^2 \tag{5.33}$$

Thus, in the harmonic approximation, the only terms different from zero are

$$\mathcal{R}_{f\leftarrow i} = \frac{\pi\,\omega_0^2}{16}S(0)(2i+1)^2 \tag{5.34}$$

$$\mathcal{R}_{f\leftarrow i\pm 2} = \frac{\pi\,\omega_0^2}{16}S(2\omega_0)(i+1\pm 1)(i\pm 1) \tag{5.35}$$

These rates can be used to deduced, that the heating rate in a harmonic trap has exponential character and depends on the modulation frequency ω_0. An exponential heating rate is typical for a parametric excitation processes. Consider the probability $P(i,t)$ that the atom occupies a state $|i\rangle$ at time t. The average heating rate is then given by the sum of the different contributions of all processes involved which cause a change of state to another level. In the harmonic model these are only the rates 5.35. Hence the heating rate is given by [56] [57] [68]

$$\begin{aligned} \left\langle \dot{E}(t) \right\rangle &= \sum_i P(i,t)\, 2\hbar\omega_0 \left(\mathcal{R}_{f\leftarrow i+2} - \mathcal{R}_{f\leftarrow i-2} \right) \\ &= \frac{\pi\omega_0}{2}\, S(2\omega_0) \left\langle E(t) \right\rangle \end{aligned} \tag{5.36}$$

where we have introduced the average energy as

$$\langle E(t) \rangle = \sum_i P(i,t) \left(i + \frac{1}{2} \right) \hbar\omega_0 \tag{5.37}$$

Hence equation 5.36 shows that the heating rate is proportional to the average energy 5.37 itself, i.e. follows an exponential behaviour. Additionally it is proportional to the vibrational frequency ω_0 of the lattice. This allows the introduction of a characteristic time t_e, also called the energy e-folding time, in which the average energy $\langle E(t) \rangle$ increases by a factor e as [56]

$$t_e = \left(\pi\, i\, u_0 \right)^{-2} \left(S(2\omega_0) \right)^{-1} \tag{5.38}$$

It is interesting to note that in the expression for the heating rate $\hbar$ does not appear as a factor explicitly, stipulating that it can be calculated classically.

So far we only have considered resonances at a frequency $2\omega_0$. Classically there are also resonances possible at $2\omega_0/n$, with $n \in \mathbb{N}$. These resonances cannot be described with first-order perturbation theory. It can be shown that one needs to consider n-th order perturbation theory to be able to model a resonance at $\omega = 2\omega_0/n$ [59]. Since the aim of this exercise is to model the experimental results of our group which show resonances at $2\omega_0$ and ω_0, the formalism is extended to second-order perturbation theory in the next section.

5.3.3 Second-order Perturbation Theory

In this section we apply second order perturbation theory to the problem of parametric excitation. The previous section discussed parametric excitation in the light of harmonic traps. Optical lattices in general are governed by anharmonic potentials. Thus only deeply bound states are well described by the harmonic approximation and the energy band structure differs significantly for higher lying levels due to anharmonicity. In the paper by Jáuregui *et al.* [55] an extension to the model described in [56] was proposed which includes features like broad spectral lines and the effect of anharmonicity. Our theoretical model of parametric excitation is based on this modified formalism. Employing second-order perturbation theory results in a second-order correction to the transition rates between states $|i\rangle$ and $|f\rangle$ described by

$$\mathcal{R}^{(2)}_{i\to f} = \sum_k \left(\frac{-i}{\hbar}\right)^2 V_{ik}V_{kf} \int_{t_0}^{t} e^{i\omega_{ik}t'}\varepsilon(t')dt' \int_{t_0}^{t} e^{i\omega_{kf}t''}\varepsilon(t'')dt'' \tag{5.39}$$

allowing for the transition process to be viewed as a two-step procedure: a first step $|i\rangle \longrightarrow |k\rangle$ and a second step $|k\rangle \longrightarrow |f\rangle$. For harmonic parametric excitation, as shown in the previous section, only matrix elements for the space part of the perturbation with $\Delta n \in \{0, \pm 2\}$ are non-zero. This leaves us with the possible transitions between states $|n\rangle \longrightarrow |n\rangle$ and $|n\rangle \longrightarrow |n \pm 2\rangle$.

Consider now a first virtual transition $|n\rangle \longrightarrow |n\rangle$ and a second virtual transition $|n\rangle \longrightarrow |n \pm 2\rangle$. Here the net energy change is $2\hbar\Omega$ and a resonance occurs when the total energy if the two excitations coincides with the net energy change, i.e. if $\Omega = \omega_0$. These ideas can readily be extended to include the effect of anharmonicity, where the difference is that the transition matrix elements are non-zero for a wider set of level pairs (i, f) and the calculated energies of the underlying anharmonic optical lattice can be used instead of the harmonic ones. The work presented here takes for the first time these ideas into account. Calculated transition anharmonic transition matrix elements are shown in table 5.1.

Within this scheme of average transition rates, the probability $P_i(t)$ of finding an atom in a level $|i\rangle$, is then described by a set of finite difference equations for each level $|i\rangle$ as

$$P_i(t) = P_i(t_0) + \sum_f \mathcal{R}^{(1)}_{f\leftarrow i}\left(P_k(t_0) - P_i(t_0)\right)(t - t_0) \tag{5.40}$$

$$+ \sum_k \mathcal{R}^{(2)}_{f\leftarrow i}\left(P_k(t_0) - P_i(t_0)\right)(t - t_0)^2 \tag{5.41}$$

valid up to second order perturbation theory providing $t \sim t_0$ and subject to the condition $\sum_n P_n(t_0) = 1$.

Following further the suggestion in [55] in assuming a Gaussian distribution for the density of states, we can introduce broad spectral lines by considering an effective spectral density $S_{\text{eff}}(\omega)$ given by

$$S_{\text{eff}}(\omega) = S_0 \exp -\frac{\left(\omega - \omega_{\text{eff}}\right)^2}{2\sigma_{\text{eff}}^2} \tag{5.42}$$

where ω_{eff} is dependent in the modulation frequency and energies of the appropriate transition. This allows us to introduce broadening effects not only originating from the anharmonicity of the potential, but also from other sources, such as laser intensity, pointing fluctuations and intensity inhomogeneities over the lattice region. These sources are absorbed into an effective width σ_{eff} already containing information about the frequency widths of the atomic levels involved and the excitation source. The functional forms of σ_{eff} and ω_{eff} are deduced in appendix E. They are given by

$$\sigma_{\text{eff}}^2 = \sigma_{\text{i}}^2 + \sigma_{\text{f}}^2 + \sigma_0^2 \tag{5.43}$$

$$\omega_{\text{eff}} = \omega_{\text{mod}} - \left(\omega_{\text{f}} - \omega_{\text{i}}\right) \tag{5.44}$$

where $\sigma_{\mathrm{i,f}}$ are the frequency widths of the levels involved ($|i\rangle$ and $|f\rangle$), σ_0 the frequency width of the excitation source and ω_{mod} the frequency of the modulation. We have now reached a stage where it is possible to implement simulations of parametric excitation in anharmonic potentials with the problem being reduced to one of solving a set of simple coupled rate-equations for the time-evolution of the populations of the bound bands.

5.3.4 Outline of the Simulation

This section describes the implementation of simulations of parametric excitations in shallow traps using the theory described in the previous section. The simulation is split into different parts: First the band structure of the optical potential used to trap the atoms is calculated using the method discussed in section 2.6 on page 75. The results are used to deduce the initial population distribution over the vibrational levels as described in section 2.7.1 on page 81. The user has to specify the characteristic parameters describing the parametric excitation. These are the range of modulation frequencies for which the simulation should be run, the initial width of the atomic sample σ_0 (cf. equation 5.43 on the preceding page), the fractional modulation in the spring constant ε (cf. equation 5.13 on page 181) and the duration of the parametric excitation t_ω in units of the modulation frequency ω. The simulation results of the variation in the mean energy of the atoms trapped in the lattice and the number of atoms remaining are plotted. In addition the results are saved into a file to allow for subsequent data analysis. In preparation of the paper [69], the calculation of anharmonic transition matrix elements was added to the code and a future plan is to use these calculated transition matrix elements in future simulations.

In principle, the rates 5.39 need to be determined for each of the N states belonging to every band. However, we simplify the problem by representing each band by a single state, which we choose to be the appropriate Wannier state localized on a particular site of the lattice. Since the light-shift potential $U(x)$ is not harmonic, the spatial matrix-elements are non-zero for larger range of pairs mn than in the harmonic approximation. This is illustrated in table 5.1 where some of the calculated matrix-elements connecting bound Wannier states for the case of a maximum light-shift of $170E_R$ are tabulated. For low f and i the only matrix elements with a non-negligible value are those for $|f-i|=2$, consistent with the harmonic approximation, whilst for larger values of f and i it is clear that other transitions need to be taken into account.

5.3.5 Results of simulation

Simulations were run for a range of values of the modulation frequency from well below the mean vibrational frequency in the harmonic oscillator approximation to several times this value and for various values of the duration of the modulation phase. At the end of the modulation phase, the mean kinetic energy of the atoms was evaluated to facilitate comparison with experimental time-of-flight measurements of the temperature of the atoms. To gain qualitative information on the modulation-induced loss of atoms from the lattice, a simple cut-off procedure was used: the population in bands higher in energy

Table 5.1: Shown are the squares of some representative anharmonic transition matrix elements $|T_{mn}|^2$ in units of $\mathrm{E_R}^2$ for an optical lattice with $U_{max} = 170$ $\mathrm{E_R}$, for which approximately ten bands are bound. The principal non-zero matrix elements are those for which $\Delta n = 0$ and $\Delta n = \pm 2$, as in the harmonic approximation. However, for bands near the top of the potential well the values of some matrix elements with $\Delta_n \neq 0, \pm 2$ become significant.

	Band			
Δn	2	4	6	9
-4	-	0.14	2.6	0.15
-3	-	$< 10^{-4}$	$< 10^{-4}$	120
-2	34	180	410	110
-1	$< 10^{-4}$	$< 10^{-4}$	$< 10^{-4}$	1.2×10^3
0	450	1.5×10^3	3.2×10^3	8.0×10^4
1	$< 10^{-4}$	$< 10^{-4}$	0.92	1.1×10^3
2	18	410	170	150
3	$< 10^{-4}$	0.13	120	120
4	2.6	3.6	32	120

than the y-direction shoulder in the potential was deemed to have escaped the lattice. This procedure was expected to give good qualitative agreement with the true loss rate, since, for atoms with an energy above the shoulder, there are unbound trajectories which take the atom out of the lattice, the effectiveness of these channels being enhanced in the vertically oriented lattice used in the experiments by the action of gravity. It is worth noting that the band structure is nearly identical for cuts through the x and y-directions with energies below the shoulder in the y-direction. The potential wells have almost spherical symmetry and hence justifies our use of a 1D band structure calculation weighted with the appropriate geometrical factor. Sample results from the simulations are shown in figures 5.4 and 5.5.

Figure 5.4 shows, as a function of the modulation frequency and the duration

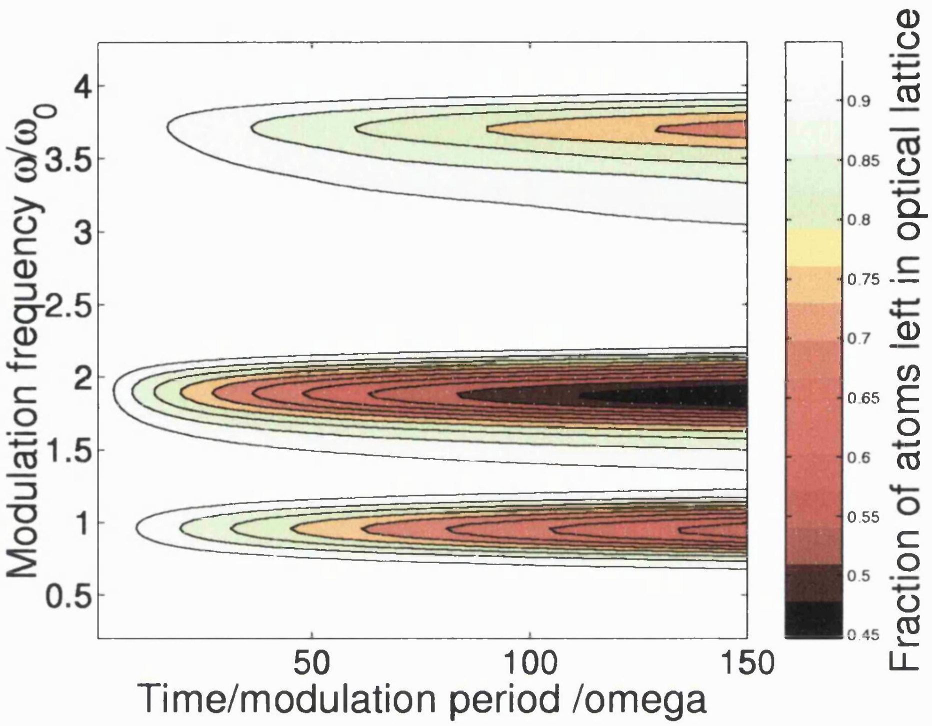

Figure 5.4: Simulation of the modulation-induced loss versus modulation frequency and time for: $U_{max} = 170\,E_R$, $m_F = -4$, $T_{in} = 3\mu K$, $\epsilon_0 = 0.1$, $\sigma_0 = 1.5\,E_R$.

of the modulation-phase, the fraction of the atoms loaded into the far-detuned lattice remaining trapped at the end of the modulation phase. In this simulation, the maximum potential depth was set equal to $170\,E_R$, corresponding to a harmonic-approximation vibrational frequency $\omega_0 = 17\,E_R/\hbar$ and the initial kinetic temperature of the sample is taken to be $30\,E_R/k_B$, close to the typical value realized in the experiments of $3\,\mu$K (corresponding to a population of the ground vibrational state of approximately 54%). The plot exhibits features corresponding to the principal resonance at modulation frequency $\omega \approx 2\omega_0$ and some higher-order resonances. It is clear that the centre

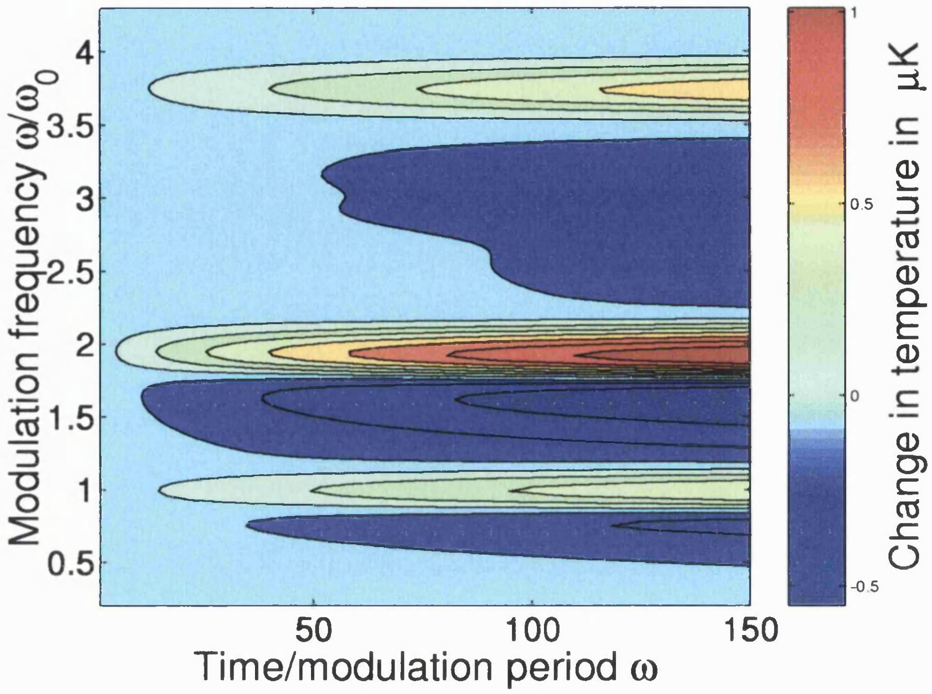

Figure 5.5: Simulation of the modulation-induced temperature variation versus modulation frequency and time for: $U_{max} = 170E_R$, $m_F = -4$, $T_{in} = 3\mu$K, $\epsilon_0 = 0.1$, $\sigma_0 = 1.5\,E_R$.

of mass of the $2\omega_0$ resonance occurs at a frequency lower than $2\omega_0$, an effect that may be ascribed to the anharmonicity of the wells. In the contrast to the harmonic case, where the energy level spacing is equi-distant, the energy level separation between energy level pairs decreases. This results in a decrease in the average energy separation and the position of the resonance is below the harmonic value. Another effect of anharmonicity is that the resonances are spread over a wider frequency range making the resonance feature less well resolved than in the harmonic case.

Figure 5.5 shows, as a function of the modulation frequency and of the duration of the modulation-phase, the mean kinetic energy of the atoms remaining trapped in the lattice at the end of the modulation phase. These results suggest that it should be possible to induce either heating or cooling of the sample remaining trapped, depending on the chosen modulation frequency. An analysis of the simulation data reveals that for a modulation frequency for which higher-lying bound states are predominantly excited, a parametric excitation sequence results in the expulsion from the lattice of these energetic atoms and therefore in a net cooling of the remaining trapped sample. Conversely, when it is predominantly the population in lower-lying bound levels that is excited, the excitation results a net transfer of this population into higher vibrational bands and thus in a net heating of the trapped sample, which is not, however, accompanied by a significant population loss from the lattice. However, whilst the distinction between the processes occurring for low-frequency and high-frequency excitation can clearly be drawn from the simulation data, it has to be borne in mind that the inhomogeneous broadening arising from the intensity inhomogeneity in a real lattice and the multiplicity of resonances arising from the non-zero matrix elements in the case of anharmonic wells, would be expected to make difficult such a precise phenomenological interpretation of real experimental data.

Furthermore, Zeeman-state population measurements made of the atoms in the far-detuned lattice showed that atoms could significantly populate several distinct Zeeman states if the experimental configuration was not properly calibrated. Potentials associated with different Zeeman states have different depths and spring-constants and therefore the characteristics of the excitation dynamics depend on the m_F quantum number as well. Indeed we were able to characterize the contribution of different Zeeman states averaging the cal-

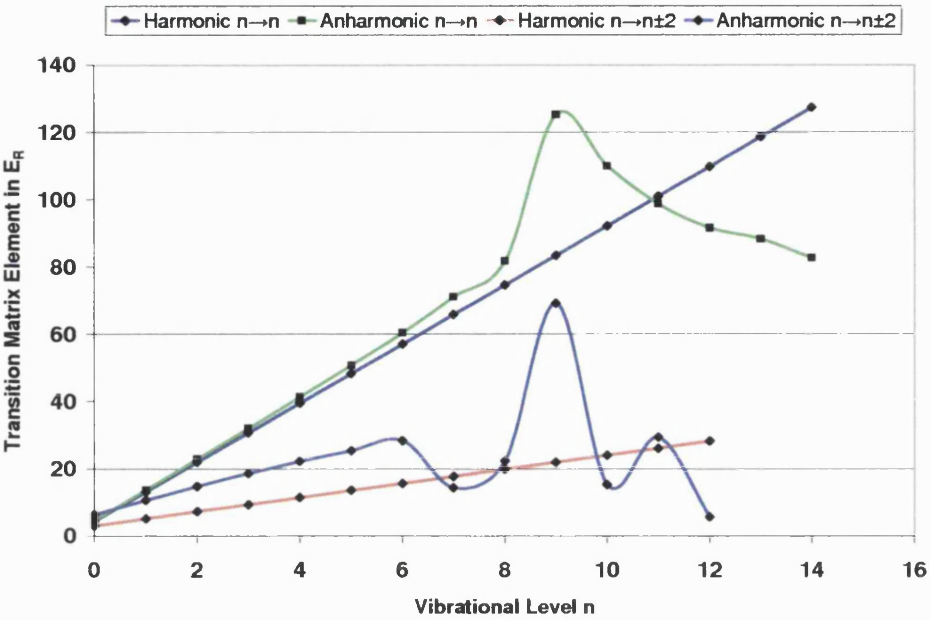

Figure 5.6: The graph compares the harmonic matrix elements with the calculated anharmonic ones. We see good agreement for tightly bound states and the effect of anharmonicity for higher lying states.

culated results over the different Zeeman states and deduce the corresponding time-of-arrival spectrum. It was found that the Zeeman state population distribution can play a significant role in the broadening of the resonances and can make the interpretation of experimental results very difficult or nearly impossible in the light of selective excitation measurements and the determination of characteristic parameters of the lattice. Hence the Zeeman state analysis measurements and simulations discussed in section 5.2 on page 169 offered us a convenient way to optimize and check our experimental configuration before carrying out experiments on selective parametric excitation in optical lattices.

5.3.6 Results of Experiment and Discussion

The experiments described in this section were carried out by Silvia Bergamini and presented in her thesis [41]. In the experiments a sample of atoms was prepared in a far-detuned lattice induced by light with a detuning to the low-frequency side of the $D2$ resonance of $\Delta = -(2000 \pm 100)\Gamma$ and a single-beam intensity of $I_{beam} = (400 \pm 50)$ mW/cm^2, giving a maximum light-shift of $170 \pm 15\, E_R$ and a harmonic-oscillator vibrational frequency for the lowest-lying potential surface of $\omega_0 = 2\pi \times (33 \pm 3)$ kHz. This was achieved by polarization-gradient cooling in a two-dimensional near-resonance lattice followed by adiabatic transfer to a spatially-coincident, far-off resonant lattice as in [70]. After a period of 10 ms, a time sufficient for all atoms not trapped after the adiabatic transfer to leave the interaction region, the intensity of the lattice light was modulated with a depth of 10% for a fixed period of 25 ms. This was achieved by modulating the power of the radio-frequency drive of an acousto-optic modulator placed in the path of the lattice beams.

At the end of the modulation phase, the lattice optical field was suddenly extinguished in less than 10 μs, using the acousto-optic modulator and an auxiliary shutter. The number of atoms remaining trapped in the lattice and their kinetic temperature were determined using a time-of-flight method. For this purpose, a thin sheet of light tuned close to resonance with the caesium D2 transition was located 6 cm below the trapping region and the absorption of this light by the atoms falling through the beam was recorded. Thus the temperature measured was in a single dimension, corresponding to the x–direction of our lattice (cf. figure 2.7 on page 69). However, owing to

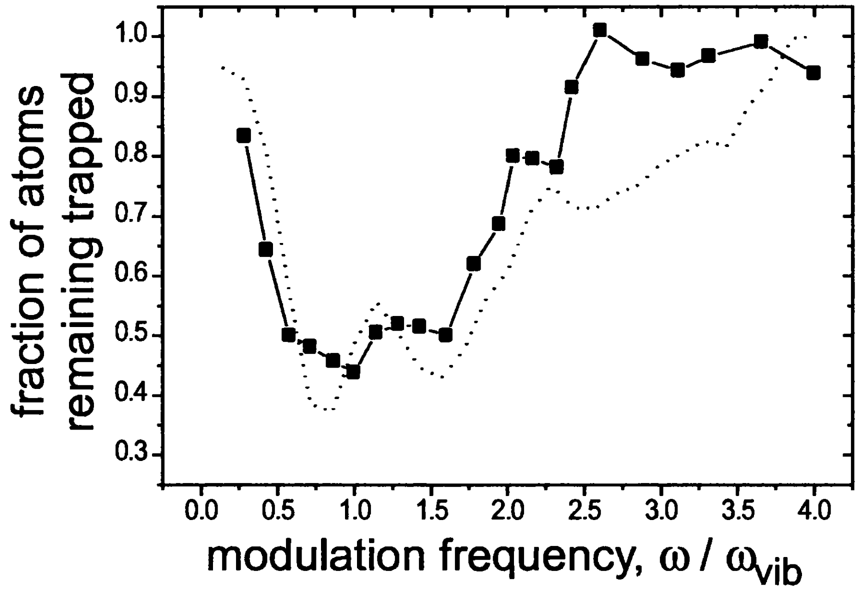

Figure 5.7: Comparison between experimental data and the predictions of numerical simulations for the modulation-induced population loss. The solid line shows, as a function of the modulation frequency, the measured number of atoms remaining in the lattice after a fixed period of 25 ms of modulation whilst the dotted line shows the result of the corresponding simulations.

the rotational symmetry of the lattice potential below the shoulder in the y-direction, we expected this temperature to be isotropic. Measurements were taken for a range of modulation frequencies from well below the mean harmonic-oscillator vibrational frequency of the atoms in the lattice to several times this frequency.

In figure 5.7, the measured fraction of atoms remaining in the lattice at the end of the modulation phase is plotted as a function of the modulation frequency and is compared with the fraction predicted by the numerical simulations. The classical theory of the harmonic oscillator predicts a reso-

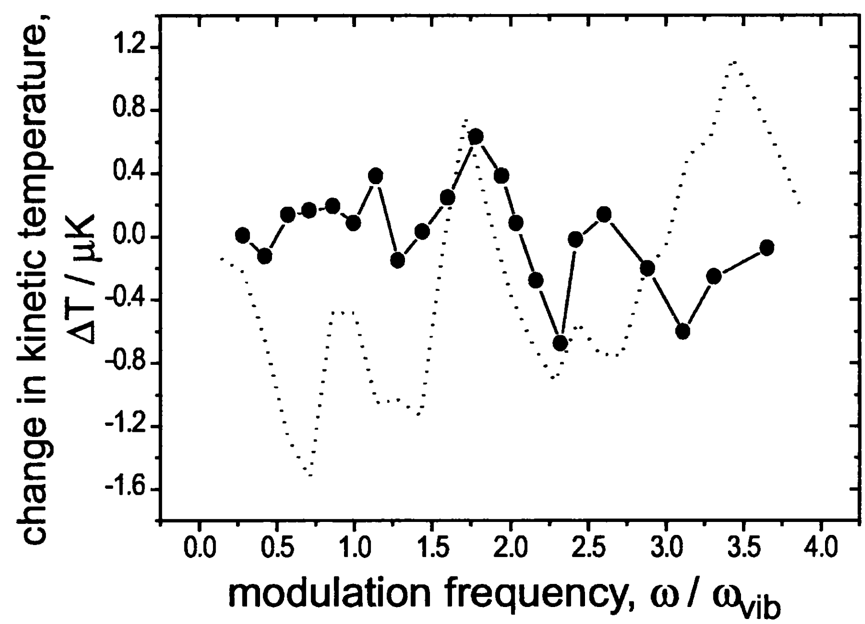

Figure 5.8: Comparison between experimental and simulation data for the modulation-induced heating. The data shown by the solid line depict, as a function of the modulation frequency, the change in the kinetic temperature of the atoms remaining in the lattice after a fixed period of 25 ms of modulation whilst the dotted line shows the result of the simulations.

nance in the loss rate of atoms at twice the vibrational frequency, $\omega \approx 2\omega_0$, and a secondary resonance at $\omega \approx \omega_0$. The data in figure 5.7 shows losses over a broad range of frequencies, with a width comparable to the resonance frequency itself. However, two resonances are just resolved, at frequencies, $\omega = 2\pi \times 35\,\text{kHz} \approx \omega_0$ and $\omega = 2\pi \times 58\,\text{kHz} \approx 1.7\omega_0$. The frequencies of these resonances do not agree with those predicted within the harmonic approximation, but are, however, in good agreement with those predicted by the anharmonic model. This follows from the fact that atoms in the lowest levels are partly excited to higher lying levels but are not lost (as would happen for a harmonic potential), while the most energetic atoms, which have a smaller excitation energy due to the anharmonicity come into resonance at a lower modulation frequency and are immediately excited out of the lattice. This explains why the resonance expected for $\omega = 2\omega_0$ in the harmonic approximation actually appears shifted to the low-frequency side. The asymmetry of the resonances is also well reproduced by the model and reinforces the role of anharmonicity in the loss rate of the atoms. Higher harmonic resonances are also predicted by the model, leading to the broad feature of width comparable to ω_0 seen in figure 5.7, at $\omega \simeq 3\omega_0$. Here the experimental data is not in good agreement with the simulations and the resonance is poorly resolved. This due to the fact that the simulation used to produce the graphs only considers transitions with $\Delta n \in \{0, \pm 2\}$ and neglects any other possible transitions.

The kinetic temperature of the sample of atoms remaining trapped at the end of the modulation phase was also measured as a function of the modulation frequency. Typical results are plotted in figure 5.8. Whilst the correlation in the frequency-dependence of the experimental and simulation data is poor, both numerical and experimental results do confirm that both cooling and heating of the remaining trapped atoms can be achieved for a suitable choice of the modulation frequency. This result is in agreement with those of [71], in which the exploitation of the anharmonicity of shallow traps in parametric excitation processes was proposed as a method to boost evaporative cooling. We ascribe differences between the data from the simulations and those from the experiment to the difficulty of quantifying precisely the inhomogenous broadening of the vibrational transitions due to the spatial profile of the lattice laser beams.

5.3.7 Conclusion

Numerical simulations and experiments aimed at studying the excitation dynamics in an intensity-modulated, two-dimensional optical lattice have been performed. The simulations were based on a perturbative approach that was applied in [59] to a one-dimensional, sinusoidal optical lattice and incorporated explicitly the effects of the anharmonicity of the lattice potential and the inhomogeneous broadening of the vibrational resonances. In particular, the experimental results show qualitative agreement with the numerical model, when the latter is modified to account for the effects of the broadening of the vibrational transitions arising from the anharmonicity of the lattice potential, the intensity-modulation itself and the non-uniform spatial intensity profile of the lattice optical beams. It is worth noting that the affect of a discrete distribution of resonance frequencies that would arise from atoms occupying differently light-shifted potential surfaces could not be well accounted for by the effective level-width model and monitored the distribution over Zeeman sub-states obtained on loading the far-detuned lattice in order to be able to eliminate this as a source of broadening in our experiments as discussed earlier. From the results, we infer that the anharmonicity of the lattice potential wells could enable the selective vibrational excitation of atoms originating in particular bound motional states of the lattice. This offers the prospect that vibrational-state selective excitation could be manipulated to prepare samples of atoms in a desired motional band of the lattice. However, for this to be achieved, the limitations arising from the various broadening mechanisms that have been investigated, would clearly have to be addressed and the inclusion of transitions encompassing a wider range of level pairs pursued.

Chapter 6

Conclusion

In this thesis I have investigated atoms in far-detuned optical lattices with semi-classical and quantum Monte Carlo simulations. Far-detuned systems offer the advantage of a reduced spontaneous scattering rate and hence less unwanted associated heating. They also have the advantages of long decoherence times and are only weakly coupled to their environment. Furthermore, these systems possess a low filling factor typical of optical lattices, which provides additional isolation of the atoms from each other. In these systems, perturbations to the atomic environment can be introduced in a controlled manner and studied individually. Hence far-detuned optical lattices are an ideal tool for quantum state preparation and control, quantum transport and quantum chaos studies and provide a rich and flexible system. Furthermore, through altering the beam geometry, beam intensity and beam polarization or by the action of external fields one can control depth, shape and periodicity of the trapping potential. Being able to control and manipulate neutral atoms in optical lattices provides the basic requirements to implement quantum computational schemes in these system, as was suggested by several groups [31]. Tools to manipulate and read-out q-bits for each atom separately have been discussed in the literature recently [72, 73]. The similarity to condensed matter periodic structures, albeit on an entirely different length scale, that of the optical wavelength, allows the investigation of solid state physics problems in a context of much more favourable time scales. Hence these far-detuned systems provide an ideal starting point for quantum state preparation based on a resolved-sideband Raman cooling scheme [42]. This research aimed to optimize the preparation of a large fraction of atoms in the vibrational ground-state of the 2D lattice and get a better and detailed understanding of experimental results.

I now provide a brief chapter by chapter summary of the contents of this thesis. Chapter 1 discusses the principles of laser cooling and provides a short historical overview. The atom-light interaction and light-induced forces exploited in laser cooling are introduced. This is followed by a discussion of the principles of Doppler cooling, a Magneto-Optical Trap (MOT) and Sisyphus polarization-gradient cooling.

After having discussed the theoretical background of laser cooling, Chapter 2 provides an introduction to optical lattices and their properties. First the light-shift operator in the near and far-detuned regime is deduced and the advantages of non-dissipative optical lattices discussed. Examples of lattices in one, two and three dimensions are deduced from their lattice beam configuration. Having derived the form of the optical potential allows us to calculate the band-structure of the lattice. The rest of the chapter is dedicated to a discussion of the population distribution of the atoms over the vibrational levels of the lattice taking the anharmonicity of the lattice into account.

Chapter 3 introduces the concept of resolved-sideband Raman cooling in two and three dimensions. The functional form of the Raman coupling is deduced using the formalism described in [42] and a new scheme for cooling in 3D is suggested. The three dimensional case is especially interesting in connection with atomic fountains and atomic clocks.

Chapters 1 to 3 provide the necessary tools to implement QMCWF simulations of resolved-sideband Raman cooling in a far-detuned optical lattice, and this is thoroughly discussed in chapter 4. First, a theoretical system is introduced which includes all the necessary physics to model resolved-sideband Raman cooling. The second part of the chapter discusses the results of our QMCWF simulations and shows for the first time the influence of the quantum Zeno effect on the efficiency of resolved-sideband Raman cooling and the choice of experimental parameters. Furthermore, a procedure for how to suppress the impact of the quantum Zeno effect which leads to most favourable populations in the vibrational ground-state of an optical lattice is presented.

Chapter 5 discusses diagnostic tools for atoms in optical lattices, Zeeman state analysis and parametric excitation. Zeeman state analysis is a useful tool to monitor the population distribution of atoms over the different Zeeman sub-states and quantify the overall magnetization of an atomic sample. It was a useful tool to check, that a significant fraction of atoms ended up in the stretched states $|F=4, m=\pm 4\rangle$. This provided us with a more favourable starting population for resolved-sideband Raman cooling to either of the $|F=4, m=\pm 4\rangle$ vibrational ground states. In this manner, the overall efficiency of our quantum state preparation experiments was improved.

The second part of the chapter is dedicated to an investigation of parametric excitation in optical lattices. Perturbative simulations implemented in this chapter allowed the study of the effects of anharmonicity of the optical potential and the effects of non-uniform intensity profiles of the lattice beams. Contrary to the harmonic case these cause a significant spreading of the vibrational resonances. These simulations are also used to simulate heating induced by intensity fluctuations in the laser beams. It emerged that they are reasonably low for atoms in far-detuned optical lattices and do not affect the efficiency of sideband cooling significantly.

In conclusion, this thesis presents an extensive study of neutral atoms in far-detuned optical lattices using theoretical models to simulate and better understand their behaviour. The simulations were aimed at optimizing the efficiency of our resolved-sideband Raman cooling experiments. An interesting by-product from this investigation was the first observation of the influence of the quantum Zeno effect on the efficiency of this quantum state preparation technique. Furthermore, an original three dimensional scheme to implement sideband cooling was suggested, of which the experimental realisation could be used to improve the accuracy of atomic clocks and the efficiency of atomic fountains which are important in high precision measurements [74]. Thus the conclusions of this work open up the possibility of performing a wide range of experiments to investigate coherent manipulation of single quantum states using adiabatic rapid passage, which is closely related to the method of resolved-sideband Raman cooling as it uses the same coherent coupling. Eventually further investigations into this area may open up the way to controlled engineering of individual quantum states and to useful techniques for quantum computation.

Appendix A

Caesium Data

A.1 Spectroscopic Properties

The following table contains data on the D_2 line of caesium used for the laser cooling experiments of this thesis. Further data is available in reference [75].

Quantity	Symbol	Value	Unit
wavelength (vacuum)	λ	852.347	nm
wavevector	k	$2\pi \times 1.17 \times 10^6$	m^{-1}
excited state lifetime	τ	30.5	ns
natural linewidth	Γ	$2\pi \times 5.22$	MHz
saturation intensity	I_{sat}	1.12	mWcm^{-2}
recoil energy	E_{Rec}	1.37×10^{-30}	J
recoil frequency	ν_{Rec}	2.07	kHz
recoil velocity	v_{Rec}	3.5	mms^{-1}
recoil temperature	T_{Rec}	198	nK
Doppler temperature	T_D	125	μK
Zeeman shift $6^2S_{1/2}(F=4)$		$+351m_F$ $+0.170m_F$	kHz/G E_{Rec}/mG
Zeeman shift $6^2P_{3/2}(F'=5)$		$+560m_{F'}$ $+0.271m_{F'}$	kHz/G E_{Rec}/mG

Table A.1: Caesium $6^2S_{1/2} \rightarrow 6^2P_{3/2}$ transition spectroscopic data.

A.2 Physical Properties

The next table is a summary of useful physical properties of caesium.

Quantity	Symbol	Value	Unit
mass	m_{Cs}	2.207×10^{-25}	kg
atomic number	Z	55	
melting point	T_m	28.44	°C
boiling point	T_b	671	°C

Table A.2: Caesium Physical data

A.3 Other data

A detailed description of the level scheme, transition strengths and is available in reference [75] and [22].

A.4 Clebsch-Gordan Coefficients

J_e	-5	-4	-3	-2	-1	0	1	2	3	4	5
-4	1	0.447214	0.149071	0	0	0	0	0	0	0	0
-3	0	0.894427	0.596285	0.258199	0	0	0	0	0	0	0
-2	0	0	0.788811	0.68313	0.365148	0	0	0	0	0	0
-1	0	0	0	0.68313	0.730297	0.471405	0	0	0	0	0
0	0	0	0	0	0.57735	0.745356	0.57735	0	0	0	0
1	0	0	0	0	0	0.471405	0.730297	0.68313	0	0	0
2	0	0	0	0	0	0	0.365148	0.68313	0.788811	0	0
3	0	0	0	0	0	0	0	0.258199	0.596285	0.894427	0
4	0	0	0	0	0	0	0	0	0.149071	0.447214	1
J_g											

Table A.3: This table shows the Clebsch-Gordan coefficients for $J_g = 4 \leftrightarrow J_e = 5$.

Appendix B

Supplements to the derivation of the light-shift operator

This appendix supplements the derivation of the light-shift operator in the near-detuned limit in section 2.1 on page 37. Each supplement is referenced in the corresponding section in the main text.

B.1 Supplement 1

$$
\begin{aligned}
\left[\hat{\mathbf{H}},\hat{\varrho}\right] &= \hat{\mathbf{H}}\hat{\varrho} - \hat{\varrho}\hat{\mathbf{H}} \\
&= \begin{pmatrix} \hat{\mathrm{a}}_1 & \hat{\mathrm{a}}_2 \\ \hat{\mathrm{a}}_3 & \hat{\mathrm{a}}_4 \end{pmatrix}
\end{aligned}
$$

$$
\begin{aligned}
\hat{\mathbf{H}}\hat{\varrho} &= \begin{pmatrix} \hat{\mathbf{H}}_{gg} & \hat{\mathbf{H}}_{ge} \\ \hat{\mathbf{H}}_{eg} & \hat{\mathbf{H}}_{ee} \end{pmatrix} \begin{pmatrix} \hat{\varrho}_{gg} & \hat{\varrho}_{ge} \\ \hat{\varrho}_{eg} & \hat{\varrho}_{ee} \end{pmatrix} \\
&= \begin{pmatrix} \hat{\mathbf{H}}_{gg}\hat{\varrho}_{gg} + \hat{\mathbf{H}}_{ge}\hat{\varrho}_{eg} & \hat{\mathbf{H}}_{gg}\hat{\varrho}_{ge} + \hat{\mathbf{H}}_{ge}\hat{\varrho}_{ee} \\ \hat{\mathbf{H}}_{eg}\hat{\varrho}_{gg} + \hat{\mathbf{H}}_{ee}\hat{\varrho}_{eg} & \hat{\mathbf{H}}_{eg}\hat{\varrho}_{ge} + \hat{\mathbf{H}}_{ee}\hat{\varrho}_{ee} \end{pmatrix} \qquad \text{(B.1)}
\end{aligned}
$$

$$
\begin{aligned}
\hat{\varrho}\hat{\mathbf{H}} &= \begin{pmatrix} \hat{\varrho}_{gg} & \hat{\varrho}_{ge} \\ \hat{\varrho}_{eg} & \hat{\varrho}_{ee} \end{pmatrix} \begin{pmatrix} \hat{\mathbf{H}}_{gg} & \hat{\mathbf{H}}_{ge} \\ \hat{\mathbf{H}}_{eg} & \hat{\mathbf{H}}_{ee} \end{pmatrix} \\
&= \begin{pmatrix} \hat{\varrho}_{gg}\hat{\mathbf{H}}_{gg} + \hat{\varrho}_{ge}\hat{\mathbf{H}}_{eg} & \hat{\varrho}_{gg}\hat{\mathbf{H}}_{ge} + \hat{\varrho}_{ge}\hat{\mathbf{H}}_{ee} \\ \hat{\varrho}_{eg}\hat{\mathbf{H}}_{gg} + \hat{\varrho}_{ee}\hat{\mathbf{H}}_{eg} & \hat{\varrho}_{eg}\hat{\mathbf{H}}_{ge} + \hat{\varrho}_{ee}\hat{\mathbf{H}}_{ee} \end{pmatrix} \qquad \text{(B.2)}
\end{aligned}
$$

$$
\begin{aligned}
\therefore \hat{\mathrm{a}}_1 &= \left[\hat{\mathbf{H}}_{gg},\hat{\varrho}_{gg}\right] + \hat{\mathbf{H}}_{ge}\hat{\varrho}_{eg} - \hat{\varrho}_{ge}\hat{\mathbf{H}}_{eg} \\
&= \hat{\mathbf{H}}_{ge}\hat{\varrho}_{eg} - \hat{\varrho}_{ge}\hat{\mathbf{H}}_{eg} && \text{(B.3)} \\
\hat{\mathrm{a}}_2 &= \hat{\mathbf{H}}_{gg}\hat{\varrho}_{ge} + \hat{\mathbf{H}}_{ge}\hat{\varrho}_{ee} - \hat{\varrho}_{gg}\hat{\mathbf{H}}_{eg} - \hat{\varrho}_{ge}\hat{\mathbf{H}}_{ee} && \text{(B.4)} \\
\hat{\mathrm{a}}_3 &= \hat{\mathbf{H}}_{eg}\hat{\varrho}_{gg} + \hat{\mathbf{H}}_{ee}\hat{\varrho}_{eg} - \hat{\varrho}_{eg}\hat{\mathbf{H}}_{gg} - \hat{\varrho}_{ee}\hat{\mathbf{H}}_{eg} && \text{(B.5)} \\
\hat{\mathrm{a}}_4 &= \left[\hat{\mathbf{H}}_{ee},\hat{\varrho}_{ee}\right] + \hat{\mathbf{H}}_{eg}\hat{\varrho}_{ge} - \hat{\varrho}_{eg}\hat{\mathbf{H}}_{ge} \\
&= \hat{\mathbf{H}}_{eg}\hat{\varrho}_{ge} - \hat{\varrho}_{eg}\hat{\mathbf{H}}_{ge} && \text{(B.6)}
\end{aligned}
$$

The last step in equations B.3 and B.6 follows, since 2.9 and 2.13 are hermitian matrices,.i.e. $\left[\hat{\mathbf{H}}_{gg}, \hat{\varrho}_{gg}\right] = 0$ and $\left[\hat{\mathbf{H}}_{ee}, \hat{\varrho}_{ee}\right] = 0$. To get a better understanding for the terms involved in the above expressions, the formalism is apply to a two level atom with a ground state $|g\rangle$ and an excited state $|e\rangle$. The two-level atoms is assumed to have a similar Hamiltonian as used in the rapid adiabatic passage formalism, where two levels are coupled with a coupling strength of V and the ground and excited state have energies E_g and E_e respectively. This gives for the above matrices

$$\hat{\varrho} = \begin{pmatrix} \hat{\varrho}_{gg} & \hat{\varrho}_{ge} \\ \hat{\varrho}_{eg} & \hat{\varrho}_{ee} \end{pmatrix} \propto \begin{pmatrix} |g\rangle\langle g| & |g\rangle\langle e| \\ |e\rangle\langle g| & |e\rangle\langle e| \end{pmatrix}$$

$$\hat{\mathbf{H}} = \begin{pmatrix} \hat{\mathbf{H}}_{gg} & \hat{\mathbf{H}}_{ge} \\ \hat{\mathbf{H}}_{eg} & \hat{\mathbf{H}}_{ee} \end{pmatrix} = \begin{pmatrix} E_g & V \\ V^* & E_e \end{pmatrix}$$

$$\left[\hat{\mathbf{H}},\hat{\varrho}\right]=\hat{\mathbf{H}}\hat{\varrho}-\hat{\varrho}\hat{\mathbf{H}}$$

$$\hat{\mathbf{H}}\hat{\varrho}=\begin{pmatrix}\hat{\mathbf{H}}_{gg}\hat{\varrho}_{gg}+\hat{\mathbf{H}}_{ge}\hat{\varrho}_{eg} & \hat{\mathbf{H}}_{gg}\hat{\varrho}_{ge}+\hat{\mathbf{H}}_{ge}\hat{\varrho}_{ee}\\ \hat{\mathbf{H}}_{eg}\hat{\varrho}_{gg}+\hat{\mathbf{H}}_{ee}\hat{\varrho}_{eg} & \hat{\mathbf{H}}_{eg}\hat{\varrho}_{ge}+\hat{\mathbf{H}}_{ee}\hat{\varrho}_{ee}\end{pmatrix} \tag{B.7}$$

$$\propto\begin{pmatrix}E_g\left|g\right\rangle\left\langle g\right|+V\left|e\right\rangle\left\langle g\right| & E_g\left|g\right\rangle\left\langle e\right|+V\left|e\right\rangle\left\langle e\right|\\ V^*\left|g\right\rangle\left\langle g\right|+E_e\left|e\right\rangle\left\langle g\right| & V^*\left|g\right\rangle\left\langle e\right|+E_e\left|e\right\rangle\left\langle e\right|\end{pmatrix} \tag{B.8}$$

$$\hat{\varrho}\hat{\mathbf{H}}=\begin{pmatrix}\hat{\varrho}_{gg}\hat{\mathbf{H}}_{gg}+\hat{\varrho}_{ge}\hat{\mathbf{H}}_{eg} & \hat{\varrho}_{gg}\hat{\mathbf{H}}_{ge}+\hat{\varrho}_{ge}\hat{\mathbf{H}}_{ee}\\ \hat{\varrho}_{eg}\hat{\mathbf{H}}_{gg}+\hat{\varrho}_{ee}\hat{\mathbf{H}}_{eg} & \hat{\varrho}_{eg}\hat{\mathbf{H}}_{ge}+\hat{\varrho}_{ee}\hat{\mathbf{H}}_{ee}\end{pmatrix} \tag{B.9}$$

$$\propto\begin{pmatrix}E_g\left|g\right\rangle\left\langle g\right|+V^*\left|g\right\rangle\left\langle e\right| & V\left|g\right\rangle\left\langle g\right|+E_e\left|g\right\rangle\left\langle e\right|\\ E_g\left|e\right\rangle\left\langle g\right|+V^*\left|e\right\rangle\left\langle e\right| & V\left|e\right\rangle\left\langle g\right|+E_e\left|e\right\rangle\left\langle e\right|\end{pmatrix} \tag{B.10}$$

$$\left[\hat{\mathbf{H}},\hat{\varrho}\right]=\hat{\mathbf{H}}\hat{\varrho}-\hat{\varrho}\hat{\mathbf{H}}$$

$$=\begin{pmatrix}c_1 & c_2\\ c_3 & c_4\end{pmatrix} \tag{B.11}$$

$$c_1=V\left|e\right\rangle\left\langle g\right|-V^*\left|g\right\rangle\left\langle e\right| \tag{B.12}$$

$$c_2=\left(E_g-E_e\right)\left|g\right\rangle\left\langle e\right|+V\left(\left|e\right\rangle\left\langle e\right|-\left|g\right\rangle\left\langle g\right|\right) \tag{B.13}$$

$$c_3=V^*\left(\left|g\right\rangle\left\langle g\right|-\left|e\right\rangle\left\langle e\right|\right)+\left(E_e-E_g\right)\left|e\right\rangle\left\langle g\right| \tag{B.14}$$

$$c_4=V^*\left|g\right\rangle\left\langle e\right|-V\left|e\right\rangle\left\langle g\right| \tag{B.15}$$

This ends the example.

B.2 Supplement 2

This section supplements the deduction of the steady state ground state density matrix 2.1 after the excited state and its coherences were eliminated. The ground state density matrix is then given by

$$\frac{d\hat{\boldsymbol{\varrho}}_{gg}}{dt} = -\frac{i}{\hbar}\left\{\hat{\mathbf{H}}_{ge}\,\hat{\boldsymbol{\varrho}}_{eg} - \hat{\boldsymbol{\varrho}}_{ge}\,\hat{\mathbf{H}}_{eg}\right\} + \left(\frac{d\hat{\boldsymbol{\varrho}}}{dt}\right)_{\textbf{relax}} \tag{B.16}$$

$$\approx \frac{i}{\hbar}\left\{\left(\mathbf{d}^- \cdot \mathbf{E}^-\right)\tilde{\boldsymbol{\varrho}}_{eg} - \tilde{\boldsymbol{\varrho}}_{ge}\left(\mathbf{d}^+ \cdot \mathbf{E}^+\right)\right\} + \left(\frac{d\hat{\boldsymbol{\varrho}}}{dt}\right)_{\textbf{relax}} \tag{B.17}$$

$$\begin{aligned} =&\frac{i}{\hbar}\Big\{ \left(\mathbf{d}^- \cdot \mathbf{E}^-\right)\frac{1}{\hbar\left(\Delta + \frac{i\Gamma}{2}\right)}\left\{-\left(\mathbf{d}^+ \cdot \mathbf{E}^+\right)\hat{\boldsymbol{\varrho}}_{gg} + \hat{\boldsymbol{\varrho}}_{eg}\left(\mathbf{d}^+ \cdot \mathbf{E}^+\right)\right\} \\ &+ \frac{1}{\hbar\left(\Delta - \frac{i\Gamma}{2}\right)}\left\{-\left(\mathbf{d}^- \cdot \mathbf{E}^-\right)\hat{\boldsymbol{\varrho}}_{ee} + \hat{\boldsymbol{\varrho}}_{gg}\left(\mathbf{d}^- \cdot \mathbf{E}^-\right)\right\}\left(\mathbf{d}^- \cdot \mathbf{E}^-\right)\Big\} \\ &+ \left(\frac{d\hat{\boldsymbol{\varrho}}}{dt}\right)_{\textbf{relax}} \end{aligned} \tag{B.18}$$

$$\begin{aligned} =&\frac{i}{\hbar}\Big\{\frac{1}{\hbar\left(\Delta + \frac{i\Gamma}{2}\right)}\left(\mathbf{d}^- \cdot \mathbf{E}^-\right)\left(\mathbf{d}^+ \cdot \mathbf{E}^+\right)\hat{\boldsymbol{\varrho}}_{gg} \\ &+ \frac{1}{\hbar\left(\Delta + \frac{i\Gamma}{2}\right)}\left(\mathbf{d}^- \cdot \mathbf{E}^-\right)\hat{\boldsymbol{\varrho}}_{ee}\left(\mathbf{d}^+ \cdot \mathbf{E}^+\right) \\ &- \frac{1}{\hbar\left(\Delta - \frac{i\Gamma}{2}\right)}\left(\mathbf{d}^- \cdot \mathbf{E}^-\right)\hat{\boldsymbol{\varrho}}_{ee}\left(\mathbf{d}^+ \cdot \mathbf{E}^+\right) \\ &+ \frac{1}{\hbar\left(\Delta - \frac{i\Gamma}{2}\right)}\hat{\boldsymbol{\varrho}}_{gg}\left(\mathbf{d}^- \cdot \mathbf{E}^-\right)\left(\mathbf{d}^+ \cdot \mathbf{E}^+\right)\Big\} \\ &+ \left(\frac{d\hat{\boldsymbol{\varrho}}}{dt}\right)_{\textbf{relax}} \end{aligned} \tag{B.19}$$

$$
\begin{aligned}
&= -\frac{i}{\hbar^2}\Big\{\frac{1}{\left(\Delta+\frac{i\Gamma}{2}\right)}\left(\mathbf{d}^-\cdot\mathbf{E}^-\right)\left(\mathbf{d}^+\cdot\mathbf{E}^+\right)\hat{\varrho}_{gg} \\
&\quad -\frac{1}{\left(\Delta-\frac{i\Gamma}{2}\right)}\hat{\varrho}_{gg}\left(\mathbf{d}^-\cdot\mathbf{E}^-\right)\left(\mathbf{d}^+\cdot\mathbf{E}^+\right)\Big\} \\
&\quad +\left(\frac{d\hat{\varrho}}{dt}\right)_{\text{relax}}
\end{aligned} \tag{B.20}
$$

$$
\begin{aligned}
\frac{d\hat{\varrho}_{gg}}{dt} &= -\frac{i}{\hbar^2}\Big\{\left(\frac{\left(\Delta-\frac{i\Gamma}{2}\right)}{\Delta^2+\frac{\Gamma^2}{4}}\right)\left(\mathbf{d}^-\cdot\mathbf{E}^-\right)\left(\mathbf{d}^+\cdot\mathbf{E}^+\right)\hat{\varrho}_{gg} \\
&\quad -\left(\frac{\left(\Delta+\frac{i\Gamma}{2}\right)}{\Delta^2+\frac{\Gamma^2}{4}}\right)\hat{\varrho}_{gg}\left(\mathbf{d}^-\cdot\mathbf{E}^-\right)\left(\mathbf{d}^+\cdot\mathbf{E}^+\right)\Big\} \\
&\quad +\left(\frac{d\hat{\varrho}}{dt}\right)_{\text{relax}}
\end{aligned} \tag{B.21}
$$

where we have rationalized the denominators in the fractions and used the fact that

$$
\begin{aligned}
&\left(\frac{1}{\hbar\left(\Delta+\frac{i\Gamma}{2}\right)}-\frac{1}{\hbar\left(\Delta-\frac{i\Gamma}{2}\right)}\right)\left(\mathbf{d}^-\cdot\mathbf{E}^-\right)\hat{\varrho}_{ee}\left(\mathbf{d}^+\cdot\mathbf{E}^+\right) \\
&= \frac{\left(\mathbf{d}^-\cdot\mathbf{E}^-\right)\hat{\varrho}_{ee}\left(\mathbf{d}^+\cdot\mathbf{E}^+\right)}{\hbar}\left(\frac{\left(\Delta-\frac{i\Gamma}{2}\right)-\left(\Delta+\frac{i\Gamma}{2}\right)}{\Delta^2+\frac{\Gamma^2}{4}}\right) \\
&= 0.
\end{aligned} \tag{B.22}
$$

Appendix C

Pauli Spin matrices

The Pauli spin matrices are given by

$$\hat{\boldsymbol{\sigma}}_x = \begin{pmatrix} 0 & 1 \\ 1 & 0 \end{pmatrix} \quad \hat{\boldsymbol{\sigma}}_y = \begin{pmatrix} 0 & -i \\ i & 0 \end{pmatrix} \quad \hat{\boldsymbol{\sigma}}_z = \begin{pmatrix} 1 & 0 \\ 0 & -1 \end{pmatrix} \tag{C.1}$$

Using the spherical basis they can be written as

$$\hat{\boldsymbol{\sigma}}_+ = -\frac{\hat{\boldsymbol{\sigma}}_x + i\hat{\boldsymbol{\sigma}}_y}{\sqrt{2}} = -\frac{1}{2}\begin{pmatrix} 0 & 2 \\ 0 & 0 \end{pmatrix} \tag{C.2}$$

$$\hat{\boldsymbol{\sigma}}_- = \frac{\hat{\boldsymbol{\sigma}}_x - i\hat{\boldsymbol{\sigma}}_y}{\sqrt{2}} = \frac{1}{2}\begin{pmatrix} 0 & 0 \\ 2 & 0 \end{pmatrix} \tag{C.3}$$

$$\hat{\boldsymbol{\sigma}}_\pi = \hat{\boldsymbol{\sigma}}_z \tag{C.4}$$

The Pauli spin matrices and the identity matrix form a complete set and form a basis for the vector space of all 2×2 matrices.

Appendix D

The Quantum Zeno Effect

This appendix gives a short introduction to the quantum Zeno effect. The name origins from from Zeno of Elean a Greek philosophy living in southern Italy. The main source of knowledge about him and his lives comes from the dialogue *Parmenides* written by Plato. A more comprehensive summary of his life and work can be found in [76]. He was famed for his paradoxes and conundrums. One of them was that motion doesn't exist. Zeno said that [77]

> There is no motion because that which is moved must arrive at the middle of its course before it arrives at the end.

He argued that because at any given point in an arrow's flight, it must have transversed the midpoint, it actually can never move.

People had Zeno in mind when they studied the inhibition of the decay of a unstable quantum system due to sufficiently frequent observation or measurements on it. It was first proposed by Misra and Sudarshan [78] in 1977 and coined the Zeno effect. It followed the early work of Khalfin [79] and Fonda [80]. Colloquially, this can be phrased as *a watched pot never boils* [81].

Recently also the opposite of the quantum Zeno effect was proposed and demonstrated, the anti-Zeno effect. The anti-Zeno effect is described in [82]. The experiment undertaken by Raizen *et al.* [83] showed both the quantum Zeno and anti-Zeno effect using sodium atoms trapped in an accelerated far-detuned standing-wave of light by studying the escape via tunnelling. It was the first demonstration of both the Zeno and anti-Zeno effects by repeated measurements. Recent theoretical and experimental developments have initiated new research on this effect. An important motivation to study the Zeno and anti-Zeno effect is to elucidate one of quantum computing's biggest problems, errors due to the decay of coherence.

Appendix E

Derivation of the Effective Spectral Density

In this appendix the method to deduce the effective spectral density S_{eff} used in the parametric excitation simulations is described and explicit expression for the effective width σ_{eff} and effective frequency ω_{eff} are provided.

The first step is to assume a Gaussian distribution $S_i(\omega)$ for the density of states associated with a level $|i\rangle$ having an energy of $E_i = \hbar\omega_i$. This can be cast in functional form as

$$S_i(\omega) = \frac{1}{\sqrt{2\pi}\,\sigma_i} e^{-\frac{(\hbar\omega - E_i)^2}{2(\hbar\sigma_i)^2}} \tag{E.1}$$

where the Gaussian distribution is centred around $\hbar\omega_i$ having a frequency spread of σ_i. The effective spectral density S_{eff} associated with a transition between the states $|i\rangle \rightarrow |f\rangle$ can then be obtained by considering the convolution of $S_i(\omega)$ with $S_f(\omega)$.

The parametric excitation is provided by a monochromatic excitation source in our experiment. It can be included in the model by assuming also a Gaussian density distribution for its spectral density and convolution it with the convolution of $S_i(\omega)$ and $S_f(\omega)$. It is defined in that way that once integrated over all frequencies it yields the square of the intensity of the modulation source (cf. equation 5.33 on page 186).

Hence the net result is a effective spectral density $S_{\mathrm{eff}}(\omega_{if})$ given by

$$S_{\mathrm{eff}}(\omega) = S_0 \exp - \frac{(\omega - \omega_{\mathrm{eff}})^2}{2\sigma_{\mathrm{eff}}^2} \tag{E.2}$$

where

$$\sigma_{\mathrm{eff}}^2 = \sigma_{\mathrm{i}}^2 + \sigma_{\mathrm{f}}^2 + \sigma_0^2 \tag{E.3}$$

$$\omega_{\mathrm{eff}} = \omega_{\mathrm{mod}} - (\omega_{\mathrm{f}} - \omega_{\mathrm{i}}) \tag{E.4}$$

Appendix F

Magnetic Field of a Square Coil

To provide a strong magnetic field gradient across the trapping region two square coils in anti-Helmholtz configuration are used. The easiest way to calculate the magnetic field of a square coil is to use the Biot-Savart law,

$$d\mathbf{B} = \frac{\mu_0 \, I \, d\boldsymbol{\ell} \times \mathbf{r}}{4\pi \hat{\mathbf{r}}^2} \tag{F.1}$$

where $d\mathbf{B}$ is the magnetic field due to the current element $I \, d\boldsymbol{\ell}$ induced at a point with relative position vector $\mathbf{r}$ from the current element. μ_0 is the free space permeability and is defined to have the value $\mu_0 \equiv 4\pi \times 10^{-7} \, \mathrm{Hm}^{-1}$. Using the Biot-Savardt law F.1 as given in [66] on page 170, the magnetic field of any circuit can be calculated by integrating around the loop, i.e.

$$\mathbf{B} = \oint_L \frac{\mu_0 \, I \, d\boldsymbol{\ell} \times \hat{\mathbf{r}}}{4\pi r^2} \tag{F.2}$$

A square coil can be thought of as being composed of 4 straight current-carrying finite wires along each side as shown in figure F.1. The magnetic

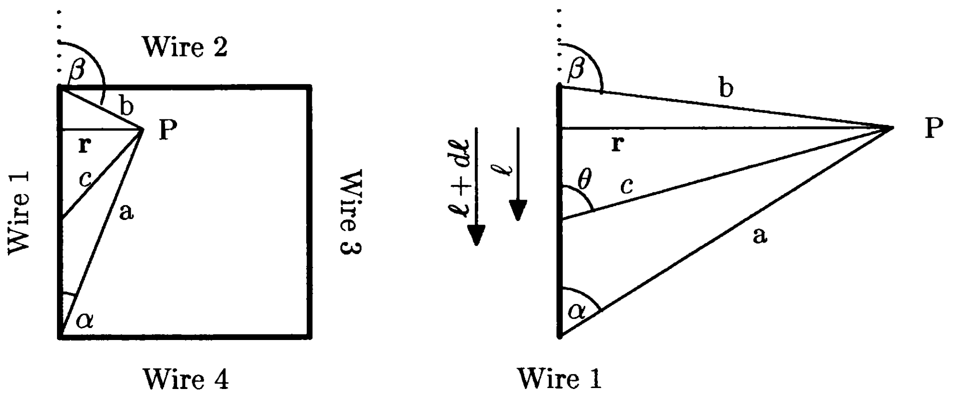

Coil 1: Front view

Coil 1: Side view

Figure F.1: The figure shows a schematic of a square coil composed of 4 straight current carrying wires. The magnetic field at a point P in space is can be calculated using the quantities angles α and β and the distance $|\mathbf{r}|$ relative to the the wire. The direction of the magnetic field vector is given by the Biot-Savart law to be $d\boldsymbol{\ell} \times \mathbf{r}$.

field of a straight current-carrying wire is deduced in [66] on page 172 to be

$$\mathbf{B} = \frac{\mu_0 I}{4\pi r}(\cos\beta - \cos\alpha)\frac{d\boldsymbol{\ell} \times \mathbf{r}}{|d\boldsymbol{\ell} \times \mathbf{r}|} \tag{F.3}$$

Four such wires are now connected into a square coil as shown on the left of figure F.1. With the help of the symbolic toolbox of Matlab the calculation of the magnetic field of a rectangular coil with arbitrary dimensions was implemented. The centre of the atomic cloud was chosen to be the origin. Then using a vectors in MatLab the two coils are created by four wires each and put a distance D away from the origin. Then by using simple vector algebra using equation F.3 the total magnetic field of two square coils can be calculated by summing up the contributions of each wire:

$$\mathbf{B} = \sum_i \mathbf{B}_i(\mathbf{r}_i) \tag{F.4}$$

where $\mathbf{B}_i(\mathbf{r}_i)$ is the induced magnetic field of wire i at a point $\mathbf{r}_i$ away from wire i. This set-up is shown in figure F.2.

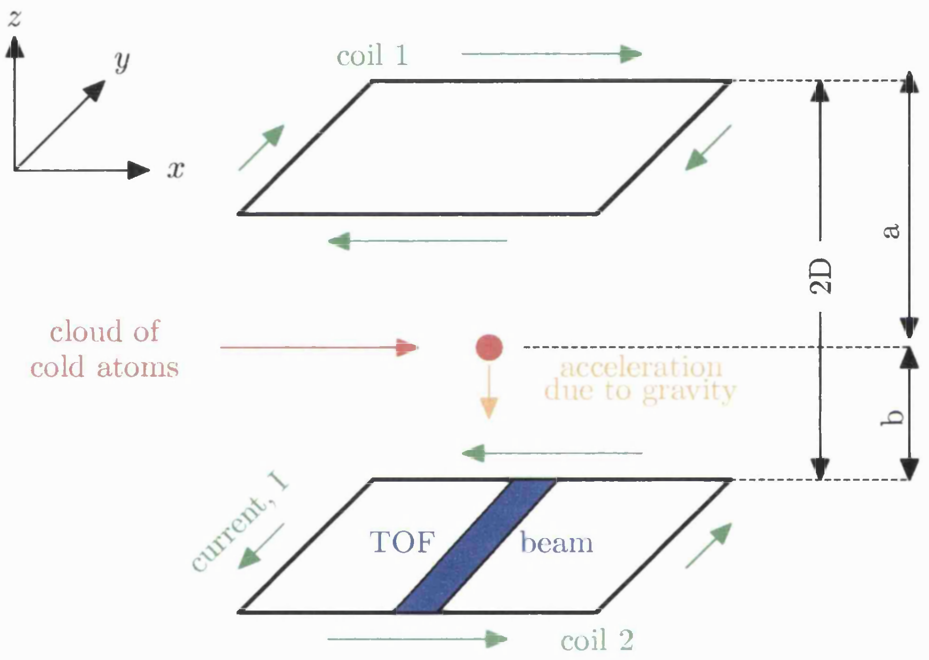

Figure F.2: The figure shows a schematic of a anti-Helmholtz square coil setup composed of two square coils a distance $2D$ apart. When the atoms are released from the optical lattice, they fall through a magnetic field gradient. Underneath the trapping region is a time of flight beam to measure the time of arrival for atoms in different m_f levels.

Bibliography

[1] D.R. Meacher. Optical lattices - crystalline structures bound by light. *Contemp. Phys.*, 39:329, 1998.

[2] P.S. Jessen and I.H. Deutsch. Optical lattices. *Adv. Atom. Mol. Opt. Phys.*, 37:95, 1996.

[3] G. Grynberg and C. Triché. Atoms in optical lattices. In A. Aspect, W. Barletta, and R. Bonifacio, editors, *Proceedings of the international school of physics Enrico Fermi, Course CXXI (1995)*, page 243. IOS Press, Amsterdam, 1996.

[4] L. Guidoni and P. Verkerk. Optical lattices: cold atoms ordered by light. *J. Opt. B: Quantum Semiclass. Opt.*, 1:R23, 1999.

[5] M.G. Prentiss. Bound by light. *Science*, 46:17, 1993.

[6] G.P. Collins. Three dimensional optical molasses binds a new type of crystal. *Physics Today*, page 17, 1993.

[7] Steve Rolston. Optical lattices. *Physics World*, 11:27, 1998.

[8] O. Morsch. Ein Baukasten für Quantensysteme. *Spektrum der Wissenschaft*, page 24, 1998.

[9] T.W. Hänsch and A.L. Schawlow. Cooling of gases by laser radiation. *Opt. Commun.*, 13:68, 1975.

[10] D. Wineland and H. Dehmelt. Proposed $10^{14}\Delta\nu < \nu$ laser fluorescence spectroscopy on Tl^+ mono-ion oscillator III. *Bull. Am. Phys. Soc.*, 20:637, 1975.

[11] S. Chu, L. Hollberg, J.E. Bjorkholm, A. Cable, and A. Ashkin. Three-dimensional viscous confinement and cooling of atoms by resonance radiation pressure. *Phys. Rev. Lett.*, 55:48, 1985.

[12] S. Chu, J.E. Bjorkholm, A. Ashkin, and A. Cable. Experimental observation of optically trapped atoms. *Phys. Rev. Lett.*, 57:314, 1986.

[13] A.L. Migdall, J.V. Prodan, W.D. Phillips, T.H. Bergeman, and H.J. Metcalf. First observation of magnetically trapped neutral atoms. *Phys. Rev. Lett.*, 54:2596, 1985.

[14] D.E. Pritchard, E.L. Raab, V. Bagnato, C.E. Wieman, and R.N. Watts. Light traps using spontaneous forces. *Phys. Rev. Lett.*, 57:310, 1986.

[15] A. Ashkin and J.P. Gordon. Stability of radiation-pressure particle traps: an optical Earnshaw theorem. *Opt. Lett.*, 8:511, 1983.

[16] E.L. Raab, M. Prentiss, A. Cable, S. Chu, and D.E. Pritchard. Trapping of neutral sodium atoms with radiation pressure. *Phys. Rev. Lett.*, 59:2631, 1987.

[17] P.D. Lett, R.N. Watts, C.I. Westbrook, W.D. Phillips, P.L. Gould, and H.J. Metcalf. Observation of atoms laser cooled below the Doppler limit. *Phys. Rev. Lett.*, 61:169, 1988.

[18] C. Cohen-Tannoudji and W.D. Phillips. New mechanisms for laser cooling. *Physics Today*, page 33, 1990.

[19] J. Dalibard and C. Cohen-Tannoudji. Laser cooling below the Doppler limit by polarization gradients. *J. Opt. Soc. Am. B*, 6:2023, 1989.

[20] P.J. Ungar, D.S. Weiss, E. Riis, and S. Chu. Optical molasses and multilevel atoms: theory. *J. Opt. Soc. Am. B*, 6:2058, 1989.

[21] P.D. Lett, W.D. Phillips, S.L. Rolston, C.E. Tanner, R.N. Watts, and C.I. Westbrook. Optical molasses. *J. Opt. Soc. Am. B*, 6:2084, 1989.

[22] Metcalf, Harold J. and Straten, Peter van. *Laser Cooling and Trapping.* Graduate Texts in Contemporary Physics. Springer, 1999.

[23] H. Metcalf and P. van der Straten. Cooling and trapping of neutral atoms. *Phys. Rep.*, 244:203, 1994.

[24] C. Cohen-Tannoudji. Atomic motion in laser light. Les Houches Summer School, Session LIII, 1990.

[25] C. Cohen-Tannoudji. Laser cooling and trapping of neutral atoms: theory. *Phys. Rep.*, 219:153, 1992.

[26] S. Stenholm. The semiclassical theory of laser cooling. *Rev. Mod. Phys.*, 58:699, 1986.

[27] M.B. Dahan, E. Peik, J. Reichel, Y. Castin, and C. Salomon. Bloch oscillations of atoms in an optical potential. *Phys. Rev. Lett.*, 76:4508, 1996.

[28] Q. Niu, X.-G. Zhao, G.A. Georgakis, and Raizen. M.G. Atomic landau-zener tunneling and Wannier-Stark ladders in optical potentials. *Phys. Rev. Lett.*, 76:4804, 1996.

[29] K.W. Madison, M.C. Fischer, and M.G. Raizen. Observation of the Wannier-Stark fan and the fractional ladder in an accelerated optical lattice. *Phys. Rev. A*, 60:R1767, 1999.

[30] C.F. Barucha, K.W. Madison, P.R. Morrow, S.R. Wilkinson, B. Sundaram, and M.G. Raizen. Observation of atomic tunneling from an accelerating optical potential. *Phys. Rev. A*, 55:R857, 1997.

[31] G.K. Brennen, C.M. Caves, P.S. Jessen, and I.H. Deutsch. Quantum logic gates in optical lattices. *Phys. Rev. Lett.*, 82:1060, 1999.

[32] H.-J. Briegel, T. Calarco, D. Jaksch, J.I. Cirac, and P. Zoller. Quantum computing with neutral atoms. *J. Mod. Opt.*, 47:415, 2000.

[33] B.G. Klappauf, Oskay. W.H., D.A. Steck, and M.G. Raizen. Experimental study of quantum dynamics in a regime of classical anomalous diffusion. *Phys. Rev. Lett.*, 81:4044, 1998.

[34] B. Brezger, T. Schulze, P.O. Schmidt, R. Mertens, T. Pfau, and J. Mlynek. Polarization gradient light masks in atom lithography. *Europhys. Lett.*, 46:148, 1999.

[35] W.D. Phillips. Atomic motion in laser light. Les Houches Summer School, Session LIII, 1990.

[36] O.R. Frisch. Experimenteller Nachweis des einsteinischen Strahlungsrückstosses. *Z. Phys.*, 86:42, 1933.

[37] C. Cohen-Tannoudji. Thèorie quantique du cycle de pompage optique. *Ann. Phys.*, 7:423, 1962.

[38] C. Monroe, W. Swann, H. Robinson, and C. Wieman. Very cold trapped atoms in a vapor cell. *Phys. Rev. Lett.*, 65:1571, 1990.

[39] I.H. Deutsch, J. Grodalski, and P.M. Alsing. Local dynamics of laser cooling in an optical lattice. *Phys. Rev. A*, 56:R1705, 1997.

[40] C. Cohen-Tannoudji. Manipulating atoms with photons. *Rev. Mod. Phys.*, 70:707, 1998.

[41] Silvia Bergamini. *Atoms in non-dissipative optical lattices.* PhD thesis, University College London, 2002.

[42] I.H. Deutsch and P.S. Jessen. Quantum-state control in optical lattices. *Phys. Rev. A*, 57(3):1972, 1998.

[43] D.R. Meacher, S. Guibal, C. Mennerat, J.-Y. Courtois, K.I. Petsas, and G. Grynberg. Paramagnetism in a caesium optical lattice. *Phys. Rev. Lett.*, 74(11):1958, 1995.

[44] D.L. Haycock, S.E. Hamann, G. Klose, G. Raithel, and P.S. Jessen. Enhanced laser cooling and state preparation in an optical lattice with a magnetic field. *Phys. Rev. A*, 57(2):R705, 1998.

[45] K.I. Petsas, A.B. Coates, and G. Grynberg. Crystallography of optical lattices. *Phys. Rev. A*, 50:5173, 1994.

[46] P. Verkerk, D.R. Meacher, A.B. Coates, J.-Y. Courtois, S. Guibal, B. Lounis, C Salomon, and G. Grynberg. Designing optical lattices: an investigation with caesium atoms. *Europhys. Lett.*, 26:171, 1994.

[47] N. Ashcroft and N. Mermin. *Solid State Physics.* Holt-Saunders International edition, 1981.

[48] S. Wolf, S.J. Oliver, and D.S. Weiss. Suppression of recoil heating by an optical lattice. *Phys. Rev. Lett.*, 85:4249, 2000.

[49] S.E. Hamann, D.L. Haycock, G. Klose, P.H. Pax, I.H. Deutsch, and P.S. Jessen. Resolved-sideband Raman cooling to the ground state of an optical lattice. *Phys. Rev. Lett.*, 80:4149, 1998.

[50] A.J. Kerman, V. Vuletić, C. Cheng, and S. Chu. Beyond optical molasses: 3d Raman sideband cooling of atomic caesium to high phase-space density. *Phys. Rev. Lett.*, 84:439, 2000.

[51] K. Mølmer, Y. Castin, and J. Dalibard. Monte-Carlo wave-function method in quantum optics. *J. Opt. Soc. Am. B*, 10:524, 1993.

[52] W.K. Woodgate. *Elementary Atomic Structure.* Oxford University Press, 2nd edition, 1986.

[53] Robert M. Ziff. Four-tap shift-register-sequence random-number generators. *Computers in Physics*, 4(12):385–392, 1998.

[54] S. Friebel, C.D. D'Andrea, J. Walz, M. Weitz, and T.W. Hänsch. CO_2-laser optical lattice with cold rubidium atoms. *Phys. Rev. A*, page R20, 1998.

[55] R. Jáuregui, N. Poli, G. Roati, and G. Modugno. Anharmonic parametric excitation in optical lattices. *Phys. Rev. A.*, 64(3):033403, 2001.

[56] T.A. Savard, K.M. O'Hara, and J.E. Thomas. Laser-noise-induced heating in far-off resonace optical traps. *Phys. Rev. A*, page R1095, 1997.

[57] C.W. Gardiner, J. Ye, H.C. Nagerl, and H.J Kimble. Evaluation of heating effects on atoms trapped in an optical trap. *Phys. Rev. A*, page 045801, 2000.

[58] M.F. Andersen, A. Kaplan, and N. Davidson. Echo spectroscopy and quantum stability of trapped atoms. *Phys. Rev. A*, 90:023001, 2003.

[59] R. J'auregui. Nonperturbative and perturbative treatments of parametric heating in atom traps. *Phys. Rev. A.*, page 053408, 2001.

[60] G. Raithel, W.D. Phillips, and S.L. Rolston. Magnetization and spin-flip dynamics of atoms in optical lattices. *Phys. Rev. A*, 58(4):R2660, 1998.

[61] R.P. Bertram, H. Merimeche, M. Mützel, H. Metcalf, D. Haubrich, and D. Meschede. Magnetic whispering-gallery mirror for atoms. *Phys. Rev. A*, 63:053405, 2001.

[62] T.M. Roach, H. Abele, M.G. Boshier, H.L. Grossman, K.P. Zetie, and E.A. Hinds. Realization of a magnetic mirror for cold atoms. *Phys. Rev. Lett.*, 75(4):629, 1995.

[63] W.G. Kaenders, F. Lison, I. Müller, A. Richter, R. Wynands, and D. Meschede. Refractive components for magnetic atom optics. *Phys. Rev. A*, 54(6):5067, 1996.

[64] E.A. Hinds, M.G. Boshier, and I.G. Hughes. Magnetic waveguide for trapping cold atom gases in two dimensions. *Phys. Rev. Lett.*, 80(4):645, 1998.

[65] G. Klose, G. Smith, and P.S. Jessen. Measuring the quantum state of a large angular momentum. *Phys. Rev. Lett.*, 86(21):4721, 2001.

[66] W.J. Duffin. *Electricity and Magnetism.* McGraw-Hill, 4th edition, 1990.

[67] B.H. Bransden and C.J. Joachain. *Physics of atoms and molecules.* Longman Scientific & Technical, 1st edition, 1991.

[68] M.E. Gehm, K.M. O'Hara, T.A. Savard, and J.E. Thomas. Dynamic of noise-induced heating in atom traps. *Phys. Rev. A.*, page 3914, 1998.

[69] S Bergamini, S.P. Winklbauer, P.H. Jones, H.E. Saunders-Singer, and D.R. Meacher. Selective parametric excitation of atoms in a two-dimensional non-dissipative optical lattices. *submitted for publication*, 2003.

[70] D. L. Haycock, S. E. Hamann, G. Klose, and P.S. Jessen. Atom trapping in deeply bound states of a far-off-resonance optical lattice. *Phys. Rev. A*, 55:R3991, 1998.

[71] N. Poli, R.J. Brecha, G. Roati, and G. Modugno. Cooling atoms in an optical trap by selective parametric excitation. *Phys. Rev. A*, page 021401, 2002.

[72] I. E. Protsenko, G. Reymond, N. Schlosser, and P. Grangier. Operation of a quantum phase gate using neutral atoms in microscopic dipole traps. *Phys. Rev. A*, 65:52301, 2002.

[73] N. Schlosser, G. Reymond, I. Protsenko, and P. Grangier. Sub-poissonian loading of single atoms in a microscopic dipole trap. *Nature (London)*, 411:1024, 2001.

[74] G. Santarelli, A. Clairon, and C. Salomon. Quantum projection noise in an atomic fountain: A high stability caesium frequency standard. *Phys. Rev. Lett.*, 82(7):4619, 1999.

[75] george.ph.utexas.edu/ dsteck/alkalidate/cesiumnumbers.pdf.

[76] www-gap.dcs.st-and.ac.uk/ history/Mathematicians/Zeno_of_Elea.html.

[77] T.L. Heath. *A History of Greek Mathematics*, volume 1. Oxford, 1931.

[78] B. Misra and E.C.G. Sudarshan. *J. Math. Phys*, 18:756, 1977.

[79] L.A. Khalfin. *JEPT Lett.*, 8:65, 1968.

[80] L. Fonda, G.C. Ghirardi, A. Rimin, and T. Weber. Frequent observations accelerate decay: the anti-Zeno effect. *Nuovo Cim.*, 15A:689, 1973.

[81] P.L. Knight. The quantum Zeno effect. *Nature (London)*, 344:493, 1990.

[82] A.G. Kofman and G. Kurizki. Frequent observations accelerate decay: The anti-zeno effect. *Z. Naturforsch. A*, 56:83, 2001.

[83] M.C. Fischer, B. Gutiérrez-Medina, and M.G. Raizen. Observation of the Quantum Zeno and Anti-Zeno effects in an unstable system. *Phys. Rev. Lett.*, 87(4):040402, 2001.